Crustal Electrical Resistivity Structure of the Sikkim Himalaya

A Thesis submitted in partial fulfillment of the requirements

for the degree of

Doctor of Philosophy

in

Earth and Space Sciences

by

Pavan Kumar Gayatri

(08ESPE05)

Centre for Earth and Space Sciences

University of Hyderabad

Hyderabad – 500 046

February, 2014

DECLARATION

I hereby declare that the matter embodied in the thesis entitled "**Crustal Electrical Resistivity Structure of the Sikkim Himalaya"** is the result of investigation carried out by me in the Centre for Earth and Space Sciences, University of Hyderabad, India, under direct supervision of Dr. Ajay Manglik, Senior Principal Scientist, CSIR-National Geophysical Research Institute, Hyderabad and Prof. K.PN. Murthy, School of Physics, University of Hyderabad, Hyderabad. This work has not been submitted for any other degree or diploma either in part or in full to this or to any other University or Institution.

Place: Hyderabad (G. Pavan Kumar)

CERTIFICATE

This is to certify that the work described in this thesis entitled "**Crustal Electrical Resistivity Structure of the Sikkim Himalaya"** is the bonafide work carried out by **Mr. G. Pavan Kumar**, under our direct supervision and this has not been submitted for any degree or diploma at this or any other University.

(**Prof. K.P.N Murthy**)
Co-Supervisor
School of Physics &
Centre for Modelling Simulation & Design
University of Hyderabad, Hyderabad

(**Dr. Ajay Manglik**)
Research Supervisor
Senior Principal Scientist
CSIR-National Geophysical Research Institute, Hyderabad

Head
Centre for Earth and Space Sciences
University of Hyderabad
Hyderabad

Place: Hyderabad

Date:

Contents

List of Figures

List of Tables

List of Publications/presentations/Technical reports

Research Papers

- **Pavan Kumar, G**. and Manglik, A., 2011. Effect of Himalayan topography on MT data interpretation. *Current Science*, 100(3): 390-395

- **Pavan Kumar, G** and Manglik A., 2012. Electrical anisotropy in the Main Central Thrust Zone of the Sikkim Himalaya: Inference from anomalous MT phase, *J. of Asian Earth Sci*., 57: 120–127

- Manglik, A., **Pavan Kumar, G**. and Thigarajan, S. 2013. Transverse Tectonics in the Sikkim Himalaya : A magnetotelluric study, *Tectonophysics*, 589: 142–150

- **Pavan Kumar, G**., Manglik, A. and Thigarajan, S. 2013. Crustal Geoelectric structure of Sikkim Himalaya and adjoin Ganga foreland basin, *Tectonophysics*. (under review)

Presentations in Workshops/ Conferences

- Manglik A., **Pavan Kumar G**., Arora T. and Suri R. 2010. Mapping of subsurface extension of the Aravalli Delhi Mobile Belt in Haryana, India. 20th EM Induction workshop, Sept.18-24, Giza, Egypt.

- **Pavan Kumar G**. and Manglik A., 2010. Anomalous magnetotelluric phase exceeding 90^{o} in the Main Central Thrust Zone, Sikkim Himalaya. 20th EM Induction workshop, Sept.18-24, Giza, Egypt.

- Manglik A., **Pavan Kumar, G.,** 2010. Crustal structure of the north Sikkim Himalaya by Magnetotellurics studies. IUGG General Assembly, June 28- July 07,2011. Melbourne, Australia.

- **Pavan Kumar G**., Manglik A., 2010. Electrical anisotropy in the Main Central Thrust Zone of the Sikkim Himalaya. IUGG General Assembly, June 28- July 07, 2011. Melbourne, Australia.

- Swetha G., **Pavan Kumar, G**. and Manglik, A., 2011. Intraplate stress analysis using Comsol multiphysics. Comsol India workshop, Nov. 4-5, Bangalore, India.

- **Pavan Kumar G.**, Peush, Manglik A., Kapil Mohan, Singh A.P. and Rastogi B.K., 2013. Shallow subsurface resistivity mapping in central part of Cambay basin, Ahmedabad using Time Domain Electromagnetic method , Near Surface Geophysics, Jan 27-29, Hyderabad, India

- **Pavan Kumar G** and Manglik A., 2013. Impedance tensor analysis for identification of transverse tectonic features in the Sikkim Himalaya, Advances in Earthquake Sciences, Feb.1-3, Gandhinagar

Technical Reports

- Manglik, A., Thigarajan, S., **Pavan Kumar, G**. and Bindu, P., 2012. Lithospheric structure of the Sikkim Himalaya by long period magnetotelluric investigations. NGRI Tech. Rep. Nr. NGRI-2012-lithos-xxxx-29pp.

- Manglik A., **Pavan Kumar G**., Swetha G., and Bindu P., 2010. Magnetotelluric investigations around Kaithal for an earth electrode station site in Haryana for a 500kV HVDC transmission system. NGRI Tech. Rep. Nr. NGRI-2010-LITHOS-xxx, 21 pp.

- Manglik A., Arora T., **Pavan Kumar G**., and Swetha G., 2010. Geophysical investigations of an earth electrode station site at Bhiwani, Haryana, for 500kV HVDC transmission system. NGRI Tech. Rep. Nr. NGRI-2010-LITHOS-722, 20 pp.

- Manglik A., Muralidharan D., Arora T., Ramakrishna N., **Pavan Kumar G**., Mahaveer Mann, Rajakishore K.V. and Praveen Kumar, 2010. Geophysical investigations of an earth electrode station site at Mahendragarh, Haryana, for 500kV HVDC transmission system. NGRI Tech. Rep. Nr. NGRI-2010-LITHOS-723, 27 pp.

- Manglik A., Muralidharan D., Arora T., Sathyanarayana U.S., **Pavan Kumar G**., Mahaveer Mann, and Praveen Kumar, 2010. Geophysical investigations of an earth electrode station site at Mundra, Gujarat, for 500kV HVDC transmission system. NGRI Tech. Rep. Nr. NGRI-2010-LITHOS-724, 28 pp.

ACKNOWLEDGEMENTS

I express my gratitude to Dr. Ajay Manglik, Senior Principal Scientist, CSIR-National Geophysical Research Institute, Hyderabad, and Prof. K.P.N. Murthy, Professor, Department of Physics, University of Hyderabad, for their supervision, advice, inspiration and guidance during the course of research work as well as providing me unflinching encouragement and support in various ways.

I am thankful to Prof. K.V. Subba Rao, Prof. A.C. Narayana previous Directors and Dr. K. Chakravarthi, present Director, and Dr. (Ms.) S. Srilakshmi, faculty, Centre for Earth and Space Sciences, for their keen interest in the work and constant encouragement.

I am grateful to Dr. V.P. Dimri, Prof. Mrinal K. Sen, previous Directors, and, Dr. Y.J. Bhaskar Rao present Acting Director, CSIR-National Geophysical Research Institute, Hyderabad, for their constant encouragement and support during my tenure in CSIR-NGRI and Ph.D. work.

I joined Institute of Seismological Research (ISR), Gandhinagar in 2012. Dr. B.K. Rastogi, Director General, ISR, very kindly permitted me to continue with my Ph.D. work. I am extremely grateful to him for his support and encouragement.

The work carried out in the present thesis involved extensive magnetotelluric field survey in Sikkim and West Bengal which was supported under a project [ESS/16/272/2006] sponsored by Department of Science and Technology (DST), Govt. of India. Dr. S.K. Verma and Dr. Ajay Manglik (CSIR-NGRI) initiated this project. I thank them for giving me an opportunity to work under this project as a project JRF. The financial support provided by DST is gratefully acknowledged. The field survey also required permissions from various State Govt. Agencies and Defense Establishment. I thank Sikkim State DST, Home Dept., Forest Dept., and various other Agencies as well as Indian Army for according permission to us for setting up MT sites in restricted and protected areas.

I am extremely grateful to Dr. S. Thiagarajan, Senior Technical Officer (3), CSIR-NGRI, for his continuous help, friendly nature and encouragement during entire work. Dr. Tanvi

Arora for her help in field survey. The support given by P. Bindu, G. Swetha and K.V. Rajakishore during my work and other field related matters is gratefully acknowledged.

Several friends, V. Sai Kiran, P. Mahesh, P.Gopala Krishna, B. Vijay Kumar and P.L Srinivasa Rao deserve much credit for their advice, help and moral support throughout the years.

I am especially indebted to my parents (AMMA, NANNA), Brother (Srihari Prasad), Sisters (Srilakshmi Rajeswari and Ramavalli) and brothers-in-laws (Venkat and Anand) for their blessings, tolerance, their belief in me, their understanding and patience over the past years.

(PAVAN KUMAR GAYATRI)

Date:

Summary

The Himalayan collision belt is a unique natural laboratory to understand the process of continent-continent collision and to test probable models of earthquake genesis in a convergent environment. The region offers vast opportunities to all sub-disciplines of earth system science to explore various aspects. Several diverse geophysical experiments have been carried out in different segments of the Himalaya to delineate the deep structure of the region and to understand the evolutionary processes as well as earthquake genesis. These studies have provided valuable insights for crustal and mantle architecture, identification of seismically active zones, causes for recurrent seismicity, seismic hazard scenario, and dynamics of various tectonic blocks.

An important inference that can be drawn from synthesis of these studies is that the eastern Himalaya seems to be having a different geotectonic setup than the western and central Himalaya and the seismotectonic models of continental collision, proposed mainly based on the data from the western Himalaya, might not be suited to the eastern Himalayan segment. However, majority of geophysical studies have been concentrated in the western and northwestern part of the Himalaya and very little work, barring seismological studies, have been carried out in the eastern region.

The Sikkim Himalaya in eastern part of the Himalayan collision belt is one such place known for its recurrent moderate to strong magnitude earthquakes and distinct geotectonic setup. This region, like other parts of the Himalayan collision belt, exhibits four major geological sub-domains namely Sub Himalayan Domain (SHD), Lesser Himalayan Domain (LHD) High Himalayan Crystallines (HHC) and Tethyan Sedimentary Sequence (TSS). SHD

in the south overrides Quaternary deposits of the Indo-Gangetic alluvium, termed as Ganga Foreland Basin (GFB). These sub-domains are separated from each other by major thrust faults namely Main Frontal Thrust (MFT), Main Boundary Thrust (MBT), Main Central Thrust (MCT) and South Tibetan detachment (STD) respectively. However, there are some issues related to the geo- and seismo-tectonics of the region. For example, (i) structure of the Sikkim dome and its role in the exhumation process, (ii) subsurface location of MBT, MCT-1, MCT-2 and other major faults to constrain the estimates of the strain accumulation through crustal shortening for earthquake hazard assessment, (iii) deep crustal and sub-crustal structure of the region in terms of different tectonic blocks, etc. These necessitate extensive geophysical surveys that can add significantly to the state of knowledge of the region. The present work is motivated by this data gap and has been undertaken with the view to delineate the detailed crustal structure of the Sikkim Himalaya in terms of electrical resistivity image because electrical conductivity is very sensitive to the presence of fluids expected in tectonically active regions. Magnetotelluric (MT) method is a useful technique to delineate the electrical image of the crustal structure. Therefore, the present work deals with MT study in the Sikkim Himalaya.

In the present study, MT data in broad frequency range (0.001 - 4096s) were acquired at 48 sites during 2008-2011 along an approximately north-south 200 km long profile that starts from south of Siliguri in the north Bengal basin and ends in north Sikkim at an altitude of ~5km. It traverses the major geotectonic domains of the region. The average distance between two successive MT sites is about 5-6km. At every site, MT time series were recorded for about one week duration. We used Pb-$Pbcl_2$ electrodes and induction coil magnetic field sensors (MFS-06) for measuring the horizontal components of electric(E_x, E_y) and both horizontal and vertical magnetic fields components (H_x, H_y, H_z), respectively. The recorded timeseries were preprocessed to estimate the impedance tensors $(\mathbf{Z})$, defined as the ratio of the measured horizontal **E** and **B** fields. After preprocessing, we selected impedance tenors of 31 sites based on the data quality for further analysis and modeling. Groom-Bailey (GB) tensor decomposition technique and phase tensor (PT) analysis were performed to estimate possible 3-D affects in the recorded MT data and recover regional 2-D impedances and regional strike of the region. The distortions due to 3-D local inhomogeneities present in the data in terms of shear, twist and anisotropy were corrected using GB decomposition technique. The regional geoelectric strike was estimated for both single-site multi-frequency

(SSMF) and multi-site multi-frequency (MSMF) modes. The analyses yield a regional geoelectric strike direction of N5^{o}E that is consistent with the strike of the under-thrusting Indian plate within the 90^{o} ambiguity limit of the MT strikes. The observed impedance tensors of 31 sites were then decomposed into TE- and TM-modes after fixing the regional strike direction to N95^{o}E to get the distortion corrected TE- and TM-mode data for 2-D inversion. The TE-mode is aligned in N95^{o}E direction, the strike of the Indian plate, and TM-mode is orthogonal to it.

The detailed strike analyses of the entire dataset by GB and PT approaches show some interesting features. The local strikes estimated by SSMF analysis as well as the RMS errors of misfit of each site obtained after MSMF approach provide evidence for dominant transverse tectonic features in the MCTZ. The strike estimates from PT approach at large periods also provide supportive evidence for transverse strike in the region. Here, major axes of the phase ellipses for the sites in MCTZ are oriented in NNW-SSE direction. We have correlated these results with the aftershock data of 18th September 2011 strong Sikkim earthquake (Mw 6.9, focal depth 50km). The epicenters of these aftershocks align in NNW-SSE direction and the focal mechanism of the main shock reveals strike-slip motion on a steeply dipping fault indicating the presence of transverse nearly vertical fault in this region. The present MT results corroborate the predominance of transverse tectonics in the Sikkim Himalaya, especially in MCTZ region. Further, a close observation of strikes in GFB exhibits strike direction at shallow levels different from that at the deeper levels.

The TE- and TM-mode impedances were of all 31 sites were then inverted jointly by using 2-D inversion algorithm of Rodi & Mackie (2001) to construct a model of the subsurface resistivity distribution. The algorithm is based on the nonlinear conjugate gradient method (NLCG) and computes regularized solution of a 2-D MT inverse problem based on Tikhonov regularization scheme. Smoothing parameter (τ) was estimated from L-curve method. Other inversion parameters including error floors, half-space resistivity, weight parameters etc., were appropriately set. A half-space of 100 Ω-m resistivity, digitized into a non-uniform finite difference mesh of 180 rows and 180 columns, was considered as the initial model for joint inversion of the data. The RMS error decreased very fast within the initial iterations and then convergence was gradual. We stopped the inversion after 120 iterations beyond which the RMS error of 3.0 remained almost stable. After inspecting the site-specific RMS errors, three sites contributing very large errors to the total RMS error were removed and the

inversion exercise was performed for the remaining 28 sites. The final RMS error now reduced to 2.5. Constrained inversions and sensitivity analyses for the final inverted model were performed to check the robustness of the salient features in the final model. These analyses suggest that the majority of features observed in the model are robust and sensitive to the observed data.

The delineated crustal geoelectric structure reveals several interesting features. GFB shows the presence of a 4-6 km thick sedimentary layer overlying the basement (top of the Indian plate). The LHD consists of an assemblage of conductive and resistive blocks down to about 15km depth, below which the resistivity is moderate. The conductive zone at the profile location of about 100km coincides with the Rangit Window exposing Gondwana rocks. The MCTZ occurs as a resistive nearly vertical zone bounded by two thrust planes. A moderate decrease in the resistivity within this zone at the depth of 20-30km could be due to the Main Himalayan Thrust (MHT) but it is not resolve in the 2-D section. We therefore attempted the inversion of the data set incorporating transverse feature inferred in the MCTZ. The computed model shows a high conductivity zone (< 20 Ω.m) at depth of 20-22km beneath MCTZ. The location of the conductive zone correlates well with the projection of MHT obtained by INDEPTH study (International Deep Profiling of Tibet and Himalaya), further north to this region.

The 2-D results also reveal the presence of a conductive zone in the High Himalayan Crystallines (HHC) north of MCTZ. We infer that this conductive zone could be due to possible presence of partial melts linked to mid-crustal fluids beneath southern Tibet or sedimentary rocks at depth of the Tethyan sequence exposed north of STDS. A correlation with the depth distribution of seismicity for the region reveals that a fault within LHD, rather than MBT as suggested earlier, could be the main seismogenic fault causing recurrent seismicity in the region. The surface location of this inferred fault correlates with the Ramgarh Thrust along which Gondwana rocks are exposed in the Rangit Window.

A close look of the estimated apparent resistivity and phase vs. period curves reveals anomalous behavior of phase exceeding 90^{o} at some sites. Interestingly, these sites are situated in the vicinity of major faults in the region. In particular, a site located at the northern boundary of the MCTZ, close to MCT-1 exhibit anomalous phase for frequencies smaller than 1 Hz whereas other sites further north and south of the site show normal behavior. Such anomalous phase behavior has been explained earlier in terms of strong anisotropy in the

medium and special configuration of local 3-D conductors leading to current channeling. We observed that there is an enhancement of magnetic field at the anomalous site compared to neighboring site. We, therefore corroborate the channeling of telluric currents leading to the filed enhancement. We analyzed the observed anomalous phase behavior in terms of electric anisotropy because local geology of the region supports the presence of alternating bands of graphitic schists within high-grade crystalline gneisses. The anisotropic strike has been estimated through study of the vertical and horizontal magnetic field measurements at these two successive sites, which are time synchronous. Among various models analyzed, a model with strong anisotropy contrast between a shallow anisotropic block and an underlying anisotropic layer provides good fit to the observed data. We, thus, infer the presence of a localized strongly anisotropic block at the northern boundary of MCTZ to explain the observed anomalous phase behavior.

In view of the findings from the detailed local and regional strike analyses and current channeling effects observed at some sites, we infer that the structure of the Sikkim Himalaya is highly complex. MT data acquisition suitable for 3-D analysis, subject to accessibility to suitable sites in this tough terrain, could be attempted to resolve the 3-D nature of the subsurface structure, especially that of MCTZ. In addition, the upper crustal anisotropy with high value of anisotropic ratio inferred in the MCTZ necessitates the MT data inversion for 2-D anisotropic models might enhance understanding/state of knowledge on the region.

Thesis Architecture

The thesis consists of eight chapters.

Chapter1 introduces the general geology and tectonics of the Himalayan collision belt. A brief note on the seismicity scenario of the region and proposed seismotectonics models of the Himalaya is included in this chapter. The chapter also describes some of the geophysical studies carried out in the region and concentrates on MT studies in different segments of the Himalaya belt. In subsequent discussion, the chapter introduces the main objective of the present work and motivation. The salient geological, geophysical and seismological results highlighting the complex geotectonic scenario of the Sikkim Himalaya region are discussed. Finally, the chapter concludes with the work plan.

In *chapter 2,* a description of the general geology and tectonics of the Sikkim Himalaya is presented. A detailed discussion on seismological studies carried out in the Sikkim Himalaya

and outcome of the work including seismotectonic model of the region is presented. Finally, the chapter describes the finding of various geophysical studies carried out in the region.

To achieve the goal of the present work, we used MT method. The method gives the information about the deep structure of the Earth in terms of its resistivity by using the natural time-varying electromagnetic signals measured on the surface. *Chapter 3* contains detailed description on the MT method, inversion and MT data processing. In the first section, mathematical theory of MT is presented. The chapter also deals with the various types of boundary conditions and 2-D formulation of MT. In subsequent sections, the chapter describes the basics of time series processing and elaborates on the steps for estimation of earth response functions from observed data. Finally, the chapter brings out the concept of geophysical inversion and a brief note on some of the 2-D inversion algorithms proposed by various researchers for modeling of MT data including presently used 2-D MT nonlinear conjugate gradient scheme of Rodi & Mackie (2001).

In *chapter 4*, MT field survey, sources of noise, sensors and recording unit, data acquisition and various types of frequency bands used are discussed in detail. The total MT field survey, various field sessions, recording duration and processing of the MT timeseries to estimate the earth response function are discussed subsequently. The apparent resistivity and phase vs. period curves for some sites along the profile are shown in this chapter. A discussion on the data quality and broad observations from the observed apparent resistivity and phase curves is also included in this chapter.

In general observed MT data are distorted by local 3-D imhomogneities leading to galvanic and inductive effects. It is therefore necessary to minimize these distortions before inverting the data. *Chapter 5* brings out the distortion analyses of observed impedance tensors following brief introduction of decomposition methods used in the present study. We have used three types of decomposition techniques, namely LaTorraca (LT) decomposition technique (LaTorraca *et al.* 1987), Groom-Bailey (GB) decomposition scheme (Groom & Bailey, 1989) and Phase tensor (PT) approaches (Caldwell *et al.* 2004). The GB method extended for multi-site multi-frequency (MSMF) method is implemented in a code known as ‘strike’(McNeice & Jones, 2001). This code is used to estimate the decomposed regional 2-D impedance tensors and to estimate the tensor principal direction. A brief discussion of the strike code is presented in this chapter. After decomposition analysis of the processed data, the average geoelectric strike of the region for the entire profile and strike directions for

various tectonic domains is estimated. Detailed strike analyses of the data are presented in this chapter. Finally, the chapter concludes with the analyses of distortion parameters and comparisons of local/regional strikes estimated from the GB and PT techniques. Strong evidence for transfer tectonic features in the MCTZ and interpretation along with existing seismological observations are presented in this chapter. After finding the geoelectric strike, the impedance tensors are decoupled into transverse magnetic (TM-mode, perpendicular to strike) and transverse electric (TE-mode, parallel to strike) modes.

In *chapter 6*, 2-D inversion of the MT data is discussed. We have used the 2-D inversion code of Rodi & Mackie (2001). The code is implemented in a data interpretation package *WinGLink*. A brief discussion of various inversion parameters used in the code is presented. Joint TE- and TM-mode inversion results and their interpretation in terms of geology and tectonics are discussed in this chapter. Individual TE and TM inversion results are also presented in this chapter. The chapter also contains detailed sensitivity analyses along with results of constrained inversion. The chapter brings out interpretation of the 2-D geoelectric structure of the Sikkim Himalaya and adjoining Ganga Foreland Basin with regional geology, tectonics and seismicity.

Chapter 7 introduces the concept of current channeling and phenomenon of MT impedance phases leaving quadrant. This chapter mainly describes the analysis of anomalous phase behavior observed at a sites located in the proximity of the northern boundary of MCTZ. 2-D anisotropic forward modeling and comparison of the synthetic response with field data is discussed in this chapter.

C*hapter 8* summarizes the major results obtained in the present study and the scope for further extension of the work.

x-x-x-x

Chapter 1

Introduction

The Himalayan mountain belt formed by recent mountain building activity in the earth's history configures an arc extending from Kashmir in North-West to Arunachal Pradesh in North-East. The mountain belt and adjoining Tibetan Plateau in its north at an average elevation of 5km are the two important regions globally for studying the diverse geological processes related to mountain building, crustal and lithospheric structure, geodynamics and seismicity.

1.1 Evolution of the Himalayan mountain range

Earlier, it was considered that the Himalayan mountain belt is a consequence of simple collision between two continents, India and Asia, via the concept of continental drift before the hypothesis of plate tectonics (Gansser, 1964; Dewey & Bird, 1970). According to the hypothesis of plate tectonics (Wegener, 1912), the Earth's outer shell called lithosphere consists of several plates, which are in constant motion travelling at a speed of a few centimeters per year. These plates converge, diverge, or slide past each other forming different plate boundaries. These plate boundaries are the sites of intense tectonic activities such as earthquakes, volcanoes and mountain building. The earth's crust and upper most part of the mantle down to average 100 km depth constitute the lithosphere.

The Indian and the Eurasian plates are two such plates among the seven major tectonic plates (Wilson, 1965; McKenzie & Parker, 1967; Morgan, 1968; Kious & Tilling, 1994) in the present Earth. The Indian plate, constituted of India and Australia and a very large oceanic domain, is considered as one of the active tectonic plates. This plate moved northward at a high speed of 18-20 cm/yr after breakup of the Gondwanaland (possibly due to heating of the lithosphere by a large plume (Kumar *et al.* 2007) and the Tethys ocean north of the Indian continental mass subducted beneath the Eurasian plate at shallow angle. The

Tethys ocean basin got progressively narrowed until about 50 millions years at which time the subduction phase got over and the Indian continental mass collided with the Eurasian plate (Gansser, 1964; Powell & Cohaghan, 1973; Lefort, 1979; Bird, 1978, 1983, Molnar, 1984; Lyon-Cean & Molnar, 1985). Further convergence occurred as continent-continent collision and the speed of the Indian plate has been reduced to about 5 cm/yr (Minister *et al.* 1974; Molnar, 1984). The continued convergence between India and Eurasia led to the formation of about 2500km long arc of the Himalayan mountain belt encompassing the Tibetan Plateau having average elevation of 5km. The Himalayan mountain belt hosts several high peaks of the world (10 among 14 peaks above 8000m elevation above mean sea level with Mt. Everest at 8848m elevation) and exhibits intense seismicity along the entire arc.

Many researchers have proposed plate tectonics models explaining the evolution and tectonic fabric of the Himalayan mountain belt (Gansser, 1964, 1979; LeFort, 1979; Molnar *et al.* 1977; Molnar & Gray, 1979; Seeber *et al.* 1981; Seeber & Armbruster, 1981; Valdiya, 1976, 1980, 1981; Barazangi & Ni, 1982; Ni & Barazangi, 1984; Molnar & Lyon-Caen, 1988, 1997). The common inferences among these models are that the early convergence took place along the Indus-Tsangpo Suture which ended in Eocene (Tapponnier & Molnar, 1977). Subsequently, development of intra-continental crustal fractures within the Indian continent during middle Tertiary and uplift of Tibetan mass as a result of under-thrusting of the Indian continent from Miocene to Recent led to rise of the Himalaya. The estimated amount of total convergence at this plate boundary is about 2000 to 3000km (Molnar *et al.* 1977,1984) of which about 300-500km of convergence is expected to be accommodated by shortening within the Himalayan mountain belt (Gansser, 1977). Some estimates of the convergence suggest that, of the total convergence, 15-20mm/year is accommodated across the Himalaya and remaining convergence is adjusted farther north in Tibet and Central Asia (Peltzer & Saucier, 1996; Bilham *et al.* 1997; Feldl & Bilham, 2006).

An interesting feature of the Himalaya is the knee bends in the north-western and north-eastern ends of the mountain chain. At the north-western end, in Kashmir, the entire mountain system turns abruptly southwards from its NW trend making an acute angle (40^{o}) as a consequence of bending of the whole pile of rock formations and succession of faults and thrust planes giving rise to the concept of syntaxial bend (Wadia, 1931; Valdiya, 2010). The two syntaxial bends are characterized by mountain knots, the Naga Parbat (8125m) in the west and Namcha Barwa (7755m) in the east.

1.2 Geotectonic domains of the Himalaya

Stacking of the crustal slabs gave rise to the present architectural framework of the Himalaya (Molnar, 1984). Based the concept, several authors have divided the entire Himalayan belt into five physiographic litho-morpho-tectonic zones (domains) (Gansser, 1964; Powell & Conaghan, 1973; Valdiya, 1973; LeFort, 1975, 1996). These terrenes are considered to be physio-graphically contrasted and litho-structurally distinctive domains trending parallel to the range. These from north to south are: (i) Indus-Tsangpo (or Indus-Brahmaputra suture Zone), (ii) Tethys Himalaya (or Tibetan Himalaya), (iii) Higher (Greater) Himalaya, (iv) Lesser Himalaya, and (v) Sub (outer) Himalaya (Figure 1.01). Further south, the Foreland Basin of the Ganga-Brahmaputra plains, formed due to the flexure of Indian lithosphere, encompasses the Himalayan belt. These domains are separated from each other by major thrust faults which from north to south are: (i) Indus-Brahmaputra Suture Thrust (IST), (ii) South Tibet Detachment (STD), (iii) Main Central Thrust (MCT), (iv) Main Boundary Thrust (MBT) and (v) Main Frontal Thrust (MFT) or Himalaya Frontal Thrust (HFT) (Gansser, 1964; Nakata, 1972; Valdiya, 1973,1976; Powell & Conaghan, 1973; LeFort, 1975; Ni, 1989; Powers *et al.* 1998) (Figure 1.01). These thrusts are inferred to be formed as a result of the collision to accommodate the deformation due to continental convergence (Gansser, 1964; LeFort, 1975). Steady southward progression of the thrusting and faulting is proposed beginning with IST when the collision occurred in Eocene time. Subsequently, MCT was formed and slip of 100km occurred. Later, slip on MBT began with the cessation of activity on the MCT. Recently, approximately 100-150km of slip has occurred on MFT (Powel & Conaghan, 1973; Seeber *et al.* 1981; Lyon-Caen & Molnar, 1983; Molnar, 1984). LeFort (1975) deduced the ages of MCT and MBT as Miocene-Pliocene and Pliocene-Recent, respectively. All these thrusts run almost parallel over the entire strike of the Himalayan belt except in some regions where these are disturbed by transverse tectonic features and strike-slip faults.

Geographically the 2500km long Himalayan arc is also divided into five segments namely, (i) Northwestern Himalaya (Kashmir and Himachal Himalaya), (ii) Western Himalaya (Kumaun - Garhwal Himalaya), (iii) Central Himalaya (Nepal Himalaya), (iv) Eastern Himalaya (Sikkim and Bhutan Himalaya), and (v) Northeastern Himalaya (Arunachal Himalaya). Generalized geotectonic map of entire Himalayan arc is shown in Figure 1.01. In the following, I will discuss these geotectonics domains in brief starting from extreme north.

The Indus Suture Thrust or Indus-Tsangpo suture zone (ITSZ) and its western prolongation, the Main Mantle Thrust (Figure 1.01) is belonging to Cretaceous to Eocene period (Powel & Conaghan, 1973; LeFort, 1975). The morphotectonic zone in the extreme north of the Himalaya represents the convergent boundary between Indian and Eurasian plates. The 50-60 km wide highly deformed zone is characterized by presence of nearly vertical thrust faults and chain of 60-48 my old volcanic islands (some of the volcanoes are active until the late Quaternary period) which were squeezed up when the continents collided (Valdiya, 1973). The zone is made up of imbricated melanges of flysch sediments, radiolatite, pillow lavas, volcanic and basic and ultra basic rocks (Ni & Barazangi, 1984).

The Tethys (Tibetan) Himalaya (also known as High Himalaya sedimentaries, Tethyan Sedimentary Sequence (TSS)) the south of ITSZ comprises fossiliferous sediments deposited almost continuously in the Tethys basin from the Cambrian to the Eocene. The sequence occurs as a sedimentary cover on the High Himalaya Crystallines (HHC) on north of it. The meta-sedimentary rocks are in the domain are the distal correlatives of the Lesser Himalaya further south. The South Tibetan detachment system (STDS, also known as Trasns-Himadri fault, THF (Valdiya, 1976)) defines the boundary between Tethys Himalaya (or Tethys Sedimentary Sequence (TSS)) and Higher Himalaya Crystallines (HHC) in south.

Greater or Higher Himalaya Crystallines (HHC) south of TSS is of Precambrian to Tertiary period formed of crystalline terrain contains most of the famous peaks of the Himalaya mountain range (Mt. Everest, Kangchendzonga, Annapurna etc.). The HHC composed of high grade crystalline metamorphic rocks (schists and gneisses) and crystalline granites. The granites thrust over the lesser Himalaya Domain (LHD) on the Main Central Thrust (MCT) south of it (Sinha Roy, 1974; Le Fort, 1975; Valdiya 1976). The MCT at the base of the central crystalline zone dips northward at an angle of 30^{o}-45^{o} (Ni & Barazangi, 1984). The MCT (from mid-crustal level to the surface) is considered as a thick intracontinental thrusting ductile zone (Catlos *et al.* 2004, 2007). This range of Himalaya is primarily snow-capped and extremely rugged, rises to an elevation ranging from 3000m to more than 8000m.

Lesser Himalaya Domain (LHD) south of HHC is composed of metasediments mainly from Precambrian-Cretaceous and Lesser Himalaya Crystalline rocks from Precambrian-Lower Paleozoic. The meta-sedimentary rocks are thrust over the sub Himalaya on the imbricated Main Boundary thrust (MBT). The domain also has extremely rugged ranges

(with topography ranging between 1000-2500m) and is thickly forested. The Gondwana and the Siwalik Groups occur progressively south of the Lesser Himalaya (Gansser, 1964), i.e. MBT has detached the upper crustal rocks of the LHD from the crystalline basement (HHC). Some researchers considered the MBT as a series of steep thrusts planes that dip northward at 60^{o}-90^{o} and appear to flatten out at depth (Ni & Barazangi, 1984).

Sub Himalaya Domain (SHD) contains Siwaliks from Mid Miocene to Pleistocene, Tertiary mollase type deposits which over-thrust the foreland basin of Gangetic alluvium on the imbricated Main Frontal Thrust (MFT). This mountain province abruptly raises about the vast flat expanse of the Indo-Gangetic plans. 250-800m high Siwalik ranges from the southern front of the Himalaya consists of sediments deposited by ancient Himalayan rivers in their channels and flood plains in the last 16 my to 1.5 my (Valdiya, 2010). The neotectonic activity is reported along the MFT (Nakata *et al.* 1990, Thakur, 2008). Powers *et al.* (1998) suggested that the HFT/HFF is the primary surface expression of shortening between the Himalaya and the Indian plates at a rate of 6-16mm/yr (Kayal, 2001).

Foreland basin infront of the Himalaya mountain arc lie as a vast expanse of the alluvial plains built in the Holocene time by rivers of the Ganga, Brahmaputra and Sindhu systems. It mainly consists of Indian basement and Paleozoic platform sediments overlain by Tertiary to Holocene sediments. The Plain extends 3200 km from the southern limit of Ganga-Brahmaputra delta in the east to the terminal of the Sindhu delta and the Rann of Kachchh, Gujarat in the west.

In the Himalaya literature, the politically geographically, structurally and stratigraphically defined Himalaya is often assumed to be interchangeable. So in view of the interchangeable relationship, this domain can be stated as (Yin, 2006) follows;

Domain	**Structurally Defined**	**Lithologically Defined**	**Topographically defined**
SHD	MBT footwall	Siwaliks	Sub-Himalaya
LHD	MBT hanging wall	Lesser Himalaya	Lower Himalaya
HHC	MCT hanging wall	Higher Himalaya Crystallines	Great or Higher Himalaya
TSS	STD hanging wall	Tethyan Sedimentary sequence	Tethyan Himalaya

1.3 Seismicity and broad seismotectonic models of the Himalaya

1.3.1 Seismicity

The Himalayan collision belt is one of the most seismically active regions of the world that has frequently experienced devastating earthquake since the historical past (Oldham 1882; Gutenberg & Richter, 1954; Chandra, 1992). The belt was rocked by two great earthquakes ($M \geq 8$) that occurred along the arc within fifty-five years (1897-1950). These are:, Bihar-Nepal Earthquake (1934/01/05, M 8.1), and Assam earthquake (1950/08/15, M 8.7). Another great earthquake took place at Shillong (1897/06/12, M 8.7) in the vicinity of the Himalayan arc. Besides, some strong and major ($6 \leq M < 8$) earthquakes also shook this region causing huge loss of lives and property. These are: Kangra Earthquake, NW India (1905/04/04; M 7.8); Bihar-Nepal boarder (1988/08/20, M 6.6), Uttarkashi earthquake (1991/10/20, M 6.6), Chamoli Earthquake (1999/03/28, M 6.8), Kashmir earthquake (2005/10/08, M 7.6), and Sikkim-Nepal earthquake (2001/09/18, M 6.9) (Figure 1.02).

The active seismicity in the region is attested to current tectonic/geodynamic activity. Since the mountain building process is still under progress, the seismic activity in the Himalaya collision belt is attributed to continued collision between the Indian and the Eurasian plates. Underthrusting of the Indian plate beneath the Himalaya causing stress buildup in the entire length of the mountain arc. This stress is being released in the form of earthquakes of various magnitudes (Dewey & Burke, 1973; Minster *et al*. 1974; Molnar & Tapponnier, 1975, 1978; Bilham, 2000). Molnar & Chen (1982) have explained the seismicity as indicative of active deformation in the wide region between Indian and Eurasian plates and is directly associated to the convergence of these plates. There are some transverse strike-slip faults cutting the arc into different segments and causing lateral displacement of the arc along these faults. Valdiya (1976) suggested that transverse faults cutting the arc into different segments might be causing later displacements of the arc and could be zones of localized stress concentration causing earthquakes.

The high level of seismic activity and associated hazard potential of the Himalaya makes this region a frontier area for geoscientists and geotechnical engineers to understand the mechanism of stress buildup and release as seismic energy on one hand and to develop technologies for hazard mitigation on the other hand.

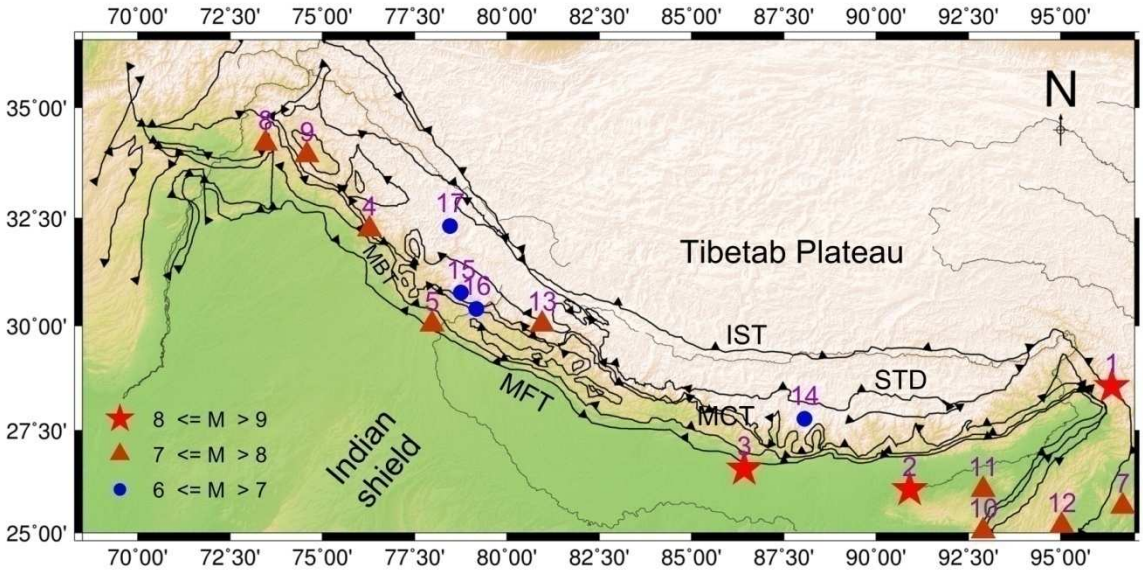

Figure 1.02: Map showing location of the great and significant earthquakes in the Himalayan region listed in Table 1.0

Table 1.01: List of significant earthquakes in last two centuries along the Himalayan arc

Sr. Nr	Date	Lat.	Long.	Mag.	Location
1	Aug. 15, 1950	28.5	96.5	8.7	Assam, Northeast Himalaya
2	Jun. 12, 1897	26.0	91.0	8.1	Shillong,NE India
3	Jan. 15, 1934	26.5	86.5	8.1	Bihar-Nepar Boarder, Central H.
4	Apr. 04, 1905	32.3	76.3	7.8	Kangra,Northwestern H.
5	Sept. xx.1803	30.0	78.0	7.7	Kumaun Himalaya
6	Jul. 08, 1918	24.5	91.0	7.6	Srimangal, NE India
7	Jan. 27, 1931	25.6	96.8	7.6	Assam, NE India
8	Oct. 08, 2005	34.4	73.5	7.6	Kashmir, Wester Himalaya
9	May. 30, 1985	34.1	74.6	7.5	Kashmir, Wester Himalaya
10	Jan. 10, 1869	25.0	93.0	7.4	Cachar, NE India
11	Oct. 23, 1943	26.0	93.0	7.2	Assam, NE India
12	Aug. 06, 1988	25.1	95.1	7.2	Manipur,NE Inida
13	Aug. 28, 1916	30.0	81.0	7.1	Darchula, Northwestern H.
14	Sept. 18, 2011	27.7	88.1	6.9	Sikkim, Northeastern H.
15	Oct. 19, 1991	30.8	78.8	6.8	Uttarkashi, Northwest H.
16	Mar. 28, 1999	30.4	79.2	6.5	Chamoli, Northwest H.
17	Jan. 19, 1975	32.4	78.5	6.1	Kinnaur, Northwestern

1.3.2 Seismotectonic models of the Himalaya

Several published studies of fault plane solutions of earthquakes occurred in the Himalaya region give general pattern of thrust faulting, with one plane dipping gently beneath the Himalaya (Molnar *et al.* 1973; Rastogi *et al.* 1973; Armbruster *et al.* 1976; Tandan & Srivastava, 1975; Chen & Molnar, 1977; Ni & Barazangi, 1984). The solutions of the earthquakes in the Himalaya in general imply that thrust faulting is consistent with the Indian subcontinent undethrusting the Himalaya at shallow angle and also imply that the processes that formed the Himalaya are continuing. Based on the nature of faulting and their parameters tectonic models for the evolution of the Himalaya have been proposed. Among these, two conventional models are proposed to describe the contemporary seismicity and tectonics of the Himalaya (e.g. LeFort, 1975; Seeber *et al.* 1981; Ni & Barazangi, 1984; Valdiya, 1984). The main tectonic features of the models are:

i) ***Plane of Detachment***- low-angle (shallow dipping) thrust that extends beneath the Foredeep, SHD and LHD. The detachment plane separates the Himalaya sedimentary wedge from the Indian shield basement.

ii) ***Basement Thrust*** - A steeply dipping thrust that juxtaposes the basement of the Indian shield with the Tethyan slab; the pre-collision leading edge of the Indian shield (Powell, 1979).

iii) ***Basement Thrust Front*** - The transition between the *plane of detachment* and the *basement thrust*.

These are the major features of the Himalayan tectonics and underlying causes for the prominent surface features, e.g. (a) the high topographic gradient between the Lesser Himalaya and the Higher Himalayas, and (b) the surface trace of the MCT. Based on these tectonic features and knowledge of the teleseismic events, two seismotectonic models have been suggested. These are (i) *Steady-state model*, and (ii) E*volutionary model*.

(a) Steady-state subduction model

Seeber & Armbruster (1981) and Seeber *et al.* (1981) proposed a hypothesis for the occurrence of strong to great earthquakes in the Himalaya based on the concept of detachment and steady-state tectonics known as steady-state model (Figure 1.03). The model comprises a subducting slab (the Indian shield) an overriding slab (the Tethyan slab), and a sedimentary wedge that is decoupled from the two converging slabs. They proposed an interface between the subducting slab (top surface of the northward thrusting Indian plate)

and the sedimentary wedge (southward propagating thrust wedges of the Himalayan strata) underlying the entire Himalaya, known as the plane of detachment (decollement). They analyzed the teleseismic hypocentral data of the Himalayan region and proposed that the Himalayan earthquakes are associated with the plane of detachment and MBT and MCT converge at depth with the plane of detachment. In this model, MBT and MCT are active thrust faults and contemporaneous features.

In addition to plane of detachment, they further identified an interface between the Tethyan slab and under-thrusting Indian plate, termed as the basement thrust. The zone between the plane of detachment and the basement thrust, known as the Basement Thrust Front (BFT), coincides with the high topographic gradient between LHD and HHC. Lyon-Caen & Molnar (1983) and Pandey *et al.* (1995) proposed that the change in the elevation as well as the steep dip of MCT is caused by 'ramping' of the Himalayan crust over the northern edge of the Indian plate. The BFT in the steady-state model coincides with this ramp and is inferred to be responsible for occurrence of moderate magnitude earthquakes in the region.

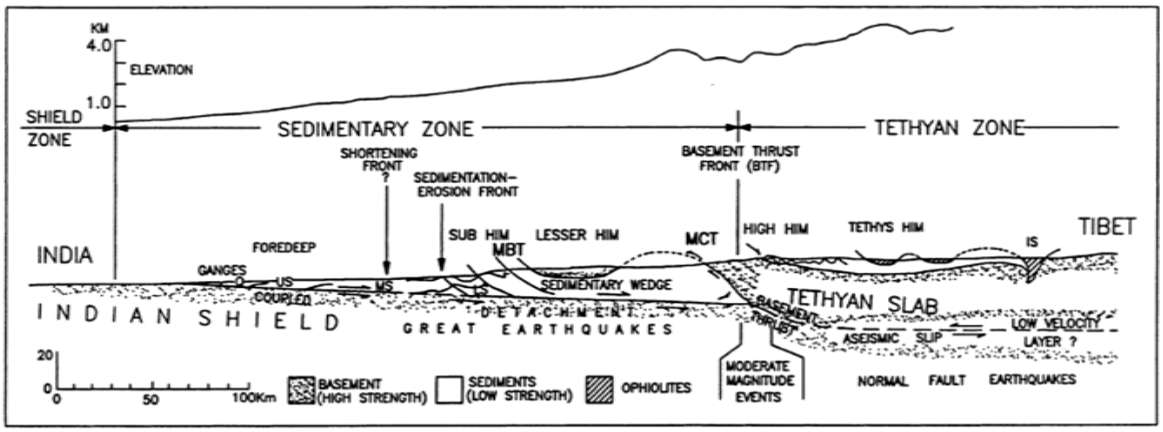

Figure 1.03: Steady-state tectonic model of the Himalaya; Q: Quaternary, US, MS,and LS: Upper, Middle and Lower Siwalik IS: Indus Suture (modified by Kayal, 2001 from Seeber *et al.* 1981; Valdiya, 1988).

The existence of decollement beneath the sub-Himalaya was recognized by several workers (Powers *et al.* 1998; Schulte-Pelkum *et al.* 2005). A decollement underneath the Tethys Himalaya, Tsangpo Suture Zone and southern Tibet was imaged in seismic reflection and magnetotelluric surveys of the INDEPTH project. It was named as the Main Himalayan Thrust (MHT) (Nelson *et al.* 1996; Brown *et al.* 1996).

(b) Evolutionary model

Ni & Barazangi (1984) proposed a seismotectonic model of the Himalaya based on the evolutionary model of Powell & Conaghan (1973). In this model, they suggested that ruptures of the great Himalaya earthquakes may have started in the inter-plate thrust zone and propagated south of MBT along the plane of detachment. According to the model, MCT and MBT are similar but are successive tectonic boundary thrusts. The southern thrust zone, MBT is the recently developed boundary of the continental convergent zone while the older thrust zone, MCT is a less active and dormant feature. Most of the seismic activity in the region is clustered beneath LHD and is concentrated in a 50km wide zone lying between MCT and MBT, known as the Main Himalayan Seismic Belt (MHSB). All the larger earthquakes having thrust mechanism occurred within MHSB that gradually steepens northward beneath LHD. The model postulates that all Himalayan thrust earthquakes would occur along the detachment surface between the under-thrusting Indian plate and the upper Himalayan blocks whereas the Tibetan normal fault earthquakes would occur in the shallow crust as well as in the upper most mantle (Figure 1.04).

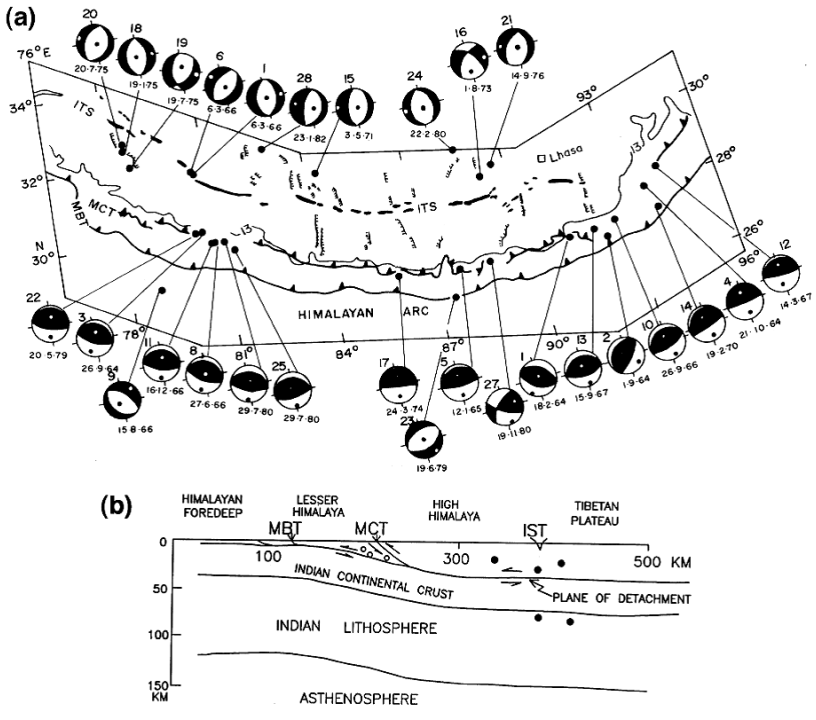

Figure 1.04: (a) Seismotectonic map of the Himalaya region showing thrust- fault regime to the south of MCT, and normal fault regime to the north in Tethyan slab (after Ni, 1989). (b) schematic diagram of the Evolutionary tectonic model of the Himalaya; open circles indicate earthquakes of thrust faulting and solid circles indicate earthquakes of normal faulting zones (Ni & Barazangi, 1984).

1.4 Micro-earthquake surveys in various parts of the Himalayan collision belt

Microseismic studies have contributed significantly in deciphering the seismicity patterns, demarcation of active faults and their seismic hazard potential as well as in furthering our understanding of the regional tectonics of the Himalayan collision belt. Although a number of microearthquake surveys have been carried out by various organizations, we briefly summarize only some of those available in published literature.

In the northwestern and western Himalaya (Kashmir, Himachal and Garhwal Himalaya) a number of microearthquake surveys have been carried out (Chatterjee & Bhattacharya, 1992; Khattri *et al.* 1989, 1992; Kayal *et al.* 1995, 1996; Kayal, 2001). These studies revealed that the high seismic activity was associated with MBT and a majority of earthquakes was of thrust faulting type. These events were occurred above the plane of detachment. The two significant earthquakes, Uttarkashi (Mb 6.6, Focal depth: 12km) and Chamoli (Mb 6.3; Focal depth: 21km) occurred on BFT by thrust faulting and the hypocenters are above the plane of detachment (Kayal, 2001). This seismic environment coincides well with the proposed steady state seismotectonic model of the Himalaya.

In the northeastern Himalaya, GSI has carried out microseismic surveys to understand the seismicity pattern in the region (Kayal *et al.* 1993; Bhattacharya & Kayal, 2001). The observed seismicity shows N-S trend and focal depths fall in the depth range of 15-80km, well below the trace of MBT. Such a seismicity distribution does not correlate with the proposed plane of detachment model. Further, composite fault plane solutions of some of the events show reverse faulting with strike-slip component. Kayal *et al.* (1993) inferred that an N-S trending deep-seated hidden fault could be a seismogenic fault in the region rather than MBT or MCT.

Similar to the northeastern Himalaya, the microseismic studies in the eastern Himalaya (Sikkim-Darjeeling Himalaya) also suggest distinct seismotectonic model for the region. A large number of earthquakes were located well below the plane of detachment (Figure 1.06). In this segment of the Himalaya, the deep-seated MBT, which does not converge with the plane of detachment, was inferred as responsible for the seismic activity. Composite fault plane solutions of some of the events also show dominant strike-slip faulting in the region (Kayal *et al* .2001; De & Kayal, 2003, 2004; Nath *et al.* 2005; Hazarika *et al.* 2010).

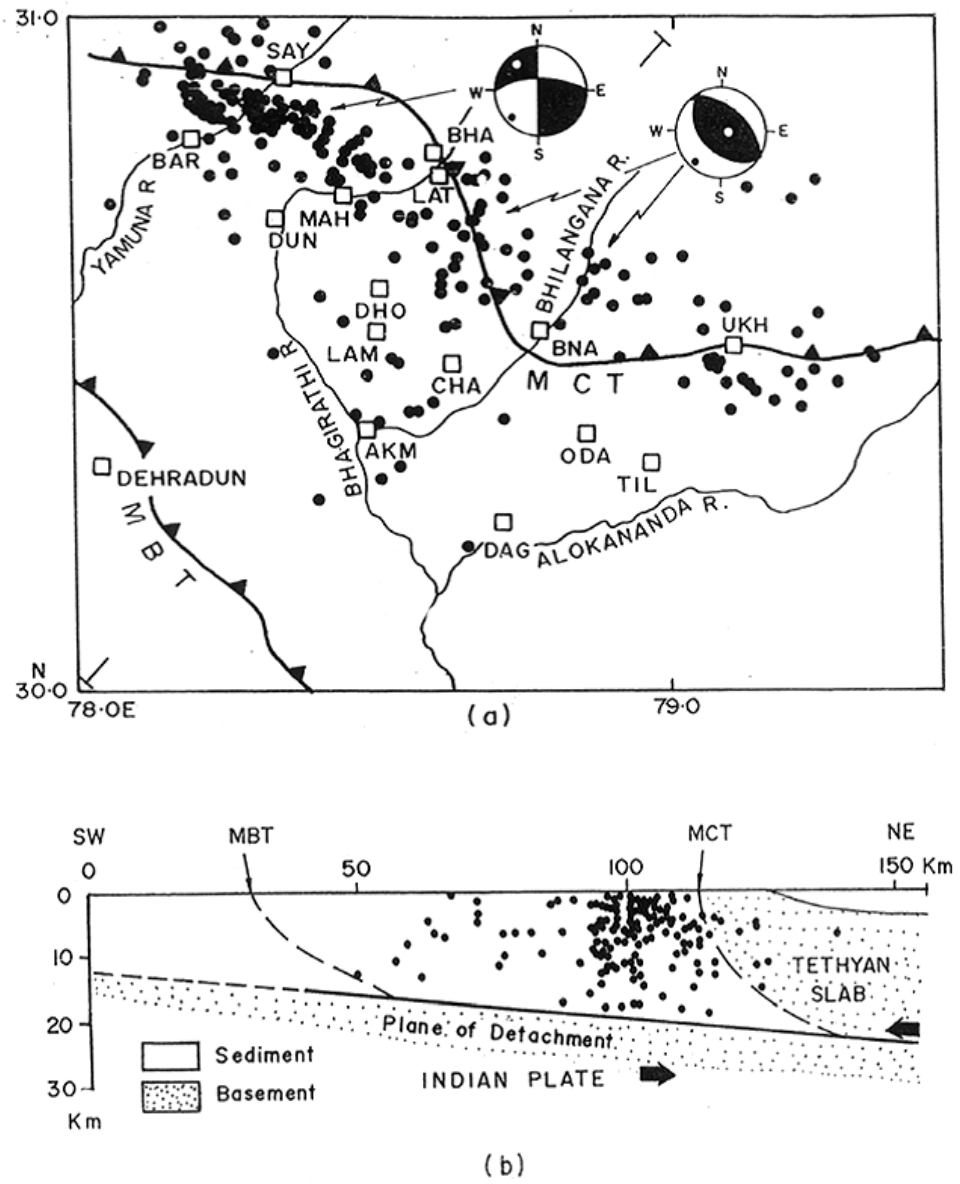

Figure 1.05 Microseismicity in the western (Garhwal-Kumaun) Himalaya area recorded during 1979-1984, composite fault plane solutions of two clusters are shown by beach ball representations; seismic stations are shown by small rectangles. (b) A NE-SW seismic cross section indicates that the earthquakes occurred above the plane of detachment (Khattri, 1992)

Pandey *et al.* (1995, 1999) have carried out similar study to understand the seismotectonics of the central Himalaya (Nepal Himalaya). The recorded earthquakes are generally shallower than 30km and are clustered in the depth range of 10-20km, coinciding with the mid-crustal ramp structure of the Himalayan crust beneath HHC.

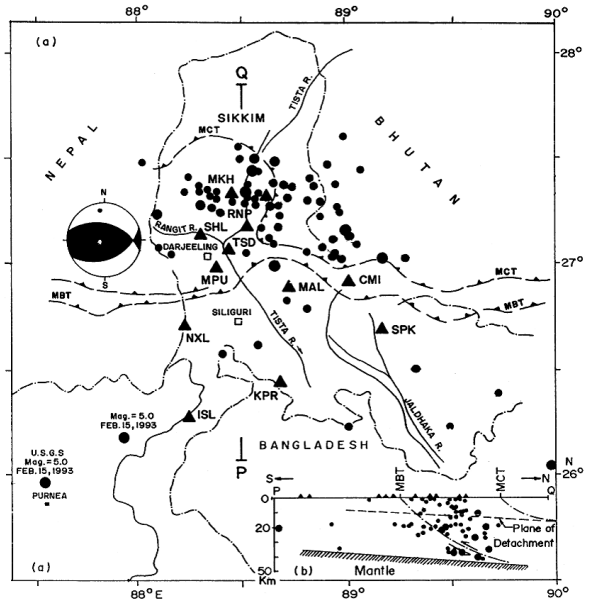

Figure 1.06: (a) Microseismic map of the Sikkim-Darjeeling Himalaya, eastern Himalaya .Larger earthquakes,>= 3.5 are shown by bigger solid circle. Two locations of the earthquake (mb 5.0) of 15 Feb. 1993 are shown. A composite fault plane solution of the microequrthquake is shown with the usual notation. (b)- N-S depth section of the earthquakes (Kayal. 2001)

1.4.1 Limitations of proposed seismotectonic model of the Himalaya

Analyses of spatial distribution of earthquake epicenters in the Himalaya geologic province brought out the oblique zones of seismicity, roughly NE and NW directions with respect to the thrust front on which strike-slip faulting was predicted (Khattri *et al.* 1983). The present of transverse structural deformation in the Himalaya in both NE and NW directions are supported by the existing seismological data. In addition to movements along the major thrust, several faults and lineaments (Tista, Gangtok, Purnia, Arun etc.) traverse to the trend of the Himalayas have been found and are inferred to be active. Kayal (2001) based on his detailed analysis of the result from microearthquakes studies all along the arc and considering the transverse trend, argued that the proposed seismotectonic model of the Himalayan region could not be valid for the entire length of the arc. Since the tectonic architecture and hence seismicity scenario is different from western Himalaya to the eastern/central Himalaya and the northeastern Himalaya.

The outcome of these studies does not support the steady state or the evolutionary model particularly in eastern and northeastern Himalaya. Further, The seismic study by Monsalve *et al.* (2006) in the Nepal Himalaya and Tibet infers two zones of deeper micro-earthquakes; a southern cluster of events at 30-70km which take place at the top of a ramp where Indian

crust bends downward to underthrust the Himalaya at a steeper dip (Schulte-Pelkum *et al.* 2005), and a northern WNW-ESE trending zone of events at 50-100km depth beneath the HHC and southern Tibet which occurs at the bottom of the ramp where Indian crust flattens out beneath southern Tibet (Priestley *et al.* 2008). Thus, the micro-seismic studies in various segments of the Himalaya strongly suggest that the tectonic behavior of the Himalaya is not uniform over the entire arc length.

1.5 Seismic surveys

Segments of the Himalayan collision belt have been explored in great detail, due to its earthquake hazard potential, by various geophysical methods to constrain the crustal and upper mantle architecture. These studies have provided new insights into the lithospheric structure (mapping of MHT and Moho), mantle anisotropy, and deformation processes in the region. Active source experiments such as seismic reflection and refraction studies provided a detailed description of the crustal architecture over limited region (e.g. Beloussov *et al.* 1980; Hirn *et al*. 1984; Kalia *et al*. 1984, Brown *et al.* 1996; Rajendra Prasad *et al.* 2011) where as passive techniques, e.g. receiver function analysis, surface wave analysis etc., have provided gross features of the crust over large areas (e.g. Kumar *et al.* 2005; Singh *et al.* 2007; Rai *et al* 2006; Umadevi *et al.* 2011; Caldwell *et al.* 2013). In addition to these, P- and S-wave seismic tomography studies have been carried out to map the source zones of strong to significant earthquakes for deciphering the cause of earthquake activity (e.g. Kayal & Bhattacharya, 2004; Mahesh *et al.* 2012). Many of these studies inferred that the source regions are characterized by low Vp/Vs values suggesting possible presence of fluids and local heterogeneities. Here, we present a brief account of some of these surveys rather than an exhaustive review of all studies carried out till date in the Himalaya.

Wide angle reflection profiling in the western Himalaya and in the Nepal-Tibet region have indicated substantial crustal thickening (Beloussov *et al.* 1980; Hirn *et al*. 1984; Kalia *et al*. 1984) in the region. The reflection profiles indicate maximum crustal thickness of about 75km beneath the western as well as central Himalaya. In the western Himalaya, the Moho is delineated as a steeply dipping interface from the Kashmir valley towards the great Himalaya. A step in the Moho has been suggested just north of the Himalaya (Lipine *et al.* 1984). A seismic reflection study along two profiles by Rajendra Prasad *et al.* (2011) provides the first crustal seismic images of the Sub-Himalayan region beyond 4s TWT (Two-way-time), deeper than any previous hydrocarbon exploration efforts. A southwest-dipping reflection

fabric is observed from 3.5 to 12s TWT in seismic profiles appears to have been formed in a compressional environment prior to the India–Asia collision and acts as structural basement to the younger Himalayan thrust sheets. The dipping fabric marks compressional strain during a 1850Ma "Ulleri-Wangtu" arc accretionary event at the margin of the Columbia super-continent limiting the thickness of Meso- to Neoproterozoic sedimentary rocks beneath the Kangra recess.

Surface wave dispersion studies have estimated an average crustal thickness of 70km beneath the Tibetan plateau (Gupta & Narin, 1967; Patton, 1980). Continental subduction of the Asian lithosphere is advocated based on receiver function mapping of the lithosphere-asthenosphere boundary (LAB) from Tien-Shan to the south of Karakoram (Kumar *et al*. 2005). The study estimated the crustal thickness of 45-65km in the Tien-Shan and adjoining regions. The thickness increases to about 70km in the Pamir and Karakoram region. The thickness of the lithosphere varies between 90 and 120km underneath Tien-Shan and increases to 160km beneath the Tarim basin. A similar study across the Nepal and Tibet Himalaya imaged the Moho at 40-70km (Schulte-Pelkum *et al.* 2005) and in the northeastern Himalaya at 35-50km (Ramesh *et al.* 2005).

Kumar *et al.* (2006) imaged the collision architecture of the Indian and Asian continental plates beneath the Tibetan Plateau from the study of *S*-to-*P* converted seismic waves in the region. The study infers that the base of the Indian lithosphere dips northward from the depth of 160km beneath the Himalaya to 220km depth just south of Bangong suture. The base of the Asian lithosphere is nearly horizontal at the depth of 160-180 km from central to northern Tibet. The Moho depth constrained by P- and S- receiver functions (Singh *et al.* 2006) indicates penetration of the Indian lower crust several hundred kilometers to the north of Zangbo suture. Partial melt in the upper-middle crust (~30km) of the northwest Himalaya associated with a low velocity zone has been revealed by Caldwell *et al.* (2009) through Rayleigh wave dispersion analysis of regional earthquakes in the western Himalaya and Tibet.

Receiver function analyses (Mitra *et al*. 2005, 2006; Yuan *et al.* 1997) have been carried out to image the Moho of the Indian crust as well as the Himalaya and southeast Tibet. The results indicated a slight deepening of the Moho northward due to the downward bending of the crystalline Indian crust as it is thrust beneath the Himalaya and accumulation of sediments in the Himalayan foredeep. Further, it was estimated that the crust beneath the Bengal basin and Shillong Plateau is 40-45 km whereas the Moho deepens from 58 km beneath LHD to 68

km beneath HHC. Below SE Tibet, the Moho deepens further from 79km to 87km below Lhasa. Simultaneous inversion of receiver functions and surface wave dispersion data in NW Himalaya (Rai *et al* .2006) along a 700km long profile from Delhi to Karakoram estimated the Moho depth beneath Delhi as about 40 km. The crust thickens to 50km beneath the foothills and to 60-65km below HHC. Further north of it, from the south of ITZ the Moho deepens to 70-75km. The Moho depth beneath the central Himalaya and south central Tibet was imaged by Schulte-Pelkum *et al.* (2005) from similar analysis. In this part of the region, the Indian Moho is offset smoothly downward, from 45 km depth in southern Nepal to 75 km depth in south-central Tibet.

Imaging of the Indian lithosphere beneath the Eastern Himalaya through the receiver function analysis was carried out by Umadevi *et al.* (2011). Northward thickening of the lithosphere from 135 km at the foredeep to 180 km beneath southern Tibet was obtained from this study. Thickening of the lithosphere towards east underneath the Burmese arc region supports the presence of a cold subducted Indian slab below the Burmese Plate. Recently, Caldwell *et al.* (2013) have carried out receiver function analysis to image Indian Moho along a profile in western Himalaya. Nearly horizontal Moho at 35–45 km depth beneath the Sub-Himalaya and Lower Himalaya which deepens to 50 km or more beneath the Higher Himalaya is observed in the study (Figure 1.08). This depth is 10–25 km shallower than in the NW Indian Himalaya and 5–10 km shallower than that in the central Nepal. Thickness of subducted Indian crust in the Garhwal Himalaya region is estimated to be 20–28 km. These results suggest that, across the Himalaya belt, the Indian crust appears to thicken gradually from about 40km at the southern edge of the Himalaya foredeep to 60-65km beneath the High Himalaya and 75-85km beneath the western and southern Tibet.

One of the detailed integrated geophysical studies that has been done in the Himalaya and Tibet region is INDEPTH (International Deep Profiling of Tibet and Himalaya) study. This extensive geophysical work was carried out to map the crustal structure of the Tibetan Plateau and the Himalaya through integrated seismic and electromagnetic studies. The geophysical observations made by the China, US, Germany and Canadian collaborative project INDEPTH included common midpoint reflection, wide angle reflection, receiver function and magnetotelluric investigations (Brown *et al.* 1996; Nelson & Zhao *et al.* 1996; Huang *et al.* 2000; Haines *et al.* 2003).

A major feature revealed by seismic experiments in southern Tibet is a strong mid-crustal reflector at a depth of 35-40 km. The existence of this reflector was first suggested by wide-angle seismic reflection studies (Hirn & Sapin, 1984); later, it was better imaged by the common midpoint (CMP) deep seismic profiles run during the INDEPTH experiment (Zhao, 1993; Brown, *et al.* 1996; Nelson *et al.* 1996). As shown in Figure 1.08, this conspicuous reflector was found to coincide with the mid-crustal decollement inferred from the structural sections across the range, and it was consequently termed the Main Himalayan Thrust fault, or MHT (Brown *et al.* 1996). The reflectivity in the south provides information on the geometry of the crustal structure, the thrust plane along which India is currently under-thrusting southern Tibet. This plane is traceable as a discrete gently north-dipping reflector upto ~28°54'where it disappears beneath Kangmar dome. The surface trace of the plane meets the MFT to the south.

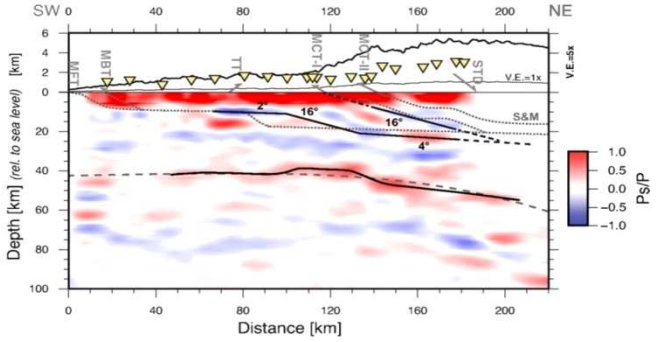

Figure 1.07: Image of MHT and Moho after Receiver function analyses of teleseismic events along a profile in Garhwal Himalaya (Caldwell *et al.* 2013)

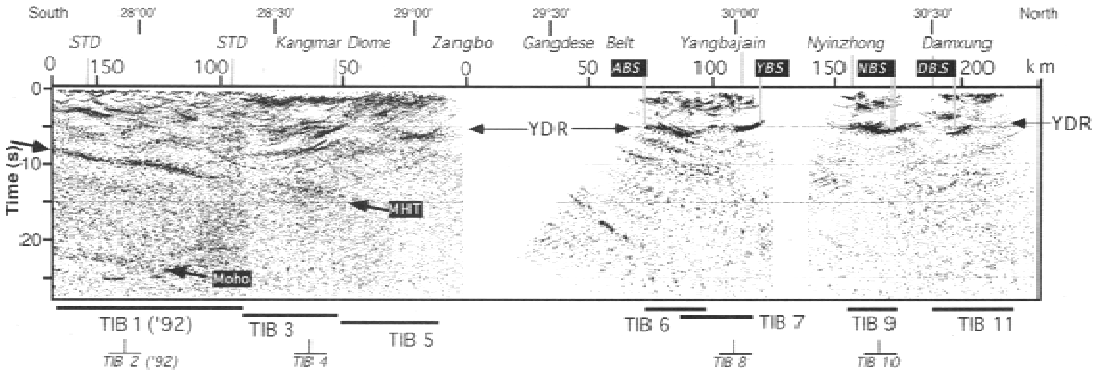

Figure 1.08: Composite migrated depth section of reflection profiles collected during INDEPTH-1 (1992) and 11 (1994). MHT, Main Himalaya Thrust; STD, South Tibetan Detachment System; YDR, Yamdrok-Damxung Reflection band; ABS, Angang bright spot; YBS, Yangbajain bright spot; NBS, Nyinzhong bright spot; DBS, Damxung bright spot (taken from Brown *et al.*1996)

1.6 Gravity surveys

Receiver function studies across the eastern Nepal Himalaya (*Schulte-Pelkum et al.* 2005) and northeastern India (Mitra *et al.* 2005) show the Moho can be traced as a continuous feature across the arc. This observation agrees with the modeling of gravity measurements (Cattin *et al.* 2001; Hetenyi *et al.* 2006). The Bouguer anomaly in India and in Tibet primarily indicates local Airy compensation but important deviations from Airy isostasy are observed below the Himalayan range and its foreland (Lyon-Caen & Molnar, 1983; 1985; Jin *et al.*1996; Cattin *et al.* 2001), and are particularly evident in the gravity data across the central Nepal Himalaya. Values more negative than those expected from local isostasy are observed over the Gangetic plain, indicating some mass deficit there. By contrast, mass excess is indicated below the adjacent Himalaya range. These deviations are the signature of flexural support of the range, meaning that the weight of the Himalaya is supported by the strength of the underthrusting Indian plate. The steep gravity gradient, on the order of 1.3 mGal/km, beneath the high Himalaya suggests a locally steepening of the Moho's dip. Flexural modeling of a thin elastic plate overlying an inviscid fluid (Lyon-Caen & Molnar, 1983; 1985; Maggi *et al.* 2000) successfully reproduces the observed gravity anomalies.

An isostatic gravity map of the Himalaya given by Qureshy & Kumar (1992) shows negative and positive anomalies coupled over the foredeep and the Himalaya. The Himalaya is associated with a positive isostatic anomaly running between HFT and MCT. Isostatic anomalies of the order of -120mGal over the foredeep represent the presence of about 5km thick Quaternary-Tertiary sediments in the Indo Gangetic plains. The +100mGal anomaly over the Himalaya is attributed to densification as well as thickening of the curst beneath the Himalaya (Qureshy & Midha, 1986). Other gravity studies (Warsi & Molnar, 1977; Qureshy & Warsi, 1980; Layon-Caen & Molnar, 1983; Molnar, 1984; Verma & Prasad, 1987) exhibit negative Bouguer anomaly of 60 mGal to about 500 mGal suggesting thickening of the curst in the Higher Himalaya and Tibet. The excess mass of the Himalaya topography is compensated at depth by the thickened crust. Gravity studies inferred that the crustal thickness increases form 46km beneath the north of GFB to about 72km in HHC suggesting the smoothly increasing Moho depth. From the Modeling of gravity data, Lyon-caen & Molnar (1983) inferred that the dip of the under-thrusting Indian Plate increases from about 3^{o} beneath the Ganga basin and Lesser Himalaya to about 15^{o} beneath the Higher Himalaya. They also inferred a decrease in the flexural rigidity of the plate as it moves northward. The model suggested by them inferred ramping of the Himalayan curst over the steep northern

edge of the Indian plate which is correlated with abrupt change in the elevation at the foot of the greater Himalaya and steep dip of MCT (Lyon-Caen & Molnar, 1983; Pandey *et al.* 1995).

Bouguer gravity map by Jin *et al.* (1996) suggests that the mantle portion of the gravitationally heavy Indian plate is subducted beneath the Eurasian plate for a distance of 500-700km north of MBT (Figure 1.09). They determined that the Main mantle Thrust lies about 100km north of the IST. Geomagnetic investigations in the western Himalayas revealed the presence of a localized conductive zone at depth embedded in a narrow high seismicity zone (Arora & Singh, 1992). Combined interpretation of gravity and magnetic data collected across the eastern Himalaya revealed variation in the Moho depth from 36km to 74 km (Tiwari *et al.* 2006). Flexure of the Indian lithosphere with an effective elastic thickness of 50 $\pm$10 could be the cause for these variations in the Moho depth. The study provided density structure across a complete litho-tectonic package and covering the entire Himalaya range from the Indian shield to the Tibetan plateau (Tiwari *et al.* 2006). Based on gravity data across the NW Himalaya, Mishra & Rajasekhar (2006) have examined the crustal architecture. They pointed out thickening of the curst from 40 km at south of Lahore-Sargodha ridge to about 70 km under Karakoram range and further reduction to 45-50 km under Tarim basin. Results obtained from elevation, gravity and geoid studies indicated that the coldest past of the mantle underlies southern Tibet and that the hottest part underlies north Tibet (Munt *et al.* 2004).

1.7 GPS surveys

Global Positioning System (GPS) studies of the Himalaya have provided three fundamental constraints concerning the seismotectonic framework of the Indian plate; its overall stability (<0.01μ strain/year), velocity of collision with Asia (58$\pm$4 mm/yr at N44E), and rate of collision with southern Tibet (20.5$\pm$2 mm/yr) (Larson *et al.* 1999; Bilham *et al.* 1997). GPS measurements along the northwest Himalaya have yielded slip rate of 14$\pm$1 mm/yr order for HFT, consistent with the geologic studies (Powers *et al.* 1998). Using GPS measurements and studies on deformed terraces in Nepal, Bilham *et al.* (2001) and Lave & Avouac (2001) suggested that the surface faulting in the Himalaya currently occurs only along the MFT. Further, MFT defines the southern limit of the deformation in the Himalaya and consumes nearly the entire slip on the MHT. Recent shortening and uplift about 100 km north of MFT (near the distinctive Higher to Lesser Himalaya physiographic break) in this region is due to

passive deformation over a mid-crustal ramp in MHT. However, out-of-sequence thrusting in the Lesser Himalaya (Schelling & Arita, 1991; Wobus *et al*. 2003, 2005) indicates that the deformation on the mid-crustal MHT ramp is not entirely passive. A 3-D finite element modeling of the deformation and stress field for the Himalaya-Tibet plateau indicates an EW extension of the Tibetan plateau at a rate of about 6mm/yr and maximum uplift rate of 4 mm/yr at the Greater Himalaya (Rao *et al*. 2003).

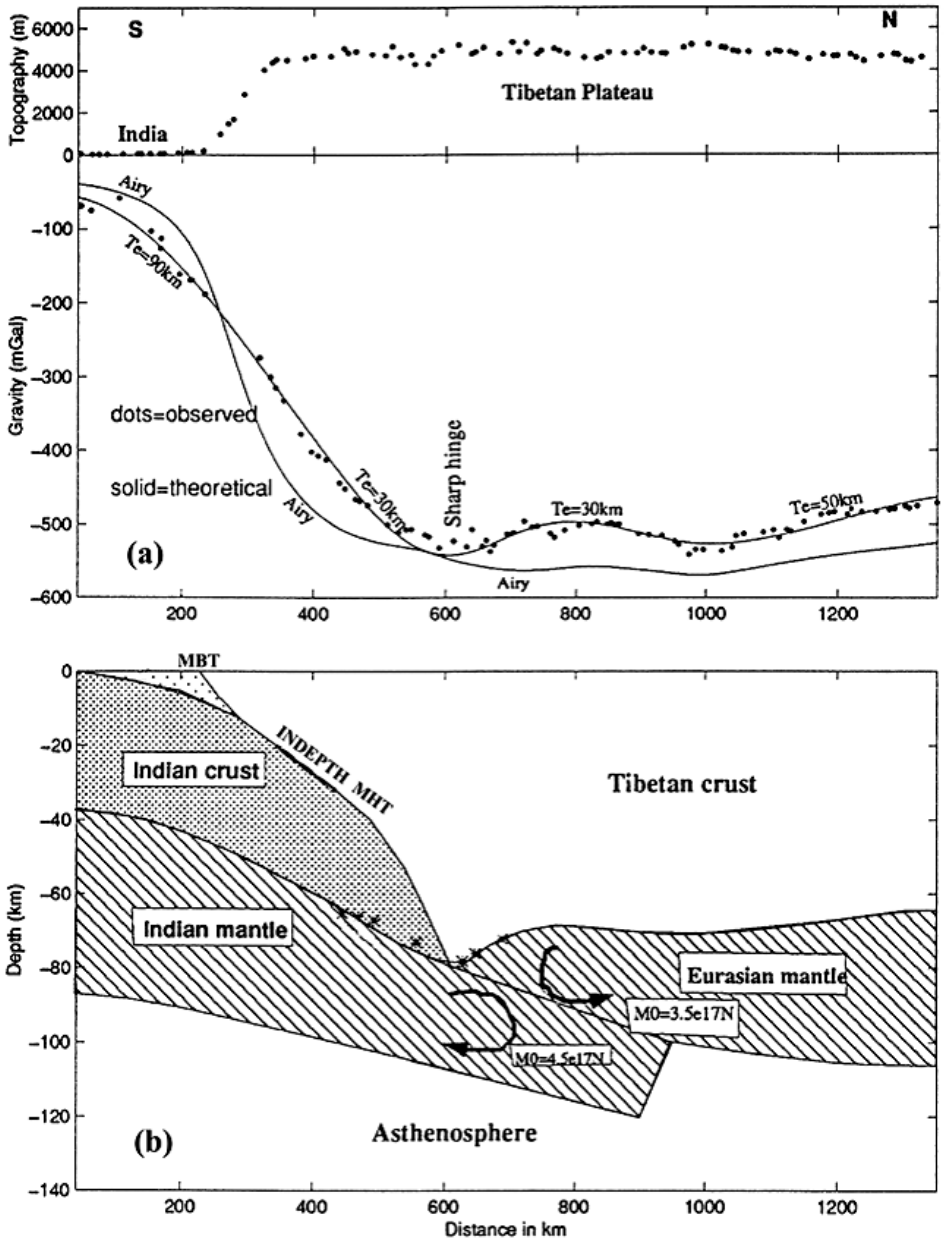

Figure 1.09: (a) Topography and Bouguer gravity anomaly along a NE-SW profile from Himalayan foredeep to Qaidam Basin. (b) A model in which the Indian plate has an initial elastic thickness of 90 km, reduces to 30 km after it passes beneath the High Himalaya (Jin *et al*. 1996).

1.8 Electromagnetic surveys

Electromagnetic (EM) surveys in the Himalaya for the mapping of crustal architecture of this structurally complex mountain belt mainly involve magnetotelluric (MT) technique in which natural source EM signals are used to delineate the electrical conductivity distribution within the subsurface. Various seismological techniques discussed above have inferred the presence of low velocity zones (LVZ) zones, correlating with seismicity clusters, in the crust of the Himalayan and Tibetan regions, possibly representing partial melts and/or metamorphic fluids. However, only a limited number of MT surveys have been carried out in the 2500 km long Himalayan belt (Figure 1.10) despite its highly complex geotectonic scenario and active seismicity

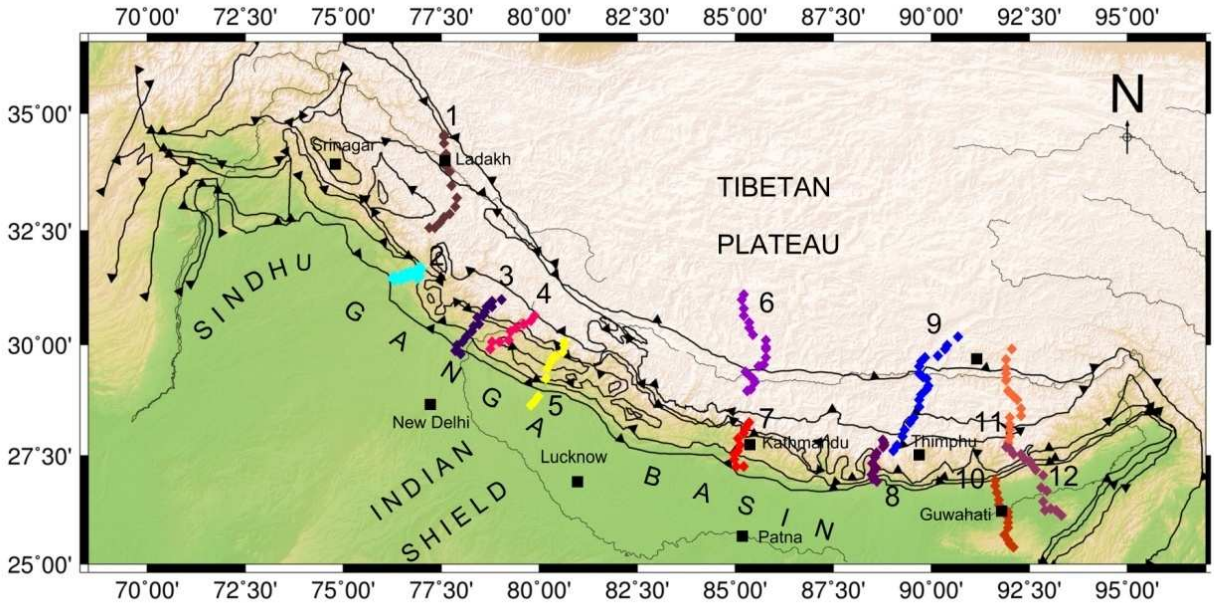

Figure 1.10: Figure showing various MT profiles in the Himalaya collision zone with various thrust faults (1. Project Himprobe, 2: Siwalik Himalaya (Gokarn *et al.* 2005); 3, 4, 5. Kumaun-Garhwal Himalaya (Israil *et al* .2008; Arora and Ravat, 2013); 6,9,11: Project INDEPTH; 7: Nepal Himalaya (Leminneir *et al.*1999); 10, 12: Northeast Himalaya (Gokarn *et al.* 2008)

In the Tibetan region, north of collision belt integrated seismic and MT study under INDEPTH has revealed the presence of partially molten mid-crustal layer/ wide spread fluids in the crust beneath southern Tibet (Chen *et al.* 1996; Nelson *et al.*1996; Wei *et al* .2001 and Li *et al*. 2003) as well as other part of the Tibeten plateau. Figure 1.11 shows the electrical resistivity section along the 100, 700 and 800-line of INDEPTH. The anomalous conductive zone in the middle and lower crust beneath the Tibetan Plateau has conductance of 3000 - 20,000 Siemens. In the southern Tibet the high conductivity zone is at the depth of 10 to

20km and is interpreted in terms of regionally interconnected fluid phases in the crust. In the northern Tibet the conductive zone at 30-40 km depth has been correlated with the presence of partial melts (Nelson *et al* .1996; Chen *et al.* 1996; Brown *et al.* 1996; Unsworth *et al.* 2005).

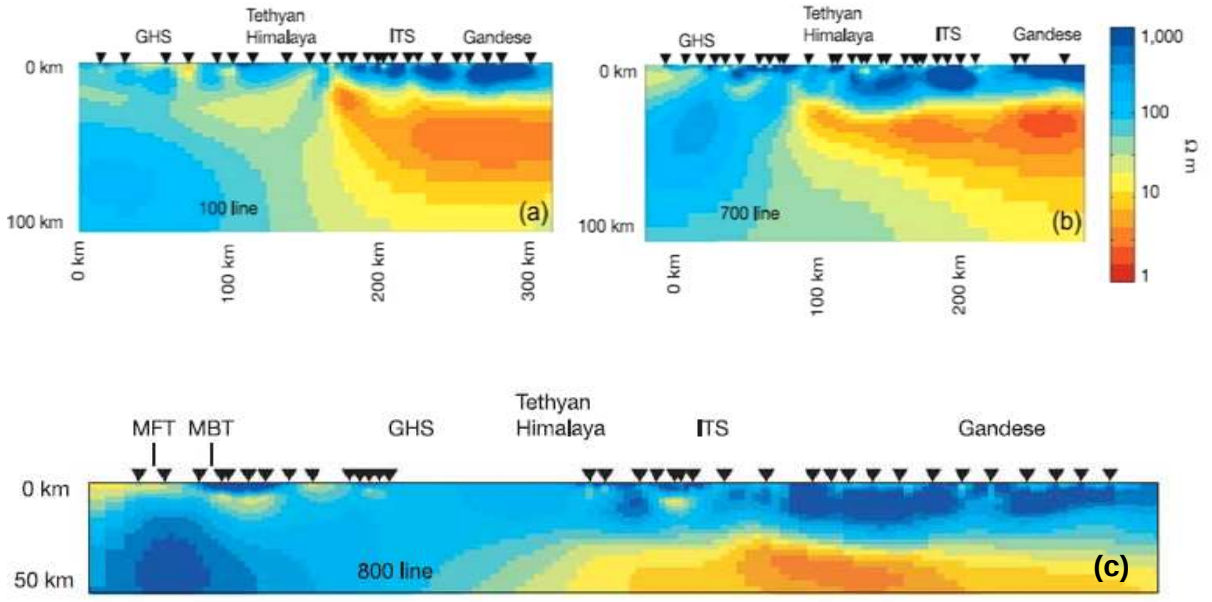

Figure 1.11: Geoelectric structure of southern Tibet along three profiles, line 800; 100 and 700 lines. (Unsworth *et al.* 2005)

Gokarn *et al.* (2002a) delineated the crustal electrical resistivity structure of the Zhanskar range, Tso-Morari dome and Ladakh batholith in the NW Himalaya under project HIMPROBE. The 2-D geoelectric cross-section (Figure 1.12) shows a 70km wide high conductivity zone (<10 Ω.m) beneath ITZ and Ladakh batholith extending from shallow depth to about 15 km depth. The conductance of 20,000 Siemens is much higher than the values of 200-300 Siemens normally observed elsewhere for the Indian plate. This high conductivity zone was correlated with the presence of wide-spread partial melts generated from the subducted Indian crust based on high heat flow and high attenuation of seismic waves.

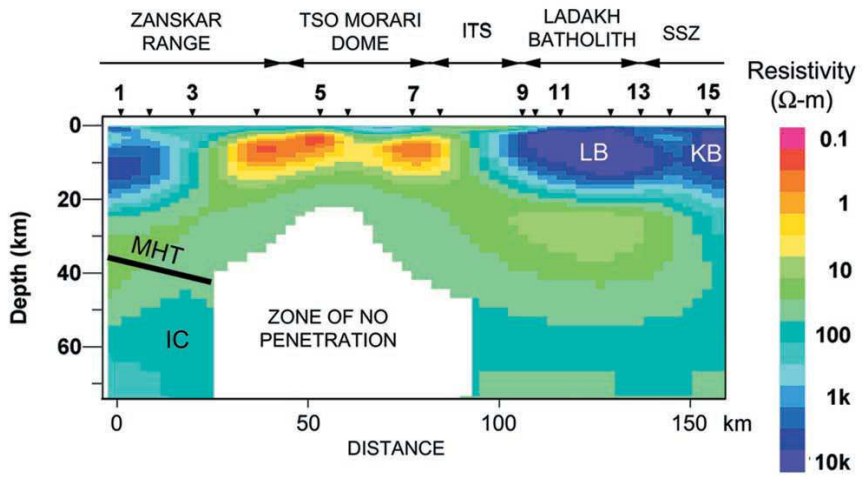

Figure 1.12: NW Himalaya resistivity section obtained by Gokarn *et al.* 2002

Arora *et al.* (2007) carried out long-period (10-3000s) MT study along the same profile and delineated a low resistivity zone north of ISZ with resistivity of 5-10 Ω.m at the depth of 20-25 km (Figure 1.13). They inferred the presence of partial melt beneath the Indus Tsangpo Suture Zone (ITSZ) and Ladakh based on the estimated high conductance for this region. The underlying Indian plate, occurring as a resistive layer, extends significantly north of ITSZ.

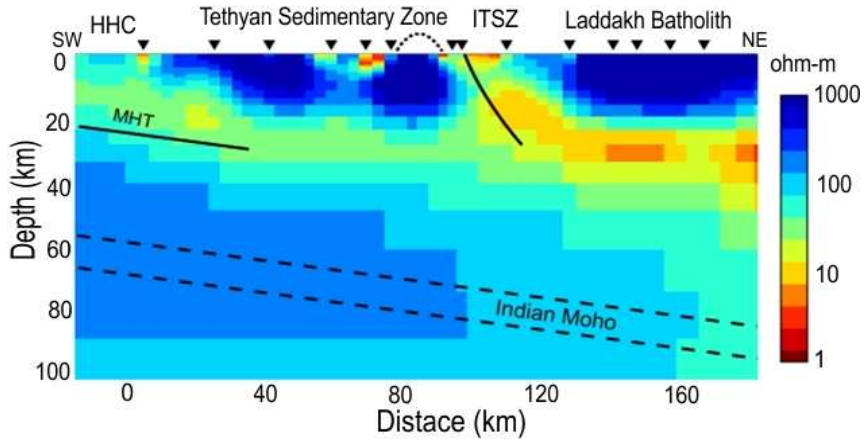

Figure 1.13: 2-D geoelectric section of NW Himalaya by Arora *et al.* 2007

Gokarn *et al.* (2002b) delineated the crustal structure of the Siwalik Himalaya (Figure 1.14) along Una-Mandi profile (Himachal Himalaya). The experiment reveals that the crust in this part of the Himalaya is underlain by a conductive layer with a resistivity of about 100 Ω-m at the depth of about 50 km below the Palampur thrust and Sarkaghat anticline. The low resistivity layer is displaced to shallow depths (35km) NE of MBT.

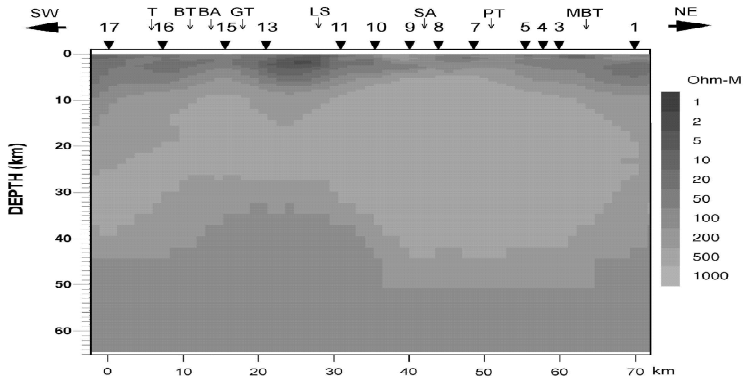

Figure 1.14: Geo-electric section of Siwalik Himalaya (Gokarn *et al.* 2002)

Arora & Rawat of WIHG have carried out magnetotelluric field survey along a profile in the Kumaun Himalaya to delineate the crustal geoelectric structure of the region (Caldwell *et al.* 2013). The profile passes across the Chamoli earthquake source zone. The MT result (Figure 1.15) along the profile reveals a low resistivity zone at shallow depth of 10-15 km beneath the Indo-Gangetic plain that dips at a low angle and extends as a continuous layer right up to MCT. The section also displays a high conductivity zone beneath MCT which correlates well with the result obtained by Isaril *et al.* (2008) and Lemonnier *et al.* (1999). The ramp structure of MHT is also observed in the derived MT model.

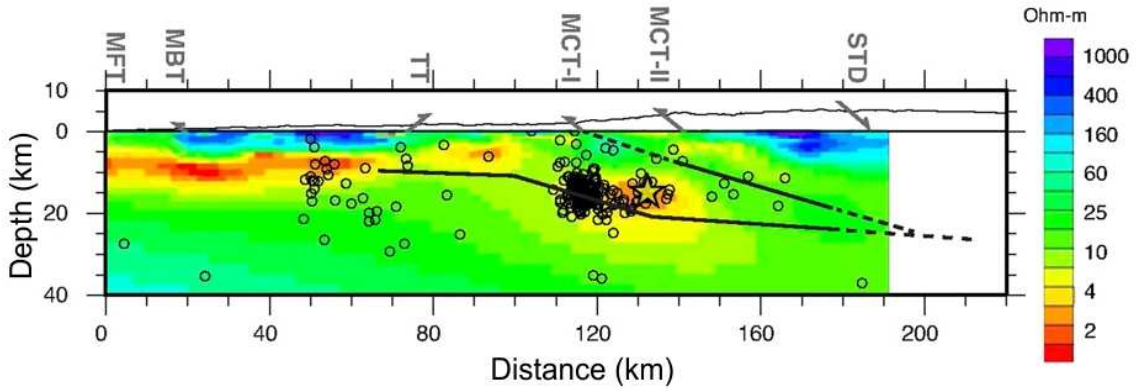

Figure 1.15: 2-D Geoelectric section of Kumaun Himalaya by Arora & Ravat (taken from Caldwell *et al* .2013)

Geoelectric structure of the western Himalaya (Garhwal Himalaya) has been studied by Israil *et al*. (2008). From the study, they found a correlation between the seismicity in the region and the delineated high conductivity zone beneath MCT (Figure 1.16). They inferred the high conductivity zone beneath MCT to be due to the presence of metamorphic fluids released due to underthrusting mechanism. This study also brings out the smooth dip of the

Indian plate as it under-thrusts the Himalaya supporting the ramp type structure of MHT in the region.

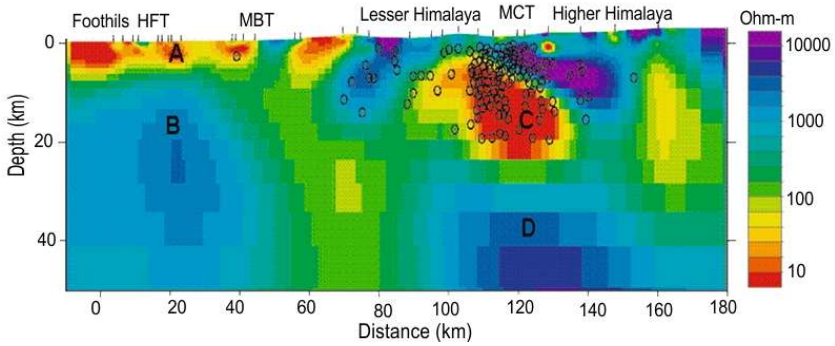

Figure 1.16: 2-D geoelectric structure of the Kumaun-Garhwal Himalaya (Israil *et al.* 2008)

In the central Himalaya, Lemonnier *et al.* (1999) carried out MT survey along a profile in Nepal. The result (Figure 1.17) reveals a high conductivity zone with the resistivity of about 30Ω-m at the depth of 20-30km beneath the Higher Himalaya. The high conductivity is explained in terms of the presence of metamorphic fluids released due to the under-thrusting of the Indian plate and/or distributed brittle deformation around the ramp by inter-seismic stress build-up. In this region also, the seismicity gets concentrated at the ramp structure and correlates with the conductive zone. The southern foreland basin at the foothills appears as a conductive zone of about 5km thickness overlying the resistive (300-1000Ω-m) Indian shield.

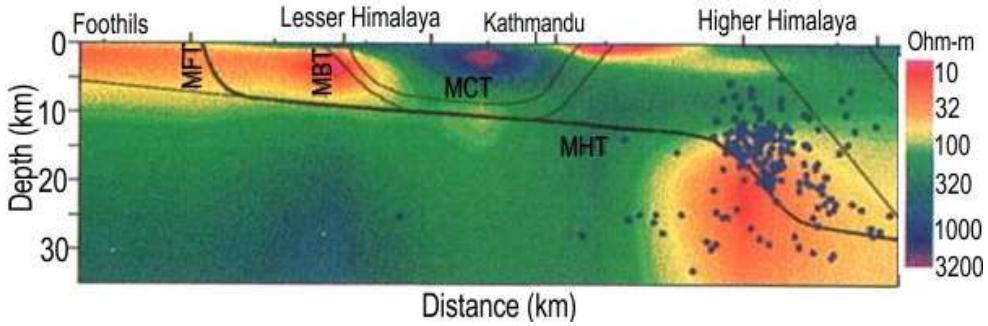

Figure 1.17: Section of resistivity model obtained from the MT profile along the central Himalaya, Nepal (Lmenonnier *et al.*1999)

MT investigations in the Sikkim region (Eastern Himalaya) along an approximately N-S profile show the presence of some high conductivity zones at the mid-crustal levels (Patro & Harinarayana, 2009), marked as zones of metamorphic fluids. These zones are associated with major thrust faults in the region (Figure 1.18). The possible reason for these fluids is

inferred as the same geodynamic process that was suggested for the central and western Himalaya.

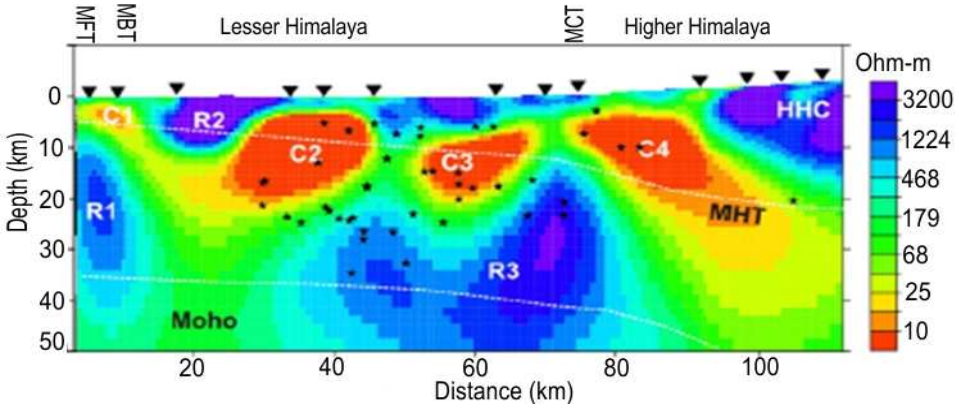

Figure 1.18: Geoelectric structure of the Sikkim Himalaya by Patro & Harinarayana (2009).

Gokarn *et al.* (2008) analyzed MT data along a profile covering the Shillong Plateau and the Brahmaputra valley in NE India. The 2-D section (Figure 1.19) reveals the Shilling Plateau and northernmost unclassified crystalline zones as high resistivity zones. The lower Brahmaputra sediments are imaged as conductive zone with resistivity in the range of 10-20 Ω-m. The result also suggests that the conductive sediments of the Bengal basin thrust under the Shillong Plateau.

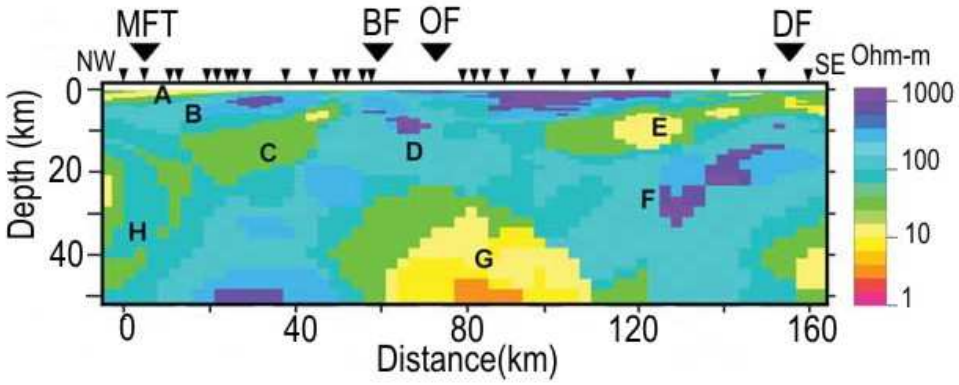

Figure 1.19: Resistivity structure of the Shillong plateau in NE India by Gokarn *et al.* (2008)

These MT studies have provided significant information on the subsurface structure of different segments of the Himalaya. Main inferences drawn from these studies are: (i) The Kumaun-Garhwal and central Himalaya sectors have a ramp structure at mid-crustal depth beneath the Higher Himalaya that is associated with the seismicity in that region, (ii) conductive zone at the ramp structure implies possible role of fluids in earthquake genesis in this region, (iii) Eastern Himalaya seems to have the crustal structure significantly different

from the western Himalaya, and (iv) conductive zones within crust possibly signify the presence of metamorphic fluids.

1.9 Motivation

The Himalayan collision belt is a unique natural laboratory to understand the process of continent-continent collision and to test probable models of earthquake genesis in a convergent environment. The region offers vast opportunities to all sub-disciplines of earth system science to explore various aspects. As discussed in the previous section, several diverse geophysical experiments have been carried out in different segments of the Himalaya to delineate the deep structure of the region and to understand the evolutionary processes as well as earthquake genesis. These studies have provided valuable insights for lithospheric and mantle architecture, identification of seismically active zones, causes for recurrent seismicity, seismic hazard scenario, and dynamics of various tectonic blocks.

An important inference that can be drawn from synthesis of these studies is that the eastern Himalaya seems to be having a different geotectonic setup than the western and central Himalaya and the seismotectonic models of continental collision, proposed mainly based on the data from the western Himalaya, might not be suited to the eastern Himalayan segment. However, majority of geophysical studies have been concentrated in the western and northwestern part of the Himalaya and very little work, barring seismological studies, have been carried out in the eastern region, especially in the Sikkim Himalaya, leading to significant gaps in our understanding of the subsurface structure/tectonics of seemingly different eastern Himalaya. There are some unresolved questions related to the geo- and seismotectonics of the region. For example, (i) structure of the Sikkim dome and its role in the exhumation process, (ii) subsurface location of MBT, MCT-1, MCT-2 and other major faults to constrain the estimates of the strain accumulation through crustal shortening for earthquake hazard assessment (Dasgupta & Sivaji, 2004), (iii) deep crustal and sub-crustal structure of the region in terms of different tectonic blocks, etc. These necessitate an extensive geophysical survey that can add significantly to the state of knowledge of the region. The present work is motivated by this data gap and has been undertaken with the view to delineate the detailed crustal structure of the Sikkim Himalaya in terms of electrical resistivity image by covering the profile with closely spaced MT sites and utilizing MT data of longer periods (up to 1000s).

In the subsequent subsections, I bring in the Sikkim Himalaya region and highlight some of the salient features of the region that suggest distinct seismotectonic environment of the Sikkim Himalaya.

1.9.1 The Sikkim Himalaya

The Sikkim Himalaya, bounded by the Nepal Himalaya on the western side and the Bhutan Himalaya on the eastern side, shares the broad thrust geometries of the Himalayan belt but differs geo-tectonically from elsewhere along the arc (Figure 1.01). This sector of the Himalaya geographically comes under the limits of Sikkim state and Darjeeling district of West Bengal.

Sikkim is a mountain state with enchanting beauty. It is bounded in north by the Tibetan plateau, in south by the state of West Bengal, in east by Bhutan and Tibet and in west by Nepal. The state lies between $N27^{0}05'00''$ to $N28^{0}08'00''$ and $E88^{0}01'00''$ to $E88^{0}55'00''$, covers an area of 7096 sq. km and soars from an altitude below 200m at the southern end to above 6000m in the north, culminating into the magnificent Kangchendzonga rising to 8598m above mean sea level (msl). A large portion of the Sikkim Himalaya is extremely rugged and shows a highly immature positive topography with several typical geomorphological features of the folded mountains belts of the Higher and Lesser Himalaya, such as high ridges and steep slopes. The river valleys are mostly V–shaped with moderately steep stream abutments. The southern fringe of Sikkim, devoid of a Himalayan barrier opens out to the Plains of Bengal and it is towards this direction that Sikkim's two major river systems, Tista and Rangit flow down to drain the land.

Darjeeling, a hilly district in the state of West Bengal, occupies southern and southwestern part of Sikkim and has similar geographical as well as geological features.

1.9.2 Salient geotectonic features of the region

Tectonically, the Sikkim Himalaya shows some spectacular deviations from the general tectonic setup of the Himalayan trend. Primarily, it is one such region where MBT follows an E-W trend but MCT takes an Omega-shape, encompassing a dome-shaped structure, with a narrow neck at the southern end (Ray, 2000; Dasgupta *et al.* 2004 and Mitra *et al.* 2010). MCT in this region is not a well-demarcated sharp boundary but occurs as a several-km-wide ductile deformation zone, often referred as the Main Central Thrust Zone (MCTZ), and consists of schists and gneisses representing both the Lesser and the Higher Himalaya (Sinha

Roy, 1982; Dasgupta *et al.* 2004). The zone is bounded by two fault systems, MCT-1 and MCT-2 on either side of the zone which could be rarely seen elsewhere in rest of the Himalaya. Several approximately N-S trending gravity faults (Nath *et al*. 2005) along with NNW-SSE trending sub-parallel Gangtok and Tista lineaments (GSI, 2000) further complicate the tectonic setup of the Sikkim Himalaya.

Seismically, the Sikkim Himalaya region is considered to be one of the active zones of the Himalayan collision belt due to occurrence of frequent moderate magnitude earthquakes. Recently, the region witnessed a strong earthquake of magnitude 6.9 on 18thSeptember, 2011. The region falls in the zone IV of the seismic zonation of map India (Figure 1.20) and expected an intensity of VII (Nath, 2012) In the region, seismicity is mainly clustered to the north of MBT in the depth range of 10-60 km well below the detachment zone (also termed as MHT) (De & Kayal, 2004; Nath *et al.* 2005, Hazarika *et al*. 2010). Tectonics of the region as revealed by the focal mechanism solutions of the earthquakes and composite focal mechanism is predominantly of strike-slip nature. All these observations differ from the conceptual thrust tectonics models of the Himalaya proposed by Seeber *et al.* (1981) and Ni & Barazangi (1984) implying a distinct seismotectonic scenario for the region. It is inferred that MBT in this part of the Himalaya is responsible for the seismic activity (De & Kayal, 2004).

1.10 Objective of the study

The present work focuses on delineation of the deep crustal electrical resistivity structure of the Sikkim Himalaya through a broadband MT survey along an approximately N-W profile cutting across various geo-tectonic units of the region. Since electrical conductivity is highly sensitive to the presence of interconnected fluids and partial melts, the proposed work is expected to bring out such anomalous zones and would help in improved understanding of the seismotectonics of the region as well as in highlighting whether such zones have any implications for the earthquake genesis in this part of the Himalayan belt. These results are also expected to shed light on the nature of major thrusts at mid-to-deep crustal levels.

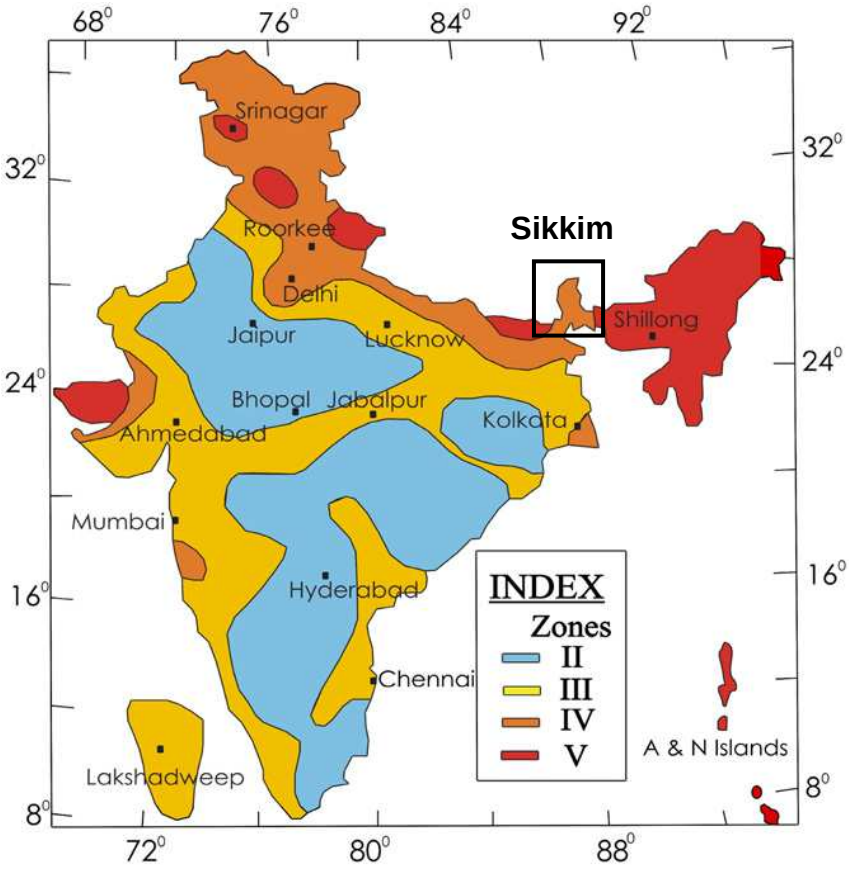

Figure 1.20: Seismic Zoning map of India (Source: BIS, 2001, New Delhi)

1.11 Work plan

To achieve the objective, the entire work plan has been split into several stages. These are briefly mentioned below. The detailed description is given in respective chapters.

Selection of profile:

We have selected MT profile in such a way that it would pass through various thrust faults such as MFT, MBT, MCT (MCT-1 and MCT-2) and would also lie approximately at the southern end of the INDEPTH profile (with offset in the western direction) to complement the results obtained by INDEPTH study. As the general strike of the Indian plate as well as MFT and MBT is E-W, the profile is aligned in approximately N-S direction. Previous MT survey in Sikkim (Patro & Harinarayana, 2009) had covered LHD and some part of HHC. We decided to extend the profile in both directions such that it can span the GFB in the south and STDS in the north. Even in the overlap region of LHD and MCTZ we decided to acquire more data at close station spacing and to the west of the previous profile. Finally, the

proposed MT profile starts from a location south of Siliguri in GFB and terminates at a location close to STDS and covers a lateral distance of about 200 km.

Data acquisition:

We decided to record broadband MT data along the profile with an average station spacing of 5-6 km between two successive MT sites. In some regions, we decided to have dense MT stations (subjected to availability of suitable sites) particularly in MCTZ for detailed mapping of the ductile shear zone. At each station, we planned to record MT time series for about one week duration each to recover impedance data in broad frequency range of 0.001-4096s. The long duration of recording will help in overcoming the dead-band problem in some extent.

Preprocessing of MT time series:

The processing of MT data involves manual checking of recorded MT time series, removal of bad data segments and conventional processing to extract impedance tensors (**Z**) and tipper (**T**) in frequency domain from time series. This includes transformations and spectral analysis tecniques. The estimated impedance tensor is generally expressed in terms of apparent resistivity and phase values as a function of frequency (period).

Distortion analysis and estimation of regional strike:

MT impedance tensors are generally affected by localized geological noise causing galvanic distortions. Once reliable estimates of impedance tensor **Z** are obtained, the next important step is to perform distortion analysis and determine regional strike direction for 2-D analysis of the data. Various distortion analysis techniques have been proposed. Generally used distortion techniques are: LaTorraca decomposition technique (LaToracca *et al.* 1986), Groom–Bailey decomposition technique (Groom & Bailey, 1989), phase tensor approach (Caldwell *et al.* 2004), and electric polarization state based technique (Becken & Burkhartdt, 2004). For the present work, we plan to use some of these techniques to estimate distortion corrected impedance tensors compatible with dominant regional strike. We also plan to analyze the lateral and depth (period) variations in the regional and local strike directions to find their correlation with the geotectonic features.

2-D inversion of impedance tensors:

Once the decomposition analysis is performed, we get impedance tensors decomposed into TE- and TM-mode under the assumption that the regional structure is 2-D in nature. In TE-mode, the electric field polarization is along the strike direction whereas in TM-mode it is orthogonal to the strike. These data will be used to perform inverse modeling to delineate the

subsurface electrical resistivity distribution. We shall use the 2-D non-linear conjugate gradient inversion (NLCG) algorithm of Rodi & Mackie (2001) for the regularized solution of 2-D inverse problem which needs considerably less computing time to estimate the best possible fit model. Smoothing parameter τ will be estimated by following the method of L-curve test (plot drawn between roughness and RMS value per each inversion). Joint inversion of TE- and TM-mode data will be performed to obtain an optimum model of the subsurface structure. The effect of topography will also be included in the inversion process. Sensitivity test shall be performed for the final model in order to examine sensitivity of major features observed in the final model.

Correlation with geology and seismicity patterns:

The derived final 2-D geoelectric structure of the region shall be integrated with geology and available seismological and other geophysical data for interpreting the model in terms of seismotectonics of the region. We expect the new geophysical information from this area would extend the results of INDEPTH, thereby filling the data gap.

Analysis of the effect of anisotropy:

Seismic results from the Sikkim Himalaya (Singh *et al.* 2007) indicate the presence of seismic anisotropy in the mid-crust. We shall also analyze MT data carefully to identify possible signatures of electrical anisotropy, if any. Electrical anisotropy and special configurations of localized 3-D electrical conductors (Pek & Verner, 1997; Heise & Pouse, 2004; Ichihara & Mogi, 2009) can cause current channeling leading to out-of-quadrant phase values. We shall look for such signature in the recorded data.

1.12 Summary

Closure of the Tethys Ocean and subsequent collision of India plate with Eurasia produced the Himalayan mountain chain. The collision zone is the most interesting region from the geological point of view. It provides natures' window on the geodynamic processes that shape the geological features of the globe. Earthquakes of large, medium and small magnitudes occur in this region since the historical past. Various researchers have explained the seismicity as an indicator of active deformation in the region between Indian and Eurasian plates and is directly associated to the convergence of these plates. Himalayan belt was rocked by three great earthquakes (1897 Assam, 1934 Nepal-Bihar border and 1950 Assam) within fifty-five years (1897-1950) and large number of strong earthquakes caused huge loss of lives and property. Various geophysical investigations are carrying out to understand

geodynamics and seismicity of the region including gravity & magnetic, electromagnetics (MT), active and passive seismic investigations which provided significant knowledge on the active mountain belt interms of crustal deformation, presence of low velocity zones and/or partial melts and metamorthic fluids.

The Sikkim Himalaya situated in the eastern part of the collision zone occupies special status in view of its distinct seismotectonics nature and experiences frequent moderate magnitude earthquakes. We therefore plan to carryout natural EM investigations namely magnetotelluric studies in the region to image the crustal structure of the region interms of resistivity for better understanding of seismicity and tectonics by correlating with existing seismological data. In the next chapter, I present detailed description on the geology and tectonics of the Sikkim Himalaya including findings of various geophysical/seismological investigations carried out in the region.

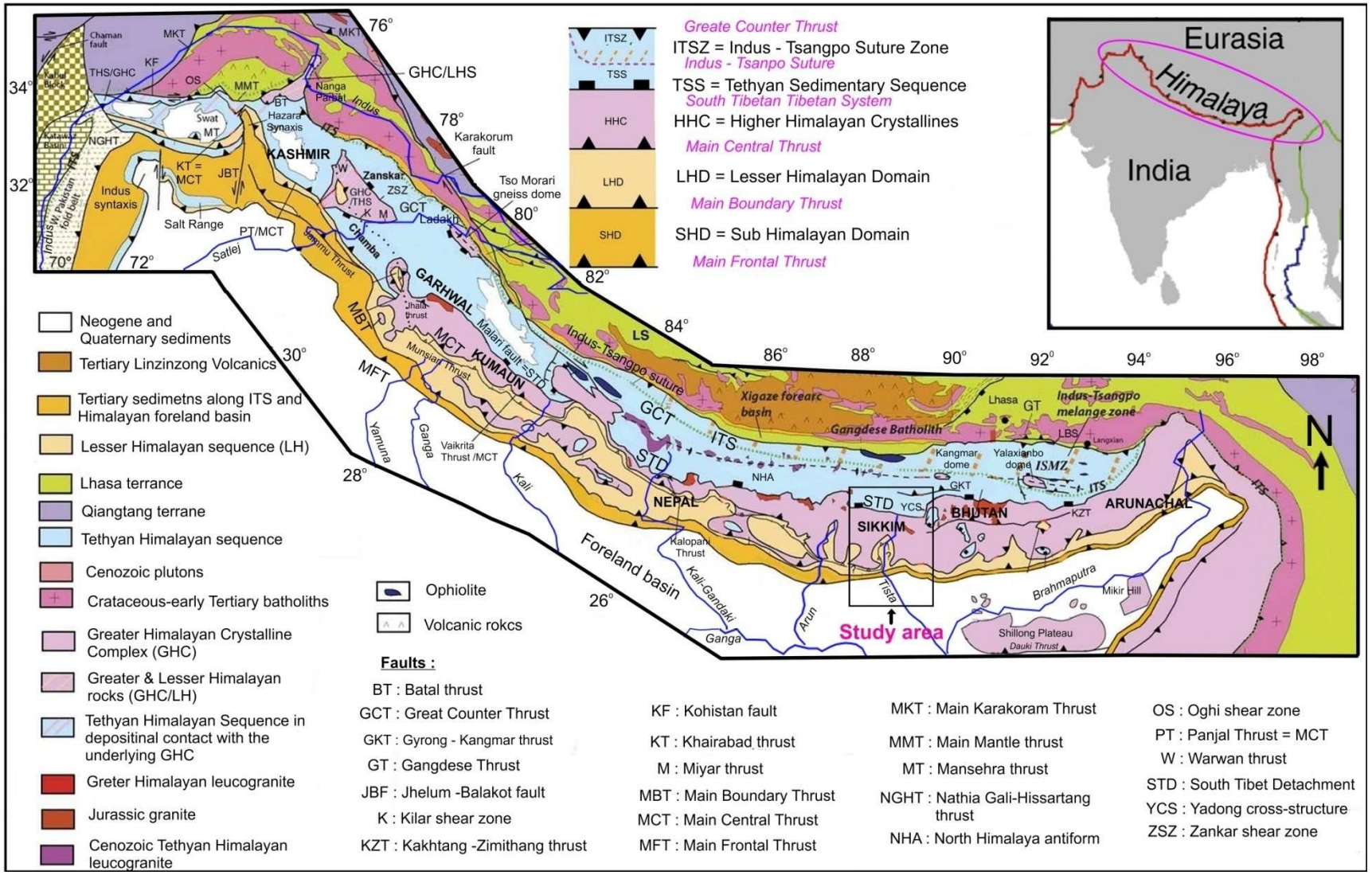

Figure 1.01 Generalized Geotectonic domains of the Himalaya Collision Zone (modified after Yin, 2000) showing study area

Chapter 2

Geology and Tectonics of the Sikkim Himalaya

The Sikkim Himalaya together with the Darjeeling segment exhibits a highly complex structural configuration and it is one of the highly seismically active regions of the Himalayan collision belt. Almost all major geological sequences that are present in the Himalaya are also seen in this region. The tectonic setup of this Himalayan segment is however distinct from the dominant thrust-type environment and is dominated by transverse tectonics. Seismological studies, both focal mechanisms of moderate earthquakes and local microseismic surveys, have further supported the transverse nature of the active deformation in this region. The crustal and sub-crustal structure of the Sikkim Himalaya however not been explored in detail. Only very few geophysical studies, mainly confined along a N-S corridor following the main road connecting Lachen / Lachung and Chungthang to Siliguri, have been carried out leaving vast stretches of East, West and North Sikkim unexplored.

In this chapter, I present the general geology and tectonics of the Sikkim Himalaya along with various seismological studies and geophysical investigations carried out in the region.

2.1 General geology

The Sikkim Himalaya, like other parts of the Himalayan collision belt, exhibits four major geological sub-domains (Figure 2.01) namely the Sub Himalayan Domain (SHD), the Lesser Himalayan Domain (LHD), the Higher Himalayan Crystallines (HHC), and the Tethyan Sedimentary Sequence (TSS). SHD in the south overrides Quaternary deposits of the Indo-Gangetic alluvium, termed as Ganga Foreland Basin (GFB). These sub-domains are separated from each other by major thrust faults. A brief description of these sub-domains is given below.

- **Ganga Foreland Basin (GFB)**: GFB is formed due to the flexure of the Indian plate by the load of the mountain belt. It consists of Indian plate basement with Paleozoic platform

sediments overlain by Tertiary to Holocene syn-orogenic sediments. The sediments deposited in this basin are transported by the major Himalayan Rivers such as Ganga and Brahmaputra and their subsidiaries. Average elevation in the region is about 20-50m above mean sea level (msl).

- **Sub Himalayan Domain (SHD)**: SHD, separated from GFB by the Main Frontal Thrust (MFT) (also called Himalayan Frontal Thrust (HFT)), consists of mollase-type deposits of the Siwaliks (sandstone, shale and conglomerates formed as terrestrial or shallow marine deposits in front of rising mountain chains). It has an average elevation of about 100-500m. The Main Boundary Thrust (MBT) marks the northern boundary of SHD.

- **Lesser Himalayan Domain (LHD)**: LHD, located north of MBT, exposes vast expanse of pre-Tertiary rocks arranged in a pile of thrust sheets (Ray, 2000; Dasgupta *et al.* 2005 and Mitra *et al.* 2010). It mainly consists of low-grade to un-metamorphosed rocks particularly a thin strip of Gondwana rocks, carbonate rocks and a thick meta-sedimentary sequence of dominantly pelites with subordinate psammite and wacke ranging in age from Precambrian to Late Paleozoic. Daling group representing Precambrian metamorphites of low to medium grade composed of phyllites interlayered with quartzite and granitic ortho-gneiss (Mohan *et al.* 1989).The LHD has an average elevation of 2500 m with a slight gradient towards the north. The domain shows a straight east-west trending outcrop pattern and has been identified as a moderate to steeply dipping zone of thrusting (Gupta *et al.* 2010). It also displays a complex splay duplex geometry with footwall imbrications, folding and rotating overlying beds and fault surfaces, known as Lesser Himalayan Duplex (LHD) (Mitra *et al.* 2010; Mukul, 2000, 2010; Mukul *et al* 2007).

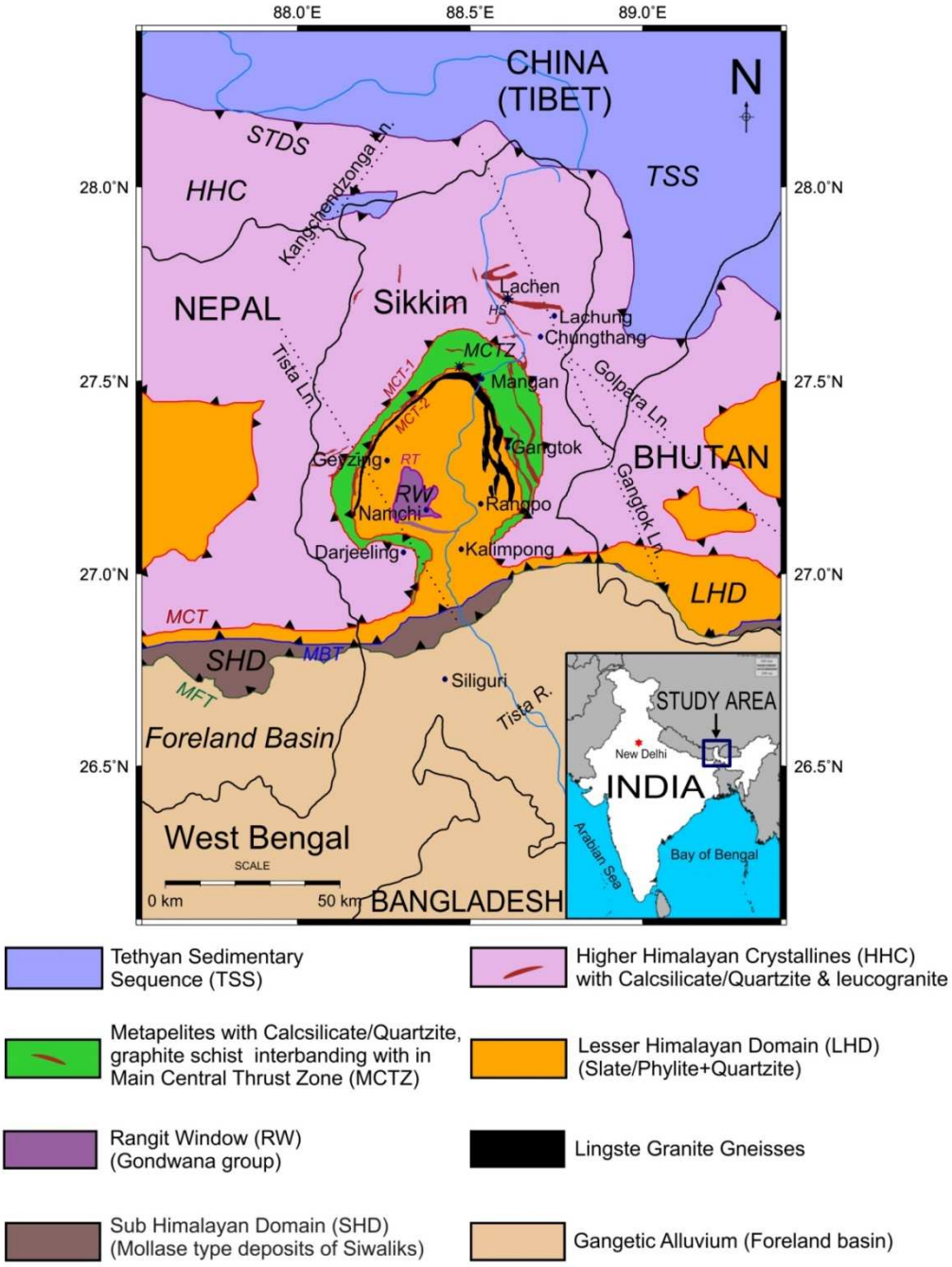

Figure 2.01: Generalized geotectonic map of the Sikkim Himalaya (modified after GSI, 2001; Dasgupta *et al.* 2004)

- **Higher Himalayan Crystallines (HHC)**: HHC, further north of LHD, occupies E-W to NNW-SSE trending zone in the northern part of the Sikkim Himalaya. The zone is composed of medium to high-grade crystalline rocks which are dominantly of pelitic composition with quartzites, calc-silicate rocks, meta-sedimentary rocks represented by the calc-silicate/quartzite, high grade schist and their fine interlaminations along with

small bodies of granite(Neogi *et al.* 1986; Dasgupta *et al*. 2004). In the local Sikkim geological literature these high grade gneisses containing quartz, feldspar with streaks of biotite are classified as Kangchendzonga Gneiss and Darjeeling gneisses (GSI, 2010). The high grade metamorphic rocks represented by quartzite, quartz-biotite, marble, graphite schist and quartzite,calc-silicate and garnet-bearing amphibolites are termed as Chungthang formations.

The MCT separating HHC from LHD is not a sharp boundary in the Sikkim Himalaya. It occurs as a several-km-wide zone of intense deformation known as Main Central Thrust Zone (MCTZ). The northern boundary of this zone separating HHC from the Daling group of the LHD juxtaposes high-grade gneisses of HHC over lower-grade slates, phyllites and schists of LHD. The topography in this region rises steeply to about 4500m.

- **Tethyan Sedimentary Sequence (TSS)**: In the extreme northern part of Sikkim, a thick pile of fossiliferous Cambrian to Eocene sedimentary rocks belonging to the Tethyan belt overlies HHC on the hanging wall side of a series of north-dipping normal faults. The South Tibet Detachment System (STDS) separates HHC from TSS. In some Indian literature STDS is also known as Trans Himadri Fault (THT) (Valdiya, 1976; Kayal, 2001).

Beside the above major geological sub-domains there are other significant geological units exposed in the Sikkim Himalaya. These are:

- **Main Central Thrust Zone (MCTZ)**: In the Sikkim Himalaya, the thrust (MCT) separating LHD and HHC is not a sharp interface as observed in the broad tectonic setup of the Himalaya along its arc. Here, MCT occurs as a several-km-wide ductile shear zone of intense deformation (Mohan *et al.* 1989; Neogi *et al.* 2004; Catlos *et al.* 2004; Dasgupta *et al.* 2004) and is referred as MCTZ. Its surface expression resembles an omega-shape encompassing LHD. MCTZ primarily consists of schists and gneisses representing both LHD and HHC. The southern and the northern boundaries of this zone are referred as MCT-1 and MCT-2, respectively (Mitra *et al.* 2010). The high grade meta-sedimentary rocks representing HHC occur as linear alternate bands with Darjeeling gneisses in the western part and Kanchenjunga gneiss in the eastern part. The high grade cal-silicate gneiss and biotite schists occur as a NW-SE trending linear band within the quartz schists,

graphitic schists and quarzites. Graphitic quartz schists are also exposed at some locations within HHC bearing quartzites and quartz schists.

- **Rangit Window (RW)**: Another important aspect of the geology of the Sikkim Himalaya is exposure of rocks of the Gondwana Group in a small tectonic window within LHD, called Rangit Window (RW). This tectonic window is bounded by Ramgarh Thrust (RT), equivalent of the Ramgarh Thrust in the western Himalaya and Nepal (Valdiya, 1980; Pearson & Decelles, 2005) and Shumar thrust in Bhutan (Mc Quarrie *et al.* 2008). In the Sikkim Himalaya it is also mapped as the North Kalijhora Thrust (NKT) (Mukul, 2000). Similar litho-units are also exposed further south in the form a lenticular tectonic wedge along the MBT (Narula *et al*. 2000).

In addition to the above, foliated granitic gneisses also occur at different tectonic levels and are found within the Daling group as well as along the contact between HHC and LHD. These granitic formations are termed as Lingtse granite gneisses (Acharya,1975; 1979). These Lingtse granite gneisses occurred as NE-SW to N-S trending of rocks and form a general line of separation between Daling group of LHD and the high grade Kangchendzonga gneiss of MCTZ Further, it has been observed that an inverted metamorphic zonation is present in the Sikkim Himalaya particularly in the LHD and MCTZ exposing the rocks of higher metamorphic grade at structural levels higher than those of the lower grade rocks (Dasgupta *et al.* 2004).

2.2 Tectonics

Tectonically, the Sikkim Himalaya is traversed by NNW-SSE trending Gangtok and Tista lineaments which are sub-parallel and traverse across Sikkim and WNW-ESE trending Golpara lineament and SW-NE trending Kangchendzonga fault/lineament (GSI, 2000; De & Kayal, 2003) besides the major thrust faults mentioned above (Figure 2.01). Significant information about the present-day tectonics comes from seismological data. Based on these data it is inferred that the Sikkim Himalaya has been experiencing transverse tectonic deformation even though the Himalayan collision belt is dominated by thrust type tectonic deformation (De & Kayal, 2003, 2004; Nath *et al.* 2005; Hazarika *et al*. 2010).

2.3 Seismicity and seismotectonic models

The Sikkim–Darjeeling Himalaya is considered to be one of the seismically active regions of the Himalayan collision belt with the occurrence of frequent moderate magnitude earthquakes. This region falls in the Zone IV of the seismic zone map of India (IS:1893-2002). Figure 2.02 show the epicentral distribution of earthquakes recorded World Wide Seismograph Station Network (WWSSN) from the eastern Himalaya during 1964-2002 (De & Kayal, 2003). Although the region has not experienced great earthquakes in recent years or in the known historical past, occurrence of frequent moderate magnitude earthquakes makes the region seismically vulnerable. Recent earthquake on 18th September, 2010 (Mw 6.9) with epicentre at the Sikkim-Nepal border caused severe damage in Sikkim. Table 2.2 shows a list of earthquakes in the Sikkim region during the period 1842 – 2013. Some events that were significant are also included.

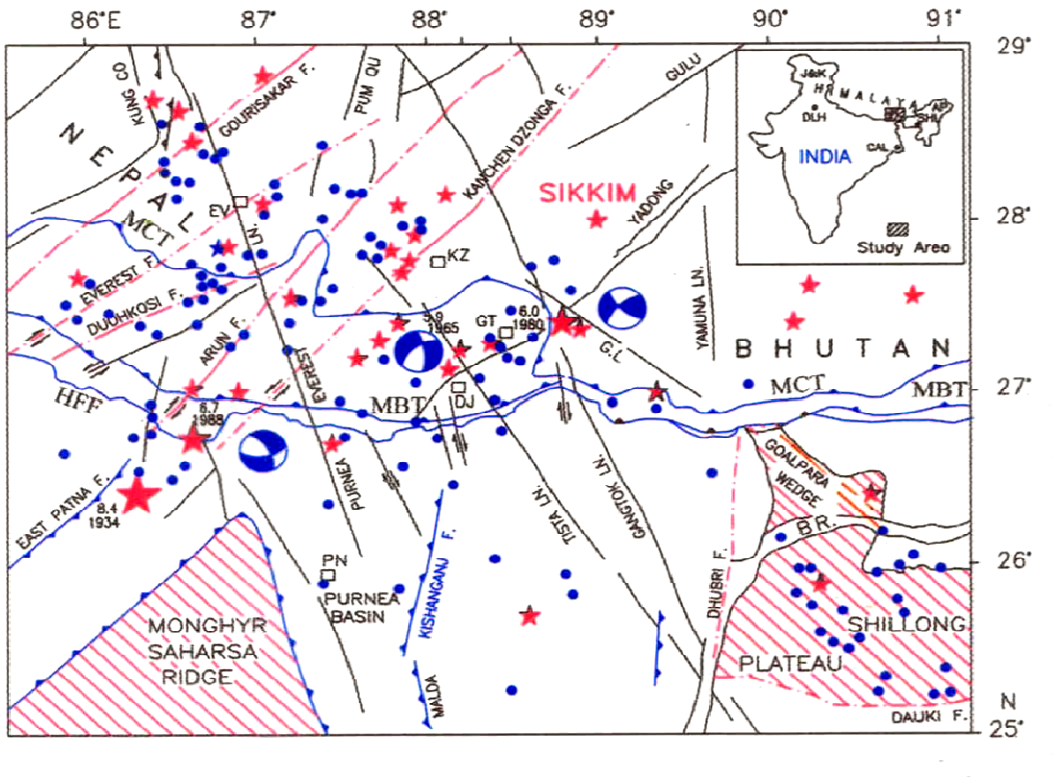

Figure 2.02: Seismotectonics map of the Eastern Himalaya with several transverse faults are mapped (The seismicity mapped by WWSSN are also shown with closed circles (taken from Kayal, 2001)

Table 2.02: List of significant earthquakes (earthquakes of magnitude > 5.0) in the Sikkim-Darjeeling Himalaya compiled from various sources during 1850 to 2013

Date	Lat. [N]	Long. [E]	Magnitude/Intensity	Depth (km)	Reference
05/1852	27.00	88.30	IX	-	Chandra, 1992
18/06/1862	27.00	88.30	VI	-	Chandra, 1992
29/031863	27.00	88.30	VII	-	Chandra, 1992
08/07/1863	27.00	88.30	VI	-	Chandra, 1992
11/08/1863	27.00	88.30	VI	-	-do-
16/12/1865	27.00	88.30	VI	-	-do-
23/03/1869	27.00	88.30	V	-	-do-
09/08/1869	27.00	88.30	VII	-	-do-
16/04/1875	27.00	88.30	V	-	-do-
25/09/1899	27.00	88.30	VIII	-	-do-
15/01/1934	26.50	86.50	8.0(8.4)/ VIII	-	-do-
21/05/1935	28.8	89.3	5.9	140	-do-
11/02/1936	27.50	87.00	5.6	-	-do-
29/01/1938	27.50	87.00	5.5	-	-do-
15/12/1959	27.00	88.30	V	-	-do-
21/08/1960	27.00	88.50	5.5	29	Chandra, 1992
30/08/1964	27.36	88.21	5.1	21	ISC
01/02/1964	27.3	87.8	5.1	33	ISC
27/03/1964	27.1	89.4	5.0	29	ISC
12/01/1965	27.40	87.84	5.8	23	Dasgupta et al. 1987
1965	27.60	88.00	6.1(5.9)	-	CSIR-NGRI
4/12/1971	27.9	88.00	5.2	29	ISC
21/08/1972	27.22	88.02	5.1	-	ISC
26/11/1975	28.34	87.64	5.1	33	ISC
24/04/1975	27.24	87.90	5.1	33	ISC
24/06/1975	27.47	87.29	5.2	33	ISC
24/03/1974	27.24	86.11	5.7	33	ISC
23/10/1976	28.676	86.228	5.1	63	ISC
19/06/1979	26.74	87.51	5.1	24	ISC
19/06/1980	27.40	88.80	6.0	47	Dasgupta et al. 1987
09/02/1981	27.038	89.75	5.1	33	ISC
05/04/1982	27.38	88.38	5.0	9	ISC
07/01/1986	26.93	88.32	5.0	69.6	ISC
20/08/1988	26.75	86.62	6.8 (6.9)/VII	57.4	Kayal, 2012; ISC
20/04/1988	27.04	86.67	5.4	54.8	ISC

27/09/1988	27.17	88.29	5.0	33	ISC
22/05/1989	27.243	87.89	5.0	33.8	ISC
09/01/1990	28.225	86.16	5.5	79.1	ISC
20/03/1993	28.994	87.38	5.2	21.1	ISC
26/04/1996	27.82	87.82	5.0	33	ISC
25/09/1996	27.433	88.552	5.0	33	ISC
30/12/1996	27.435	86.638	5.0	33	ISC
08/12/1997	27.475	87.17	5.0	33	ISC
03/09/1998	27.85	86.94	5.6	33	ISC
26/11/1998	27.753	87.894	5.1	73.1	ISC
01/08/1999	28.44	86.73	5.2	40.2	ISC
31/05/2000	27.55	88.4	5	7.4	Nath et al, 2004
02/06/2000	27.2	88.48	5.1	22.3	-do-
10/06/2000	27.18	88.31	5.1	23.41	-do-
04/07/2000	27.17	88.45	5.1	24.52	-do-
21/09/2000	27.38	88.52	5.1	17.86	-do-
13/06/2000	27.5	88.36	5.3	10	-do-
16/06/2000	27.68	88.29	5.2	10	-do-
02/12/2001	27.15	88.17	5.1	33	ISC
03/10/2001	27.23	88.48	5.3	34.27	Nath et al, 2004
22/04/2002	27.09	88.86	5	19.4	-do-
28/04/2002	27.18	88.71	5.0	24.1	-do-
29/04/2002	27.20	88.70	5.0	27.83	-do-
25/04/2002	27.28	88.63	5.1	22.9	-do-
25/04/2002	27.15	88.83	5.1	10	-do-
25/04/2002	27.32	88.3	5.1	26.4	-do-
30/04/2002	27.91	88.54	5.2	10.00	-do-
25/04/2002	27.24	88.78	5.3	32.37	-do-
02/05/2002	27.97	88.87	5.3	10.00	-do-
25/03/2003	27.26	89.33	5.5	47.1	ISC
14/02/2006	27.42	88.55	5.3	20	CSIR-NGRI
11/08/2007	27.53	87.74	5.0	35	ISC
20/05/2007	27.5	88.3	5.0	15	IMD
02/12/2008	27.37	88.05	5.2	24.7	ISC
26/02/2010	28.47	86.74	5.1	89.1	ISC
03/06/2011	27.53	88.02	5.0	45.7	ISC
19/10/2011	27.72	88.14	6.9	50	CSIR-NGRI;USGS
27/03/2012	26.09	87.78	5.0	28.8	ISC
03/10/2013	27.40	88.57	5.3	8	EMSC

In view of recurrent moderate seismic activity, several micro-earthquake surveys by various research/academic institutions have also been carried out in this region by installing local temporary/semi-permanent networks of seismic stations to understand the seismicity pattern and delineate causative active faults as well as to assess seismic hazard assessment of the Sikkim Himalaya.

The Indian Meteorological Department (IMD) operated a network during 1982 -1992. During the period 15 moderate earthquakes (> 4.5) were recorded (De, 1996). Then after, Geological Survey of India (GSI) operated a network of closely spaced seismic stations in the Sikkim-Darjeeling Himalaya intermittently during 1992 to 1999. The network was operated for about five months during Dec. 1992- April 1993 in the Darjeeling Himalaya and then in the Sikkim Himalaya during Dec. 1994- March 1995. Nearly 400 earthquakes were recorded during the two surveys of which 100 events of magnitude 1.0-5.0 were located within the 50 km distance of the networks (Figure 2.03). Four events of magnitude ~4.0 were recorded during the period. It was observed that the earthquakes were mostly clustered to the north MBT and focal mechanisms of moderate earthquakes show dominantly strike-slip faulting (De, 1996, 2000; De & Kayal, 2003, 2004).

Analysis of these data sets reveals that majority of the earthquakes are not confined to shallow depths (<25 km). The focal depths of these events fall well below the plane of detachments (also called MHT) and even below the Moho (Figure 2.04). These events are clustered to the north of MBT (10-40km), well below the detachment plane. This observation does not obey the conventional seismotectonics model of the Himalaya proposed by Seeber *et al.* (1981) and Ni & Barazangi (1984) where MBT is recognized as a major fault that is inferred to merge with MHT based on the extensive studies in the western Himalaya.

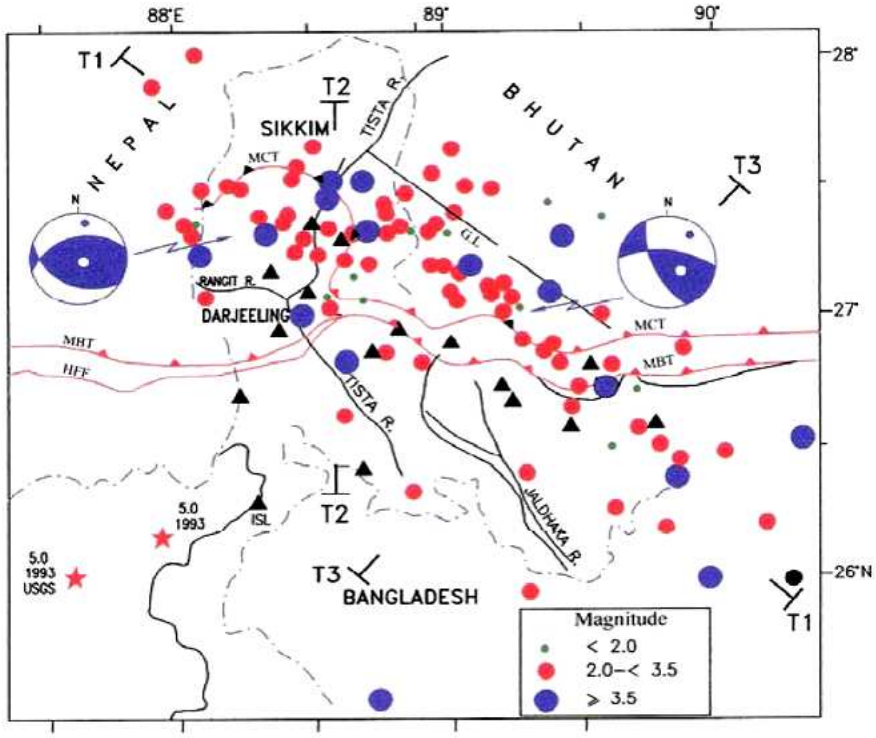

Figure 2.03: Microseismicity observed during the survey by GSI (De & Kayal, 2003)

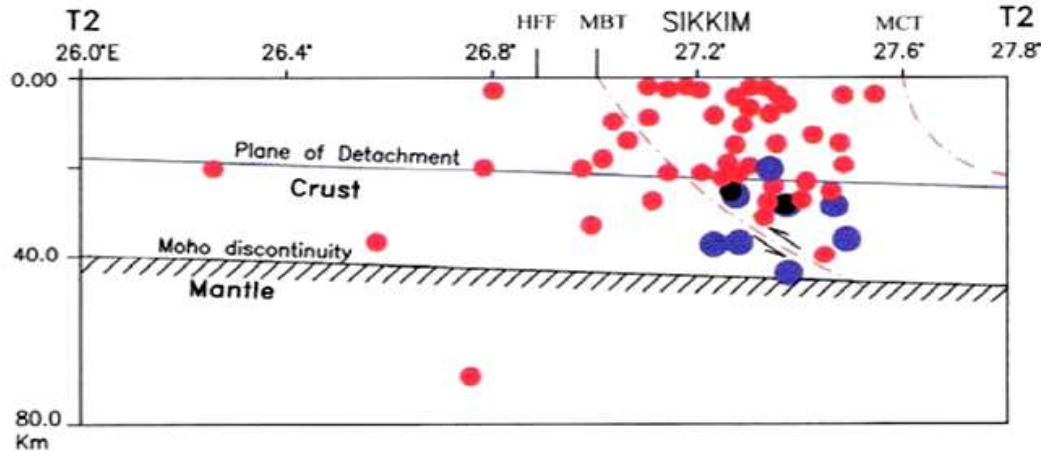

Figure 2.04: Depth section along T2 profile marked in Figure 2.03 which shows deeper source (De & Kayal, 2003). Symbols have the same meaning as in Figure 2.03.

Thus, the conventional seismotectonic model of Himalaya (Seeber *et al*. 1981; Ni & Barazangi, 1984) does not fit the complex seismotectonic scenario of the Sikkim Himalaya as inferred mainly from the seismological data. De & Kayal (2003) proposed that MBT is a seismogenic mantle reaching fault cutting across the entire crust rather than converging with the plane of detachment unlike in the western Himalaya and the tectonics of the region is well influenced by it. The clustering of epicenters of micro-earthquakes along the NW-SE

trending Tista and Gangtok lineaments and dominance of strike-slip motion revealed by composite fault plane solutions of these earthquakes adds another dimension to the complex seismotectonic model of the region in terms of the presence of transverse tectonic features. De & Kayal (2003, 2004) reported right-lateral strike-slip motion on a NNE-SSW trending nearly vertical fault.

Another micro-earthquake survey was carried out by GSI in the southern part of Sikkim and northern part of West Bengal for about two months duration in 2007. Here, a four-station network was operated. Majority of the recorded seismic events were concentrated on the eastern side of Tista lineament suggesting that this lineament has an important bearing on the accumulation of stresses and release of tectonic strain in the region (Joshi *et al.* 2010). Analysis of focal mechanism of 2011/09/18 earthquake and its aftershocks indicated seismic activity along a NW-SE trending mantle reaching transverse fault causing earthquakes down to the depth of 60 km (Kayal *et al.* 2011). Tectonic stresses estimated for some past earthquakes also suggest a NNW-SSE horizontal compression direction (Kayal *et al.* 2012).

CSIR-National Geophysical Research Institute (CSIR-NGRI) installed a network of 11 broadband seismic stations in October 2004 along an N-S profile cutting across both MBT and MCT. This network was operational upto Nov. 2010. The data from this network have been analyzed by various seismological techniques (e.g. focal mechanism solutions, receiver function analysis etc.) in order to understand the seismotectonics of the region as well to characterize the seismic behavior of the crust and lithosphere. Composite focal mechanism solutions of the dataset during Jan. 2006 to Nov. 2007 yield NNW-SSE orientation of the P-axes instead of conventional NNE-SSW direction of the Indian plate motion with respect to the Eurasian plate. This transverse trend of the P-axis indicates the presence of transverse tectonics in the region and has been interpreted in terms of accommodation of the Indian plate convergence through shear along vertical planes in the proximity of the Moho (Hazarika *et al*. 2010). In another survey to monitor the aftershock activity of the 2010/09/18 Sikkim earthquake of magnitude Mw 6.9 and focal depth 50km, CSIR-NGRI established a network of 5 seismographs and recorded a total of 292 aftershocks including six events > 4.0 magnitude events during Sept. 22, 20011 to Nov. 23, 2011. Out of these 292 recorded events, a total of 189 aftershocks could be well constrained using data from three or more stations. Focal depths these events go down to 60 km depth, well below the inferred plane of detachment (MHT) (Ravi Kumar *et al.* 2012). Analysis of these earthquakes further supports dominance of continued transverse tectonics in the region. Ravi Kumar *et al.* (2012) inferred

that the convergence of the Indian plate is accommodated by dextral motion along steeply dipping fault systems.

Another seismological network, Sikkim Strong Motion Array (SSMA), was operated by Indian Institute of Technology, Kharagpur (IIT-KGP) during 1998-2003 for the understanding of the Seismic Hazard scenario of the Sikkim Himalaya. More than 150 earthquakes were recorded during the period, of which 12 were of moderate (≥ 5) magnitude (Figure 2.05). The study has assigned expected peak ground acceleration (PGA) > 0.4 KGal to Sikkim along with North-Eastern India (Nath *et al.* 2005). This survey also supports the strike-slip nature of deformation in the region. Further, the presence of several approximately N-S trending gravity faults, besides MCT and MBT, is also inferred from this study.

There are also some tectonic models proposed for the Sikkim Himalaya from the structural geology perspective. Mukul (2000) and Mitra *et al.* (2010) suggest that the MCT has been folded by the younger LHD structure and eroded. It has been known that fault get folded by younger footwall faults in fold-thrust belt once they become inactive (Boyer & Elliott, 1982). This suggests the MCT is inactive and probably not the dominantly active seismogentic structure in the region. The Lesser Himalayan Duplex in the region is recognized as a prominent geological structure involving Daling, Buxa and Gandwana units. In the model proposed by Mukul (2000, 2012) and Mitra *et al.* (2010), the Ramgarh Thrust (RT) is inferred as the roof thrust and converge with MHT/decollement plane at a depth of ~10km with a dip of ~3.5^{o}N under LHD similar to dip of MHT at the base of the LHD (Bhattacharya & Mitra, 2009; Mitra *et al.* 2010). Recent studies by Mukul (2000, 2012) argued that MBT in this part of Himalaya is also unlikely to be active or seismogenic. They pointed out that, even though majority of seismic events fall north of MBT but the hypocenters distribution is diffused and distributed over large area instead of clustering over the inferred seismogenic MBT. In addition, Similar to MCT, MBT is also folded in the region by the another thrust sheet in the LHD known as Ramgarh Thrust (RT).

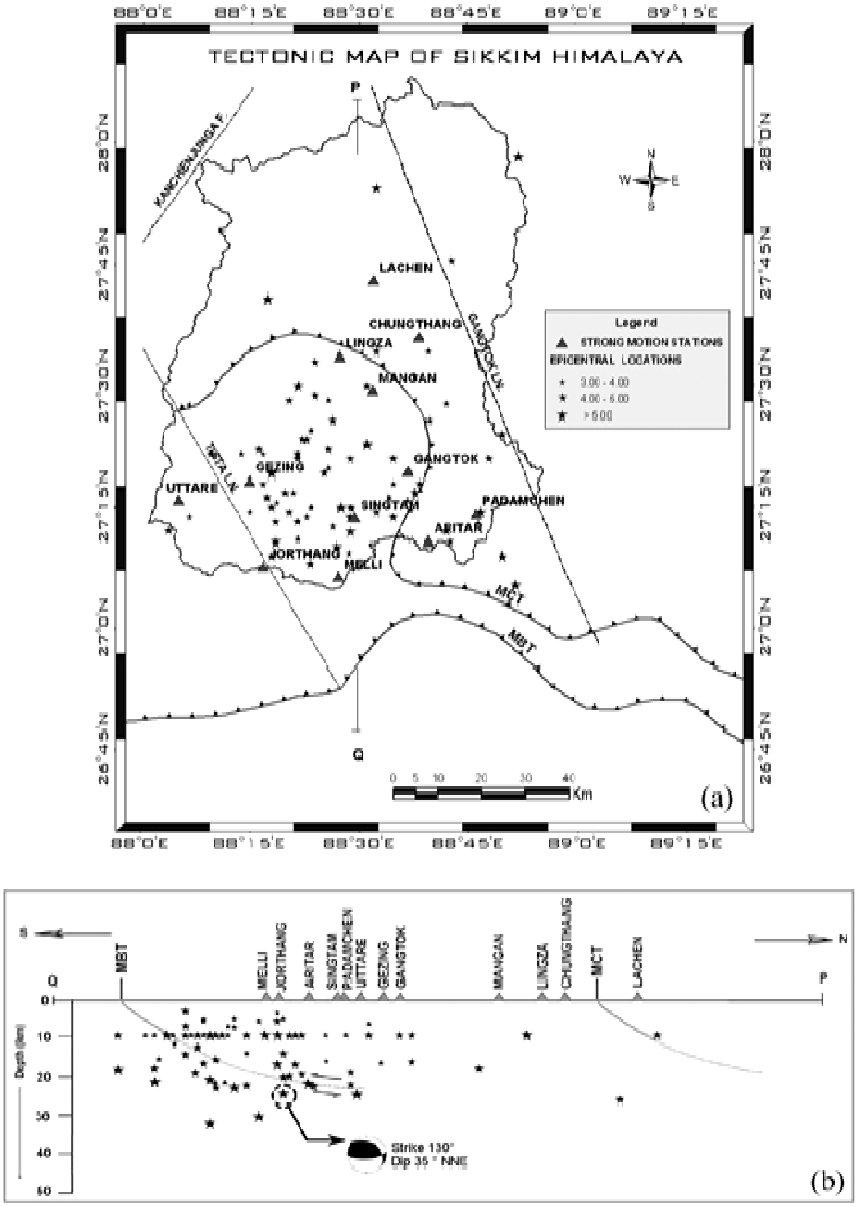

Figure 2.05: (a) Epicentral distribution of earthquakes recorded by the SSMA, and (b) depth section along a N-S profile QP showing focal depths (from Nath *et al.* 2005)

2.4 Subsurface structure from geophysical studies

Although several geophysical studies have been carried out in the western sector of the Himalaya (Qureshy & Kumar, 1992; Rai *et al*. 2006; Arora *et al.* 2007, Israil *et al.* 2008; Caldwell *et al.* 2013) and in the Tibetan region (INDPETH program I & II; Schulte-Pelkum *et al.* (2005), very little geophysical information is available for the Sikkim Himalayan region despite its seismic vulnerability and complex geotectonic setting. Most of the geophysical studies in this region have focused on seismological component. A few studies involving other geophysical methods such as gravity and magnetic and magnetotelluric have been

carried out mainly along N-S corridor across Sikkim. This corridor follows mainly the Siliguri-Gangtok-Lachung road leaving vast off-profile regions untouched. This section summarized salient results obtained by these studies.

2.4.1 Seismic velocity structure from receiver functions analysis

Singh *et al*. (2007, 2010) analysed 3600 receiver functions using earthquakes recorded by the network operated by CSIR-NGRI to map the crustal and sub-crustal structure. The analysis of SKS/SKKS waveforms infers the presence of strong anisotropy in the crust. The fast polarization direction has NW-SE orientation which is orthogonal to the Absolute Plate Motion (APM) direction of the Indian plate. Singh *et al.* (2007) attributed crustal anisotropy to foliation of the planes within the mid crust forming a localized low velocity zone in the depth range of 20-30 km. They further advocated that the anisotropy could be due to transcurrent deformation within the mid crustal levels. The transcurrent deformation is evidenced by a conjugate system of strike-slip faulting with NW to NE trending P-axis orientations. The polarization strikes estimated from the study did not correlate with the local strike direction of MCT and MBT. They infer that this un-correlation might be due to shallow origin of these faults. The study also suggests deformation of the lithospheric mantle as a consequence of compression at the Himalayan collision front (Figure. 2.06, Singh *et al.* 2007).

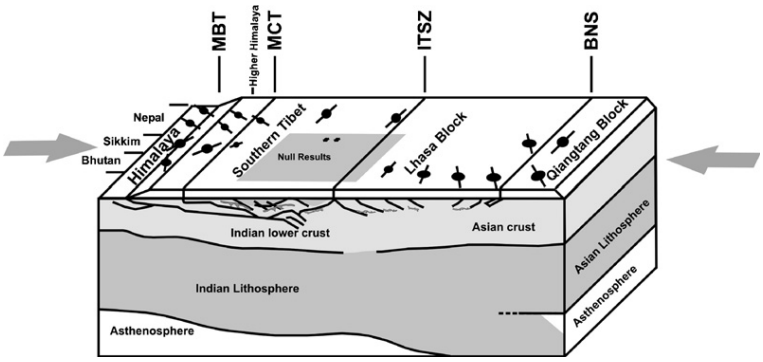

Figure 2.06: Cartoon showing the results from the study of Singh *et al.* (2007). Arrows show the direction of compression. The region where negligible anisotropy is reported is shown as a shaded portion.

Further analysis of these receiver functions reveals that the crustal thickness varies from about 40 km at the foothills to 61 km beneath the Higher Himalaya with the dip varying between 4° and 10° among stations (Singh *et al*. 2010). A prominent Moho doublet

delineated at ~40 km depth beneath the Higher Himalaya to the north of MBT has been interpreted in terms of partial eclogitization of the granulitic lower crust of the Indian plate, akin to the finding beneath southern Tibet (Zhao *et al.* 1993 (INDEPTH-II); Yuan *et al.* 1997) north of the study region (Singh *et al.* 2010)

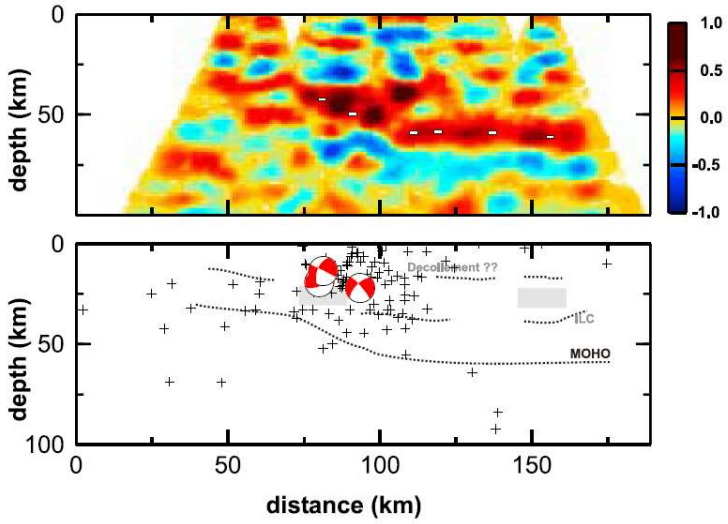

Figure 2.07 Crustal thickness estimates obtained through receiver function analysis (Singh *et al.* 2010) are plotted by small white bars in the migrated image. Bottom panel shows the major features of the image, together with seismicity and focal mechanisms in map view.

Acton *et al.* (2010) studied crustal structure of the Darjeeling-Sikkim Himalaya as well as southern Tibet and imaged the under-thrusting Indian plate by simultaneous modeling of receiver function data and Rayleigh wave group velocity dispersion. The receiver function image from the study also suggests northward gradual thickening of crust (Figure 2.08) and occurrence of Moho doublet. The study also reveals the presence of a northward dipping low velocity zone (LVZ) beneath the Darjeeling–Sikkim Himalaya to the southern edge of the Higher Himalaya. The LVZ forms a fairly smooth horizontal layer at the depth of 10-15 km south of Gangtok. It descends sharply to the depth of 20-25 km just after Gangtok forming a ramp like structure beneath the region. The Moho begins to dip northward at a sharp angle north of Chungthang. Acton *et al.* (2010) correlated the observed LVZ with the MHT in the region, the detachment separating the under-thrusting Indian plate from the hanging wall of the wedge forming the Himalaya.

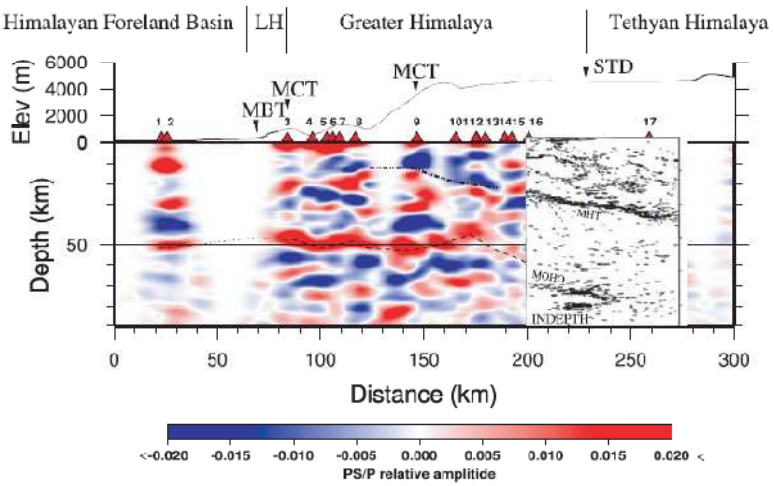

Figure 2.08 Receiver function image of the Darjeeling-Sikkim Himalaya and southern Tibet. The possible position of MHT is marked by dot-dashed line and the likely Moho by dashed line Acton *et al.* (2010)

2.4.2 Electrical resistivity structure from MT studies

A couple of magnetotelluric surveys have been carried out across the Sikkim Himalaya to delineate the electrical resistivity structure of the crust. Gokarn *et al.* (2005) have acquired MT data in board frequency range in region along Mangan-Gangtok-Siliguri-Dalkhola. Strike analysis of the MT transfer functions for 17 sites along the profile suggests a regional strike of N70^{o}E. The 2-D geoelectric section derived from the inverse modeling of the data set preliminarily inferred the present high conductivity region of 3000 Siemens in the depth range of 10 to 40 km below MFT/MBT (Figure 2.09). The shallow part of the high conductivity zone was attributed to presence of Siwaliks.

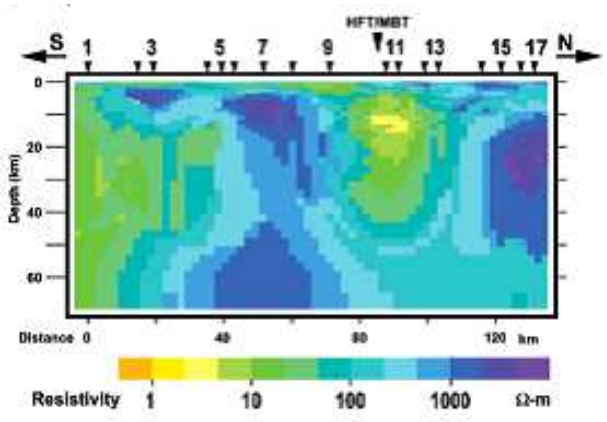

Figure 2.09 2-D geoelectric section of the Sikkim Himalaya along the profile derived by Gokarn *et al.* (2005)

Patro & Harinarayana (2010) covered almost the same profile by broadband MT. The profile starts from the southern end of the SHD and ends at Yumthang situated in HHC. They acquired MT data of 2-3 days duration in broad frequency range at 18 sites along the profile and used data of 13 sites for analysis. Regional strike analysis of the data suggests N80^{o}E MT strike that is in agreement with the E-W strike of the northward moving Indian plate. The final 2-D structure derived after the inversion of the MT data (Figure 2.10) reveals several conductive features (C1, C2 and C3 in the figure) in addition to some resistive blocks (R1, R2, R3 and HHC). High conductive zones (2-5 Ω-m) in the upper crust (C2, C3) north of MBT in the depth range of 3-20 km are inferred as a mixture of Siwalik mollasse sediments of LHD and SHD along with trapped fluids in the fault zone. Another similar high conductivity zone (C4) observed north of MCT where the location coincides with the trace of the MHT in the HHC. They have suggested that these high conductivity zones could be indicative of metamorphic fluids that might be released due to continuous under-thrusting of the Indian plate.

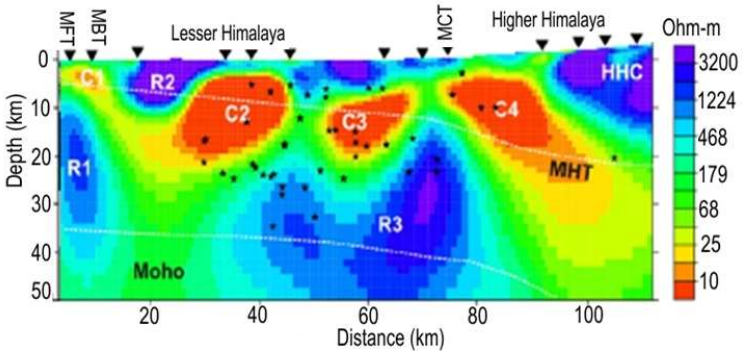

Figure 2.10: 2-D geoelectric section derived by Patro & Harinarayana (2010)

There are some considerable similarities in the two model derived from these studies. The high conductivity zone beneath the MBT and the resistivity block representing HHC are observed in both of the models. In the both studies the HHC is imaged as high resistivity block

2.4.3 Density structure from gravity studies

Gravity and magnetic measurements were made along a profile that starts from Singhbhum carton (south of GFB) and cuts across various geotectonic domains of the Sikkim Himalaya (Tiwari *et al.* 2006). Crustal structure obtained by joint modeling of gravity and magnetic data is shown in Figure 2.11. Flexure modeling of Bouguer gravity data yields the effective elastic thickness of 50±10 km for the Indian plate in the region (Tiwari *el al.* 2006). The

study suggests thinning of meta-sediments of LHD (extend up to 12 km depth) towards north indicating more uplift and erosion. The MBT and MCT in the region dip towards north at angle of 22^{o} and 16^{o} respectively.

2.4.4 GPS study

GPS study carried out in the central Nepal Himalaya region yielded N44E drift of the Indian plate with the velocity of 5.8 ± 0.4cm/yr with respect to Asia and collision with Tibet with a rate of 20.5 ± 2 mm/yr. (Bilham *et al.* 2001). In the central Bhutan region, the value is ~16mm/yr (Jade *et al.* 2007). The Sikkim region, like other parts of the collision belt, over-thrusts the Indian plate along the decollement at the rate of 18 mm/yr building up a slip deficit between great earthquakes, of about 1.8m per century (Bilham *et al.* 2001).

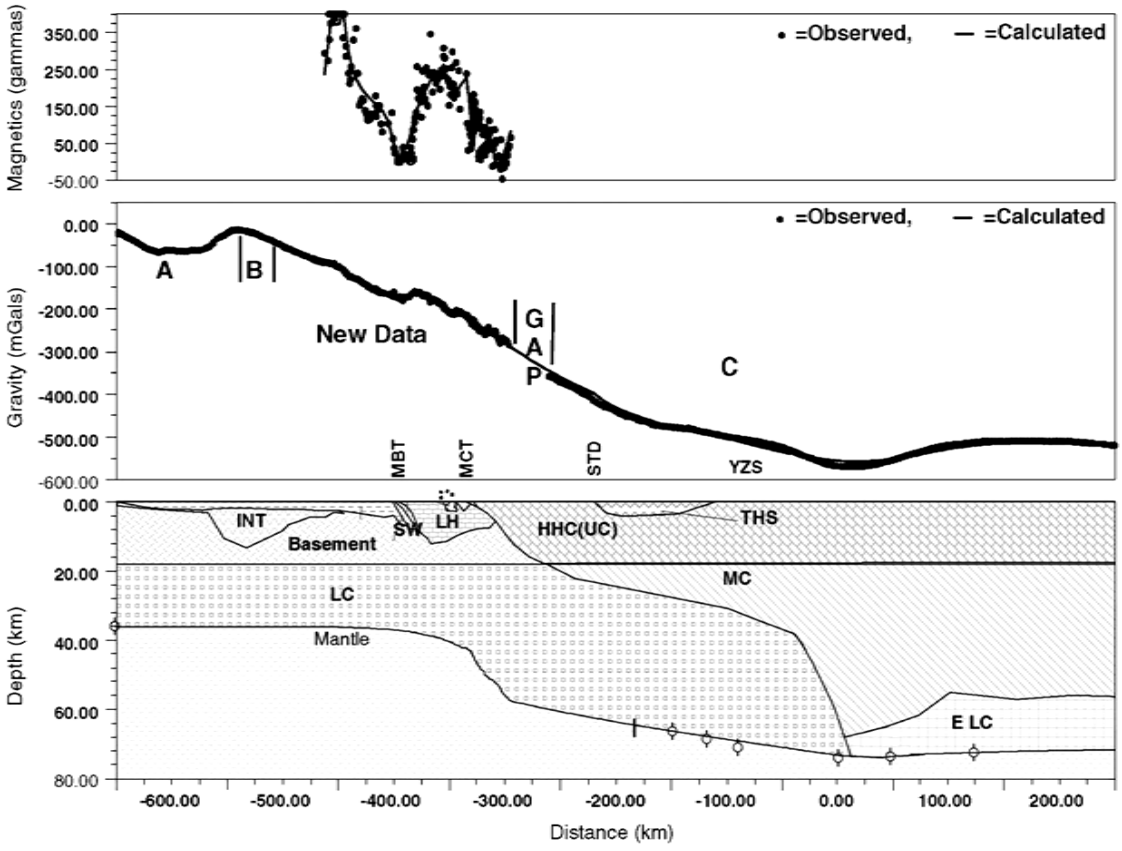

Figure 2.11: Crustal cross-section derived from joint modeling of gravity and magnetic data. The observed and calculated gravity and magnetic anomalies are also shown (Tiwari *et al.* 2006).

3.2 Summary

The seismological and other geophysical studies reveal that the Sikkim Himalaya is tectonically highly complex and vulnerable to recurrent seismic activity. The region is experiencing transverse tectonics deformation and major thrust faults appear to be cutting across the entire crust. Although significant progress has been made through seismological studies towards understanding of the active tectonics of this segment of the Himalayan collision belt, mapping of the crustal/ lithospheric structure of the Sikkim Himalaya at a reasonable scale through extensive geophysical exploration is needed for better understanding of the causative mechanisms for recurrent seismicity and complex tectonic deformation. In active tectonic regions, aqueous and metamorphic fluids can form connected pathways especially in weak zones such as faults and shear zones. Therefore, electrical methods e.g. magnetotellurics can effectively decipher the complex subsurface structure.

Chapter 3

Methodology

The major focus/aim of geophysics is to understand Earth system in terms of various physical properties, e.g. electrical conductivity, permeability, density, magnetic susceptibility, elastic properties, thermal conductivity, etc. as a function of spatial coordinates. However, it is difficult to measure these physical properties directly except on samples available on surface and within near surface. Therefore, responses of these physical properties on physical fields are measured. Generally, electrical and electromagnetic, gravity and magnetic, seismic and seismological, geomagnetic, etc. methods are used to probe the Earth's interior and to understand the physical processes operative within its interior. The behavior of these fields generated either by artificial sources or by natural sources depends on the material properties of rocks. Thus, changes in a physical field can be interpreted in terms of variations in the corresponding physical property.

3.1 Physical properties of rocks

Physical properties of rocks depend greatly on rock composition. The rock properties that are typically measured in most of the geophysical exploration methods are acoustic velocity, density, susceptibility, permeability and resistivity. Averaged values of these physical properties for some materials are listed in Table 3.01. Of these properties, resistivity (ρ) (inverse of conductivity(σ)) varies by several orders of magnitude among earth materials, far more than other physical properties. An overview of the resistivity values of various earth materials is shown in Figure 3.01.

3.1.1 Electrical resistivity

Electrical conductivity (inverse of resistivity) is the property of motion of electric charge through a material. The easier it is to move the charge through the material, the higher the conductivity. The electrical conductivity of rocks depends on the density of charge carriers and the geometry of current pathways. High porosity, high salinity pore fluid, high saturation of fluid, or partial melting of rock will give high density of charge carriers. Good interconnection between pores can give a high density of electric current pathways. The resistivity of the rock is thus a function of the above parameters. It is one of the most sensitive physical parameters that strongly depends on the composition and temperature of earth materials as well as on the presence and characteristics of interstitial fluids in rocks. Therefore, estimation of resistivity distribution inside the earth can effectively decipher geological discontinuities such as faults because of strong resistivity contrasts due to fluid movements. Variations of electrical conductivity in the crust can result from changes in fluid content, pore geometry, or lithology. Conductive zones in the crust are generally thought to reflect well-connected conductive phases, such as brines or melts, or conductive minerals like graphite (Marquis, 1995). This is one of the reasons why measuring resistivity is appealing for crust and upper mantle where the existence of partial melts/fluids/saline water is widely inferred by some seismological/geophysical studies (Nelson *et al.* 1996; Brown *et al.* 1996).

Table 3.01: Average physical properties of some materials encountered in geophysical applications. (Data compiled from Telford, 1990; Parasnis, 1986; Zhdanov & Keller, 1994)

Rock-type	Material	Density [g/cm^3]	Magnetic Susceptibility	Resistivity [log (Ohm-m)]	Dielectric constant	Seismicvelocity [km/s]
Various	Air	0.001	0	1.5	1	0.3
	Water	1.0	-7×10^{-10}	00-2	80	1.4-1.5
	Ice	0.9	$-7X10-10$	06	3-4	3.4
	Oil	0.6-0.9	2×10^{-5}	014	2	1.3
	Salt	2.2	-1×10^{-6}	015	6	4.5-5
Unconsolidated	Soil	1.5	7×10^{-4}	3	4	0.1-0.2
Sediments	Clastics	1.9	5×10^{-4}	3-4	4	1-2
	Sand	1.6	5×10^{-4}	4	4	3
Metal Ores	Oxides	3.8-9.1	3×10^{-3}	-1 to 2	10-25	5.5
	Sulfides	3.8-8.1	3×10^{-3}	-6 to -3	8-31	5.8
Sedimentary rocks	Sandstone	2.2	4×10^{-4}	2-3	5	5.5
	Shale	2.1	6×10^{-4}	0-1	6-8	2-6
	Limestone	2.7	3×10^{-4}	2-3	8-9	2.3
Igneous Rocks	Granite	2.6	2×10^{-3}	4-6	5	3-6
	Basalt	3.0	7×10^{-2}	7	15	5-6
Metamorphic rocks	All	2.6-2.7	5×10^{-3}	3.5	8-40	5.5-6

In favorable geological settings, resistivity methods can be applied to determine the subsurface geoelectric structure which can in turn be correlated with plate tectonic boundaries such as in the Himalayan collision zone where fluids are distributed along the strike of the faults and heavily mineralized zones where alteration to the host geologic structures creates conductive anomalies against unaltered rock (Lewis, 2009).

The flow of electric currents in porous and/or fractured rocks is dominantly due to the presence of electrolyte in pores and fractures. These pores are often filled with fluids, mainly water, thus allowing current flow in the form of electrolyte conduction. The bulk conductivity of the medium in such cases can vary by several orders of magnitude depending on the nature of the fluid, pore space volume (porosity) and interconnectivity of pores (permeability) as the electric current flows predominantly through the pore fluid. This mode of conduction is more common in fluid-filled sedimentary rocks and for highly fractured fault-gauge medium. The bulk electrical conductivity of fluid-saturated rocks, where fluid can be either aqueous phase or melt, can be expressed as Archie's Law (Archie, 1942; Hermance, 1979)

$$\sigma_{bulk} = \sigma_{fluid}\phi^2, \tag{3.1}$$

where σ_{bulk} is the bulk conductivity of the rock, σ_{fluid} is the conductivity of fluid contained in the pores and cracks, and ϕ is the fractional porosity of the interconnected pathways.

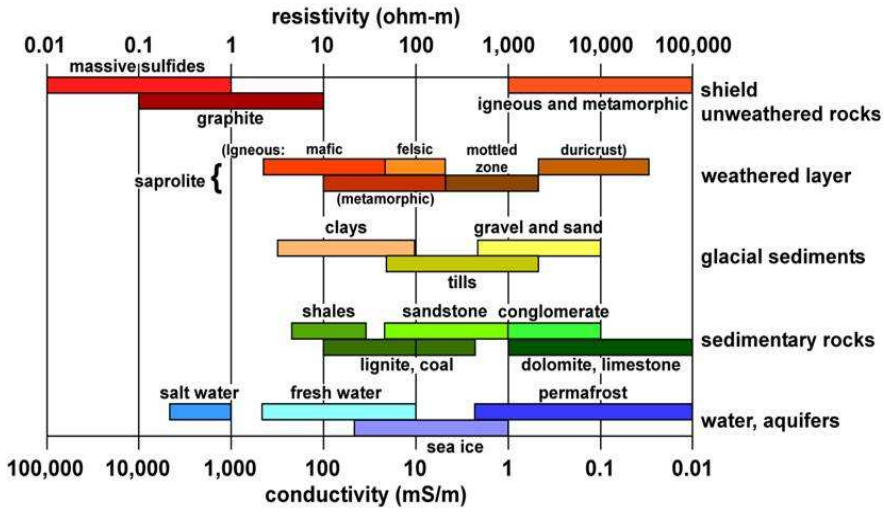

Figure 3.01: An overview of the ranges of conductivity for various types of rocks (Palacky, 1987).

3.1.2 Electrical anisotropy

A range of field and laboratory studies suggest that the both crustal and upper mantle rocks can exhibit electrical anisotropy (Wannamaker, 2005). In the case of crustal rocks, this occurs when the rocks contain a low resistivity phase that is distributed anisotropically in the rock. For example, graphite is commonly found in fractured rocks that have undergone extensive deformation. This produces electrical anisotropy that has been measured both with borehole logging (Eisel & Haak, 1999) and with magnetotelluric survey (Heise & Pous, 2003). A similar effect can occur when the crustal rocks contains fluids that are present in fractures that not uniformly distributed. By using various geophysical methods it is difficult to distinguish between heterogeneous isotropic resistivity structures and anisotropic resistivity structures. The high quality MT data set with measurements of the vertical magnetic field are very useful in this respect (Brasse *et al.* 2009).

3.1.3 Measurement of electrical resistivity of the earth at depth

Measuring the resistivity of *in situ* rocks is more challenging, since indirect methods must be employed. These can be divided into (a) well-logging that measures resistivity of rocks within a few meters of a borehole; and (b) geophysical studies that sample volumes up to depths of tens of kilometers. Resistivity log data can provide a valuable check on resistivity models derived from geophysical studies and vice versa.

In well-logging, the resistivity of the subsurface can be measured with a range of tools that use either galvanic or inductive couple (Ellis & Singer, 2008). But these methods do not provide measurements of large volume away from the borehole and are inherently limited by the depth of extent of the well. Thus, measuring the resistivity of rocks under in situ conditions at depth in the crust or upper mantle requires the use of geophysical imagining which is the focus of the following section.

For shallow investigation of subsurface electrical resistivity methods using direct electrical current are very effective. However they are also inherently limited to the depth of penetration because of the electrode spacing must be comparable to the depth of investigation. Sounding to depths in excess of 1km becomes logistically complicated. In contrast, the depth of investigations with electromagnetic methods can be varied by simply changing the frequency of signal. For deeper imaging, naturally occurring low frequency EM signals are the ideal choice. There is a well known geophysical imaging technique called

magnetotellurics (MT) which is the most suitable for studies of crustal and upper mantle resistivity (Simpson & Bahr, 2005).

3.2 Electromagnetic methods

Electromagnetic (EM) methods constitute a sub-discipline of geophysics in which subsurface structure of the earth is explored at various spatial scales in the form of electrical conductivity (resistivity) distribution through application of electromagnetic theory to earth. The first step in the development of electromagnetic theory was laid in the 1820s by Ampere with the discovery of the fact that electric currents generate magnetic fields. In 1831, it was advanced by Faraday who discovered electromagnetic induction, the process by which a time-varying magnetic field induces electric current in conductors. The applicability of EM methods to Earth was shown by Schuster in 1908 who observed that there was a relationship between the Earth's magnetic field variation and the Earth's electrical potential. Chapman and Whitehead concluded in 1919 that this relationship was related to the Earth's conductivity. In contemporary time, we are using EM induction in the Earth as an effective way to image the Earth's electrical conductivity structure from shallow levels to great depths.

The basic principle in this method is that conductive rocks affect the electromagnetic response to artificially or naturally stimulated electric and magnetic fields and generate secondary fields in the medium. Measurement of these secondary fields can give information on the earth's subsurface, both lateral and vertical, in terms of conductivity. The vertical information depends on the depth of penetration of EM signals that is a function of frequency and electrical conductivity of the medium. EM methods can be classified according the nature of the source field. The methods utilizing artificially induced source fields are called controlled source methods. These include Controlled Source EM method (CSEM), Time domain electromagnetic method (TDEM), and Controlled Source Audio Magnetotelluric (CSAMT) method. In contrast, naturally stimulated methods are Magnetotellurics (MT), Telluric and Geomagnetic Depth Sounding (GDS) methods. A wide range of these methods has been successfully employed in various sub-disciplines of geophysics, e.g. groundwater exploration, mineral exploration, hydrocarbon exploration, geothermal explorations, environmental studies, geotechnical engineering, and importantly in solid earth geophysics.

3.3 Magnetotelluric method

Scientists in the early 20th century found that measurements of the time-varying electric and magnetic fields at a given location could be used in the determination of the Earth's electrical properties at that location. Subsequently, Tikhonov (1950) applied the Ampere's law to the earth medium and showed that at low frequencies, the derivative of the horizontal magnetic field ($\vec{B}$) of the earth is proportional tothe orthogonal component of the electric field ($\vec{E}$).In 1953, Cagniard published a paper in which he independently developed formulas relating E_x and H_y on the surface of a layered medium under the assumption of plane wave incidence. The method developed by them is termed as magnetotelluric (MT) technique.

MT method is an efficient technique for mapping the subsurface electrical conductivity structure utilizing natural EM signals. Of the wide range of natural EM energy, MT uses electromagnetic field in the frequency range of $10^4 - 10^{-5}$Hz. The secondary fields measured in MT method provide information about the structure of the earth in terms of resistivity distribution that can help in understanding the ongoing tectonic processes inside the earth. The penetration of these EM fields is governed by a parameter called skin depth which decreases with increasing conductivity and increases for low frequency variations.

3.3.1 Source of MT signals

Natural EM signals come from an enormous variety of processes from sources ranging from the core of the earth to outer atmosphere. In general, the processes can be broadly categorized into two main sources that are responsible for natural EM field over this frequency range. One source region, atmosphere is responsible for the frequencies in 10^4-1Hz range, whereas the magnetosphere is the important source for signals of frequencies ranging 1 –10^{-5} Hz. Both these sources of signal induce time-varying secondary electromagnetic field in the earth's subsurface.

(a) MT Signals (< 1Hz)

The constant bombardment of solar wind on Earth's magnetosphere leads to its deformation which in turn disturbs the terrestrial magnetic field. This time varying phenomenon generates MT signals, which have periods usually above 1s. Solar wind excites charged particles in the magnetosphere at their resonant frequencies. These are called micro-pulsations and they have periods of 0.2 to 600s. Micro-pulsations are also called by equivalent names, geomagnetic pulsations or ultra low frequency (ULF) signals. These signals have amplitudes of a few

nano-Tesla classified into Pc –continuous pulsations (Pc -1 to Pc-6) and irregular pulsations. For Pc-1 ($0.3s \leq t \leq 3s$) the resonance peak occurs nearly at sunrise and sunset with average of one per month. The Pc-2 (5s-10s) and Pc-3 (10s – 45s) pulsations have common peaks near mid-day. Scientist also believe that these pulsations arise as magnetosphere hydro-magnetic (Alfven) waves are generated by the Kelvin –Helmholtz instability process in addition to interaction of solar plasma/wind with magnetosphere (Campbell, 2003).

(b) MT Signals >1Hz

The worldwide thunderstorm activity generates high frequency (> 1Hz) electromagnetic fields, which propagate around the globe in the Earth-ionosphere waveguide and constitute the high frequency part of the MT signals. In some cases, the frequencies of EM signals match with the geometry of the Earth's waveguide. One of the key resonant frequencies is called the *Schumann resonance*, at about 7.8Hz (Jiracek, 1999), where the wavelength is equal to Earth's circumference. Signals between 2-5 KHz do not travel well and their amplitude is very small because their wavelength in air is comparable to the width of the waveguide.

3.4 Basic theory

3.4.1 Maxwell's equations

J.C. Maxwell in 1873 compiled a set of equations on which the theory of classical electrodynamics is developed. These equations are popularly known as Maxwell's equations and form the fundamentalbasis of the MT theory. These equations in differential form for the source free medium are given as:

$$\nabla \times \vec{E} = -\frac{\partial \vec{B}}{\partial t}, \qquad \text{(Faraday's law)} \tag{3.02}$$

$$\nabla \times \vec{B} = \mu\vec{J} + \mu\epsilon\frac{\partial \vec{E}}{\partial t}, \qquad \text{(Maxwell-Ampere law)} \tag{3.03}$$

$$\nabla \cdot \vec{B} = 0, \quad \text{(Gauss's law- electrostatics)} \tag{3.04}$$

$$\nabla \cdot \vec{E} = \frac{\rho_q}{\varepsilon}, \quad \text{(Gauss law - magnetostatics)} \tag{3.05}$$

where $\nabla^2 = \hat{i}\frac{\partial}{\partial x} + \hat{j}\frac{\partial}{\partial y} + \hat{k}\frac{\partial}{\partial z}$.

Here $\vec{E}$ is the electrical field intensity vector (V/m),$\vec{B}$ is the magnetic induction vector in **T**, $\vec{J}$ is the electric current density vector in A/m^2 and ρ_q is the free electric charge density in C/m^3. Current continuity equation which is a consequence of eq. 3.03 & 3.05 is

$$\nabla \cdot \vec{J} = -\frac{\partial \rho_q}{\partial t}, \tag{3.06}$$

and has form of the law of conservation of charge. Eqs. (3.02) and (3.03) above are independent for the case of time varying fields and thus are called independent equations. These are in indefinite form since the number of equations is less than the number of unknowns. Maxwell's equations become definite when constitutive relations between the field quantities are specified. These equations describe the macroscopic properties of the medium being considered and relate pairs of the fields. These are

$$\vec{D} = \epsilon \vec{E}, \tag{3.07}$$

$$\vec{B} = \mu \vec{H}, \tag{3.08}$$

$$\vec{J} = \sigma \vec{E}. \tag{3.09}$$

Here $\vec{H}$ is the magnetic field intensity (A/m),$\vec{D}$ is the electric displacement vector (C/m^2),σ is the electrical conductivity in S/m, μ is the magnetic permeability of the medium in H/m, and ε is the dielectric permittivity of the medium in F/m. These can be respectively expressed as:$\mu = \mu_o \mu_r$, and $\epsilon = \varepsilon_o \varepsilon_r$.Here μ_r and ε_r are the relative permeability and relative permittivity of the medium, respectively. The magnetic permeability μ in most geophysical situations equals its free space value $\mu_o = 4\pi \times 10^{-7}$ H/m. At the frequencies used and for the targets of interest in MT, the magnetic permeability may be taken as the free space value for almost all earth materials $\varepsilon_o = \frac{10^{-9}}{36\pi} F/m$. For an isotropic earth the parameter tensors σ, ε and μ reduce to scalar and are in general functions of position only. The only other functional dependence of importance is with respect to frequency. The parameters ϵ, μ and σ are tensors for anisotropic media.

Maxwell equations (eq. 3.02 & 3.03) couple $\vec{E}$ and $\vec{B}$. These can be decoupled by taking the curl of these equations and using eq. 3.08 and 3.09, we get

$$\nabla^2 \vec{E} = \mu\sigma \frac{\partial \vec{E}}{\partial t} + \mu\epsilon \frac{\partial^2 \vec{E}}{\partial t^2}, \tag{3.10}$$

$$\nabla^2\vec{B} = \mu\sigma\frac{\partial\vec{B}}{\partial t} + \mu\epsilon\frac{\partial^2\vec{B}}{\partial t^2}. \quad (3.11)$$

The resulting equations also known as *Telegraphers'* equations describe the behavior of EM fields in a medium.

3.4.2 Assumptions in MT formulation

There are some assumptions in MT theory that arise due to the nature of the natural electromagnetic sources involved. These are:

- Plane-wave approximation: The primary electromagnetic field is a plane wave that propagates vertically downward (z-axis). This means that incident $\vec{E}$ and $\vec{H}$ are constant in direction and magnitude over planes normal to the z-axis.
- Quasi-stationary approximation: Displacement currents ($\frac{\partial\vec{D}}{\partial t}$) can be neglected relative to conductivity currents ($\vec{J}$). Since the frequencies used are less than 10^5Hz and the resistivity values of rocks are in general less than 10^4 Ω.m, the decay of free charge is almost instantaneously
- Source-free medium: The Earth is considered to be source free and a passive conductive medium.

3.4.3 Induction in a homogeneous half-space

Under the plane-wave approximation it is possible to represent an EM field by a superposition of plane waves. Using Fourier transformation time-varying field can be expressed in terms of its harmonic components with $e^{i\omega t}$ time dependency. In frequency domain, the Maxwell equations for MT become

$$\nabla \times \tilde{E} = i\omega\tilde{B}, \quad (3.12)$$

$$\nabla \times \tilde{B} = \mu_0\sigma\tilde{E} \quad (3.13)$$

and eqs. 3.10 & 3.11 become:

$$\nabla^2\tilde{E} - \gamma^2\tilde{E} = 0, \qquad \nabla^2\tilde{B} - \gamma^2\tilde{B} = 0, \quad (3.14)$$

where $(\tilde{E}, \tilde{B})(\omega) = F(\bar{E}(t), \bar{B}(t))$, and $\gamma^2 = i\epsilon\omega^2$ denotes the complex wave number.

We can write diffusion term and wave number separately so that

$\gamma^2 = \tilde{k}^2 - k^2$, where $\tilde{k}^2 = i\mu\sigma\omega$(diffusion term) & $k^2 = \mu\epsilon\omega^2$ (wavenumber).

For induction inside electrically conductive earth in the MT frequency range of interest and under the approximation of quasi-stationary field $\tilde{k} >> k$, eq. 3.14 reduces to

$$\nabla^2\tilde{E} - \tilde{k}^2\tilde{E} = 0, \qquad \nabla^2\tilde{B} - \tilde{k}^2\tilde{B} = 0. \tag{3.15}$$

These two equations are known as *Helmholtz* equations. The general solution of eq. 3.15 in the Cartesian coordinate system (x, y, z) with z positive downward for a homogeneous, isotropic medium having conductivity variation only with depth can be given as

$$\tilde{E} = E_o e^{-i\tilde{k}z} + E_1 e^{i\tilde{k}z}, \qquad \tilde{B} = B_o e^{-i\tilde{k}z} + B_1 e^{i\tilde{k}z}, \tag{3.16}$$

where $E_0, E_1, B_0, B_1$the constants which can be determined once appropriate boundary conditions are applied. For a homogeneous half-space, we can use two boundary conditions; (i) the field is prescribed at the surface ($z = 0$), and (ii) it vanishes as $z \to \infty$. With these boundary conditions, eq. 3.16 becomes

$$\tilde{E} = E_o e^{-i\tilde{k}z}, \qquad \tilde{B} = B_o e^{-i\tilde{k}z}. \tag{3.17}$$

The parameter $\tilde{k}$ can be expresses as $\tilde{k} = (\mu\sigma\omega/2)^{1/2} exp(-i\pi/4)$. Substituting this in eq. 3.17 we get the amplitude part of the field as a function of depth as

$$\left|(\tilde{E}, \tilde{B})(z)\right| = (E_0, B_0) exp\left[-(\mu\sigma\omega/2)^{1/2} z\right]. \tag{3.18}$$

An important inference from this expression is that we can get the depth at which the field amplitude decreases to e^{-1} of its surface value. This depth is known as the ***skin depth***

$$\delta = (2/(\mu\sigma\omega))^{1/2}. \tag{3.19}$$

Using $\mu = \mu_0 = 4\pi \times 10^{-7} H/m$ and $\omega = 2\pi/T$, we can write $\delta \cong 0.503\sqrt{\rho T}$, where ρ is the resistivity in Ωm and T is the time period in s. Here, δ is in km. This expression shows that the depth of penetration of a MT signal is directly proportional to the resistivity of the medium and the time period of the signal.

The inverse of $\tilde{k}$,$C(\omega) = 1/\tilde{k}$, is popularly known as the *Schmucker-Weidelt* transfer function (Schmucker, 1970; Weidelt, 1971,1972; Schmucker, 1971; Weaver, 1994). For a homogenous half-space, we can derive the expression for *Schmucker–Weidelt* transfer function by applying Faraday's law, as

$$C(\omega) = \frac{1}{\tilde{k}} = \frac{E_x}{i\omega B_y} = -\frac{E_y}{i\omega B_x}. \quad (3.20)$$

Substituting the expression for $\tilde{k}$, we get

$$\rho = \frac{1}{\sigma} = \frac{\mu}{2\omega}\left(\frac{E_x}{B_y}\right)^2 = \frac{\mu}{2\omega}\left(\frac{E_y}{B_x}\right)^2 \Longrightarrow \rho = \omega\mu_0|c(\omega)|^2. \quad (3.21)$$

The term E_x/B_y is the charateristic impedance of a medium and its unit is Ω. Therefore, simultaneous measurements of electric and magnetic field time variations are needed to construct impedance and get information about the resistivity/conductivity of the subsurface.

3.5 MT transfer functions

As described above, impedance is extracted from the measured time-variations of the electric and magnetic fields and then converted to conductivity structure. This approach circumvents the need to know the source field, which for the natural EM signals used in MT is not known. Therefore, in MT studies we deal with transfer functions rather than directly with the electrical and magnetic fields. Besides the *Schmucker-Weidelt* transfer function, there are two types of commonly used transfer functions known as impedance tensor and geomagnetic transfer functions.

3.4.4 Impedance tensor

Owing to the vector form of the EM fields, the fundamental datum in the MT method is a tensor relationship, known as magnetotelluric response function, between the surface horizontal electric and magnetic. The electric field is related to the magnetic field in frequency domain through this response function as

$$\vec{E}(\omega) = \bar{\mathbf{Z}}(\omega)\vec{B}(\omega), \quad (3.22)$$

where ω is the angular frequency and $\bar{\mathbf{Z}}$ is earth response function also know as impedance tensor. Cantwell (1960) have introduced the concept of impedance tensor to describe the relation between the electric and magnetic field components. This concept is fairly general;

that it does not make any assumption about the nature of the earth's structure and can account for any anisotropic and/or laterally inhomogeneous earth. It is also known as the transfer function. Since we measure horizontal electric and magnetic field components along two orthogonal directions x- and y- (conventionally North and East directions), $\bar{Z}$ is a rank-2 matrix that relates electric and magnetic components as

$$\begin{Bmatrix} E_x \\ E_y \end{Bmatrix} = \begin{bmatrix} Z_{xx} & Z_{xy} \\ Z_{yx} & Z_{yy} \end{bmatrix} \begin{Bmatrix} B_x \\ B_y \end{Bmatrix}. \tag{3.23}$$

The impedance tensor $\bar{\mathbf{Z}}$ is a good indicator of thedimensionality of the structure. For 1-D case consisting of homogenous isotropic layers with homogenous boundaries (formally known as *Tikhonov - Cagniard* model), no electric field is induced parallel to the inducing field and the conductivity varies only with depth. This gives

$$Z_{xx} = Z_{yy} = 0, Z_{xy} = -Z_{yx} = Z. \tag{3.24}$$

The impedance tensor $\mathbf{Z}$ may have all non-zero components for a 2-D case but actually the tensor components have the following relation in case of symmetry. The terms representing the asymmetry in medium are vanished and also due to fact that the electric components are related to orthogonal magnetic components only, i.e.

$$Z_{xx} = Z_{yy} = 0\,, \;\; Z_{xy} \neq Z_{yx}. \tag{3.25}$$

Therefore, a tensor rotation may be applied so that the above conditions are satisfied. The angle of rotation gives information about the strike of structure with the limitation of 90^o ambiguity. This leads to decoupling of impedance tensor in transverse electric (TE) and transverse magnetic modes (TM).

In 3-D models the conductivity distribution varies in all three directions, no matter what the rotation angle, there will be no angle that results in the diagonal elements vanishing. It is also no longer possible to separate Maxwell's equations into two modes. The 3-D Earth requires the determination of the four elements of the full impedance/MT tensor.

$$Z_{xx} \neq Z_{yy}, \;\; Z_{xy} \neq Z_{yx}. \tag{3.26}$$

3.5.2 Geomagnetic transfer function

The above expression for the impedance tensor does not include the vertical magnetic field that is needed to complete the 3-D representation of the field. An auxiliary equation relating the vertical and horizontal magnetic field components as

$$\vec{\mathrm{B}}_{\mathbf{z}} = \overrightarrow{\mathrm{T}}\,\vec{\mathrm{B}}_{\mathbf{h}} \Longrightarrow \quad \vec{\mathrm{B}}_{\mathbf{z}} = [T_x \quad T_y]\begin{Bmatrix}\mathrm{B_x}\\ \mathrm{B_y}\end{Bmatrix}, \tag{3.27}$$

forms another MT transfer function. Here, $\vec{\mathrm{T}}$ is a vector called the geomagnetic depth sounding transfer function or tipper function. The components $\mathrm{T_x}, \mathrm{T_y}$ are known as the tipper coefficients.

3.5.3 Apparent resistivity and phase

Using eq. 3.20 & 3.21, we find expressions for the commonly used response functions, apparent resistivity and phase, in terms of impedance components. The apparent resistivity is the resistivity of an equivalent homogenous half-space. Both apparent resistivity $(\rho^a)$and phase (ϕ) are also tensor quantities, the components of which can be expressed in terms of impedance components as

$$\rho_{pq}^{a} = \frac{1}{\omega\mu}\left|Z_{pq}\right|^2, \qquad \phi = \tan^{-1}\left(\frac{\mathrm{Im}\,(Z_{pq})}{\mathrm{Re}\,(Z_{pq})}\right), \tag{3.28}$$

where p, q represent x, y in any of four combinations.For field units of measurements, mV/km for electric field and nT for magnetic field, the apparent resistivity in Ωm can be written as

$$\rho_a^{xy} = 0.2\,T\left|\frac{E_x}{B_y}\right|^2. \tag{3.29}$$

The phase is a measure of the phase shift between the electric and magnetic field components. For a homogenous half-space $\phi = \pi/4$ implying that the electric field precedes the magnetic field by 45^{o}.

3.6 MT forward modelling

The basic aim of geophysical exploration is to decipher the structure underneath the earth's surface in terms of physical properties variations and then interpret these sections to reconstruct the subsurface geology thus adding the third (depth) dimension to the surface

geology. However, geophysical signals contain the effect of physical properties variations in the form of changes in respective physical fields. Therefore, we need to convert the changes in the physical fields to the changes in physical properties. This is a two-step process. The first step involves computation of changes in the field response for a given model of physical properties distribution, known as "*Forward modeling*", by using the governing equations relating physical field to material properties. The second step, "*Inversion*", attempts to reconstruct the distribution of physical properties from the provided physical field variations by minimizing the misfit between the observed field responses and those calculated by using forward modeling.

In MT, our objective is to reconstruct the electrical conductivity structure of the earth's interior from the observed apparent resistivity and phase data recorded at several sites and over a broad frequency range depending on the objectives of the exploration. Likewise, MT data inversion means determination of electrical resistivity variation in the crust and upper mantle form surface data. However, like any inversion, a pre-requisite of MT data inversion is the solution of corresponding forward problem obtained by solving the relevant partial differential equations. A huge volume of literature is available on MT forward modeling and inversion for 1-D, 2-D, 3-D isotropic as well as 1-D and 2-D anisotropic media (Brewitt-Taylor & Weaver, 1976a, b**;** Pek & Verner**,** 1997**;** Lee, 2001) but here I focus on only the techniques that are relevant to the present work and have been used in the interpretation of MT data of the Sikkim Himalaya. For the present work, we use the algorithm devolved by Rodi & Mackie (2001) for 2-D inversion of MT data. In the following section, I shall discuss the numerical formulation for 2-D forward modeling along with boundary conditions. Even though earth's structure is complex, it can be reasonably modeled by 2-D approach if the regional conductivity doesn't vary along one direction (the strike direction) and where data are collected approximately across the strike.

For 1-D models with simple conductivity variation with depth, it is possible to get analytical solution of the Helmholtz equation (eq. 3.15). However, the 2-D, 3-D and/or anisotropic nature of the conductivity structure demands the use of numerical techniques for forward modelling. Mainly finite difference, finite element, and integral equation approaches have been used in MT to solve the Helmholtz equation in 2-D or 3-D. In the present work, we have used a finite difference algorithm to solve for TE- and TM-mode responses through network formulation of Maxwell's equations for a 2-D model (Madden, 1972; Mackie *et al.*

1988). The curl operations in Maxwell's equations for a 2-D earth are rearranged into divergence and gradient operators by making the proper analogy between current and voltage variables with electric and magnetic field components. The resulting equations are the same as the equations for a rectangular network and can be efficiently solved for the given earth model and frequency of the inducing field (Madden, 1972). The governing equations and boundary conditions for the TE and TM modes along with boundary conditions are discussed in following sections both for isotropic and anisotropic media.

3.6.1 Forward modelling for isotropic medium

For a 2-D problem, it is assumed that the strike of the structure is significantly longer than the skin depth. All parameters and field vectors are independent of one of the horizontal coordinates, say x. Then

$$\partial/\partial \mathrm{x} = 0 \text{ and } \sigma \equiv \sigma(y,z). \tag{3.30}$$

In general, the conductivity $\sigma(y,z)$ is assumed to approach 1-D distribution $\sigma_{\pm}(z)$ as $|y| \to \infty$. Considering harmonic varying EM fields with angular frequency ω, the electric and magnetic fields can be written as a $\vec{\mathrm{E}}\mathrm{e}^{\mathrm{i}\,\omega\,\mathrm{t}}$ and $\vec{\mathrm{B}}\mathrm{e}^{\mathrm{i}\,\omega\,\mathrm{t}}$ respectively. In the Cartesian coordinate system (x, y, z) E and B can be expressed as

$$\mathrm{E_x} = \mathrm{E_x(y,z)},\ \mathrm{E_y} = \mathrm{E_y(y,z)}, \mathrm{E_z} = \mathrm{E_z(y,z)}, \tag{3.31a}$$

$$\mathrm{B_x} = \mathrm{B_x(y,z)},\ \mathrm{B_y} = \mathrm{B_y(y,z)}, \mathrm{B_z} = \mathrm{B_z(y,z)}. \tag{3.31b}$$

Using the vector induction eqs.3.2 & 3.11, we get six scalar equations

$$\frac{\partial E_x(y,z)}{\partial z} = -i\,\omega\,\mathrm{B_y(y,z)},$$

$$\frac{\partial E_x(y,z)}{\partial y} = i\,\omega\,\mathrm{B_z(y,z)},$$

$$\frac{\partial E_y(y,z)}{\partial z} - \frac{\partial E_z(y,z)}{\partial y} = i\omega \mathrm{B_x(y,z)},$$

and

$$\frac{\partial B_x(y,z)}{\partial z} = \mu_o \sigma(y,z)\mathrm{E_y(y,z)},$$

$$\frac{\partial B_x(y,z)}{\partial y} = -\mu_o \sigma(y,z) \mathrm{E_z(y,z)},$$

$$\frac{\partial B_z(y,z)}{\partial y} - \frac{\partial B_y(y,z)}{\partial z} = \mu_o \sigma(y,z) \mathrm{E_x(y,z)}.$$

These six equations can be rearranged in two groups

$$\frac{\partial E_x(y,z)}{\partial z} = -i\omega \mathrm{B_y(y,z)} \quad (3.32a)$$

$$\frac{\partial E_x(y,z)}{\partial y} = i\omega \mathrm{B_z(y,z)} \quad (3.32b)$$

$$\frac{\partial B_z(y,z)}{\partial y} - \frac{\partial B_y(y,z)}{\partial z} = \mu_o \sigma(y,z) \mathrm{E_x(y,z)} \quad (3.32c)$$

and

$$\frac{\partial B_x(y,z)}{\partial z} = \mu_o \sigma(y,z) \mathrm{E_y(y,z)} \quad (3.33a)$$

$$\frac{\partial B_x(y,z)}{\partial y} = -\mu_o \sigma(y,z) \mathrm{E_z(y,z)} \quad (3.33b)$$

$$\frac{\partial E_y(y,z)}{\partial z} - \frac{\partial E_z(y,z)}{\partial y} = i\omega \mathrm{B_x(y,z)} \quad (3.33c)$$

These set of equations (eq. 32 – eq. 33) show that 2-D isotropic structures decouple into two distinct modes (Cantwell, 1960; Bostick & Smith, 1962; Weaver, 1994). One mode considers the horizontal electric field parallel to the x-axis (strike) and is specified by single component $\mathrm{E_x}(y,z)$. This mode is called as transverse electric or E-polarization (TE) mode. The second mode uses the horizontal magnetic field parallel to the x-axis which is specified by single component $\mathrm{B_x}(y,z)$. This mode is known as transverse magnetic (TM) or B/H-polarization mode. The decoupling is valid since the EM fields are treated as plane waves (which are transverse in nature), i.e. interaction between electric and magnetic field are always orthogonal to each other and therefore the horizontal component of the magnetic field tangential to the conductivity strike does not depend on the magnetic field component perpendicular to it.

It is now evident that if the strike-parallel components $\mathrm{E_x}$ and B_x have been found, the remaining components $\mathrm{E_y}, \mathrm{E_z}, \mathrm{B_y}$ and $\mathrm{B_z}$ can be obtained from spatial derivatives of E_x and

B_x. Eqs. 3.31 & 3.32 can be combined to yield two second-order differential equations for the strike-parallel components E_x and B_x.

For TE mode, the diffusive wave equation reduces to

$$\frac{\partial^2 E_x}{\partial y^2} + \frac{\partial^2 E_x}{\partial z^2} = k^2 E_x, \qquad \text{where } k^2 = -i\omega\mu_o\sigma(y,z). \tag{3.34}$$

For TM mode, we get

$$\rho(y,z)\left(\frac{\partial^2 B_x}{\partial y^2} + \frac{\partial^2 B_x}{\partial z^2}\right) + \left(\frac{\partial B_x}{\partial y}\right)\left(\frac{\partial \rho}{\partial y}\right) + \left(\frac{\partial B_x}{\partial z}\right)\left(\frac{\partial \rho}{\partial z}\right) = k^2 B_x \,. \tag{3.35}$$

Boundary conditions

The complete description of an electromagnetic problem should include information about both the differential equations and boundary conditions. We need to supply the boundary conditions for the field components, both on the inner and outer boundaries of the model. In the literature, many authors have discussed the boundary conditions used in the EM induction in the earth (e.g. Pascoe & Jones, 1972; Weaver & Taylor, 1978; Weaver, 1994.). There are two types of boundary conditions. First one termed as 'Interface conditions' is defined at the interface where conductivity discontinuity occurs within the domain and the second one is known as 'Domain boundary conditions' at the domain boundary.

Interface (inner) conditions

On inner boundaries, where blocks of different electrical properties have common contact interface, there are four necessary conditions to be imposed on the interface separating two media. These are:

- Continuity of the tangential component of the electric field $\vec{E}$

  $$\hat{n} \times (\mathbf{E_1} - \mathbf{E}_2) = 0, \tag{3.36}$$

- Continuity of all the components of the magnetic field $\vec{B}$

  $$\hat{n} \times (\mathbf{B_1} - \mathbf{B}_2) = 0; \tag{3.37}$$

- Continuity of normal components of $\vec{E}$

  $$\hat{n} \,.\, (\mathbf{E_1} - \mathbf{E}_2) = 0; \tag{3.38}$$

- Continuity of normal components of $\vec{D}$

  $$\hat{n} \cdot (\mathbf{D_1} - \mathbf{D}_2) = 0. \tag{3.39}$$

Here $\hat{n}$ is the unit vector normal to the interface pointing from one medium to medium-another. These equations are also known as field continuity conditions. In formulating eq. 3.36 and eq. 3.39 it is assumed that neither surface currents nor charges exist at the interface. If indeed there exists a surface electric current density J_s and a surface charge densityρ_s, these two equations are modified as

$$\hat{n} \cdot (D_1 - D_2) = \rho_s, \tag{3.40}$$

implying that the discontinuity is equal to surface free charge density ρ_s, and

$$\hat{n} \times (D_1 - D_2) = J_s, \tag{3.41}$$

implying that the discontinuity is equal to the surface current density.

Domain (outer) Boundary Conditions

Outer boundary conditions are applied on the domain boundary. These are either Dirichlet or Neumann or mixed boundary conditions, which respectively specify either the field or its normal derivative or a linear superposition of the two. We can apply mixed boundary conditions (Weaver, 1994) on the two vertical side surfaces of the domain. The bottom boundary is assumed to be that of a perfectly conducting half-space. At the top surface, integral boundary condition that transfers the effect of the air half-space to the air-earth interface can be imposed (Brewitt-Taylor & Weaver, 1976a,b; Weaver,1994). On the outer boundaries of the model, Dirichlet boundary conditions can be set, constructed from 1-D solutions for the corresponding layered media at the left and right side of the model (Figure. 3.02). At the top and the bottom of the model the boundary conditions are constructed simply as linear interpolations of the respective 1-D values at the left and right margins of the model. If the layered structures on both the left-hand side and right-hand side of the model are the same, then the top boundary conditions are uniform *E,* at the top of the air layer, placed on top of the model for the higher spatial harmonics in E_x to attenuate, and uniform $\vec{B}$, directly on the surface of the earth.

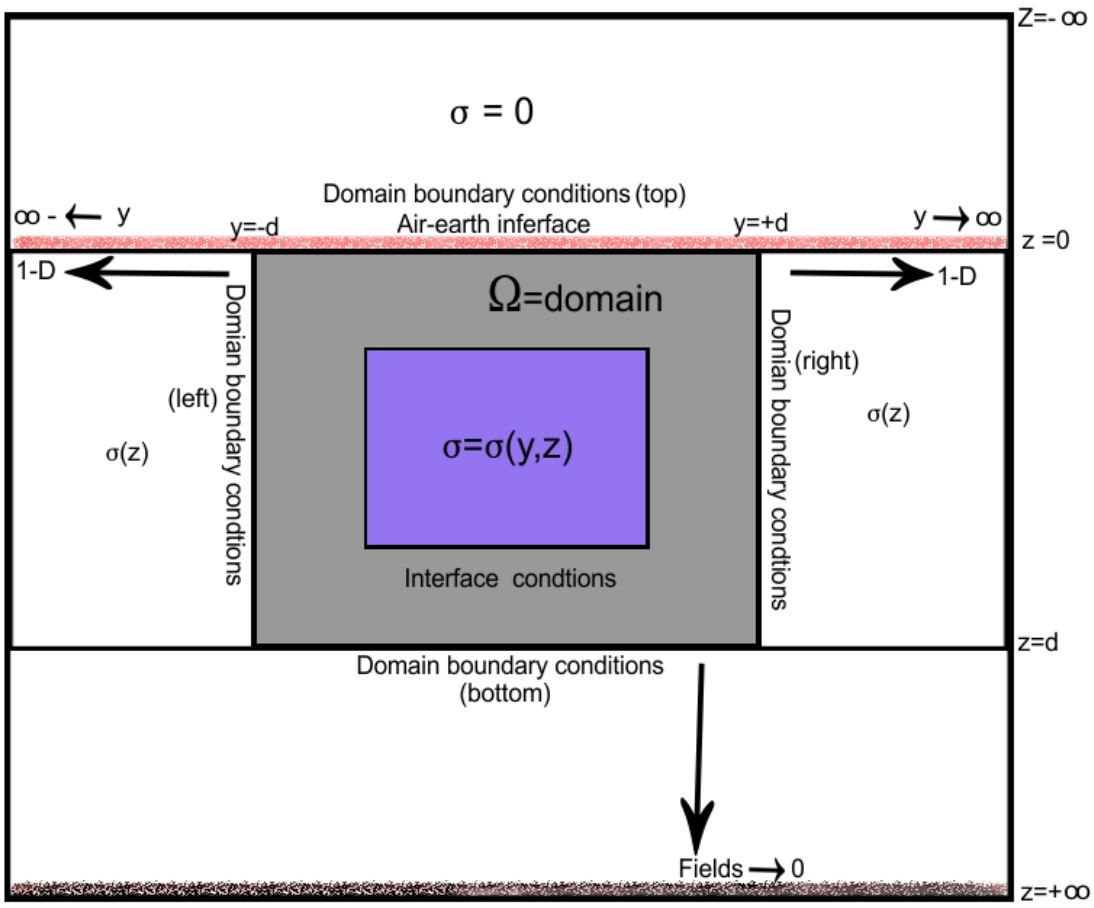

Figure 3.02: A cartoon showing typical 2-D model with domain and interface boundary conditions for a typical 2-D domain Ω

Top (surface) boundary condition

In a non-conducting region, the TM mode equations become

$$\frac{\partial B_x(y,z)}{\partial z} = \frac{\partial B_x(y,z)}{\partial y} = 0,$$

i.e. at above the earth surface there exists only B-polarization in a 2-D model given by

$$B_x(y,z) = B_{x0}(\text{constant}) \Rightarrow B_x(y,0-) = B_{xo}. \tag{3.42}$$

This equation gives the surface boundary condition in the TM mode. We make the basic assumption that σ becomes a function of z alone as $|y| \to \infty$. Thus in both modes the problem reduces at large distances toone of induction by a uniform,horizontal magnetic field in an earth whose conductivity varies only with depth. For 1-D scenario, the total magnetic field above the conductor is horizontal and independent of the conductivity distribution in the

earth. Since the inducing field is the same everywhere it follows that the total magnetic field must have the same constant limiting value B_0 as $y \to \pm\infty$ in $z < 0$. Solving for magnitude of source field for a uniform primary magnetic field of magnitude $B_{x0}$the total magnetic field above a 1-D earth is of magnitude $2B_{x0}$.

Similarly, considering uniform and horizontal primary electric field, the 1-D field reached as $|y| \to \infty$, the TE mode will be clearly indistinguishable from the corresponding 1-D field in the TM mode, i.e. $\mathrm{B_y(y,z)} \to \mathrm{B_{yo}}$ as $|y| \to \infty$, where $\mathrm{B_{yo}}$ is the twice the magnitude of the primary magnetic field in y-direction. Performing set of mathematical derivations, we can derive the surface boundary conditions for TE mode E_x as;

$$E_x'(y, 0-) = -i\omega \mathrm{B_{yo}} - \frac{1}{\pi}\int_{-\infty}^{\infty} \frac{E_x(v,0)-E_x(y,0)}{(v-y)^2}\, dv. \tag{3.43}$$

Here $v \geq 0$ is the wave number.

Side boundary conditions

As $y \to \pm\infty$, $\frac{\partial\sigma}{\partial y}, \frac{\partial B_x(y,z)}{\partial y}$ & $\frac{\partial E_x(y,z)}{\partial y}$ all vanish. Thus the boundary conditions on B_x and E_x become

$$B_x(\pm\infty, z) = B_x^{\pm}(z), \qquad E_x(\pm\infty, z) = E_x^{\pm}(z). \tag{3.44}$$

Here $B_x^{\pm}(z)$ and $E_x^{\pm}(z)$ are the solutions of

$$B''^{\pm}_x(z) = i\omega\mu_0\sigma^{\pm}(z)B_x^{\pm}(z), \qquad E''^{\pm}_x(z) = i\omega\mu_0\sigma^{\pm}(z)E_x^{\pm}(z), \tag{3.45}$$

subject to the boundary conditions

$$B_x^{\pm}(0) = B_{xo}, \qquad E'^{\pm}_x(0) = -i\omega \mathrm{B_{yo}}, \tag{3.46}$$

where $\sigma^{\pm}(z)$ is the 1-D layered model conductivity distribution.

Asymptotic Boundary conditions of TE mode fields on surface and sides of the domain

In TE mode, the anomalous electric field $E_x(y,0) - E_x^{\pm}(0)$ actually decays rather slowly to zero as $y \to \pm\infty$. Thus the end nodes in the model must be placed at great distance (at least several skin depths of the underlying half-space) from the anomalous conductor. More

accurate boundary conditions which reflect the asymptotic behavior of the electric field need often improved accuracy without requiring an unreasonable number of electric field along y-axis/negative side of z-axis. These are given as (Weaver, 1994)

$$E_x(y,z) = k - i\omega B_{yo} - if_+(0)\arctan\frac{y}{|z|} - f_-(0)\log r - \frac{iyf'_+(0)}{r^2} - \frac{zf'_-(0)}{r^2} + O\left(\frac{1}{r^2}\right) \quad (3.47)$$

Here, k is the constant of integration, $r = (y^2 + z^2)^{1/2}$ and $f_\pm(\eta) = \omega\eta\left[\widehat{\Omega}(\eta,0) \pm \widehat{\Omega}(-\eta,0)\right]/\sqrt{2\pi}$ with $\widehat{\Omega}(\eta)$ is the Fourier magnetic scalar potential with complex variable η.

Bottom boundary conditions

The simplest boundary conditions applicable at the bottom of the model are

$$B_x(y,\infty) = 0, \quad E_x(y,\infty) = 0. \quad (3.48)$$

These come from the fact that the EM field is attenuated by the conductive medium. If basement of the model is homogeneous half space z > d of uniform conductivity σ_o . Then the boundary condition may be replaced by

$$B'_x(y,d) = 0, \qquad E_x(y,d) = 0. \quad (3.49)$$

Otherwise integral boundary conditions applicable on the plane $z = d$ can be derived (Weaver, 1994), these are

$$B'_x(y,d+) = 0, \qquad E'_x(y,d+) = \frac{1}{\pi}\int_{-\infty}^{\infty}\frac{E_x(v,d)-E_x(y,d)}{(v-y)^2}dv. \quad (3.50)$$

This is equivalent to the surface boundary conditions when sources are absent.

3.6.2 Forward modelling for anisotropic medium

For an anisotropic medium, the conductivity σ is represented as a second rank tensor and hence the general form of the Ohm's law becomes

$$\begin{Bmatrix} J_x \\ J_y \\ J_z \end{Bmatrix} = \begin{bmatrix} \sigma_{xx} & \sigma_{xy} & \sigma_{xz} \\ \sigma_{yx} & \sigma_{yy} & \sigma_{yz} \\ \sigma_{zx} & \sigma_{zy} & \sigma_{zz} \end{bmatrix} \begin{Bmatrix} E_x \\ E_y \\ E_z \end{Bmatrix}. \quad (3.51)$$

Therefore, six scalar equations obtained for the 2-D isotropic case (Eqs. 3.32-3.33) are modified as

$$\frac{\partial E_y(y,z)}{\partial z} - \frac{\partial E_z(y,z)}{\partial y} = i\omega \mathrm{B_x}(\mathrm{y},\mathrm{z}), \tag{3.52a}$$

$$\frac{\partial E_x(y,z)}{\partial z} = -i\omega \mathrm{B_y}(\mathrm{y},\mathrm{z}), \tag{3.52b}$$

$$\frac{\partial E_x(y,z)}{\partial y} = i\omega \mathrm{B_z}(\mathrm{y},\mathrm{z}), \tag{3.52c}$$

and

$$\frac{\partial B_z(y,z)}{\partial y} - \frac{\partial B_y(y,z)}{\partial z} = \mu_o \left(\sigma_{xx}(y,z)\mathrm{E_x}(\mathrm{y},\mathrm{z}) + \sigma_{xy}(y,z)\mathrm{E_y}(\mathrm{y},\mathrm{z}) + \sigma_{xz}(y,z)\mathrm{E_z}(\mathrm{y},\mathrm{z})\right), \tag{3.53a}$$

$$\frac{\partial B_x(y,z)}{\partial z} = \mu_o \left(\sigma_{yx}(y,z)\mathrm{E_x}(\mathrm{y},\mathrm{z}) + \sigma_{yy}(y,z)\mathrm{E_y}(\mathrm{y},\mathrm{z}) + \sigma_{yz}(y,z)\mathrm{E_z}(\mathrm{y},\mathrm{z})\right), \tag{3.53b}$$

$$\frac{\partial B_x(y,z)}{\partial y} = -\mu_o \left(\sigma_{zx}(y,z)\mathrm{E_x}(\mathrm{y},\mathrm{z}) + \sigma_{zy}(y,z)\mathrm{E_y}(\mathrm{y},\mathrm{z}) + \sigma_{zz}(y,z)\mathrm{E_z}(\mathrm{y},\mathrm{z})\right). \tag{3.53c}$$

Combining above six equations to yield two second order differential equations for strike parallel components E_x and $\mathrm{B_x}$, we get

$$\frac{\partial^2 \mathrm{E_x}}{\partial \mathrm{y}^2} + \frac{\partial^2 \mathrm{E_x}}{\partial \mathrm{z}^2} + \mathrm{i}\omega(\sigma_{\mathrm{xx}} + \mathrm{P}\sigma_{\mathrm{xx}} + \mathrm{Q}\sigma_{\mathrm{xx}})\mathrm{E_x} + \mathrm{i}\omega\mathrm{P}\frac{\partial \mathrm{B_x}}{\partial \mathrm{y}} - \mathrm{i}\omega\mathrm{Q}\frac{\partial \mathrm{B_x}}{\partial \mathrm{z}} = 0, \tag{3.54}$$

$$\frac{\partial}{\partial \mathrm{y}}\left\{\frac{\sigma_{\mathrm{yy}}}{\mathrm{R}} \cdot \frac{\partial \mathrm{B_x}}{\partial \mathrm{y}}\right\} + \frac{\partial}{\partial \mathrm{z}}\left\{\frac{\sigma_{\mathrm{zz}}}{\mathrm{R}} \cdot \frac{\partial \mathrm{B_x}}{\partial \mathrm{z}}\right\} + \frac{\partial}{\partial \mathrm{y}}\left\{\frac{\sigma_{\mathrm{yz}}}{\mathrm{R}} \cdot \frac{\partial \mathrm{B_x}}{\partial \mathrm{z}}\right\} + \frac{\partial}{\partial \mathrm{z}}\left\{\frac{\sigma_{\mathrm{yz}}}{\mathrm{R}} \cdot \frac{\partial \mathrm{B_x}}{\partial \mathrm{y}}\right\} + \mathrm{i}\omega\mathrm{B_x} - \frac{\partial}{\partial \mathrm{y}}(\mathrm{QE_x}) + \frac{\partial}{\partial \mathrm{y}}(\mathrm{PE_x}) = 0, \tag{3.55}$$

where $\mathrm{P} = (\sigma_{\mathrm{xy}}\sigma_{\mathrm{yz}} - \sigma_{\mathrm{xz}}\sigma_{\mathrm{yy}})/\mathrm{R}$, $\mathrm{Q} = (\sigma_{\mathrm{xz}}\sigma_{\mathrm{yz}} - \sigma_{\mathrm{xy}}\sigma_{\mathrm{zz}})/\mathrm{R}$, and $\mathrm{R} = (\sigma_{\mathrm{yy}}\sigma_{\mathrm{zz}} - \sigma_{\mathrm{yz}}\sigma_{\mathrm{zy}})$.

Anisotropic conductivity structure couples the otherwise independent strike-parallel components E_x and $\mathrm{B_x}$ through first-order derivatives. Thus, there are no individual TE or TM modes.

The conductivity tensor $\boldsymbol{\sigma}$ is symmetric ($\sigma_{ij} = \sigma_{ji}$)and non-negative definite (Weidelt,1999). Following these two conditions, the resultant conductivity tensor when rotated in the direction of its principle axes (x', y', z'), is given by

$$\sigma' = \begin{pmatrix} \sigma_{x'} & 0 & 0 \\ 0 & \sigma_{y'} & 0 \\ 0 & 0 & \sigma_{z'} \end{pmatrix}. \tag{3.56}$$

The principal conductivities can be linked to the original coordinate frame through direction cosines, i.e. we can have strike, dip and slant with respect the reference frame (x, y, z), respectively. Considering the properties of the resultant conductivity tensor various forms of anisotropy have been proposed (Pek & Verner, 1997; Li, 2002) to simplify the mathematical treatment. These are:

Dipping anisotropy: The principal axis x' of the conductivity tensor is horizontal and is in the strike direction. Thus,$\sigma_{xy} = \sigma_{xz} = 0$ and eqs.(3.51) & (3.52) simplify to:

$$\frac{\partial^2 \mathrm{E_x}}{\partial \mathrm{y}^2} + \frac{\partial^2 \mathrm{E_x}}{\partial \mathrm{z}^2} + \mathrm{i}\omega\sigma_{\mathrm{xx}}\mathrm{E_x} = 0, \tag{3.57}$$

$$\frac{\partial}{\partial \mathrm{y}}\left\{\frac{\sigma_{\mathrm{yy}}}{\mathrm{R}} \cdot \frac{\partial \mathrm{B_x}}{\partial \mathrm{y}}\right\} + \frac{\partial}{\partial \mathrm{z}}\left\{\frac{\sigma_{\mathrm{zz}}}{\mathrm{R}} \cdot \frac{\partial \mathrm{B_x}}{\partial \mathrm{z}}\right\} + \frac{\partial}{\partial \mathrm{y}}\left\{\frac{\sigma_{\mathrm{yz}}}{\mathrm{R}} \cdot \frac{\partial \mathrm{B_x}}{\partial \mathrm{z}}\right\} + \frac{\partial}{\partial \mathrm{z}}\left\{\frac{\sigma_{\mathrm{yz}}}{\mathrm{R}} \cdot \frac{\partial \mathrm{B_x}}{\partial \mathrm{y}}\right\} + \mathrm{i}\omega\mathrm{B_x} = 0. \tag{3.58}$$

The TE polarization equation is similar to that of isotropic case. However, the TM mode is still complicated.

Horizontal anisotropy: The principle axis z' is vertical and $\sigma_{\mathrm{xz}} = \sigma_{\mathrm{yz}} = 0$. Eqs.(3.51) & (3.52) become:

$$\frac{\partial^2 \mathrm{E_x}}{\partial \mathrm{y}^2} + \frac{\partial^2 \mathrm{E_x}}{\partial \mathrm{z}^2} + \mathrm{i}\omega\left(\sigma_{\mathrm{xx}} - \frac{\sigma_{\mathrm{xy}}{}^2}{\sigma_{\mathrm{yy}}}\right)\mathrm{E_x} + \mathrm{i}\omega\mathrm{P}\frac{\partial \mathrm{B_x}}{\partial \mathrm{y}} - \mathrm{i}\omega\frac{\sigma_{\mathrm{xy}}}{\sigma_{\mathrm{yy}}} \cdot \frac{\partial \mathrm{B_x}}{\partial \mathrm{z}} = 0, \tag{3.59}$$

$$\frac{\partial}{\partial y}\left\{\frac{1}{\sigma_{zz}}\frac{\partial B_x}{\partial y}\right\} + \frac{\partial}{\partial z}\left\{\frac{1}{\sigma_{yy}}\frac{\partial B_x}{\partial z}\right\} + i\omega B_x + \frac{\partial}{\partial y}\left(\frac{\sigma_{xy}}{\sigma_{yy}}E_x\right) = 0. \tag{3.60}$$

Vertical anisotropy: All principal axes of the tensor coincide with the axes of (x,y,z) coordinates and $\sigma_{xy} = \sigma_{xz} = \sigma_{yz} = 0$.In addition, including axial symmetric situation w.r.t. z,$\sigma_{xx} = \sigma_{yy} = \sigma_h$ and conductivity for any horizontal direction differs solely from $\sigma_{zz} = \sigma_v$ in the vertical direction. Equations now are:

$$\frac{\partial^2 E_x}{\partial y^2} + \frac{\partial^2 E_x}{\partial z^2} + i\omega\sigma_h E_x = 0, \tag{3.61}$$

$$\frac{\partial}{\partial y}\left\{\frac{1}{\sigma_v}\frac{\partial B_x}{\partial y}\right\} + \frac{\partial}{\partial z}\left\{\frac{1}{\sigma_h}\frac{\partial B_x}{\partial z}\right\} + i\omega B_x = 0. \tag{3.62}$$

Boundary conditions

The numerical solutions of these set of equations are presented by Pek & Verner (1997) using finite difference method and by Li (2002) using finite element approach. In both approaches they have used slightly modified boundary conditions developed by Reddy & Rankin (1971) and Loewenthal & Landisman (1973) very similar to isotropic case. The top and bottom of the model boundary conditions are constructed simply as linear interpolations of the respective 1-D value at the left and right hand margins of the model. If the layered structures on both the sides of the model are same, then the top boundary conditions are uniform E_x at the top of the air layer, placed on top of the model for the higher spatial harmonics in E_x to attenuate and uniform B_x directly on the surface of the earth.

3.6.3 Solution methods

Except in the case of very simple conductivity variations, the solution of above 2-D equations requires appropriate numerical techniques. Finite difference method (FDM), finite element method (FEM) and integral equation method (IEM) have been used to model MT forward responses. For examples, Jones & Price (1970), Brewitt-Taylor & Weaver (1976), Mancke *et al.* (1988) have used classical finite differences. Swift (1967) and Madden & Swift (1969) used FD schemes based on network analogy. Coggan (1971), Rodi (1976), Silvister & Haslam (1972) have solved the EM induction equations using FEM and Hohmann (1971) and Lee (1975); Weidelt (1975) have used IEM for 2-D electromagnetic modeling.

Finite difference method is one of the most sought after choices because of its simplicity. In this method, the domain is discretized into rectangular spatial mesh with grid lines parallel to the x- and z- coordinate axes and the derivatives in the governing equations are expressed in difference form using Taylor series expansion. Thus, the differential equations are converted into a set of linear equations which can be solved by using any standard matrix solver. In finite element method, a weak formulation of the governing equations is derived and then the domain is discretized into small elements of any shape, e.g. triangular, rectangular, and curvilinear, etc. In this method, interpolation polynomials are used to define

the field in the interior of any element from its value at the nodes of the element. The FEM has advantage that the solution domain can be of any irregular shape contrary to finite difference approach wherein model domains of only regular shapes are used. In integral equation method, the original boundary value problem for Maxwell's equations is reformulated in the form of integral equations over the entire volume of the domain. Although this method in many cases is flexible and efficient for solving various electromagnetic problems, an additional numerical difficulty arises from the singular integral kernels. This method is extremely useful when the causative body is of confined nature e.g. in mineral exploration. Since the algorithm implemented in WinGLink is based on finite difference method, I shall discuss only this formulation in detail in the next section.

3.6.3.1 Finite difference formulation

In FDM, the model domain (yz-plane, $z > 0$) is discretized into a 2-D mesh having M nodes $[y_m\ (m = 1,2,3, \dots, M)]$ in horizontal direction and N nodes $[z_n\ (n = 1,2,3 \dots N)]$ in vertical direction. In this notation, left, right, top, and bottom boundaries are at $y = y_1, y = y_M;\ z = z_1 <= 0$ and $= z_n > 0$, respectively, and the interior node (m, n) is at $y = y_m,\ z = z_n$.The dimensions of the cell on the positive y and z sides of the node (m, n) are denoted by

$$h_m = y_{m+1} - y_m, \qquad k_m = z_{n+1} - z_n. \tag{3.63}$$

A schematic diagram of the discretization is shown in Figure 3.03. In the discretized domain, the top boundary of the grid $z = z_1 = 0$ is chosen to be coincident with surface of the earth and we consider that the region below $z = z_N$, the bottom boundary of the grid, is a stratified half-space of N' layers whose conductivities and thicknesses are σ_n and $d_n (n = 1, 2, 3, \dots, N')$ respectively with $d_{N'} \to \infty$. Side boundaries defined by the lines $y = y_1$ and $y = y_M$ are assumed to be well within the 1-D structures on the left- and right-hand edges of the model respectively, i.e.

$$\sigma_{\frac{3}{2},n+\frac{1}{2}} \equiv \sigma_- \left(z_n + \frac{k_n}{2}\right) \text{ and } \quad \sigma_{m-\frac{1}{2},n+\frac{1}{2}} \equiv \sigma_+ \left(z_n + \frac{k_n}{2}\right), \tag{3.64}$$

The conductivity distribution at node (m, n) is estimated to be the weighted average of the conductivities in the four cells surrounding it, i.e.

$$\sigma_{m,n} = \frac{h_m \sigma_{m+\frac{1}{2},n} + h_{m-1} \sigma_{m-\frac{1}{2},n}}{h_m + h_{m-1}} = \frac{k_n \sigma_{m+\frac{1}{2},n} + k_{n-1} \sigma_{m,n-\frac{1}{2}}}{k_n + k_{n-1}}, \tag{3.65}$$

where

$$\sigma_{m\pm\frac{1}{2},n} = \frac{k_m\sigma_{m\pm\frac{1}{2},n+\frac{1}{2}}+k_{n-1}\sigma_{m\pm\frac{1}{2},n-\frac{1}{2}}}{k_n+k_{n-1}} \qquad ,\sigma_{m\pm\frac{1}{2},n} = \frac{h_m\sigma_{m+\frac{1}{2},n\pm\frac{1}{2}}+h_{m-1}\sigma_{m-\frac{1}{2},n\pm\frac{1}{2}}}{h_m+h_{m-1}} \qquad (3.66)$$

The most important interface is the air-earth boundary which need not be flat but may have topography. In this case, the mesh is extended into the air for E- polarization but is terminated at the highest topographic point for B-polarization.

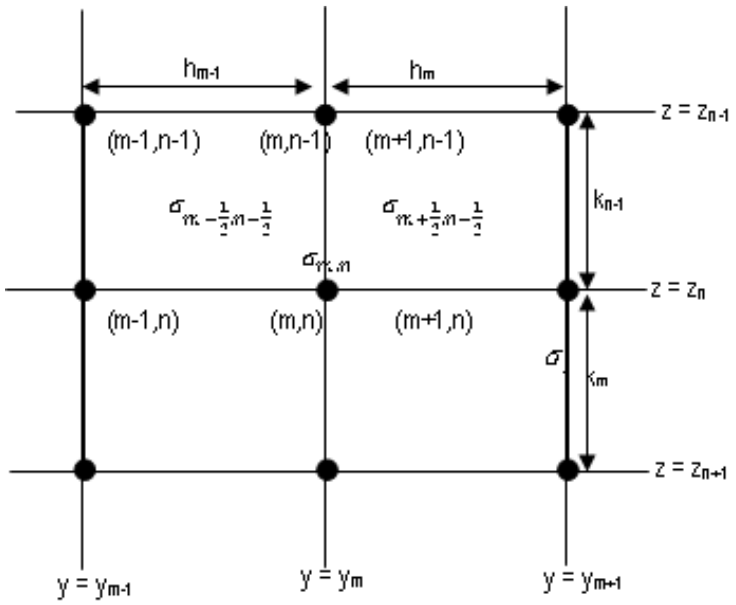

Figure 3.03: A typical node (m,n) in a 2-D grid (Redrawn from Weaver, 1994)

Finite Difference Equations for TE mode

The TE mode equation (eq. 3.33) can be written in the finite difference form at any interior node (m,n) with the conductivity defined at the node by eq. 3.62. Performing some algebraic rearrangement, we get the electric field $E_{x(m,n)} = E_x(y_m, z_n)$ which is related to its four neighbouring nodal values by five-point equation (Weaver, 1994) (representing E_x with E)

$$\frac{E_{m+1,n}}{h_m h_m^+} + \frac{E_{m-1,n}}{h_{m-1}h_m^+} + \frac{E_{m,n+1}}{k_n k_n^+} + \frac{E_{m,n-1}}{k_{n-1}k_n^+} = \left(\frac{1}{h_m h_{m-1}} + \frac{1}{k_n k_{n-1}} + \frac{1}{2}i\alpha_{m,n}^2\right)E_{m,n}, \qquad (3.67)$$

$2 \le m \le M-1; \quad 2 \le n \le N-1$, where $h_m^+ = h_m + h_{m-1}$ and $k_n^+ = k_n + k_{n-1}$

Various methods have been devised for dealing with the edges of the grid and they lead to quite different FD formulations at the boundary nodes. Jones & Price (1970) used a grid that

extended from deep inside the earth to high altitude above its surface assuming the top and bottom boundaries of the grid were sufficiently remote. This facilitates the interpolation of electric field linearly across them between the values given by the 1-D solution on the side boundaries of the grid. The asymptotic boundary conditions discussed in the previous session are alternatively applied on the top and sides of the grid and the model could be terminated at some depth by a perfect conductor on which E_x vanishes (Brewitt-Taylor & Weaver, 1976; Weaver & Brewitt-Taylor, 1978; Weaver, 1994). Unnecessary gridding of the non-conducting region above the earth can be avoided altogether by also applying integral boundary conditions (eqs. 3.47, 3.50) on the surface $z = 0$ and on the plane $z = z_n$.

Finite difference equations for TM mode

Similar to the TE mode, expressing the partial differential equation (eq. 3.34) at any interior node (m, n) as the five point difference equation

$$\frac{2\rho_{m,n}+h_{m-1}\rho_{m,n}}{h_m h_m^+} B_{m+1,n} + \frac{2\rho_{m,n}-h_m\rho_{m,n}}{h_{m-1}h_m^+} B_{m-1,n} + \frac{2\rho_{m,n}+h_{n-1}\rho'_{m,n}}{k_m k_m^+} B_{m,n+1} +$$

$$\frac{2\rho_{m,n}+h_{m-1}\rho_{m,n}}{h_m h_m^+} B_{m+1,n} = \left(\frac{2\rho_{m,n}-h_m^-\dot{\rho}_{m,n}}{h_m h_{m-1}} B_{m+1,n} + \frac{2\rho_{m,n}+k_n^-\rho'_{m,n}}{k_m k_m^+} B_{m+1,n} + i\omega\mu_o\right) B_{m,n} \quad (3.68)$$

$$2 \le m \le M-1; \quad 2 \le n \le N-1, \text{ with } \dot{\rho} = \frac{\partial \rho}{\partial y} \quad and \quad \rho' = \frac{\partial \rho}{\partial z}$$

From the equations for resistivities equivalent to eq. 3.63, we get equations

$$2\rho_{m,n} + h_{m-1}\dot{\rho}_{m,n} = 2\rho_{m+\frac{1}{2},n}, \quad 2\rho_{m,n} - h_{m-1}\dot{\rho}_{m,n} = 2\rho_{m-\frac{1}{2},n} \quad (3.69)$$

$$2\rho_{m,n} + h_{m-1}\rho'_{m,n} = 2\rho_{m,n+\frac{1}{2}}, \quad 2\rho_{m,n} - h_{m-1}\rho'_{m,n} = 2\rho_{m,n-\frac{1}{2}} \quad (3.70)$$

and

$$2\rho_{m,n} - h_m^-\dot{\rho}_{m,n} = \frac{2}{h_m^+}\left(h_m\rho_{m-\frac{1}{2},n} + h_{m-1}\rho_{m+\frac{1}{2},n}\right); 2\rho_{m,n} - k_n^-\rho'_{m,n} = \frac{2}{k_n^+}(k_n\rho_{m,n-\frac{1}{2}} + h_{m-1}\rho_{m,n+\frac{1}{2}}). \quad (3.71)$$

The boundary conditions on the top and sides of the grid are trivial in the TM mode. By virtue of constant magnetic field at the surface of the grid and exponential decay of the anomalous field as $|y| \to \infty$, we have

$$B_{m,1} = B_0 \quad B_{1,n} = B_-(z_n),\ B_{M,n} = B_+(z_n) \quad \text{for } 2 \le m \le M-1;\ \le n \le N-1 \quad (3.72)$$

3.6.3.2 Numerical considerations

Assembling the difference equations (Eqs. 3.63 or 3.64) for all nodes and applying boundary conditions, we end up with a system of linear equations of the form

$$Ax = b, \quad (3.73)$$

where elements of A contain coefficients involving physical properties, x is the vector of unknown nodal field values, and b is the column vector comprising the known elements for top, left and right hand nodes of the boundaries. Matrix A is sparse of dimension (MN x MN). For the TE mode

$$x = \left\{E_{1,1}, E_{2,1\ldots..}, E_{M,1}, E_{1,2} \ldots\ldots E_{M,2} \ldots. E_{1,N} \ldots. E_{M,N}\right\}^T \quad (3.74)$$

For the TM mode, the corresponding boundary conditions effectively reduce the number of unknowns by M+2N-2. Thus, x becomes a K-dimensional column vector where $K = MN - M - 2N + 2$ and is represented as

$$x = \left\{B_{2,2}, B_{3,2\ldots..}, B_{M-1,2}, B_{2,3} \ldots\ldots B_{M-1,3} \ldots. B_{2,N} \ldots. E_{M-1,N}\right\}^T \quad (3.75)$$

and A becomes a $(K \times K)$ matrix whose elements are the coefficients of eq. 3.64.

Since the finite difference equations for TE and TM mode consist of five-point stencil, the matrix A is a band matrix containing a tri-diagonal structure and two additional non-zero diagonals located (M-1) positions away from the main diagonal. However in TE mode, the structure is distorted by the integral boundary conditions which fill $M \times (M-2)$ blocks at the top left-hand and bottom right-hand corners of the matrix. But in TM mode only the bottom right-hand corner is filled because of the simple boundary condition applied on the surface. Thus, instead of using integral boundary conditions we extend the grids beyond the maximum depth of the model domain so that the fields can be assumed to vanish. Similarly, for the TE mode the field is extended up into the atmosphere.

The above system of equations (eq. 3.66) can be solved numerically by using either direct solver for small-sized problems of by iterative methods with pre-conditioners for fast convergences in the case of medium-to-large model domain. Thus, the values of the fields

can be obtained on every node of the model domain which can be used to compute impedance tensor on the surface of the model.

3.7 Inversion of MT data

Two dimensional inverse problems in MT have been addressed by several researchers, the most commonly used approaches being those developed by deGroot-Hedlin & Constable (1990), Smith & Booker (1984) and Rodi & Mackie (2001). The 2-D code used within this thesis is the one by Rodi & Mackie (2001) implemented in WinGLink. The forward part of the code is described by Mackie *et al.* (1988). It is based on a finite difference approximation of the Maxwell's Equations, as discussed in the previous section, and uses rectangular mesh. The inversion part of the code (Rodi & Mackie, 2001) is based on nonlinear conjugate gradients scheme to minimise a regularized objective function. Here, I shall briefly discuss the nonlinear inverse problem, regularization and finally minimization algorithm using conjugate gradient method.

The two-dimensional magnetotelluric inverse problem can be formulated as a numerical solution of the operator equation:

$$\mathrm{d} = \mathbf{G}(\mathrm{m}) + \mathrm{e}. \tag{3.76}$$

Here, $\boldsymbol{G}$ is a forward operator symbolizing the governing equations of the MT modeling. d is the observed data and m represents the model parameters. e is a measure of residuals. If we assume N measurements are performed in the MT field survey then d is the real and imaginary part of a particular element of the impedance tensor $\boldsymbol{Z}$ at particular observation site and frequency (ω), represented as

$$d = \{d^1, d^2, d^3, \ldots\ldots d^N\}^T. \tag{3.77}$$

Similarly, model parameters can be represented as the components of a vector m of order $(M \times 1)$ defining the electrical conductivity/resistivity function in the subsurface, with **e** as the residual vectors of $(M \times 1)$.

$$m = \{m^1, m^2, m^3, \ldots\ldots m^M\}^T \tag{3.78}$$

Here, superscript T denotes the transpose of the two vectors.

If the forward operator is linear, the simplest of method for solving the linear inverse problem is based on the measures of the size, or length of the estimated model parameters $\mathrm{m}^{\mathrm{est}}$ and of the predicted data $\mathrm{d}^{\mathrm{pre}} = \mathrm{G}\,\mathrm{m}^{\mathrm{est}}$. Least square solution of linear inverse problem with estimated model parameters $\mathrm{m}^{\mathrm{est}}$ is given by (Manke, 1984)

$$\mathrm{m}^{\mathrm{est}} = (G^T G)^{-1} G^T \mathrm{d}. \tag{3.79}$$

The method of least squares estimates the solution of the inverse problem by finding the model parameters that minimize a particular measure of the length of the estimated data known as Euclidian distance from the observations. The method of least squares uses the L2 norm to quantify the length is given as

$$q = (\mathrm{d} - G\mathrm{m})^T (\mathrm{d} - G\mathrm{m}). \tag{3.80}$$

3.7.1 Nonlinear inverse problem - Regularization

The solution to this problem depends heavily on the nature of the relation between data and model as well as the number of data points and model parameters. In electromagnetics as in other geophysical applications, this relation is usually not linear and the problem can be mixed or under-determined, i.e. the number of independent data points is much smaller than the number of model parameters for atleast some parts of the problem. Further, the magnetotelluric inverse problem is ill-posed and the inversion results are unstable and non-unique. It means that different geo-electric models could fit the observed data with the same accuracy. A stable solution of the ill-posed inverse problem can be obtained by utilizing the regularization methods in the objective functional subjected to minimum.

In practical non-linear problems, the data and the model parameters are related via a nonlinear functional *f* and this relationship is expressed as;

$$d = f(\mathrm{m}^{\mathrm{est}}) + e, \tag{3.81}$$

where $f(\mathrm{m}^{\mathrm{est}})$ is a nonlinear functional that maps the model on the datum d. The data fitting can be achieved by minimising the difference between real data $\mathrm{d_i}$ and estimated data $f(\mathrm{m}^{\mathrm{est}})$ as a function of the estimated $\mathrm{m}^{\mathrm{est}}$, which is given by

$$\varphi_d = (\mathrm{d} - f(\mathrm{m}))^T {C_d}^{-1} (\mathrm{d} - f(\mathrm{m})), \tag{3.82}$$

where c_d is the data covariance matrix which is diagonal and contains the data uncertainties e. In principle the inverse problem formulated in eq. 3.71 will converge. However the resulting solution may be unstable and it may not be very physical and unique. In general one adds additional terms to the above expression to make the solution well behaved. An approach to overcome the non-uniqueness is to incorporate some a-priori information in order to define a unique solution. Classical remedies that advocate a-priori preferences into the model fall under two classes. One class assumes that the model parameters are random variables so that statistical information can be introduced to constrain the model. Important approaches include: Bayesian inference, stochastic inversion, and maximum likelihood method. The second class assumes some 'regularity' properties of the solution such as a constraint on the spatial smoothness of the model parameter. This idea is familiar from the modern method of data interpolation. The original idea of a penalty for complexity is due to Tikhonov who named the general procedure "regularization" introducing it in order to overcome mathematical difficulties in theory of ill-posed problems (Tikhonov & Arsenin, 1977).

In Occam's inversion (Constable *et al.* 1987), smoothest solution that is consistent with the data is achieved by adding a term to eq. 3.82 that penalizes the squared gradient of the model. Another regularization technique is Bayesian inference which provides a way to include statistical information of the data and model in the misfit criterion (e.g. Tarantola, 1987, 2004). The misfit function (eq. 3.71) possibly supplemented with regularization term is usually referred to as penalty function (Snieder, 1998). For minimizing the penalty function, in general, we can use either descent method (conjugate gradients, steepest descent, and line search) where we iteratively update an estimate of the model that minimizes the penalty function or employing techniques that sample model space in many different locations as a way of minimization. Descent methods can relatively easily be implemented for large scale inverse problems

In General dataset is usually contaminated with noise, which can affect the results to produce a formal solution which is far from any realistic model. In other words, small variations in the dataset produced by the noise can generate dramatic variations in the inversion solution, for this reason the inverse problem is ill-posed. To avoid structures that are actually not required by the data, the roughness of the model, as measured by the model norm is minimized towards prior information or a minimum-structure constraint:

$$\varphi_m = (\mathrm{m}^{\mathrm{est}} - \mathrm{m}^{\mathrm{o}})^T {C_m}^{-1} (\mathrm{m}^{\mathrm{est}} - \mathrm{m}^{\mathrm{o}}), \tag{3.83}$$

with m^o as the prior model, C_m as the model covariance matrix, which characterizes the magnitude and smoothness of resistivity variation with respect to the prior model m^o.

Tikhonov Regularization

Tikhonov regularization defines a solution that is a joint minimization of data and a 'stabilizing functional' given as

$$\psi(m,\tau)v = \phi(m) + \tau s(m), \tag{3.84}$$

where $\phi(m)$ is a misfit functional determined as a square norm of the difference between observed and predicted (theoretical) data. $\phi(m) = \left\|\mathrm{Gm^{est}} - \mathrm{d^{obs}}\right\|^2 . \tau$ is a positive number known as regularization parameter. $s(m)$ is a stabilizing functional (stabilizer) which measures the spatial roughness of the model. The main role of the stabilizer is to select an appropriate class of models for the inverse solution. Actually the stabilizer can be treated as a tool for including a-priori information about the geological structure in the inverse problem (Mehanee & Zhdanov, 2002).

The applied error functional differs between inversion algorithm, but most of them belong to one of two forms; namely the unconstrained functional or the constrained functional. In unconstrained functional

$$\psi(\mathrm{m^{est}},\lambda) = \left(\mathrm{d^{obs}} - \mathrm{G(m)}\right)^{\mathrm{T}} \mathrm{R_{dd}^{-1}}(\mathrm{d} - \mathrm{G(m)} - \Upsilon^2) + \lambda(\mathrm{m^{est}} - \mathrm{m^o})^{-1}\mathrm{L^T L}(\mathrm{m^{est}} - \mathrm{m^o}) = \min \tag{3.85}$$

where R_{dd} is the data covariance matrix, Υ is the desired level of misfit, $\mathrm{m^o}$ is an a-priori model and λ is a Lagrange multiplier. L is a linear operator. The unconstrained functional is used mostly in Occam's inversions (Constable *et al.*1987; Degroot-Hedlin & Constable, 1990; Siripunvaraporn & Egbert, 2000, 2009; and Siripunvaraporn *et al.*2002, 2005).

In constrained functional (also referred to as objective functional or penalty functional):

$$\psi(\mathrm{m^{est}},\tau) = \left(\mathrm{d^{obs}} - \mathrm{G(m)}\right)^{\mathrm{T}} \mathrm{R_{dd}^{-1}}\left(\mathrm{d} - \mathrm{G(m)}\right) + \tau.(\mathrm{m^{est}} - \mathrm{m^o})^{-1}\mathrm{L^T L}(\mathrm{m^{est}} - \mathrm{m^o}) = \min \tag{3.86}$$

Here τ is a trade-off parameter controlling whether to heavily minimize the data misfit or the model norm. For large τ the data misfit is less important and therefore the model norm is

minimized to produce a smother model. For small τ the inversion tends to fit the data better. This is closer to the least squares inversion problem and often produces rough model. The constrained functional is used in most algorithms, for example in nonlinear conjugate gradient (NLCG) (e.g. Newman & Alumbaugh, 2000; Rodi & Mackie, 2001), Gauss-Newton (GN) (e.g. Haber *et al.*2000; Sasaki, 2001), quasi-Newton (QN) (Haber *et al.*2005), and GN with conjugate gradient (GN-CG) (Mackie & Madden, 1993).

There are several common choices for stabilizers which lead to different classes of geological model used for inversion. In the stochastic or maximum likelihood inversion, m^o is taken to be the a-priori mean of m and L is chosen such that $(L^T L)^{-1} = R_{mm}$ is an a-priori covariance of m. In minimum norm apporch, L is a differential operator and m^o is taken to be simple a-priori model. In least squares criterion (L2-norm) minimum norm of the difference between the selected model and some a priori model m^o;

$$L = I, \ (m^{est} - m^o)^{-1} L^T L (m^{est} - m^o) = \int dx\, dy\, dz \ |m^{est} - m^o|^2, \tag{3.87}$$

The conventional maximum smoothness stabilizing functional uses the minimum norm of the gradient of model parameter ∇m. (Constable *et al.* 1987, Smith & Booker, 1988)

$$L = \nabla, (m^{est} - m^o)^{-1} L^T L (m^{est} - m^o) = \int dx\, dy\, dz \ |\nabla(m^{est} - m^o)|^2. \tag{3.88}$$

In some cases, the minimum norm of Laplacian of model parameter $\nabla^2 m$ is also used. Rodi & Mackie (2001) have used minimum norm of Laplacian of model parameter as the stabilizer in the minimizing functional

$$L = \nabla^2, \ (m^{est} - m^o)^{-1} L^T L (m^{est} - m^o) = \int dx\, dy\, dz \ |\nabla^2(m^{est} - m^o)|^2. \tag{3.89}$$

For 2-D or 3-D inversion problems, additional smoothness parameters can be applied to separately control the smoothness in horizontal and vertical directions. In WinGLink, horizontal and vertical smoothness are controlled by coefficients α and β, respectively, where α is a multiplier of the horizontal derivatives enforcing an increase of horizontal smoothness whereas β controls weighting of the cell size dependent influence of the smoothness operator τ. Different values of the smoothing parameters have been proposed, e.g. Mackie (2002): α = 1 (unless reasons for a higher degree of horizontal smoothness are found), $\beta \in [0{:}3; 3]$ and $\tau \in [3; 300]$. However, the optimal set of values is certainly dependent on the local

subsurface and the mesh used during the inversion. It is therefore strongly advised to test a range of values in order to identify their effect on the final model.

Table 3.02: Proposed values for the factor β by Mackie (2002)

Regularisation operator	Regularisation order	Proposed value for β
Standard grid	$(\nabla^2 m)^2$	3.0
	$\|\nabla m\|^2$	1.0
Uniform grid	$(\nabla^2 m)^2$	3.0
	$\|\nabla m\|^2$	0.3

Selection of regularization parameter value

The approach based on L-curve is commonly used to select appropriate value of the regularization parameter for a given set of data. The method offers a convenient way to display regularization information as a function of the regularization parameterτ. The L-curve is a parametric plot of the norm of a regularized solution versus the norm of the corresponding residuals. The parameter can be chosen by characteristic L-shaped corner of the L-curve which corresponds to an optimum balance between the minimization of these two quantities. Mathematically, the L-curve's corner is defined as a point on the curve (Sripanya, 2013)

$$(\mathrm{R}(\alpha), \mathrm{S}(\alpha)) = (\log\|\mathrm{G}\,\mathrm{m}_\alpha - \mathrm{d}\|, \log\|\mathrm{m}_\alpha\|), \tag{3.90}$$

which has the maximum curvature. The curvature k is usually given by the formula

$$\mathrm{k}(\alpha) = \frac{\mathrm{R}'\mathrm{S}'' - \mathrm{R}''\mathrm{S}'}{((\mathrm{R}')^2 + (\mathrm{S}')^2)^{\frac{3}{2}}}, \text{ where the differentiation is with respect to } \alpha. \tag{3.91}$$

3.7.2 Linearization of nonlinear problems – Occam method

In the Occam method, out of all the infinity possible solutions that fit the data, we choose the smoothest solution which is the one with the fewest features required to fit the data. The idea follows from the philosophy of Occam's razor: all else being equal, the simplest explanation is the best (Scientific hypotheses and reasoning should be as simple as possible). In geophysical inversion it is known as Occam's inversion. The principle is attributed to the 14thcentury logician and Franciscan friar William of Ockham (Occam). MT inversion scheme based on Occam razor to solve a layered conductivity model fitting MT data at a single

station was first developed by Constable *et al.* (1987). It was extended to 2-D scenario by deGroot-Hedlin & Constable (1990).

Linearized inversion schemes provide one method for dealing with non-linear inverse problems (those problems where the data are non-linearly related to the model parameters). They involve expanding the model predictions in a Taylor series around some point in the model space, and then solving for the model changes that minimize the error between the observed and predicted data using the standard least-square method or maximum likelihood method or minimum norm method.

$$g(m) \approx g(m^o) + A\Delta m. \tag{3.92}$$

In this case, we assume that $g(m)$ is linear around some initial model m^o, such that a small change of the model responses about m^o can be expressed using Taylor's theorem as,

$$f(m) = f(m^o) + \sum_{i=1}^{p} \frac{\partial f(m^o)}{\partial m_j^o} (m_i - m_i^o) \quad \text{or} \quad f(\mathbf{m}^{est}) = f(m^o) + A\Delta m. \tag{3.93}$$

This comes by neglecting terms higher than first order and with sensitivity matrix $A = \frac{\partial f(m^o)}{\partial m_j^o}$ is the $M \times N$ jacobian matrix of partial derivatives (known as Frechet derivatives) and $\Delta m = (\mathbf{m}^{est} - m^o)$ is a vecror of the sought parameter increments which describes only local changes in m so the inversion must be iterated, each time updating the model.

For simplicity we re-write the eq. 3.81 as

$$g(m_{k+1}) \approx g(m^k) + A\Delta m_k \quad \text{where} \quad m_{k+1} = m_k + \Delta m_k \tag{3.94}$$

The subscript k is the iteration number. In order to find the stationary points, eq. 3.46 is substituted in eq. 3.54 which yields iterative solution:

$$m_{k+1}(\lambda) = (\lambda C_{mm}^{-1} + \Gamma_k^m)^{-1} A_k^T C_{dd}^{-1} X_k + m_o, \tag{3.95}$$

with $X_k = d - g(m_k) + A_k(m_k - m_O)$, and the $M \times M$ model space cross-product matrix

$$\Gamma_k^m = A_k^T C_{dd}^{-1} A_k, \tag{3.96}$$

The Occam inversion runs through two different stages before it reaches the final solution. The Lagrange multiplier λ is used both as a step length control and a smoothing parameter. A series of values of λ are used to minimise the misfit of each iteration in phase-1. The aim is to reduce the misfit to the desired level ϒ . However in the early iterations the misfit leverl ϒ will not reach for a series of values for λ. For each iteration, the Occam code uses the minimum misfit from the best λ as a basis for the next iteration. Once the desired misfit ϒ is reached, phase-2 commences by keeping the misfit at the desired level and varying λ to search for the smallest norm, i.e. the smoothest model. The downside of the Occam inversion is that the sensitivity matrix A must be calculated for every iteration. This process is both time-consuming and requires much computer memory to store A. Nonlinear minimization algorithms like conjugate gradients methods offer improvement in speed due to preconditioning and the computation of only the gradient rather than the sensitivities A.

3.7.3 Nonlinear Minimization Algorithm

In the previous section, we have defined the solution of the MT inverse problem by minimizing the objective function $\psi(m^{est}, \tau)$ in eq. 3.56. Since the forward modeling operator G depends nonlinearly on m, ψ is non-quadratic and an iterative minimization is required. Rodi & Mackie code uses nonlinear conjugate gradient method for minimizing the objective functional.

Non-linear conjugate gradient (NLCG) method

The Gauss-Newton method is based on expanding G in Taylor series and calculating model correction at every iteration. This way of linearization may result in slow convergence for the nonlinear inversion problems when ψ is far from a quadratic function. Another potentially more efficient algorithm for minimization problems is nonlinear conjugate gradient (NLCG) method.

The technique of the conjugate gradients was developed by Hestenes & Stiefel (1952) to solve a linear system of equations $Bx = y$ for sparse matrices B. The underlying principle is to find a set of orthogonal directions and to compute accompanying weights in a manner that every search direction is used only once. As a result, convergence is generally fast compared to steepest descent equation solvers. This technique has been used for non-linear minimization problems by Fletcher & Reeves (1959) and for inversion of magnetotelluric (Mackie & Madden, 1993; Rodi & Mackie, 2001) and DC resistivity (Zhang *et al.*1995; Ellis

& Oldenburg, 1994). Conjugate gradient method uses updated model vectors which are conjugate versions of each successive gradient vector, i.e. the directions of updates are not specified a-priori but are determined sequentially as linear combinations of previous direction vectors. Use of these conjugate directions helps the minimization procedure to make uniform progress towards convergence which is not so important in quadratic problems but can be crucial importance in non-quadratic problems (e.g. non-linear inversion). NLCG method yields an alternative minimization a nonlinear function directly without making any assumptions about its linearity.

Adopting the Tikhonov regularization concept, the regularized equation eq.3.86 can be solved by applying the nonlinear conjugate gradient method (NLCG). This technique generates a sequence m_k for $k >= 1$, starting from an initial guess m_o using the recurrence relation,

$$m_{k+1} = m_k + \lambda_{k+1} h_{k+1}, \tag{3.97}$$

where λ_k is a positive step size obtained by a line search and h_{k+1} is a search direction generated by the rule

$$h_o = -g_0 , \qquad h_{k+1} = C_k g_{k+1} + \gamma_k h_k , \tag{3.98}$$

where $g_k = \nabla F_\alpha(m_k)$and γ_k is an update parameter which can be determined by using the Fletcher-Reeves formula

$$\gamma_k = \frac{g_{k+1}^T g_{k+1}}{g_k^T g_k}. \tag{3.99}$$

The operator C_k is known as the pre-conditioner.

Unlike linear conjugate gradients, λ_{k+1} is computed to minimize the exact $\psi(m)$. This involves an interative line minimization procedure. In the NLCG algorithm, the line minimization automatically defaults to a one-step computation of λ_{k+1} when F can be well-approximated by its linear expansion about the previous model. In the algorithm, the pre-conditioner has big impact on efficiency. Two competing considerations in choosing C_k are (1) how well it steers g_{k+1} in the direction of true solution, and (2) the amount of computation involved in applying the operator. The pre-conditioner used in the algorithm is

$$C_k = (\gamma I + \tau L^T L)^{-1}, \quad (3.100)$$

where γ is proportional to the matrix norm of $R_{dd}^{-1/2} A_k$ with A_k as Frechet derivative of F evaluated at m_k.

Rodi & Mackie (2001) compared the performance of the scheme in terms of computational requirements and processing time with the other gradient type methods (e.g. steepest-descent and Gauss-Newton) and demonstrated that conjugate gradient is more efficient and is a favorable gradient type method to solve 2-D MT inverse problems.

3.8 MT time series processing

The above section described inversion of apparent resistivity and phase data to get models for 2-D structure. However, MT data are recorded in the form of time series of electric and magnetic field components and we need to extract transfer functions from these time series. Therefore, processing of time series data is an important step in MT studies. This section describes the approaches for this purpose. Extraction of transfer functions from time series involves a series of pre-processing steps such as: preconditioning of the data, transformation from the time to the frequency domain, and estimation of transfer functions.

Preconditioning of data

Preconditioning of time series data is done to reduce the effect of trends, removal of severe noise (spikes), and minimization of the effects caused by having data of finite length. The time series is split into segments, the size of which depends on the period band being analyzed, and segments having good stable signals are separated out. These segments are then multiplied with a window function, normally Hanning or Hamming window, to reduce the frequency leakage.

Estimation of spectra

Since analysis of MT data is mostly done in the frequency domain, spectral analysis of raw data is an important aspect of data processing.Once pre-conditioned, windowed time series data are transformed to the frequency domain, normally using either Fourier Transform or wavelet transform. These spectra are then calibrated using appropriate instrument response function. This step is especially necessary for the induction coil data which gives the rate of

change of magnetic field rather than the magnetic field values. The transfer functions of every induction coil are needed to estimate the respective magnetic field components.

Although, the total number of samples is large in each segment of the data to minimize the windowing effect, transfer functions are evaluated at six to ten frequencies per decade. More values per decade are unnecessary as the dispersion relation of Weidelt (1972) predicts similar results for neighbouring frequencies. Never-the-less, fewer could result in aliasing in the frequency domain (Simpson & Bahr, 2005). Once the spectra of all the five components ($\mathrm{E_x}, \mathrm{E_y}, \mathrm{B_x}, \mathrm{B_y}, \mathrm{B}_z$) and for all the segments of acceptable time series are obtained, these can be used to compute auto- and cross-power spectra as $X_a.Y_b^*$, where Y^* is complex conjugate of Y, and their ensemble average $<.>$ and standard deviations.

Estimation of transfer functions

Once the spectra and power spectra are estimated, the next step involves estimating the elements of the impedance tensor and tipper coefficients. Various methods have been proposed to estimate the tensor elements from the complex Fourier field coefficients (Cantwell, 1960; Bostick & Smith, 1962; Blackman & Tukey, 1959; Smis *et al.* 1971; Tick, 1963; Madden & Nelson, 1964). Sims & Bostick (1969) and Vozoff (1972) suggested simulating the smoothed auto-power and cross-power spectral density estimates by averaging a number of Fourier harmonics over a discrete band of frequencies.

Impedance Tensor

Multiplying eq. 3.23 by complex conjugate of B_x and then by complex conjugate of B_y, we get

$$\langle E_x B_x^* \rangle = \mathrm{Z_{xx}} \langle B_x B_x^* \rangle + \mathrm{Z_{xy}} \langle B_y B_x^* \rangle, \tag{3.101a}$$

$$\langle E_x B_y^* \rangle = \mathrm{Z_{xx}} \langle B_x B_y^* \rangle + \mathrm{Z_{xy}} \langle B_y B_y^* \rangle, \tag{3.101b}$$

where $\langle . \rangle$ denotes the ensemble averages over many adjacent frequencies for a single record at single site, i.e. averaging over a frequency band as an approximations to smoothed power spectral estimates. Similarly, the expressions can be obtained for $\mathrm{E_y}$. Above equation contains auto- and cross-powers, which amplify the correlated noise present in the data causing the respective Z component to be biased. The inherent noise in the measured electric fields will bias the estimated Z component upwards while the inherent noise in the measured magnetic

fields will bias the Z component downwards. One of the methods to solve this problem is to deploy a remote reference site at a distance sufficiently away from the measuring or local site so that it can be presumed that the noise is uncorrelated. After some mathematical treatment, we obtain the expressions for the impedance tensor components as:

$$Z_{xx} = \frac{\langle E_x B_x^* \rangle \langle B_y B_y^* \rangle - \langle E_x B_y^* \rangle \langle B_y B_x^* \rangle}{\langle B_x B_x^* \rangle \langle B_y B_y^* \rangle - \langle B_x B_y^* \rangle \langle B_y B_x^* \rangle}, \qquad Z_{xy} = \frac{\langle E_x B_x^* \rangle \langle B_x B_y^* \rangle - \langle E_y B_y^* \rangle \langle B_x B_x^* \rangle}{\langle B_y B_x^* \rangle \langle B_x B_y^* \rangle - \langle B_x B_y^* \rangle \langle B_x B_x^* \rangle}, \tag{3.102}$$

$$Z_{yx} = \frac{\langle E_y B_x^* \rangle \langle B_x B_y^* \rangle - \langle E_y B_y^* \rangle \langle B_x B_x^* \rangle}{\langle B_x B_x^* \rangle \langle B_y B_y^* \rangle - \langle B_x B_y^* \rangle \langle B_y B_x^* \rangle}, \qquad Z_{yy} = \frac{\langle E_y B_x^* \rangle \langle B_x B_y^* \rangle - \langle E_y B_y^* \rangle \langle B_x B_x^* \rangle}{\langle B_y B_x^* \rangle \langle B_x B_y^* \rangle - \langle B_y B_y^* \rangle \langle B_x B_x^* \rangle}. \tag{3.103}$$

$\langle E_a B_b^* \rangle$ are the average estimates of the tensor elements over the smoothing band-width.

Tipper

Following the similar procedure as used to estimate impedance tensor components we get expressions for the tipper components as

$$T_x = \frac{\langle B_z B_x^* \rangle \langle B_y B_y^* \rangle - \langle B_z B_y^* \rangle \langle B_y B_x^* \rangle}{\langle B_x B_x^* \rangle \langle B_y B_y^* \rangle - \langle B_x B_y^* \rangle \langle B_y B_x^* \rangle}, \qquad T_y = \frac{\langle B_z B_y^* \rangle \langle B_x B_x^* \rangle - \langle B_z B_x^* \rangle \langle B_x B_y^* \rangle}{\langle B_y B_y^* \rangle \langle B_x B_x^* \rangle - \langle B_y B_x^* \rangle \langle B_x B_y^* \rangle}. \tag{3.104}$$

Once T_x and T_y are estimated, the tipper magnitude ($|T|$) and tipper phase (ϕ_T) can be defined as:

$$|T| = \sqrt{|T_x|^2 + |T_y|^2}, \quad \phi_T = \frac{|T_x|^2 \tan^{-1}\left(\frac{\text{Im Tx}}{\text{Re Tx}}\right) + |T_y|^2 \tan^{-1}\left(\frac{\text{im Ty}}{\text{Re Ty}}\right)}{|T_x|^2 + |T_y|^2}. \tag{3.105}$$

The tipper relation given by eq. 3.27 may be solved by using either local (B_x, B_y)or remote reference fields(R_x, R_y). Tipper coefficients can be plotted as vectors popularly known as induction arrows (Parkinson, 1962; Schmucker, 1970).The magnitude and phase angle of the tipper define the length of the arrow and the orientation of the induction vector, respectively. Induction arrows can be used to indicate the presence or absence of lateral variations in conductivity, since the vertical magnetic field is generated by lateral conductivity gradients (Jones & Price, 1970; Jones, 1986; Simpson & Bahr, 2005). There exist two conventions concerning the real tipper direction. In the Parkinson convention (1962), it is oriented towards the high conductivity region. In Wiese convention (Wiese, 1962), the real part of T points away from the zone of high conductivity. Induction arrow of the real part is given by the real part of the tipper magnitude and phase.

There are a number of processing codes available, both commercial (e.g. Mapros by M/s Metronix GmbH, Germany) and research purpose (e.g. Egbert & Booker, 1986; Egbert, 1997; Chave & Thomson, 2004) that perform differently depending on the nature and quantity of the noise contained within the recorded signal. If the noise contamination is coherent between the local and remote station, then remote reference processing will not remove this. If the noise contamination (signal to noise ratio) is poor enough, it is possible that robust processing codes could regard the signal as noise, since there is less of it, and merely enhance the noise by rejecting signal.

Rotation of impedance tensor

After calculating the tensor elements in the measurement coordinate system, the last step in the processing procedure is determination of the principle coordinate system. The rotation angle for this purpose can be obtained by minimizing the diagonal elements (Z_{xx}, Z_{yy}) of the impedance tensor. Let θ be the angle between the horizontal x- axes of the measurement and the rotated coordinate system. Then a rotation matrix R can be operated on the impedance tensor to get impedance tensor $\bar{Z}_m$ in the rotated frame of reference. This can be written as:

$$\bar{\mathrm{Z}}_{\mathrm{m}} = \mathrm{R}\mathbf{Z}\mathrm{R}^{\mathrm{T}}, \qquad \text{where} \qquad \mathrm{R} = \begin{pmatrix} \cos\theta & \sin\theta \\ -\sin\theta & \cos\theta \end{pmatrix}, \tag{3.106}$$

with positive θ describing a clockwise rotation from the coordinate system of $\bar{Z}_{\mathrm{m}}$. A special case of this rotation is the angle for which the diagonal elements of the impedance tensor are minimized. This angle rotates the coordinate system to the principal coordinate system and the angle is called as the principal rotation direction that can be treated as the strike direction within the ambiguity of 90^{o}.

$$2\,\mathrm{Z}'_{\mathrm{xx}}(\theta) = \left(\mathrm{Z}_{\mathrm{xx}} + \mathrm{Z}_{\mathrm{yy}}\right) + \left(\mathrm{Z}_{\mathrm{xx}} - \mathrm{Z}_{\mathrm{yy}}\right)\cos 2\theta + \left(\mathrm{Z}_{\mathrm{xy}} + \mathrm{Z}_{\mathrm{yx}}\right)\sin 2\theta \tag{3.107a}$$

$$2\,\mathrm{Z}'_{\mathrm{xy}}(\theta) = \left(\mathrm{Z}_{\mathrm{xy}} - \mathrm{Z}_{\mathrm{yx}}\right) + \left(\mathrm{Z}_{\mathrm{xy}} + \mathrm{Z}_{\mathrm{yx}}\right)\cos 2\theta - \left(\mathrm{Z}_{\mathrm{xx}} - \mathrm{Z}_{\mathrm{yy}}\right)\sin 2\theta \tag{3.107b}$$

$$2\,\mathrm{Z}'_{\mathrm{yx}}(\theta) = -\left(\mathrm{Z}_{\mathrm{xy}} - \mathrm{Z}_{\mathrm{yx}}\right) + \left(\mathrm{Z}_{\mathrm{xy}} + \mathrm{Z}_{\mathrm{yx}}\right)\cos 2\theta - \left(\mathrm{Z}_{\mathrm{xx}} - \mathrm{Z}_{\mathrm{yy}}\right)\sin 2\theta \tag{3.107c}$$

$$2\,\mathrm{Z}'_{\mathrm{yy}}(\theta) = \left(\mathrm{Z}_{\mathrm{xx}} + \mathrm{Z}_{\mathrm{yy}}\right) - \left(\mathrm{Z}_{\mathrm{xx}} - \mathrm{Z}_{\mathrm{yy}}\right)\cos 2\theta - \left(\mathrm{Z}_{\mathrm{xy}} + \mathrm{Z}_{\mathrm{yx}}\right)\sin 2\theta \tag{3.107d}$$

The principle axes of Z are the values for which Z'_{xy} and Z'_{yx} take on their largest and smallest values, respectively. The angel θ_o for which

$$\left|Z'_{xy}(\theta_o)\right|^2 + \left|Z'_{yx}(\theta_o)\right|^2 = maximum.$$

Setting the derivative with respect to θ of this sum equal to zero gives (Swift, 1967), i.e.

$$\tan 4\theta_o = \frac{(Z_{xx}-Z_{yy})(Z_{xy}+Z_{yx})^* + (Z_{xx}+Z_{yy})^*(Z_{xy}+Z_{yx})}{|Z_{xx}-Z_{yy}|^2 - |Z_{xy}+Z_{yx}|^2}; \quad (3.108)$$

The same value of θ_o also satisfies $|Z'_{xx}(\theta_o)|^2 + \left|Z'_{yy}(\theta_o)\right|^2 = minimum$

MT transfer functions contain information about the dimensionality of the subsurface structures at different depth levels but these are sensitive to noise and can contain distortions due to localized 3D near-surface conductors, current channeling, geological and cultural noise. Hence, for distorted MT data the estimation of strike angle by the above approach may not give robust estimates. Therefore, advanced analyses are performed on transfer functions to minimize the effect of distortions and to extract mode information about the complexity of the subsurface structure. These are discussed in Chapter 5.

3.9 Summary

The methodology chapter describes the fundamentals of magnetotelluric method including the source of signals, mathematical formulation of magnetotelluric method, 2-D forward modeling (both isotropic an anisotropic) and inversion of MT data. The chapters also contains the basic steps involved in the MT time series processing particularly removal of noise, transformation from time to frequency domain and estimation of MT transfer functions like, impedance tensor, tipper and apparent resistivity and phase. The next chapter deals with magnetotelluric field survey carried out in the Sikkim Himalaya in various field sessions followed by brief description of sensors, recording units and important points on MT field survey. The preprocessing of the recorded MT data is also described in the next chapter.

Chapter 4

MT data acquisition and preprocessing

Acquisition of high quality data is the first and foremost important step for any geophysical study. It requires careful field planning taking into consideration the objective of the study, geological and geo-morphological settings of the region, potential sources of noise affecting data quality, and field logistics. In MT surveys, time series of natural electromagnetic (EM) induction are recorded and converted to impedance tensors through pre-processing steps. Since natural EM variations are in general very weak compared to the EM fields generated by artificial sources, it is essential to select MT sites in remote areas away from any electrical or cultural noise. This makes MT site selection a challenging task. The inter-station spacing and duration of time series recording depend on the objective of the work. Various field aspects of MT field procedures are described by Pedersen (1982, 1988) and Simpson & Bahr (2008). This chapter describes the data acquisition and pre-processing steps followed in the present study.

4.1 Field Campaign

4.1.1 Profile selection

The general strike of the Indian plate as well as major thrust faults (MFT, MBT, and MCT) in the central segment of the Himalayan belt is approximately E-W although MCT deviates from this trend in the Sikkim segment. Therefore, we selected an approximately N-S trending profile that cuts across major geotectonic domains of the Sikkim Himalaya. This profile is also sub-parallel to the INDEPTH 100-line (Nelson *et al*. 1996) but is shifted westward and covers the regions of LHD and SHD, not explored by the INDEPTH profile. The profile (Figure 4.01) starts from the northern Bengal Basin in the south having average topography of 25-30m, traverses through SHD, LHD, MCTZ, and HHC and finally ends near STDS at an

altitude of 5,000 m at the northern end. The topography in LHD and HHC is extremely rugged and shows a highly immature positive topography with dense covered forests. The Tista River (a major river of Sikkim) valleys are mostly V–shaped with moderately steep stream abutments.

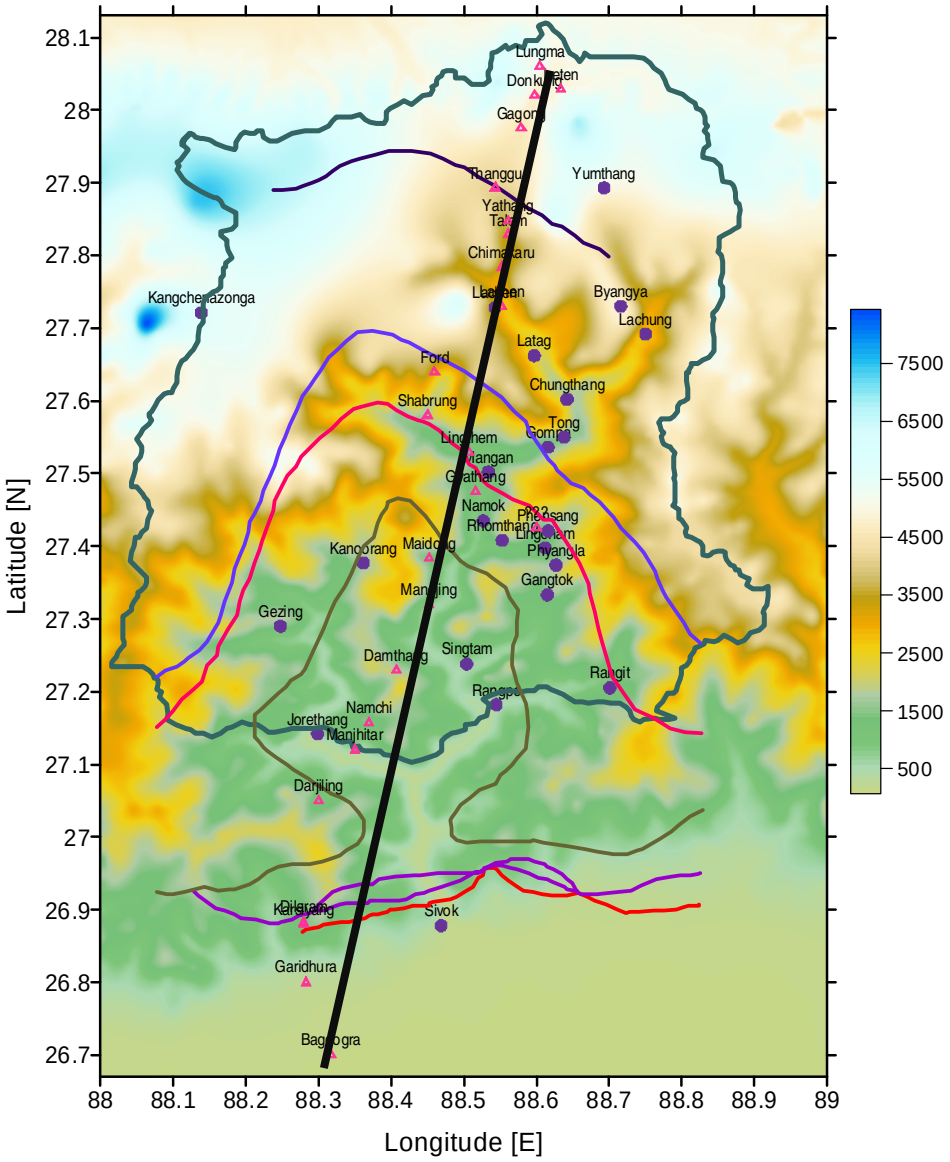

Figure 4.01: Location of the proposed MT profile across the Sikkim Superimposed on topography (taken from GTOPO30) of the region.

4.1.2 Layout of MT site

In MT survey, time-varying natural EM signals (individual electric and magnetic field components) are measured using electric and magnetic sensors and data acquisition unit. The electric field is estimated through measurement of potential difference across a pair of non-

polarizing electrodes separated by a distance of about 80-100 m forming an electric dipole. These electrodes are buried at about 0.25 m deep pits. Two horizontal components of the electric field are thus measured along N-S (E_x) and E-W (E_y) directions respectively. The three components of time-varying magnetic field (H_x, H_y, H_z) are obtained by using either induction coils (IC) for very high frequency (> 10KHz) and broadband (10 KHz to 4096 s) recordings or fluxgate magnetometer (FG) for low frequency (1Hz to DC) recordings. These sensors are also buried sufficiently deep in the ground to avoid wind noise and thermal insulation. All these sensors are connected to a data acquisition unit. Beside these five components, a GPS (Global Positioning Unit) is also connected to the acquisition unit for precise time marking. A schematic diagram of a typical MT field setup is shown in Figure 4.02. The duration of recording depends on the target depth and anticipated subsurface resistivity. It may vary from a few minutes to several weeks or months depending on the nature of investigation.

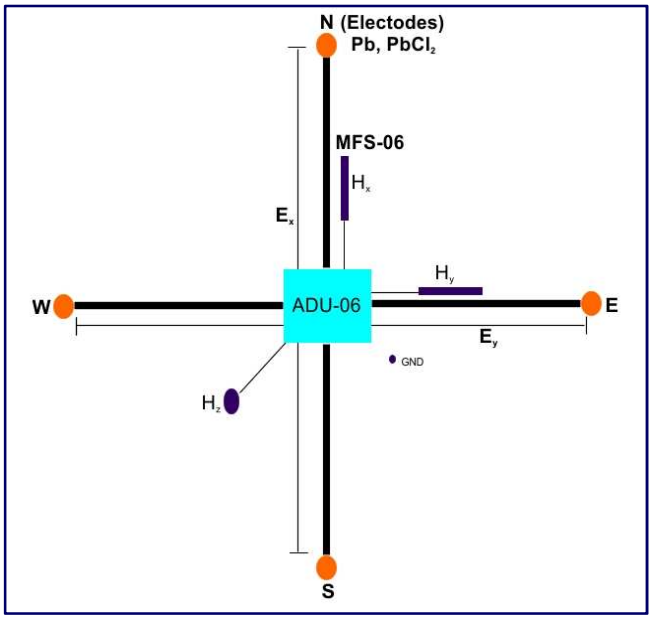

Figure 4.02: Schematic diagram showing general MT field layout

We have used the above MT layout to acquire MT data along the selected profile.

4.1.3 Instruments

As mentioned above, MT data acquisition system consists of three major parts; electric field sensors, magnetometers, and data acquisition unit. The broadband MT equipment used in the present study consists of non-polarizing $Pb - PbCl_2$ electrodes, three magnetic induction

coils MFS-06, 6-channel data acquisition unit ADU-06, and a GPS module (*M/s* Metronix GmbH, Germany).

Electric Field Sensors

A scalar component of the earth's electric field is determined by measuring the potential difference $V\ (= V_2 - V_1)$between a pair of electrodes separated by a distance d (Figure 4.03) and connected by a shielded cable forming a dipole. The electric field component is estimated by the relation:

$$E = \frac{(V_2 - V_1)}{d}, (V/m) \tag{4.1}$$

The vector electric field can be determined by measuring voltage difference along three mutually orthogonal directions and can be expressed in vector form as

$$\vec{E} = -\nabla V, \qquad \text{where} \qquad \nabla = \hat{\imath}\frac{\partial}{\partial x} + \hat{\jmath}\frac{\partial}{\partial y} + \hat{k}\frac{\partial}{\partial z} \tag{4.2}$$

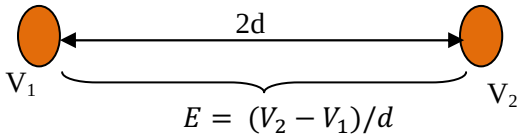

Figure 4.03: (a) Pb-$PbCl_2$ electrode, and (b) schematic diagram showing layout for e-field component measurement.

In MT, we measure two horizontal components of the vector electric field. Usual convention is to lay one dipole along the magnetic north and other orthogonal to it. Steel nails can be used as electrodes for high-frequency audiomagnetotellurics (AMT) measurements but long-period MT measurements require non-polarizing electrodes in which electrochemical effects (which modify the potential difference that is registered) are avoided as far as possible. Non-polarizing electrodes usually consist of a porous pot containing metal (e.g. silver (Ag)/lead

(Pb)) in contact with salt of the same metal (e.g. silver chloride (AgCl)/lead chloride ($PbCl_2$)).

Magnetic Field Sensors

Magnetic field variations can be recorded by using induction coils (IC) or fluxgate (FG) magnetometers. As our interest in the present study is to map the crustal structure, we have used induction coils to acquire data in the frequency range of 10 KHz to 4096 s. We have used induction coils MFS-06 (Figure 4.04a) of *M/s* Metronix GmbH, Germany for this purpose. The broadband induction coil magnetometer *MFS-06* has been developed to measure variations of the Earth´s magnetic field, particularly for applications in Magnetotellurics (MT) and Controlled Source Audio Magnetotellurics (CSAMT). It covers a wide frequency range from 0.0001 Hz up to 10 kHz. In spite of its wide bandwidth, the *MFS-06* has good low-noise characteristics (Figure 4.04b) and low temperature drift of input offset voltage and offset current and a very stable transfer function over temperature and time

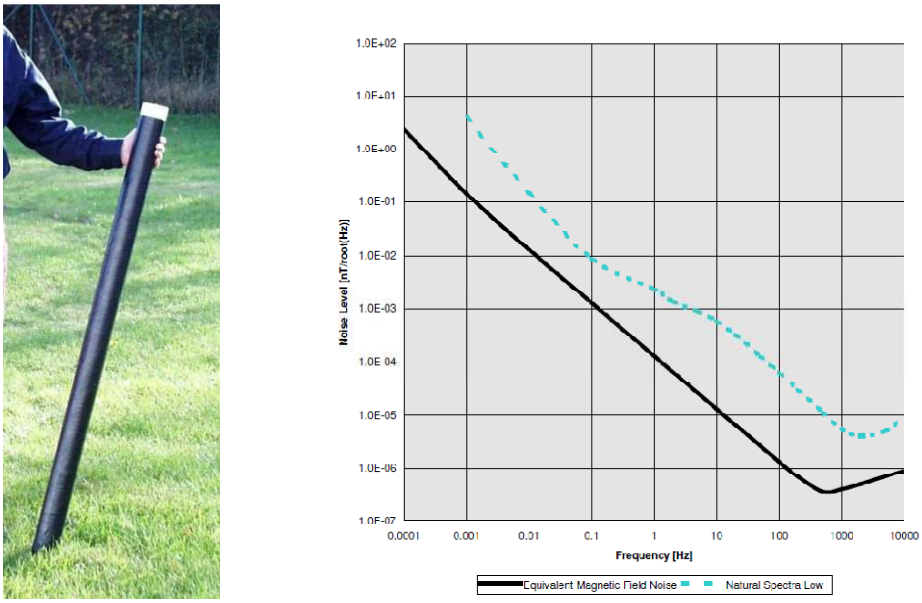

Figure 4.04: (left) Induction coil magnetometer. (Right)Typical noise chart of the MFS-06 in comparison with the natural magnetic field variations on a quiet day (taken from metronix manual)

Induction coil sensors (also called search coil sensors, pickup coil sensors and magnetic antennae) are one of the oldest and most well-known types of magnetic sensors. Induction coil works on the principle of the Ampere's law. that relates , a wire carrying a current generates a magnetic field $\vec{B}$ whose magnitude and direction at each point in space depend on

the length and shape of the wire, the current flowing through the wire, and the location of the point at which the field is determined. Induction coil sensors do not measure the magnetic field itself but its time derivative. This is expressed in the law of induction: results from the fundamental Faraday's law of induction

$$V = n \cdot \frac{\mathrm{d}\Phi}{dt}, \tag{4.3}$$

where V is the induction voltage, Φ is the magnetic flux passing through a coil with an area A and number of turns n. The flux which flows through one loop of the coil is calculated as,

$$\phi = B.A = \mu_0 . \mu_C . H . A \tag{4.4}$$

where, μ_0 and μ_C are the permeability constant and permeability of the core respectively. A is the crossection of the core. $H = H_0 e^{i\omega t}$.

Large coil sensitivity can be obtained by using a large number of turns and large active area A. Along the coil axis, if the origin of the coordinates is taken at the center of the coil and if the z axis is taken along the coil axis, the magnitude of the magnetic field B, which points in the z direction, is given by *Biot-Savart's* law

$$B = \frac{\mu_0 n a^2 I}{2(a^2+x^2)^{3/2}}. \tag{4.5}$$

The unit of B is Tesla, if $\mu_0 = 4\pi \times 10^{-7}$ is the vacuum permeability, n is the number of turns of the field coil, I is the current in the wire, in amperes, a is the radius of the coil in the meters and x is the axial distance in meters from the centre of the coil. For a sinusoidal magnetic field, which can be written with a phase as $H = H_0 e^{i\omega t}$. The induced volage of the sensor output becomes

$$\tilde{V}_{ind} = \tilde{V}_{ind}.\ e^{i\omega t} = i.2\pi.n.\mu_0 . \mu_C . A . f . H_0 e^{i\omega t}, \tag{4.5}$$

The term $S = 2\pi.n.\mu_0 . \mu_C . A$ is defined as the sensor's sensitivity constant which gives the relation between magnetic field's amplitude and the induction voltage.

Induction coil magnetometers are very sensitive to motion of the wires connecting the sensors to the data acquisition unit, especially the cable near the sensor. Induction coil should be located more than 5m apart from the recording system. To prevent vibrations due to wind, the horizontal coils are buried in shallow trenches. Coils are aligned in the N- and E-directions and leveled by means of sensitive level bubbles. Burying the coils has the added

advantage of reducing thermal transients and the resulting noise. The vertical induction coil is buried vertically to the extent possible (approximately 75% of its total length). Induction coils are laid at least 10-15 m away from each other in different quadrants to avoid electromagnetic cross talk between the coils.

Data Acquisition Unit

MT data are usually acquired using high precision, high dynamic range data loggers having a 24/16-bit Analog to Digital Converter (ADC). Analogue and Digital Unit (ADU) comprising the ADC is the core unit of a measurement system. For the present field survey, we have used ADU-06 system (Figure 4.05) of M/s Metronix, GmbH, Germany. ADU-06 is a 24-bit Geophysical Measurement system GMS-06 containing 6 channels. Two electric and three magnetic field sensors can be connected directly to it for respective field recording. The system is synchronized by an internal GPS controlled precision clock. Data are stored on a flash-disk and then downloaded on the hard disk of the connected computer through a network connection. The control of the ADU is done either by the communication package GMS207b or by data preprocessing software, Mapros(M/s Metronix, GmbH, Germany).

Figure 4.05: Figure showing ADU-06 MT data acquisition system

The ADU-06 system operates in several frequency bands designated as HF, LF1, Free, LF2 and LF3. In addition to these bands, further low frequency bands LF4 and LF5 can be created from LF3 data through digital filtering. The highest frequency data are recorded in the HF band and the lowest frequency data are contained in LF5 band. Table 4.01 shows different frequency bands and their respective sampling frequencies.

Table 4.01: Table showing different recorded frequency bands in ADU-06 & their sampling frequency

S. Nr.	Band name	Sampling frequency (Hz)	Frequency range (Hz)	Typical recording duration
1	HF	40,960	20,000-500	7 seconds
2	LF1	4096	1,000-10	5 minutes
3	Free	512	120-5	15-30 minutes
4	LF2	64	30-1	1-2 days
5	LF3	2	1-0.1	3-7 days
6	LF4	0.5	0.2-0.01	by digital filter
7	LF5	0.125	0.05-0.00025	by digital filter

MT instrumentation has improved significantly in recent decades in terms of its portability, electronics and optimization of noise characteristics.

4.1.4 Sources of noise

MT signals are in general very weak (electric field of a few mV/km and magnetic field of a fewnT) compared to artificial sources of electromagnetic noise such as power lines. Therefore, it is necessary to take extreme precaution while selecting and setting up a MT site. Some of the possible sources of artificial and natural noise are:

- Electric power lines (both domestic and high tension power lines) as well as generators
- Water pumps
- Ground vibrations due to vehicular movement (road and rail)
- Underground pipelines
- Water flow in nearby rivers/canals
- Ground vibrations induced by tree roots due to wind

An ideal MT site should be far away from these noise sources to avoid data corruption leading to bad data quality. Topographic undulations also can induce noise in the data. Since the telluric currents flow parallel to the ground surface the electric current can converge or diverge causing additional galvanic effects in the observed data. Incorrect orientation of electric and magnetic sensors can also affect the accuracy of acquired MT data and influence

the impedance tensor in the same way as near surface inhomogeneities do (Zhang *et al*. 1987; Groom & Bailey, 1989, 1991; Pedersen, 1988).

4.1.5 Data acquisition

We planned to acquire broadband MT time series data up to 4096s (maximum recordable limit of MFS-06) along the profile (Figure 4.01) with recording duration of 5-7 days at every site using induction coils. The long duration of recording was selected to achieve better signal to noise ratio and to overcome the dead band problem. For the present purpose, we recorded data in HF, Free-512, LF1, LF2 and LF3 bands for 7s, 30 minutes, 12-24 hours and 5-7 days, respectively. Many repeat runs of HF, LF1 and free bands were performed at every site to ensure good data quality. The low frequency signals designated as LF4 and LF5 were obtained through digital filtering.

We took precaution to the extent possible in site selection and tried to go away from the roads as power lines were fallowing the roads. In many instances, rugged topography and deep valleys posed challenge to site selection efforts. Generally, it was difficult to get suitable MT sites due to the presence of numerous power lines in the foothill region, rugged topography and deep valleys in the lesser and higher Himalaya. Besides, the presence of many existing and upcoming hydropower projects along the Tista River further constrained site selection. Maximum portion of the profile area lies in deep V-shaped valleys and forest area. We performed magnetic sensor test and dry run before the start of the fieldwork to ensure proper functioning of the equipment in field for good data quality. In additon, we tested signal quality by recording test jobs and analysing the noise levels in the recorded time series before submitting long duration runs. The noise level can be analysed in terms of drift in the amplitudes of E_x and E_y fields, coherency betweenelectric and magnetic fields and power spectra for possible electric powerlines noise.

We acquired MT data along the profile in four different field sessions during 11/2008 - 01/2011. The detailed schedule of the MT field survey is given Table 4.2. We tried to acquire the vertical magnetic field data at most sites but at some sites, e.g. those in north Sikkim, digging of about 0.6-0.7m to plant the vertical coil could not be performed due to difficulty in cutting hard rocks and depleted oxygen levels insufficient to take up this laborious tasks. At these sites, we recorded only horizontal components of the magnetic field. GMS206b

package was used to submit jobs to ADU-06 and to retrieve data. A brief description of the work carried out during various field sessions is mentioned below.

Field Session 1:

In the first field session, we started MT data acquisition from the southern end of the Main Central Thrust Zone. We first installed one site at Namprikthang (SK01) and then proceeded towards the LHD, i.e. towards south of the MCTZ. Geographically the region falls in the North and South districts of the Sikkim state. A total of 19 broadband MT stations were installed during this field session. The sites, Namprikthang(SK01), Namprik (SK02), Gyathang (SK03), Lindong (SK04), Gon-samdong (SK05) and Dikchu (SK06) are located in highly rugged terrain and restricted/protected areas of North Sikkim. The site Dichu is located near a water reservoir where tributaries of Tista, Dik and Chu merge with the main Tista river. At the site Lingdong, acquisition was done for 3 days due to unavailability of the site for one week. The other sites Lingee (SK07), Tonak-Makha (SK08), Yangang (SK09), Chuba Parbing (SK10), Mangley (SK11), Namchi (SK12), Temi (SK13), Yangang-II (SK14), Rollu (SK15), Rongtu (SK16), Kitam (SK17), and Tarku (SK18) are located in South Sikkim. It was difficult to get good sites in South Sikkim due toseveral existing hydropower projects (on Rangit river) and power lines. The sites Kitam, Rollu and Chuba-Parbing are situated within or close to the Rangit window (RW), where Gondwana rocks are exposed in the tectonic window bounded by a thrust known as Ramgarh Trust (RT). Preliminary preprocessing of the data set indicated that at some sites the recorded MT time series were corrupted by cultural as well as electrical noise, particularly at Namchi, Temi, Tarku, and Chuba-Parbing. Data quality at other sites was good.

Field Session 2:

In this field session, we proceeded towards the northern side of SK01 to cover the HHC region. The region is mostly covered by dense forests and deep V-shaped valleys with rugged topography up to the site Zeema (SK34) beyond which the topography becomes smooth. This is one of the geographically challenging areas where the topography suddenly increases from 900 m to about 5km. The Oxygen levels are also low above 4 km altitude. This was the toughest field session among the all. During this field session, we covered a total of 12 broadband MT sites and a few long period sites also using fluxgate (FG) magnetometer. These are Rollu (SK25-FG), Guigong (SK26), Upper Chuba (SK27), Lingza (SK28), Ford-

Bay (SK29), Zeema (SK30), Samdong (SK31), Thanggu (SK32), Guigong (SK33), Lachen (SK34), and Gurudongmar (SK36).The sites Lingza and Ford Bay within MCTZ, located in the Kangchendzonga reserve forest area, were difficult to access because of the inaccessible rugged mountainous terrain with dense forest cover. From Lachen onwards the area was free from power lines and, therefore, the data quality at these locations is considerably good.

Field Session 3:

In this field session, we recorded broadband MT time series data at 10 sites situated in the Ganga Foreland Basin (GFB) comprising alluvium and Sub Himalayan Domain (SHD) comprising Shiwaliks. These are Nazukbasti (SK40), Mongphong (SK41), Kuduvitta (SK43), Fakirdeep (SK44), Nunujote (SK45), Panigatta (SK46), Rohini (SK47), Rongchung (SK48), and Rombuk (SK49). The Data quality at most of the sites is good.

Field Session 4:

Since the first field session was conducted during the Solar minimum, we performed repeat measurements at four sites (marked in purple color in Table 4.02) covered during the previous field sessions to check if the solar minimum caused significant deterioration of the data quality. From preliminary preprocessing of recorded data we didn't see any considerable variations in the MT impedance tensors. The sites covered during this period were Gurudongmar (SK52), Thumbuk (SK54), Gyathang (SK56), Tingkyong (SK59), Kitam (SK63), Tarku (SK64), Makha-2 (Hxy, SK65), and Makha-2 (Exy, SK66).

In all, we had setup 48 MT sites along the profile. Some of these sites were winded up either due to bad data quality or due to local problems. The MT sites covered along the profile are listed in Tabel 4.02

4.2 Preprocessing of the data

Once the MT time series are recorded, these are downloaded to personal computer/laptop for preprocessing. In the present acquisition system (ADU-06) time series are recorded in different bands in binary format with file extension *.ats (adu time series). A sample time series is shown in Figure 4.06

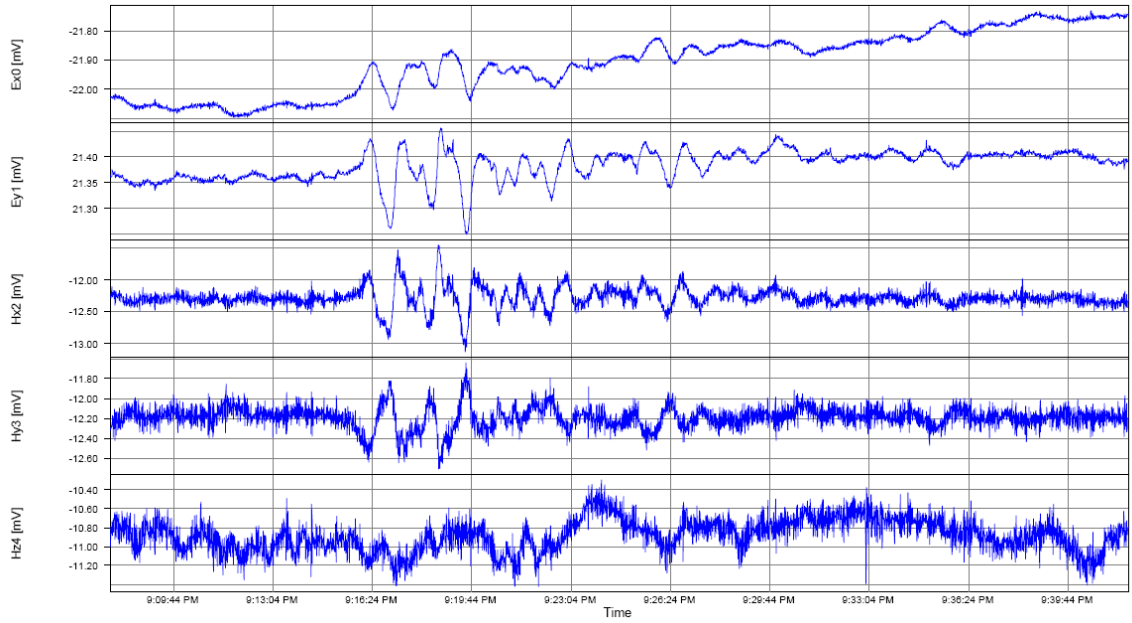

Figure 4.06: Time-series of LF3 band for the site SK22 with FFT length 4096 and sampling frequency 2Hz

The measured time series data contain the signal (induction response of the subsurface structure) as well as natural and cultural noise. It is therefore necessary to improve the signal-to-noise ratio by removing spikes and bad data segments as well as those segments corrupted by coherent electric noise. Once this is performed steps are followed to estimate impedance tensors and magnetic transfer functions (Impedance tensor and geomagnetic transfer function) as well as some other diagnostic parameters such as skewness, coherency from time series data. The following main steps are involved in preprocessing of MT time series:

1. Removal of spikes, bad data segments
2. Sub-dividing time series into different segments of finite sample length e.g. 4096 samples
3. Windowing and FFT of these data segments and parzening to get spectral estimates at selected frequencies
4. Estimation of impedance tensor and magnetic transfer function for each segment
5. Stacking of these impedance tensors (magnetic transfer functions) to get mean and standard deviation of these values at different frequencies
6. Estimation of rotation angle (preliminary), skew, tipper, etc.
7. Estimation of apparent resistivity and phase and their standard deviations from impedance tensor

The recorded time series of all sites were pre-processed to obtain impedance tensor and apparent resistivity and phase as a function of frequency. We have used commercial time series processing software MAPROS (M/s Metronix GmbH) for this purpose. The recorded $*.ats$ files are imported in MAPROS after creating proper configuration, sensor, and setup files. The header of each site is checked for site name, channel configuration, dipole length and other header information. The time series were then visually inspected and spikes/bad data segments were masked. The good data segments were used to estimate complex impedance tensor. The package provides various stacking options (such as selective stacking, stack all, and coherency threshold), windowing and window length options that can be tried to estimate the optimum estimates. Selective stacking in general gives good results and has been used in the present study. In some cases, we had to record LF3 band data in contiguous segments for example when the recording was abruptly stopped due to battery or cables problem. In such cases, we used Time Series Manipulation program (TSMP) (M/s Metronix, GmbH, Germany) to stitch contiguous data of the same frequency band to form a long-duration time series.

The estimated impedance tensors were used to compute apparent resistivity (ρ_{xy}, ρ_{yx}) and phase (ϕ_{xy}, ϕ_{yx}) curves as a function of frequency (eqs. 3.28 & 3.29) along with their standard deviations. The estimated apparentent resisvtivity and phase curves are good for most sites but the quality of these data at sites, especially those located within LHD, is bad with large error bars and low coherency. This is most likely due to the presence of large electrical noise caused by numerous high tension power lines emanating from hydroelectric projects in the region. After preprocessing of the datasets and discarding the sites having bad data quality we finally get 31 sites for which computed apparent resistivity and phase curves are of good quality. The final 31 sites selected for detailed analysis and inversion are tabulated in Table 4.03 and shown in Figure 4.07 as red colored stars.

Figure 4.07 shows some data gaps. The large gaps between sites SH16 and SH17, and SH26 and SH27 are due to the inaccessibility of the area. Starting from the southern end of the profile the inter-station spacing is good up to site SH08 but a large gap between site SH08 and SH09 is due to the inaccessibility of the area lying between these two sites. Large gaps within LHD are due to discarding of sites with poor quality data.

Observed apparent resistivity and phase curves for some sites are shown in Figure 4.08. A long duration of recording helped in obtaining consistent apparent resistivity and phase

curves in the MT dead band (1-10s) and would be useful in the future in extracting information for the periods exceeding 1000s.

Interestingly, at some sites, estimated phase data shows anomalous behavior. The obtained impedance phases are exceeded 90˚ for the sites SH13, SH15, SH17, SH19, SH26 and SK39. The apparent resistivity and phase curves for SH26 are shown in Figure 4.08c to illustrate the anomalous phase behavior. Here, the phase ϕ_{yx} starts rising steeply at around 0.5s period and exceeds 90˚. Interestingly these sites are located in the vicinity of major geological discontinuities e.g. MFT/MBT, RT, MCT-1, MCT-2, and STDS. Such anomalous phases have been earlier interpreted in terms of strong current channeling either due to localized 3-D conductors (e.g. Weckmann *et al.* 2003; Ichihara & Mogi, 2009) or due to the presence of shallow 2-D anisotropic blocks (e.g. Pek & Verner, 1997; Heise & Pous, 2003). The effects of current channeling can be minimized by distortion and/or decomposition techniques provided that the effect is caused by local shallow heterogeneities/conductors. The detailed study of this behavior is discussed in subsequent chapters.

Table 4.03: List of final MT sites with site codes to be used in the detailed analysis and inversion

S. N.	Site	Code	Lat. (deg.)	Long. (deg.)	S.N.	Site	Code	Lat. (deg.)	Long. (deg.)
1	Kusiari	SH01	26.3	88.3	17	Rongtu	SH18	27.3	88.4
2	Birpur Colony	SH02	26.4	88.2	18	Yangang-II	SH19	27.3	88.4
3	Jalalgacchah	SH03	26.4	88.2	19	Tonak-Makha	SH20	27.3	88.5
4	Pitepada	SH04	26.5	88.2	20	Kapirthang	SH21	27.4	88.5
5	Bukdhala	SH05	26.5	88.2	21	Gyathang	SH22	27.5	88.5
6	Kuduvitta	SH06	26.6	88.2	22	Tingkyong	SH23	27.5	88.5
7	Fakirdeep	SH07	26.6	88.3	23	Lingdong	SH24	27.5	88.5
8	Nunujote	SH08	26.7	88.3	24	Nampriktham	SH25	27.5	88.5
9	Phanigatta	SH09	26.8	88.2	25	Lingza	SH26	27.6	88.5
10	Rohini	SH10	26.8	88.3	26	Ford Bay	SH27	27.6	88.4
11	Mongphong	SH11	26.9	88.5	27	Lachen	SH28	RS	RS
12	Rhombhuk	SH12	26.9	88.3	28	Zeema	SH29	RS	RS
13	Nazukbasti	SH14	27.0	88.4	29	Samdong	SH30	RS	RS
14	Rollu	SH15	27.1	88.4	30	Thanggu	SH31	RS	RS
15	Kitam	SH16	27.1	88.3	31	Guigong	SH32	RS	RS
16	Upper Chuba	SH17	27.2	88.4	RS – The sites is located in the restricted area				

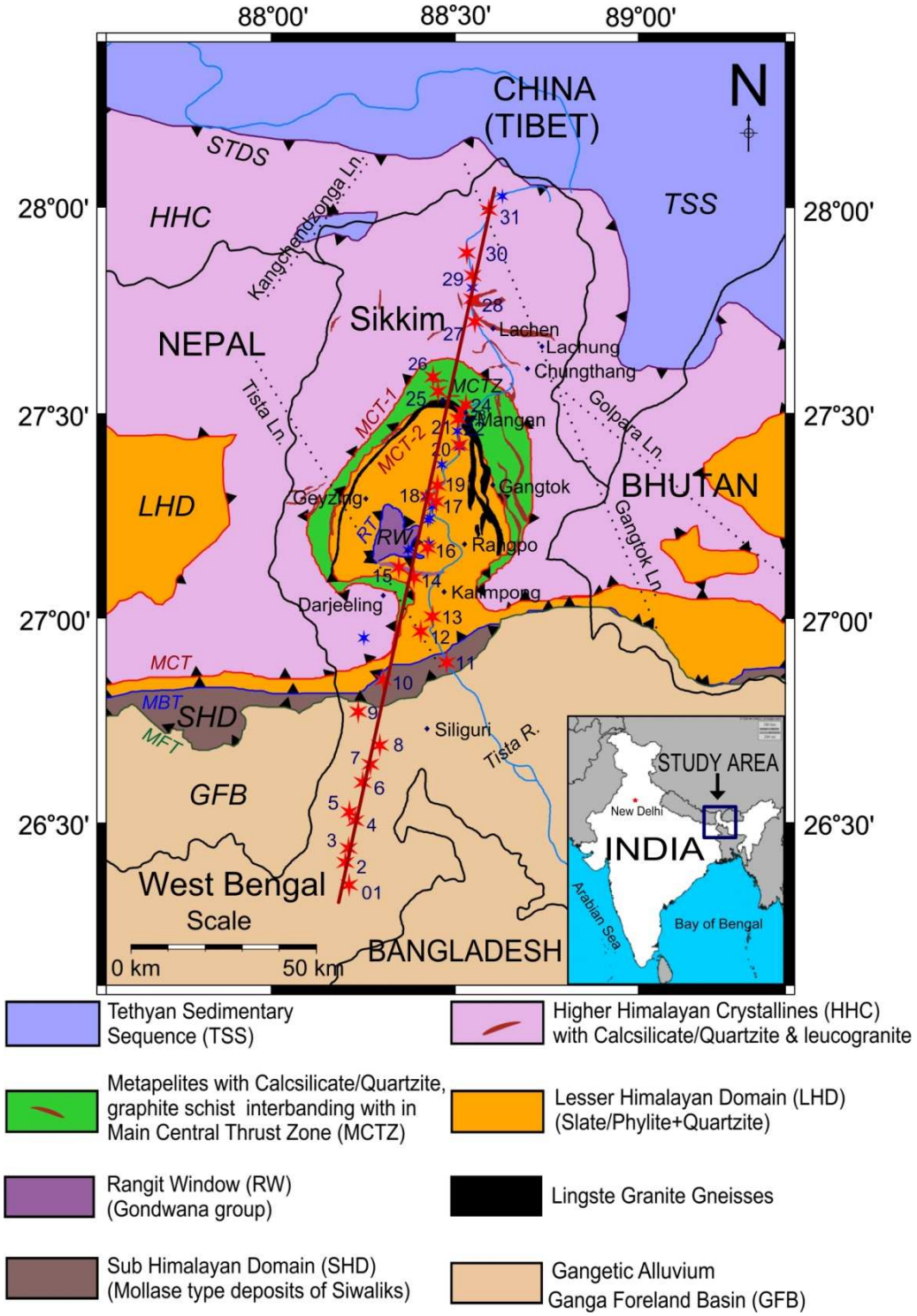

Figure 4.07: Map showing locations of the final 31 MT sites (red colored stars) and considered profile along with discarded sites (blue stars)

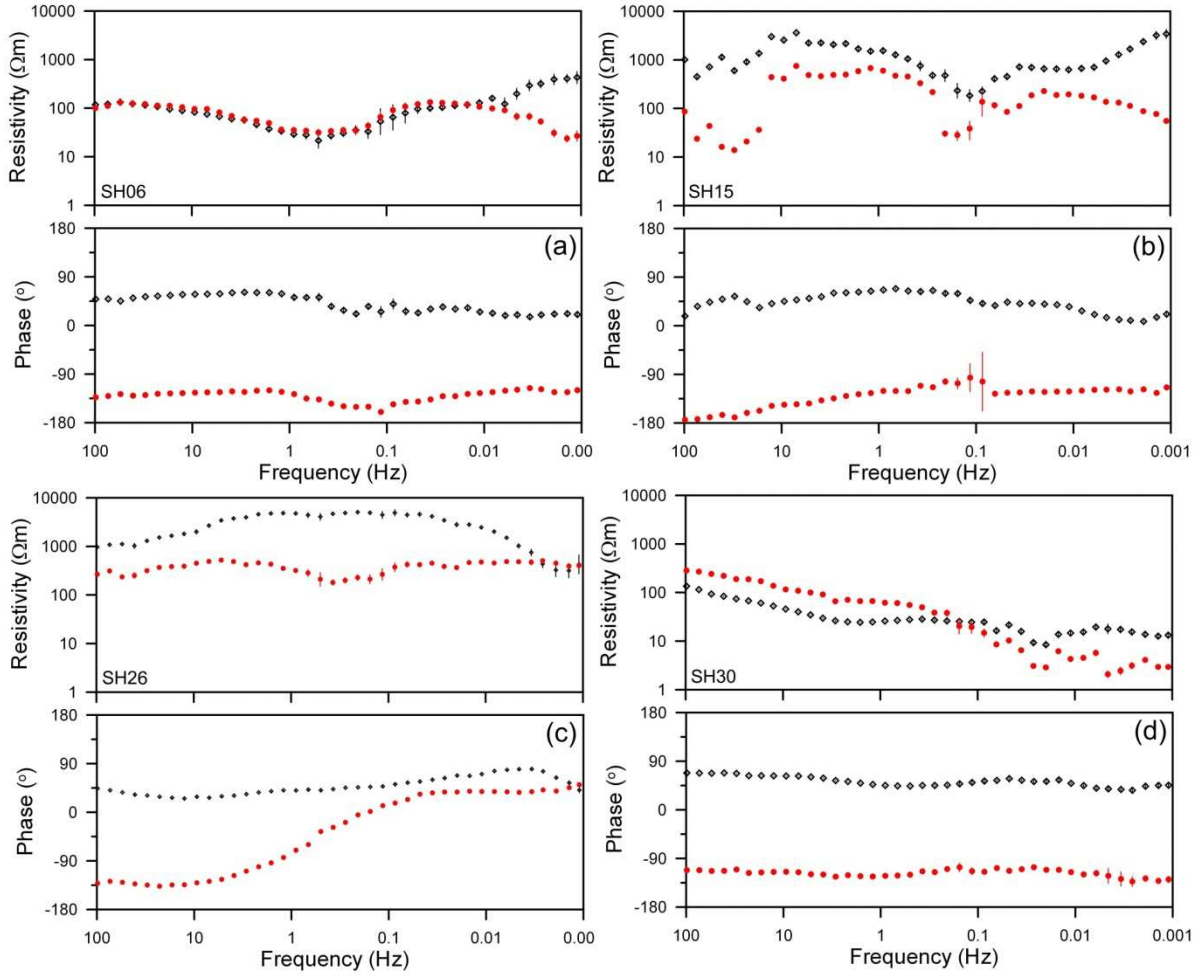

Figure 4.08: Apparent resistivity and phase curves for some sites along the profile

After preprocessing the data the results are exported in EDI (Electronic Data Interchange) file format (Industry-standard file format for handling impedance tensors obtained after processing of MT time series data) comprises four components of complex impedance tensor (Z_{xx}, Z_{xy}, Z_{yx},Z_{yy}) along with their variances, two components of complex tipper (T_x,T_y) and spectral values. The **.edi* file also contains details of site, latitude, longitude, elevation etc. Once the edi files are prepared, the next important step is to analyze transfer functions for dimensionality (1-D, 2-D or 3-D) and directionality (current flow direction/ principal axes of the impedance tensor). However, impedance tensors are generally corrupted by local heterogeneities, galvanic and inductive effects leading to distortions. The foremost step before estimation of nature of the subsurface is minimization of these distortions and estimation of realistic values of MT transfer functions representing subsurface structure.

Types of distortions and techniques to eliminate these distortions are discussed in the next chapter including regional strike analysis.

4.3 Summary

Magnetotelluric field survey has been carried out in the Sikkim Himalaya along an approximately N-S profile cutting various geotectonic domains of the region in four field sessions. In this duration we acquired MT data of about one week duration at 49 sites using metronix made data acquisition system. The acquisition system comprises ADU-06 recording system, Pb-$PbCl_2$ electrodes and induction coil magnetic field sensor (MFS-06). MT transfer functions of broad frequency range (0.001-1000s) are computed after preprocessing of the data at 49 sites. We finally choose 31 sites for further analysis and modeling of the data.

The observed impedance tensor is generally distorted by local heterogeneities causing galvanic distortions. We, therefore perform distortion analysis before finding the regional strike of the region needed for 2-D interpretation of the region. The next chapter describes distortion analysis carried out in the region and estimation of regional strike direction followed by brief description of distortion analysis techniques used in this purpose.

Table 4.02: MT sites covered along the profile in different field seasons

S.N.	Site Name	Site Code	Profile Code	Lat. (deg.)	Long. (deg.)	Mag. declination	Elev. (m)	No. of days	Local geology-geological sub-domain	Geographical description of the area
1	Namprikthan	SK01	SH25	27.5	88.5	0'W	741	8	Mixture of low-high grade metamorphic rocks, mainly gneiss-MCTZ	Protected & Kangchendzonga Reserve Forest area (KRF), North Sikkim (NSK)
2	Lingdong	SK02	SH24	27.5	88.5	0'W	898	3	MCTZ	Protected area, NSK
3	Gyathang	SK03	SH22	27.5	88.5	1'W	941	7	Schists-LHD	Protected area, NSK
4	Namprik	SK04	XXXX	27.5	88.5	1'W	1213	1	Gneisses-MCTZ	Protected & KRF area
5	Gan-Samdong	SK05	XXXX	27.5	88.5	1'W	;968	5	Schists-LHD	Protected area
6	Dikchu	SK06	XXXX	27.4	88.5	1'W	579	5	Mica schist-schist LHD	Protected area, Near the bank of Chu river
7	Lingee	SK07	XXXX	27.4	88.5	1'W	1268	7	Schists-LHD	School Ground, South Sikkim(SSK)
8	Tonak-Makha	SK08	SH20	27.3	88.5	1'W	438	7	Schists- LHD	Situated in Tista river valley, SSK
9	Yangang	SK09	XXXX	27.3	88.4	2'W	1268	5	Schists- LHD	Open Fields, SSK
10	Chuba-Parbing	SK10	XXXX	27.2	88.4	2'W	1637	7	Schists-LHD	Fields, SSK
11	Mangley	SK11	XXXX	27.3	88.4	2'W	376	2	Schist-LHD	Fields, SSK
12	Namchi	SK12	XXXX	27.2	88.4	2'W	1191	6	Siwaliks-RW	Fields, West Sikkim (WSK)
13	Temi	SK13	XXXX	27.2	88.4	2'W	1397	2	Schists-LHD	Tea estate ,SSK
14	Yangang-II	SK14	SH19	27.3	88.4	3'W	914	5	Schists-LHD	Fields (SSK)
15	Rollu	SK15	SH15	27.1	88.4	2'W	204	9	Schists-LHD	Rangit river valley (SSK)
16	Rongtu	SK16	SH18	27.3	88.4	2'W	37774	7	Schists-LHD	Tista river valley (SSK)
17	Kitam	SK17	SH16	27.1	88.3	2'W	779	7	Siwaliks-RW	Bird Century (SSK)
18	Tarku	SK18	XXXX	27.2	88.4	1'W	1146	7	Schists-LHD	Tea estate (SSK)
19	Guigong	SK19	XXXX	RS	RS	3'W	4668	2	Highly metamorphosed- Gneisses-HHC	Restricted area, North Sikkim
20	Upper Chuba	SK20	SH17	27.2	88.4	1'W	1810	7	LHD	Forest area, SSK
21	Lingza	SK21	SH26	27.6	88.5	3'W	1013	10	Mixture of schists and gneisses MCTZ	Protected KRS area, dense forest, NSK
22	Ford-Bay	SK22	SH27	27.6	88.4	0'W	1574	8	Mainly schists and Gneisses, Graphite schista are also seen-MCTZ	Protected KRF, dense forest, arrived at site after one hour walk from country road,NSK
23	Samdong	SK23	SH30	RS	RS	0'W	3536	9	High grade gneisses-HHC	Restricted area,NSK
24	Thanggu	SK24	SH31	RS	RS	0'E	3858	8	Gneisses-HHC	Restricted area, High altitude. Site is located in a river channel valley
25	Zeema	SK25	SH29	RS	RS	0'E	3108	7	Gneisses-HHC	Restricted area, NSK
26	Lachen	SK26	SH28	RS	RS	1'E	2581	6	Gneisses-HHC	Restricted area, near to river side,NSK

27	Guigong	SK19	SH32	RS	RS	1'E	4668	9	HHC, Near to TSS	Restricted area, Low oxygen level due to high altitude,NSK
28	Gurudongmar	SK27	XXXX	RS	RS	0'E	4869	6	Near to TSS	Restricted area, Low oxygen level due to high altitude,NSK
29	Nazukbasti	SK28	SH14	27.0	88.4	4'W	159	10	Intermediate grade Metamorphic rocks-SHD	Darjeeling, West Bengal
30	Mongphong	SK29	SH11	26.9	88.5	5'W	111	10	SHD	Darjeeling, West Bengal
31	Pitepada	SK30	SH04	26.5	88.2	7'W	39	8	GFB	Darjeeling, West Bengal
32	Kuduvitta	SK31	SH06	26.6	88.2	7'W	70	5	GFB	Darjeeling, West Bengal
33	Fakirdeep	SK32	SH07	26.6	88.3	5'W	78	6	Gangetic alluvium - GFB	Darjeeling, West Bengal
34	Nunujote	SK33	SH08	26.7	88.3	5'W	99	6	GFB	Darjeeling, West Bengal
35	Phanigatta	SK34	SH09	26.8	88.2	5'W	177	8	GFB	Darjeeling, West Bengal
36	Rohini	SK35	SH10	26.8	88.3	4'W	451	8	LHD	Darjeeling, West Bengal
37	Rongchung	SK36	SH11	27.0	88.4	4'W	339	5	SHD	Darjeeling, West Bengal
38	Rhombhuk	SK37	SH12	26.9	88.3	4'W	1592	6	LHD	Darjeeling, West Bengal
39	Gurudongmar	SK27	SH33	RS	RS	2'W	4869	6	Near to TSS	Restricted area
40	Thumbuk	SK38	XXXX	RS	RS	2'W	3015	1	Gneisses-HHC	Restricted area
41	Tingkyong	SK39	SH23	27.5	88.5	3'W	941	7	Schists- LHD	Protected area
42	Kapirthang	SK40	SH21	27.4	88.5	3'W	611	9	Schists- LHD	Protected area
43	Kitam	SK17	SH16	27.1	88.3	3'W	779	8	Siwaliks- RW	Kitam Bird century
44	Gyathang	SK03	SH22	27.5	88.5	2'W	941	1	Schists and small quanity of Gneisses	Protected area
45	Tarku	SK18	XXXX	27.2	88.4	2'W	1121	1	Schits - LHD	Tea estate, SSK
46	Birpur Colony	SK41	SH02	26.4	88.2	6'W	25	6	Gangateic alluvium, GFB	Darjeeling, West Bengal
47	Kusiari	SK42	SH01	26.3	88.3	7'W	25	6	Gangateic alluvium-GFB	Darjeeling, West Bengal
48	Bukdhala	SK43	SH05	26.5	88.2	6'W	22	6	Gangetic alluvium – GFB	Darjeeling, West Bengal
49	Jalalgacchah	SK44	SH03	26.4	88.2	6'W	34	6	Gangetic alluvium – GFB	Darjeeling, West Bengal

RS – The sites is located in the restricted area; The purple color names indicates the sites reacquired during high solar activity period

Chapter 5

Distortion and strike analysis

5.1 Introduction

In chapter 3 the procedure for reliable estimation of impedance tenor **Z** is described. Following that approach, MT transfer functions of all sites along the profile have been estimated. An accurate interpretation of MT data requires understanding of the distortions and dimensionality in the observed transfer functions. In general, MT transfer functions are affected by perturbations in the regional electric field due to the accumulation of electric charges at the boundaries of geological heterogeneities. These perturbations are referred as galvanic distortions. Static shift is one such distortion wherein accumulation of boundary charges reduces or enhances the total electric field (Vozoff, 1991; Berdichevsky *et al.* 1989; 1998, Simpson & Bahr, 2008). The effect of static shift is seen in apparent resistivity curves, plotted on log-log scale, as one of the curves is shifted downward (or upward) when near-surface heterogeneities below the measurement site are conductive (or resistive). This happens because the boundary charges in the presence of a conductive inclusion create a secondary field that is antiparallel to the regional field reducing the net field strength and hence downward shifting of apparent resistivity curve. The remarkable feature of the static shift is that it does not distort impedance phase curves since the secondary galvanic electric field due to the inhomogeneity is in-phase with the charging field. The static shift behavior can be treated as scaled multiplication of each of the MT responses by a real parameter (Chave & Smith, 1994). Inductive effects can also distort MT transfer functions. In the inductive effect, the time derivative of the primary magnetic field induces excess currents. These vortex currents flowing in the closed loop produce secondary magnetic field that adds to the primary magnetic field. The time derivative of the magnetic flux in the Faraday law results in the inductive response being an explicit function of frequency. This differs from the galvanic effect that is independent of frequency. Another major difference between the two

(The work in the chapter is published in Tectonophysics, 2013)

effects is the underlying lead role of the electric field in galvanic distortion in contrast to that of the magnetic field in inductive effect (Jiracek, 1990).

The distortions of regional electric field by local structures are arguably the greatest bane of MT method and affect the quality of interpretation. Therefore, removal of these distortions and recovery of the responses related to the regional structure is necessary before inverting the acquired data for subsurface conductivity distribution. In general, the subsurface structure is more complex than a simple 1-D layered model. For regions having structures with preferred geological strike, MT data can be interpreted in terms of 2-D models and the regional strike of the subsurface structures can be estimated from the observed data. Several approaches have been proposed for this purpose. In conventional analysis, the strike angle is estimated by minimizing the diagonal elements of the impedance tensor (Swift, 1967; Sims & Bostick, 1969; Vozoff, 1974), as discussed in chapter-3. In the decomposition procedures proposed by Zhang *et al.* (1987), Bahr (1988) and Chakrade *et al.* (1992), the linear dependence of the columns of the impedance tensor is also used to estimate the regional strike. However, these methods are unstable in the presence of noise or strong distortions since some of the elements of the tensor can be small in magnitude and dominated greatly by these errors, producing significant errors in the estimate of the regional strike (Jones & Groom, 1993). Therefore, some advanced methods (Larsen, 1977; Zhang *et al.* 1987; Bahr, 1988; Groom & Bailey, 1989, 1991; Chave & Smith, 1994; MacNeice & Jones, 2001) have been proposed to simultaneously minimize the effects of shallow, small-scale galvanic distortions and estimate the regional-scale rotation angle that (or its orthogonal direction) can be treated as regional strike direction. These decomposition methods assume a-priori that the regional structure is 2-D in nature. Some other methods have also been developed avoiding any a-priori assumption on the dimensionality of the structure. These are directionality and dimensionality of the impedance tensor by phase tensor approach (Caldwell *et al.* 2004), decomposition of impedance tensor considering electric polarization states and ellipticity criteria of telluric currents (Becken & Burkhardt, 2004), and dimensionality analysis by Mohr diagram technique (Lilley, 1993, 1998; Lilley & Weaver, 2010).

The literature on extraction of regional MT impedance tensors from distorted observed data is vast. Therefore, in this chapter I briefly describe only the methods that are used in the present work and then present the results on decomposition and strike analysis of the Sikkim profile data.

5.2 Decomposition approaches used in the present study

We have applied LaTorraca (LaTorraca *et al.* 1986), Groom-Bailey (Groom & Bailey, 1989, 1991; McNeice & Jones, 2001) and phase tensor (Caldwell *et al.* 2004) decomposition techniques to the MT data of the Sikkim Himalaya profile. These techniques are briefly discussed below.

5.2.1 LaTorraca decomposition (LT approach)

The Impedance tensor eigen state problem has been advanced by Swift (1967), Sims & Bostick (1967), Eggers (1982), Spitz (1985), LaTorraca *et al*. (1986), Counil *et al.* (1986) and Yee & Paulson (1987). Basically these methods determine the eigen state of 3-D impedance tensor so that the solution obtained satisfies one of the inherent properties of the 2-D impedance tensor. In this section, I restrict myself to brief description of decomposition method proposed by LaToracca *et al.* (1986).

For an ideal 2-D case, the electromagnetic field is split into two separate modes, in each of which the electric and magnetic field components are orthogonal, respectively. Therefore, the diagonal elements of the impedance tensor vanish if the coordinate axes are rotated in the reference frame of the regional strike. Eggers (1982) presented an approach for analyzing impedances using an eigen state parameterization, which uses all elements of the impedance tensor. His eigen state formulation implies that electric and magnetic field polarizations are always orthogonal. This however may not hold true in the case of distortion effects mentioned in the previous section and/or in a complex geoelectric environment. LaTorraca *et al.* (1986) have suggested a new mathematical decomposition of the impedance tensor that retains all the information contained in the four complex impedances ($Z_{xx}, Z_{xy}, Z_{yx}, Z_{yy}$) which overcomes this obstacle. It is based on the SVD (singular value decomposition) approach of Lanczos (1961).

Linear mapping of horizontal components of magnetic ($\vec{\mathrm{H}}$) and electric fields ($\vec{\mathrm{E}}$) at a site can be expressed in frequency domain as

$$\vec{\mathrm{E}} = \bar{\mathbf{Z}}\,\vec{\mathrm{H}}, \tag{5.1}$$

where $\vec{\mathrm{E}}$ and $\vec{\mathrm{H}}$ are the complex valued, two component vectors and $\bar{\mathbf{Z}}$ is the MT complex impedance tensor. The SVD of $\bar{\mathbf{Z}}$ results in two-component $\vec{\mathrm{H}}$ vectors h_1 and h_2 and $\vec{\mathrm{E}}$ vectors e_1 and e_2, which are normalized and orthogonal in the sense that $h_i^* h_j = \delta_{ij}$ and

$e_i^* e_j = \delta_{ij}$. Then we can write, $\bar{\mathbf{Z}} h_j = r_j e_j$ and $\underset{\sim}{\mathbf{Z}}\, e_j = r_j h_j$, where $\underset{\sim}{\mathbf{Z}}$ is the transposed conjugate complex of $\bar{\mathbf{Z}}$. The two equations imply that orthogonal magnetic vectors are mapped onto electric vectors which are also orthogonal. The two vectors h_j and e_j are commonly termed as right and left singular vectors respectively with singular values r_j. In matrix notation this relation can be expressed (after SVD approach) as

$$\underset{\sim}{\mathbf{Z}} = \underset{\sim}{\mathbf{U}}_{\mathrm{E}}\, \mathbf{R}\, \underset{\sim}{\tilde{\mathbf{U}}}_{\mathrm{H}}, \tag{5.2}$$

where $R\{r_1, r_2\}$ is the diagonal matrix, $\underset{\sim}{U}_H$ is the 2×2 matrix with h_1, h_2 as columns and $\underset{\sim}{U}_E$ is the 2×2 matrix with e_1, e_2 as columns. LaToracca *et al.* (1986) considered the rotation of $\bar{\mathbf{Z}}$ using two mutually orthogonal magnetic field ($\vec{\mathrm{H}}$) directions for which the associated electric fields **(**$\vec{\mathrm{E}}$**)** are orthogonal to each other but not necessarily orthogonal to the magnetic fields. The deviation of these field directions from orthogonality is defined as the skew angle, given by

$$s = \tfrac{1}{2}\pi - \gamma_H + \gamma_E, \tag{5.3}$$

where γ_{H} and $\gamma_{\mathrm{E}}$are the angles made by the major axis of the electric and magnetic polarization ellipses with the vertical axis, respectively. Decomposition parameters of the MT impedance tensor in this method are external **E/H** ratio amplitudes and their phases, skew angle (direction of the $\vec{\mathrm{E}}$ and $\vec{\mathrm{H}}$ principal axes) and the E and H ellipticities.

5.2.2 Groom – Bailey decomposition (GB Approach)

The Groom-Bailey technique (Groom & Bailey, 1989, 1991) decomposes the magnetotelluric impedance tensor into determinable and indeterminable parts and the system of equations is solved using least squares method to separate the effects of channeling (galvanic effects) from those of induction. Following the assumptions of superposition, magnetotelluric impedance tensor ($\bar{\mathbf{Z}}$) in the principal coordinate system can be written as

$$\bar{\mathbf{Z}} = \boldsymbol{C}\bar{\mathbf{Z}}^r, \tag{5.4}$$

where $\bar{\mathbf{Z}}^r$ is the regional impedance tensor and **C** is a real tensor of rank 2, also known as channeling tensor, which is frequency independent over some range (Bailey & Groom, 1987).

In GB approach, the determinable part of the galvanic distortion is characterized by two galvanic distortion parameters, shear (**S**) and twist (**T**), and induction by the regional strike

and the regional impedances. The site gain (g) and anisotropy tensor (**A**) together form the indeterminable parts of the distortion matrix. The indeterminable quantities are amplitude shifts of the two regional impedances. Usually shear, twist, and strike are iteratively constrained to find frequency-independent estimates required by the decomposition model. Therefore, the distortion tensor **C** can be represented as (Groom & Bailey, 1987)

$$\mathbf{C} = \mathrm{g}\,\mathbf{T}\,\mathbf{S}\,\mathbf{A}, \tag{5.5}$$

where g is a scalar quantity termed as site gain/gain factor/scaling factor, and **T**, **S**, and **A** are twist, shear, and anisotropy tensors, respectively. Twist and Shear tensors are given as:

$$\mathbf{T} = \frac{1}{\sqrt{1+t^2}}\begin{bmatrix} 1 & -t \\ t & 1 \end{bmatrix}; \qquad \mathbf{S} = \frac{1}{\sqrt{1+s^2}}\begin{bmatrix} 1 & s \\ s & 1 \end{bmatrix}. \tag{5.6}$$

The twist parameter ($t = \tan^{-1}\theta_t$) represents rotation of the regional electric field clockwise by an angle θ_t due to additional anomalous currents. **T**is normalized by this twist parameter. Analogues to the theory of shear deformation, the shear tensor S causes maximum angular changes in electric field vectors by shear angle θ_s. The tensor **S** is also normalized by shear parameter $s = \tan^{-1}\theta_s$. Physical meaning is the deflecting of electric field by an angle θ_s clockwise with respect to the x-axis and counter-clockwise for the y- axis. According to Groom & Bailey (1989) both twist and shear angles under maximal telluric deformation should not exceed $|45^o|$.

The site gain g scales the regional electric field without disturbing the direction of the electric field, and the anisotropy tensor $\boldsymbol{A}$ (splitting tensor) scales the electric field along the two regional principle axes by different factors, producing a distortion anisotropy that adds to the regional inductive anisotropy. This distortion anisotropy is experimentally indistinguishable from the regional inductive anisotropy without independent information. The site gain and anisotropy parameters are responsible for the magnetotelluric static shift. The anisotropy or splitting operator, which has the geometrical effect of stretching the two electric field components, in normalized form is

$$\mathbf{A} = \frac{1}{\sqrt{1+a^2}}\begin{bmatrix} 1+a & 0 \\ 0 & 1-a \end{bmatrix}. \tag{5.7}$$

The matrix **A** cannot be determined by the tensor decomposition. It can be removed (or at least reduced) by using the accepted methods (e.g. matching the two impedance curves at high frequencies or matching the impedance to controlled source constraints like time domain

electromagnetic exploration). This factorization of distortion matrix **C** reduces the distortions of regional electric field ($\mathbf{D_e}$) to scale change (g), shear (**S**), twist (**T**), and anisotropy distortions (**A**) given as

$$\mathbf{D_e} = \mathrm{g}\mathbf{TSA}. \tag{5.8}$$

Following the superposition model and considering the basic assumption of the model, we have

$$\bar{\mathbf{Z}}^{\mathrm{s}} = \mathrm{g}\,\mathbf{T}\,\mathbf{S}\,\mathbf{A}\bar{\mathbf{Z}}^{\mathrm{r}}. \tag{5.9}$$

Without normalization, we can write as

$$\mathbf{Z}^{\mathrm{s}} = \mathrm{G}\,\widetilde{\mathbf{T}}\,\widetilde{\mathbf{S}}\,\widetilde{\mathbf{A}}\bar{\mathbf{Z}}^{\mathrm{r}}, \tag{5.10}$$

where, $\boldsymbol{G} = g\frac{1}{\sqrt{(1+s^2)(1+t^2)(1+a^2)}}$ and $\bar{\boldsymbol{Z}}^{r} = \begin{pmatrix} 0 & Z_{xy}^{r} \\ Z_{yx}^{r} & 0 \end{pmatrix}$

The amplitude of the principal impedances differ from true amplitudes by a real valued frequency –independent scalar factors $G\,(1+a)$ and $G\,(1-a)$ which represents the static shift effect of near surface local inhomogeneities, which cannot be determined by the tensor decomposition (Groom & Bailey, 1989b) independently. So absorbing the site gain g and anisotropy $\widetilde{\mathrm{A}}$ into the regional impedance $\bar{\mathbf{Z}}^{r}$, equation in measurement coordinate system becomes

$$\bar{\mathbf{Z}}^{\mathrm{s}} = \mathbf{R}\widetilde{\mathbf{T}}\widetilde{\mathbf{S}}\bar{\mathbf{Z}}^{\mathrm{r}}\mathbf{R}^{\mathrm{T}}. \tag{5.11}$$

Here, $\bar{\mathbf{Z}}_s$ is the measured impedance tensor (superposition impedance tensor) and $\bar{\mathbf{Z}}_r$ is the scaled regional two-dimensional impedance tensor ($g\ \mathbf{A}\ \bar{\mathbf{Z}}_{2D}$). The regional 2-D electric strike and information about the two regional impedances can be recovered by determining $\mathbf{Z}_r$ rotation matrix. The regional impedance still represents a 2-D tensor. The final expression for the tensor decomposition reduces to

$$\begin{bmatrix} Z_{xx} & Z_{xy} \\ Z_{yx} & Z_{yy} \end{bmatrix} = \begin{bmatrix} \cos\theta & -\sin\theta \\ \sin\theta & \cos\theta \end{bmatrix}\begin{bmatrix} 1-te & e-t \\ e+t & 1+te \end{bmatrix}\begin{bmatrix} 0 & Z_{xy}^{r} \\ Z_{yx}^{r} & 0 \end{bmatrix}\begin{bmatrix} \cos\theta & \sin\theta \\ -\sin\theta & \cos\theta \end{bmatrix}. \tag{5.12}$$

The above system is solved for seven parameters of distortion analysis, regional impedance components, Re, $\mathrm{Im}\left(\boldsymbol{Z_{xy}^{r}}\right)$, Re, $\mathrm{Im}\left(\boldsymbol{Z_{xy}^{r}}\right)$ along with distortion parameters t, e and important $\boldsymbol{\theta}$ the strike angle.

Calculation of distortion parameters

The impedance tensor decomposition based on factorization of telluric distortion tensor $\boldsymbol{C}$ as a product of modified Pauli spin matrices. The impedance $\bar{\mathbf{Z}}^s$ can be expressed in terms of the Pauli spin matrices (α, β and γ) as

$$\bar{\mathbf{Z}}^s = \frac{1}{2}(a_0 I + a_1\alpha + a_2\beta + a_3\gamma), \tag{5.13}$$

where $\alpha = \begin{bmatrix}0 & 1\\ 1 & 0\end{bmatrix}, \beta = \begin{bmatrix}0 & -1\\ 1 & 0\end{bmatrix}, \gamma = \begin{bmatrix}1 & 0\\ 0 & -1\end{bmatrix}$ and

$a_0 = Z_{xx} + Z_{yy}\,;\ a_1 = Z_{xy} + Z_{yx}\,; a_2 = Z_{xy} - Z_{yx};\ a_3 = Z_{xx} - Z_{yy}$

Thereof the following system of non-linear equations in terms of the tensor decomposition of above equation can be obtained

$$a = t\left(Z^r_{xy} + Z^r_{xy}\right) + e\left(Z^r_{xy} - Z^r_{xy}\right), \tag{5.14a}$$

$$b = \left[(1 - te)Z^r_{xy} - (t + et)Z^r_{yx}\right]\cos 2\theta - \left[(e + t)Z^r_{xy} + (t - t)Z^r_{yx}\right]\sin 2\theta, \tag{5.14b}$$

$$c = -(1 - et)Z^r_{xy} - (1 + et)Z^r_{yx}, \tag{5.14c}$$

$$d = -\left[(1 - et)Z^r_{xy} - (1 + et)Z^r_{yx}\right]\cos 2\theta - \left[(e + t)Z^r_{xy} + (e - t)Z^r_{yx}\right]\sin 2\theta \tag{5.14d}$$

From these equations, the distortion parameters t and$e$, the strike angle θ and the regional impedances are obtained by using a least square method. After obtaining the model parameters through the application the physical hypotheses, the model hypotheses can be tested with a ε^2 misfit variable, relative error. This is the residual error for the fit of the model to the data, normalized by estimates for the variance (σ^2_{ij}) of each element of the tensor data. The misfit between the tensor decomposition model and the measured data is:

$$\chi^2 = \frac{1}{4}\sum_{i=1}^{2}\sum_{j=2}^{2}\frac{\left|\mathbf{Z}^m_{ij} - \mathbf{Z}_{ij}\right|^2}{\sigma^2_{ij}}, \tag{5.15}$$

where $\mathbf{Z}_{ij}$ and $\mathbf{Z}^m_{ij}$ are the modelled and measured tensor elements respectively and the variances are estimated from the sample population of the tensor elements. The misfit χ^2would beis expected to lie within the range of 0 to 4 if the errors in the mean impedance estimates are randomly distributed and the model tensor elements have been fitted to within two standard deviations of the data (Groom *et al.* 1993). If the data cannot be fit to

within these levels, it implies either not all physical effects have been included (i.e., 3-D induction), or that the variances are poorly estimated.

Inclusion of magnetic distortion effects

Chave & Smith (1994) formulated a decomposition method that includes both electric and magnetic (D_m) galvanic distortions. The inclusion of $D_m$indirectly helps in extending the frequency range favorable for LR decomposition. Groom & Bailey (1991) showed that an anomalous magnetic field B_a is originated from the galvanically distorted current that is proportional to and in-phase with the regional filed E_r, i.e.

$$\mathbf{B}_a = \boldsymbol{D}_m \mathbf{E}_r. \tag{5.16}$$

Here, $D_m$is the magnetic distortion matrix of frequency independent real numbers. Then the observed field **B** is the sum of the anomalous field $\mathbf{B}_a$ and the regional magnetic field $\mathbf{B}_r$ as

$$\mathbf{B} = B_r + B_a \Rightarrow B_r + \boldsymbol{D}_m E_r \tag{5.17}$$

The elements of the observed impedance tensor are proportional to the elements of the regional tensor $\bar{\mathbf{Z}}^r$ expressed in terms of the magnetic distortion matrix (Chave & Smith, 1994) as

$$\bar{\mathbf{Z}}^{\mathrm{s}} = \mathbf{D}_{\mathrm{e}} \bar{\mathbf{Z}}^{\mathrm{r}} (\mathrm{I} + \mathbf{D}_{\mathrm{m}} \bar{\mathbf{Z}}^{\mathrm{r}})^{-1} \tag{5.18}$$

The product $\mathbf{D}_m \mathbf{Z}^r$ is non-dimensional and corresponds to the magnetic distortion effect. Thereby the impedance is no more frequency independent distorted, since the elements of Z^{r} are contained in the magnetic effect. We can write the impedance tensor from GB decomposition as

$$\bar{\mathbf{Z}}^{\mathrm{s}} = \tilde{\mathbf{T}}\tilde{\mathbf{S}}\bar{\mathbf{Z}}^{\mathrm{r}} (\mathrm{I} + \mathbf{D}_{\mathrm{m}} \bar{\mathbf{Z}}^{\mathrm{r}})^{-1}. \tag{5.19}$$

Extended GB decomposition for multi-sites

In conventional GB analysis, the decomposition model fits measured data individually frequency-by-frequency and site-by-site (Groom & Bailey, 1987; Groom *et al*. 1993). The process is commonly known as single site single frequency (SSSF) scheme. However, for the 3D/2D distortion model or approximation of superposition model to be valid frequency independent estimates of the twist, shears and regional strike must be found over a sufficiently wide band of frequencies. In practice this was done by iteratively constraining the estimates of twist, shear and strike found at each frequency in an attempt to find a frequency

band for which the constrained values result in an acceptable misfit error (Jones & Dumas, 1993; Groom *et al.* 1993). McNeice & Jones (2001) extended GB approach to multi-site multi-frequency (MSMF) analysis for the determination of the most consistent 2-D parameters from a set of sites over a given frequency band which can statistically fit an entire dataset simultaneously. They have done this by keeping the twist and shear parameters site-dependent and frequency independent, but with the 2-D regional strike being site independent and frequency dependant. MSMF analysis improves the estimate of the regional strike, as the regional strike remains consistent over several sites falling within a geological domain (McNeice & Jones, 2001). In practice the regional geoelectric strike for either the whole frequency band or for a narrow frequency band can be calculated using MSMF.

5.2.3 Phase tensor analysis (PT approach)

The GB decomposition approach and similar decomposition techniques a-priori assume the two dimensionality of the regional structure. Some new approaches have been suggested to relax this constraint. Caldwell *et al.* (2004) proposed a phase tensor (PT) approach for distortion and dimensionality analysis of MT impedance tensors. Similar to GB and Bahr approaches, the PT method is based on the truncated low frequency decompositions neglecting the local magnetic distortions. They have introduced a magnetotelluric phase tensor, defined as the relationship between the real and imaginary parts of the observed MT impedance tensor. The PT analysis formulated through the phase relationship between the horizontal components of the electric and magnetic fields, is unaffected by galvanic distortions. Thus, it is an important tool to obtain reliable information about the dimensionality of the regional structure. This scheme can also be applied in situations when both local heterogeneities and the regional conductivity structure are 3D in nature (Caldwell *et al.* 2004). The only limitation of this approach till now is that using this method it is not possible to recover the regional responses as we only know the extent of distortions present in the recorded MT data.

The phase tensor is defined as a real valued tensor Φ^s that is the ratio of Re$\mathbf{Z}^s$ and Im $\mathbf{Z}^s$, i.e.

$$\Phi^s = \frac{\mathrm{Re}\,\bar{\mathbf{Z}}^s}{\mathrm{Im}\bar{\mathbf{Z}}^s}, \tag{5.20}$$

Neglecting local magnetic distortions, the superposed impedance tensor can be written as

$$\bar{\mathbf{Z}}^s = \mathbf{D}_e\bar{\mathbf{Z}}^r \quad \text{Here } \bar{\mathbf{Z}}^r = \mathrm{Re}\mathbf{Z}^r + \mathrm{i}\,\mathrm{Im}\mathbf{Z}^r$$

$$\bar{Z}^s = D_e Re Z^r + iD_e Im Z^r \Rightarrow Re Z^s = D_e Re Z^r;\ Im Z_s = D_e Im Z^r$$

$$\Phi^s = D_e^{-1}(ReZ^s)^{-1}D_e ImZ^s \Rightarrow (ReZ^s)^{-1}ImZ^s = \Phi^r \Longrightarrow \Phi^s = \Phi^r \quad (5.21)$$

The eq. 5.21 suggests that the regional phase tensor (Φ^r) is equal to superposition phase tensor (Φ^s) and hence phase tensor is independent of local distortions and also any assumptions of regional dimensionality. This infers that phase tensor is unaffected by galvanic distortions in observed MT impedance. The Phase tensor (Φ) can be expressed as,

$$\Phi = \begin{bmatrix} \Phi_{11} & \Phi_{12} \\ \Phi_{21} & \Phi_{22} \end{bmatrix}. \quad (5.22)$$

Here $\Phi_{11}, \Phi_{12,} \Phi_{21}$ and Φ_{22} are the elements of the phase tensor. We can derive the elements of the phase tensor directly from the superposition/observed tensor Z^s as a true representation of regional 1-D, 2-D or 3-D regional impedance Z^r. The elements of the phase tensor are expressed as (Caldwell *et al.* 2004; Berdichevsky & Dmitriev, 2011)

$$\Phi_{11} = \frac{ReZ^r_{yy}ImZ^r_{xx} - ReZ^r_{xy}ImZ^r_{yx}}{ReZ^r_{xx}ReZ^r_{yy} - ReZ^r_{xy}ReZ^r_{yx}} \quad \Phi_{12} = \frac{ReZ^r_{yy}ImZ^r_{xy} - ReZ^r_{xy}ImZ^r_{yy}}{ReZ^r_{xx}ReZ^r_{yy} - ReZ^r_{xy}ReZ^r_{yx}}, \quad (5.23a)$$

$$\Phi_{21} = \frac{ReZ^r_{yy}ImZ^r_{xx} - ReZ^r_{xy}ImZ^r_{yx}}{ReZ^r_{xx}ReZ^r_{yy} - ReZ^r_{xy}ReZ^r_{yx}} \quad \Phi_{22} = \frac{ReZ^r_{xx}ImZ^r_{yy} - ReZ^r_{yx}ImZ^r_{xy}}{ReZ^r_{xx}ReZ^r_{yy} - ReZ^r_{xy}ReZ^r_{yx}}. \quad (5.23b)$$

Rotating the tensor clockwise by an angle α, we get

$$\Phi(\alpha) = R(\alpha)\,\Phi\,R^T(\alpha), \quad (5.24)$$

from which we can derive

$$\Phi_{12} = \phi_2 + \phi_3 \sin 2\alpha + \phi_4 \cos 2\alpha\ \Phi_{12} = \phi_1 + \phi_3 \cos 2\alpha - \phi_4 \sin 2\alpha \quad (5.25a)$$

$$\Phi_{21} = -\phi_1 + \phi_3 \cos 2\alpha - \phi_4 \sin 2\alpha\ \Phi_{22} = \phi_2 - \phi_3 \sin 2\alpha - \phi_4 \cos 2\alpha \quad (5.25b)$$

Here, $\phi_1 = \frac{\phi_{12} - \phi_{21}}{2}$; $\phi_2 = \frac{\phi_{11} + \phi_{22}}{2}$; $\phi_3 = \frac{\phi_{12} + \phi_{21}}{2}$ and $\phi_4 = \frac{\phi_{11} - \phi_{22}}{2}$

Rotational invariants of the phase tensor are $tr(\Phi)$; $det\,(\Phi)$; $\|\Phi\|$ and $\Phi_{xy} - \Phi_{yx}$. Rotation of the tensor to get the coordinate invariant principal components ($\Phi max, \Phi min$) gives the strike direction with the 90^o ambiguity. We can calculate the angle α representing tensor's dependence on the coordinate system and skew angle(β), a measure of tensor's asymmetry which is rotationally invariant, as

$$\alpha = \frac{1}{2}\tan^{-1}\left(\frac{\Phi_{12} + \Phi_{21}}{\Phi_{11} - \Phi_{22}}\right) \quad \text{and} \quad \beta = \frac{1}{2}\tan^{-1}\left(\frac{\Phi_{12} - \Phi_{21}}{\Phi_{11} + \Phi_{22}}\right) \quad (5.26)$$

The coordinate invariants Φ_{max} and Φ_{min}represent the maximum and minimum values of the tensor. The principal component Φmax is aligned in the direction $(\alpha - \beta)$. The Caldwell-Bibby-Brown skew angle (β) representing tensor asymmetry is zero for one-dimensional (1-D) and 2-D isotropic cases but it is non-zero for 2-D anisotropic and 3-D structures (Heise *et al.* 2006). The phase tensor ellipse can be constructed using the angle $(\alpha - \beta)$ and principal values of the phase tensor $\Phi_{max}$and Φ_{min} as lengths of direction of major axis of the tensor ellipse, major and minor axes respectively whose values can be obtained by the formula (Caldwell *et al.*2004; Berdichevsky & Dmitriev, 2011)

$$\Phi_{max} = \frac{1}{2}\left[\sqrt{\|\Phi\|^2 + 2|\det(\Phi)|} + \sqrt{\|\Phi\|^2 - 2|\det(\Phi)|}\right], \quad (5.27a)$$

$$\Phi_{min} = \frac{1}{2}\left[\sqrt{\|\Phi\|^2 + 2|\det(\Phi)|} - \sqrt{\|\Phi\|^2 - 2|\det(\Phi)|}\right]. \quad (5.27b)$$

Here, the principal axes of the phase tensor ellipse indicate the preferred flow direction of the electrical current in a way similar to the induction arrows.The phase tensor defined by the four independent parameters is free of distortions caused by near-surface inhomogeneities. These parameters characterize the regional background and fill all four degrees of freedom possessed by the matrix Φ.

5.3 Analysis of Sikkim profile data

After preprocessing the field data, the impedance tensors of all 31 sites are used to perform distortion analyses. The preprocessed MT data along the profile in the Sikkim Himalaya suggests that the region is structurally complex as evidenced by anomalous behavior of phases exceeding 90^o for some sites. In MT data analysis literature (Livelybrooks *et al.*1996; Pek & Verner, 1997; Weckmann *et al.* 2003; Lezaeta & Haak, 2003; Heise & Pous, 2003; Ichihara & Mogi, 2009) the phenomenon has been attributed to the current channeling thorough nearby structural heterogeneities and/or 3-D environment. The detailed discussion on the phases exceeding 90^o and its interpretation with local geology is discussed in *chapter 7*. Never the less, we intend to invert the data set in terms of broad regional 2-D structure by decomposing the impedance tensors following the assumption that the observed impedance tensor regionally 2-D and is distorted by 3-D local heterogeneities. We therefore follow the GB approach. We also used phase tensor technique and LT approaches to understand the

probable 3-D effects in the observed data. In the following session, I describe the process followed for individual techniques and results obtained from the analyses.

5.3.1 GB approach

Initially, we analyzed the data by GB decomposition method in both MSMF and SSMF manners implemented in an algorithm called 'Strike code' developed by McNeice & Jones (2001). Aim of the analysis is to separate the local effects from regional and finding a single strike direction that is representative of the major tectonic fabric in the area, and then align all of the MT tensor results along the profile with that direction. We also analyzed depth variation of the strike by performing the analysis in various frequency bands in order to understand the depth-wise structural variations.

5.3.2 Strike code

The 'strike' code is an MT decomposition algorithm in Fortran 77 written by McNeice and Jones to estimate the noise free impedance tensor and hence regional geoelectric strike of the region in both SSMF and MSMF modes. The algorithm iteratively improves a user-supplied trial solution by minimizing a quadratic approximation of an objective function γ^2, to estimate the optimal model parameters satisfied by the hypothesis given by 'superposition model' approximation. The objective function is given as (McNeice & Jones, 2001)

$$\gamma^2(\alpha) = \sum_{k=1}^{S\times N}\left(\sum_{i=0}^{3}\left[\frac{Re(a_i^{obs})-Re(a_i^{model})}{\sigma_{a_i}}\right]^2 + \sum_{i=0}^{3}\left[\frac{Im(a_i^{obs})-Im(a_i^{model})}{\sigma_{a_i}}\right]^2\right). \quad (5.28)$$

where σ is the standard deviation of the decomposition coefficients. S and N are the number of MT sites and N number of frequencies. a_i are the decomposition coefficients. Minimization of the objective function is performed with a sequential quadratic programming algorithm. Iterations continue until the gradient of the objective function is zero with respect to all parameters, or when successive iterations produce changes in the estimated parameters less than a user-specified tolerance.

Input parameters used in the strike code

1. To execute the algorithm in MSMF mode, a list-file containing names of the 'edi' files of all sites along the profile was given. For SSMF approach 'edi' file of each site was supplied at a time.

2. Impedance relative error floor: We have used a value of 1.75% in impedance which adds error floors of 1degree in phase and 3.53% in apparent resistivity.

3. Normalization type: Robustness of the strike angle can be determined by using various normalizations in each time. If it varies greatly with different schemes, then the data probably have different strikes over the frequency/site ranges chosen. We used the default normalization type GAVSD2 which could give most consistent results (strike code manual).

4. Minimum and maximum period: Inductive effects are frequency dependent and decrease with decreasing frequency. We therefore used the period range between 0.01s to 1000s even though we have data from 1000Hz. This helps to some extent in getting rid of inductive effects. To study the strike variations with period/depth, we subdivided the entire band into four frequency bands, 0.1-1s, 1-10s, 10-100s and 100-1000s.

5. We used the default regional bounds for estimation of regional as well as local strike at initial stage. The default values are -1080 to +1080, -45 to +45 and -60 to +60 for strike, shear and twist respectively. Next, to decompose the impedance tensor along the strike according to 2-D approximation, the upper and lower limits of strike is fixed to estimated regional strike along with respective shear and twist values.

5.3.3 Single-site, multi-site and period-wise analyses

(a) MSMF

First, the impedance tensors of all 31 sites were used to perform MSMF decomposition analysis to obtain regional impedance tensor and estimate regional geoelectric strike in broad period (0.01-1000s) range. Input parameters used for MSMF analysis are mentioned above. The twist and shear values after the analysis in broad frequency range (0.01-1000s) at each station are listed in Table 5.01. Most of the data, despite high shear values at some sites lie below the maximum shear and twist limit (+/- 45). Low shear and twist values were observed in GFB region suggesting 1D/2D subsurface structure. However the large shear values are observed particularly at the southern boundary of LHD and MCTZ indicating large deflections in regional electric field/telluric currents. These deflections in the electric fields might be due to complex structural environment suggested from the local geology of the region. Comparably low twist values are observed at most of sites during the frequency range. But at some sites located in LHD (Site SH14) and MCTZ (sites SH21 & SH23) the large rotation of regional electric field was observed at the sites. Interestingly the high shear

and twist values are associated with major fault zones which might be responsible for the perturbation of the regional telluric currents/fields. The RMS misfit values estimated from the MSMF decomposition are listed in Table 5.01. The RMS errors for the most of the sites are below 2. Thus, the 2-D decomposition model reasonably fits the data to within the small errors.

The MSMF analysis yielded a tensor principle direction of N5˚E for the entire profile, which is orthogonal to the regional E-W strike of the Indian plate and the Himalayan belt. If we take into consideration the 90˚ ambiguity in the determination of MT strike, the estimated direction N95^{o}E coincides with the strike of the under-thrusting Indian plate beneath the Himalaya.

(b) SSMF

Next, we performed single-site multi-frequency (SSMF) analysis of all 31 MT transfer functions to understand the scatter of local strike directions along the profile for a broad period band of 0.01 – 1000s. The input parameters used for the SSMF approach are same as MSMF. The resulting decomposition parameters, strike, shear and twist are tabulated in Table 5.02. The RMS misfit for each site is shown as a bar diagram in Figure 5.02a. Considering the 90^{o} ambiguity in MT strike determination, the local strike angles were brought to the first (0^{o} - 90^{o}) quadrant and then plotted as rose diagrams in bi-directional representation. Figure 5.01a shows rose diagram (black color bars) incorporating all 31 sites. The orthogonal direction corresponding to 90^{o} ambiguity is also shown in light gray color. The scatter is large although a dominant N-S direction is seen. We also plot the rose diagram for sites within GFB (sites SH01-SH09) to check whether this sub-domain has any distinct direction. For these sites, the strike direction appears to be consistent (Figure 5.01b) and the conjugate approximately E-W strike direction in this sub-domain correlates with the strike of the northward under-thrusting Indian plate.

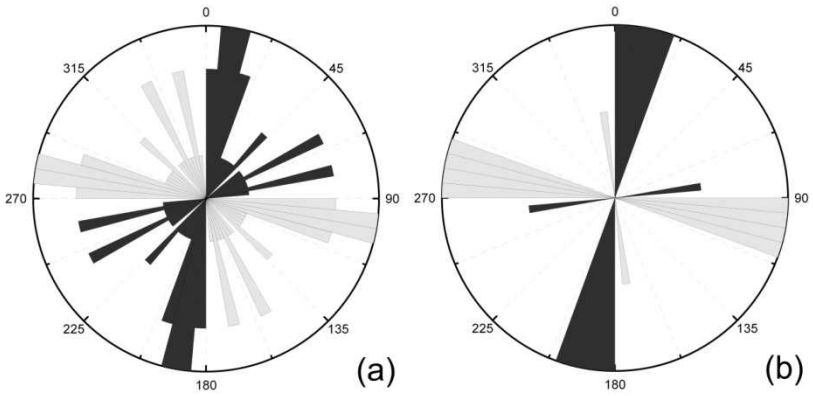

Figure 5.01: Rose diagrams showing strike directions (black color) obtained after single-site multi-frequency tensor decomposition of MT transfer functions for (a) the entire profile, and (b) Ganga Foreland Basin (sites 01-09). Orthogonal strike directions are shown in light gray color to highlight 90o ambiguity in the determination of MT strikes

(c) Period-wise variations in strike and RMS error analysis:

In view of large shear and twist values and high RMS error for some sites along the profile, we analyze period-wise (depth) variation in the strike by performing the MSMF and SSMF analyses for the entire data set in three different frequency bands (1-10; 10-100 and 100-1000s).

The local strike directions for the above three period bands and for an additional band of 0.1-1s obtained by SSMF analysis are shown in Figure 5.07. Here, the length of the arrows is scaled to $(\text{RMS error})^{-1/2}$. Thus, large arrows indicate small error. The trend of strike remains consistent over a large period band and spatially it supports an approximately E-W regional strike (with 90^o ambiguity) for GFB and HHC. However, we observe some distinct features in the strike patterns located in LHD and MCTZ. The sites SH17–SH19 within LHD show dominantly N–S strike up to 10s period and NNW strike at larger periods (Figure 5.07). It is interesting to note that the sites within MCTZ reveal strike directions transverse to the N–S (or E–W assuming 90° ambiguity in MT strike determination) direction. For example, sites SH26, SH25, and SH22 have broadly ENE to E–W strike whereas sites SH24 and SH23 show NNW to NW strike. These are consistent in view of 90° ambiguity limitation and, therefore, represent transverse nature of the subsurface geological structure within MCTZ. The presence of NNW striking lineaments in Sikkim and earthquake focal mechanisms support the presence of transverse features and therefore transverse MT strikes especially within MCTZ are not ruled out. Therefore, the strike analyses suggest that LHD and MCTZ appear to be distinct and tectonically different.

Table 5.01: The RMS misfit values for the all sites after MSMF decomposition scheme for the broad frequency range. High twist and shear values are highlighted in red color

Site Nr. (N-S)	0.01-1000s			1-10s			10-100s			100-1000s		
	RMS error	Shear	Twist	RMS error	Shear	Twist	RMS error	Shear	Twist	RMS error	Shear	Twist
SH31	0.44	32.75	3.04	1.86	-25.45	60.00	0.36	44.99	-2.84	0.36	-44.91	24.34
SH30	0.84	-35.66	-20.46	1.14	-34.79	-20.28	0.58	-28.60	-20.44	0.86	-35.58	-60.00
SH29	0.98	-2.81	2.73	1.12	-10.02	2.33	0.91	-3.39	-2.23	0.69	-15.76	-12.82
SH28	1.41	29.07	-7.93	0.58	32.00	-5.99	1.31	33.59	-1.95	1.40	-15.40	0.05
SH27	0.77	-2.47	-9.01	1.05	-9.93	-22.24	0.37	-3.76	-25.98	0.42	-11.24	-40.97
SH26	0.80	-44.10	3.47	1.48	-45.00	7.66	0.82	-45.00	16.65	0.82	-45.00	-44.77
SH25	0.55	-33.10	-21.54	1.65	-36.57	-21.50	0.60	-35.19	-16.77	0.57	-34.99	-60.00
SH24	0.94	-34.87	2.13	1.32	-38.18	4.46	0.43	-38.40	11.22	0.62	17.26	14.99
SH23	2.42	45.00	54.76	3.46	-28.88	-21.51	0.95	-30.40	-14.85	0.83	10.62	-13.35
SH22	0.71	20.54	0.93	1.48	2.56	-2.72	0.87	-0.97	-0.25	1.51	-5.56	2.52
SH21	2.60	-17.17	-32.98	1.73	-20.44	-24.03	1.03	-23.54	-17.95	0.78	6.38	-17.15
SH20	3.91	6.89	1.90	0.86	25.05	17.16	7.35	28.66	23.90	6.10	-24.71	38.06
SH19	3.93	18.51	12.24	7.03	-21.59	60.00	2.23	-10.75	60.00	0.45	-41.94	36.40
SH18	0.83	-1.36	-14.24	1.60	-0.84	-5.17	0.45	0.78	1.20	0.91	-19.46	1.57
SH17	2.02	21.61	24.49	4.92	21.88	26.84	1.58	22.89	34.79	0.71	-36.11	51.55
SH16	0.19	4.25	-14.77	0.55	5.35	-14.04	0.17	8.69	-5.18	0.07	8.71	-11.40
SH15	0.29	-40.20	19.44	0.30	-45.00	26.04	0.40	-45.00	34.99	0.42	-43.51	-27.21
SH14	0.69	-45.00	60.00	0.50	39.20	-17.64	0.26	42.01	-11.00	0.29	-43.59	15.88
SH13	1.36	-20.77	-7.83	2.26	39.75	55.18	0.56	39.08	60.00	1.17	-45.00	-60.00
SH12	2.86	28.20	25.23	1.31	37.56	33.12	0.80	41.00	43.61	1.13	45.00	-16.28
SH11	1.39	-8.78	16.72	2.33	-20.40	34.57	0.47	-13.24	34.67	0.54	-41.80	7.00
SH10	1.21	3.51	-9.62	1.09	14.02	-5.40	0.93	21.75	0.08	0.49	45.00	-60.00
SH09	2.29	-12.79	1.78	0.74	37.38	40.15	0.81	38.77	47.67	0.61	45.00	-12.78
SH08	2.37	2.28	-3.69	1.33	10.64	-2.03	1.11	15.90	0.17	1.41	-27.66	10.94
SH07	0.38	8.05	-2.14	1.22	14.82	-0.29	0.50	17.14	2.02	0.62	-29.05	13.99
SH06	0.58	0.96	1.25	2.13	5.58	4.63	0.33	9.05	7.38	0.45	-22.32	16.38
SH05	2.08	-2.19	1.81	2.28	4.16	3.78	1.57	6.27	5.16	1.24	-24.56	15.33
SH04	1.06	4.16	-1.32	4.80	10.07	0.59	0.89	13.11	3.73	2.06	-29.44	15.33
SH03	1.27	1.53	-0.94	3.19	3.35	-0.95	1.10	6.56	0.60	1.08	-25.04	13.39
SH02	3.26	0.35	-0.35	5.81	-2.71	1.89	3.75	0.31	5.18	2.41	-27.13	14.36
SH01	1.37	-6.65	0.81	1.31	-7.11	2.10	1.11	-6.65	3.19	0.90	-10.48	11.49

As the MSMF analysis of the entire dataset yields regional strike of N95°E which coincides with the strike of the Indian plate, we therefore performed the GB analysis in SSMF mode by fixing the regional strike to this value. Figure 5.02a shows RMS errors (orange bars) at individual sites after GB decomposition analysis by fixing the regional strike to N95°E. RMS errors are less than 2 for the southern and northern sites but these are large for the central segment indicating that the region is more complex than a simple 2-D structure. In order to test the transverse nature of the regional strike we have also performed GB analysis after fixing the regional strike to N30°W. Now, the RMS errors (blue bars) for

sites SH26–SH22 within MCTZ fall much below 2 suggesting that this particular strike value fits the data better compared to the N95°E direction and, thus, supporting the existence of transverse tectonics in this segment of the Sikkim Himalaya. The RMS errors for sites SH20–SH15 now deteriorate compared to the N95°E case. Site SH19 is exceptionally bad in term of RMS error.

Table 5.02: The strike, shear and twist values for the all sites after SSMF decomposition scheme for the broad frequency range

SSMF (0.01-1000s)							
Sites (S-N)	**Strike**	**Shear**	**Twist**	**Sites (S-N)**	**Strike**	**shear**	**Twist**
SH01	-89.63	7.35	1.04	SH17	10.82	21.8	21.19
SH02	-173.76	0.33	-0.36	SH18	-176.67	-1.94	-14.18
SH03	-85.86	-1.64	-0.85	SH19	8.84	18.27	9.83
SH04	-169.16	3.25	-1.78	SH20	-145	20	0.53
SH05	10.75	-2.4	1.56	SH21	-144.99	17.14	-212.2
SH06	-172.63	0.93	1.19	SH22	-13	13.4	3.37
SH07	-162.87	6.7	-2.73	SH23	65.85	22.8	-7
SH08	-70.21	-0.97	-3.84	SH24	153.45	-28	21
SH09	40.04	0.47	-9.81	SH25	78	27	-13
SH10	-14.18	-13.27	5.57	SH26	44	-38	-35
SH11	163.98	7.44	12.3	SH27	-125	9.31	-7.74
SH12	26.81	14.18	10.64	SH28	-167	29.43	-11.43
SH13	-108.89	21.69	4.63	SH29	-121.23	11.38	3.24
SH14	63.28	-36.39	6.77	SH30	-171	-33.79	-8.79
SH15	63.15	-19.38	-20.29	SH31	15.22	27.96	-0.11
SH16	23.93	15.59	-12.62				

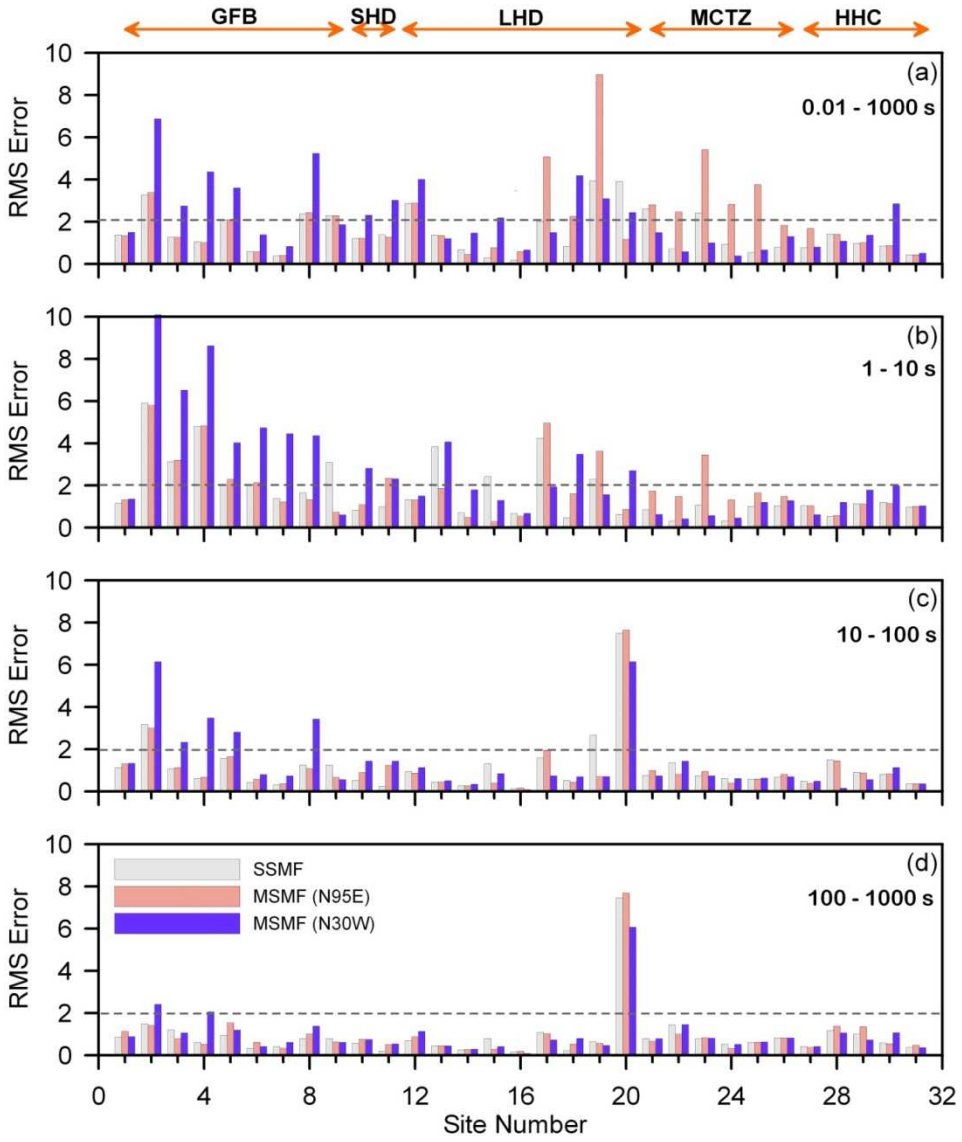

Figure 5.02: RMS error for different sites after SSMF analysis, and MSMF analysis by fixing the regional strike to N95°E and N30°W respectively. (a) entire period band, (b) 1-10s band, (c) 10-100s band, and (d) 100-1000s band. In (a) gray bars show the RMS error obtained by MSMF instead of SSMF without fixing the rotation angle.

In order to get more insight into the goodness of fit for the regional strike direction obtained by MSMF analysis we analyzed the behavior of the RMS error at every site. The error is less than 2 for most sites but it is in general large in the northern part of LHD and within MCTZ (Table 5.02). Similar to SSMF analyses, we have analyzed the error of misfit by fixing the strike direction to be N95˚E. The errors are largely similar to the previous case for the entire profile except in this region of transverse tectonics suggesting that the N95˚E azimuth can be considered as the regional strike. Here, the RMS error drastically increases for many sites between sites SH17 and SH27 (Figure 5.02a). We have also performed GB analysis after fixing the regional strike to N30^{o}W. Now, the RMS errors (Figure 5.02a) for

sites within MCTZ fall much below 2 suggesting that this particular strike value fits the data better compared to the N95^{o}E direction. The RMS errors for sites SH2-SH12 within GFB and SHD now deteriorate compared to the N95^{o}E case suggesting the dominance of the E-W strike of the Indian plate in these regions. Based on the GB analysis (by both SSMF and MSMF) we can infer that there are two dominant strike directions present along this profile, one representing the E-W strike of the Indian plate and the other a transverse strike within MCTZ.

From Figure 5.02b it is observed that the period band of 1-10s (Figure 5.02b) yields large errors for sites SH02 to SH04 within GFB and at a few sites within LHD. The RMS error at sites within MCTZ is amplified when the MSMF analysis is performed by fixing the regional strike to N95^{o}E. Fixing of the regional strike to N30^{o}W reduces the error in this region. But it is interesting to note that the RMS error for sites within GFB becomes very large for this value of regional strike. Thus, the regional strike of the shallow structures (those contributing to the period range of 1-10s) within GFB is akin to the E-W strike of the Indian plate. In the next period band of 10-100s, the RMS error at most sites is well below 2, the exception being site SH20 (Figure 5.02c) that yields abnormally large RMS error. The RMS errors obtained by MSMF analysis for regional strike of N95^{o}E and N30^{o}W respectively are not significantly different for sites SH11 to SH23 suggesting that both strike values can fit the data reasonably well. However, the error is large for sites within GFB when the regional strike is fixed at N30^{o}W indicating that the regional strike in this part has preference for E-W strike of the Indian plate. The pattern remains almost similar, albeit with relatively low RMS values, for the period band of 100-1000s (Figure 5.02d). Once again, transverse regional strike yields larger errors and high shear and twist within GFB compared to E-W strike (Figure 5.02d).

We have analyzed the probable cause for large RMS errors in the period band of 1-10s for sites within GFB by performing MSMF analysis only for sites SH1 to SH9. The results for the three different period bands are shown in Figure 5.03. The RMS errors are in general smaller than two for all three period bands. While the lower period data reveals the regional strike direction consistent with the E-W strike of the Indian plate, the data of 1-10s period yield regional strike direction of N51^{o}E, indicating the presence of NE-SW (or its conjugate) structure in the north Bengal Basin of GFB covered by these sites

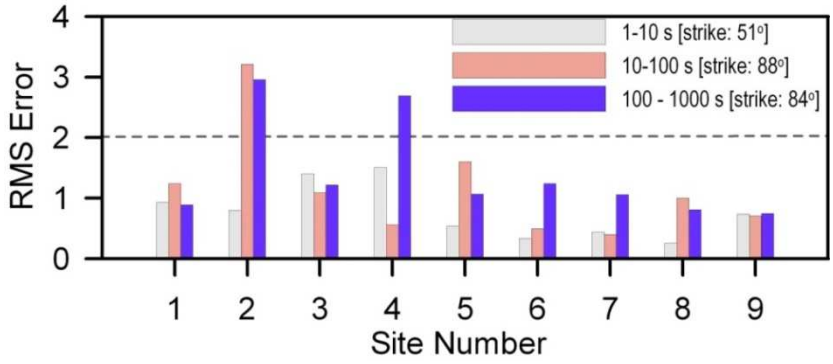

Figure 5.03: RMS error after MSMF analysis for the sites in GFB

5.3.4 LT approach

The large shear and twist values obtained by GB analyses at some sites suggest that the subsurface structure of the region is complex in nature. We, therefore analyzed the data of sites (SH15- SH27) situated in LHD and MCTZ (known as Sikkim Dome) by LT decomposition approach (LaTorraca *et al.*1986) to check if this analysis leads to the results consistent with those obtained by GB analysis, especially in the presence of anomalous phase at few sites. We used MT data interpretation package WinGLink (M/s Geosystem SRL, Italy) to perform LT decomposition analysis. The results of LT decomposition analysis of the impedance tensors for the entire frequency band of 0.01-1000s are shown in Figure 5.04 in the form of rose diagram binned at every 5^o window.

From LT analysis of the data, it is interesting to note that the sites within the Sikkim dome can be categorized into three groups based on the consistency of the strike directions. The northernmost group (sites SH27-SH25) shows NNW strike which changes to E to ENE for the central segment (sites SH24-SH20) and then to approximately N-S direction in the southern segment (sites SH15-SH19). Site SH26 shows two dominant strike directions. At this site, the NNW dominant strike direction is obtained for high frequencies, up to 10 Hz, beyond which the strike angle gradually rotates in clockwise direction (Figure 5.05) and yields dominant N-S strike. The skew angle estimated for the site increases and goes to even 90^o at longer periods (Figure 5.06). Sites SH27-SH25 reveal a consistent strike direction that is transverse to the general ENE strike obtained by the GB approach (with the ambiguity of 90^o. It is interesting to note that site SH27 has consistent strike direction even though it is located about 20 km NNE of site SH26 and falls within HHC north of MCT-1. Sites SH26-SH25 falling within the MCTZ has two distinctly different strike directions implying a

complex tectonic setup for this region. The LT approach never-the-less does not resolve the 90^o ambiguity. Therefore, the strike directions orthogonal to these strikes are also possible.

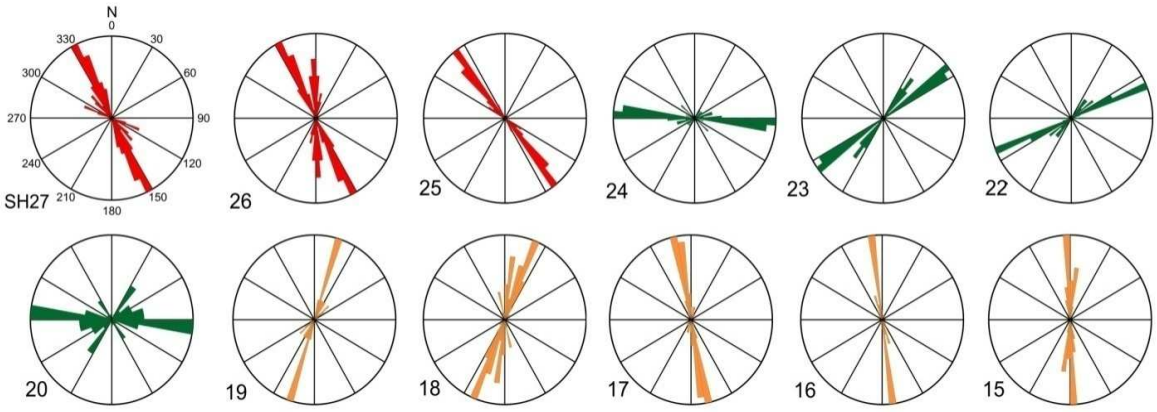

Figure 5.04: Rose diagrams showing strike directions at various sites in the frequency band of 10^{-3} to 10^{2} Hz obtained by LT approach.

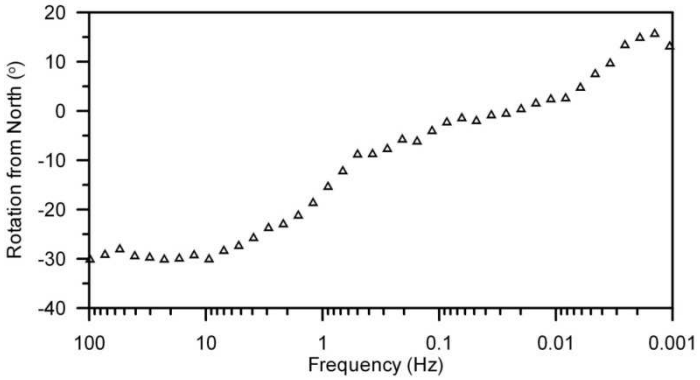

Figure 5.05: Variation of rotation angle with frequency obtained by LT approach for site SH26 showing two dominant strike directions

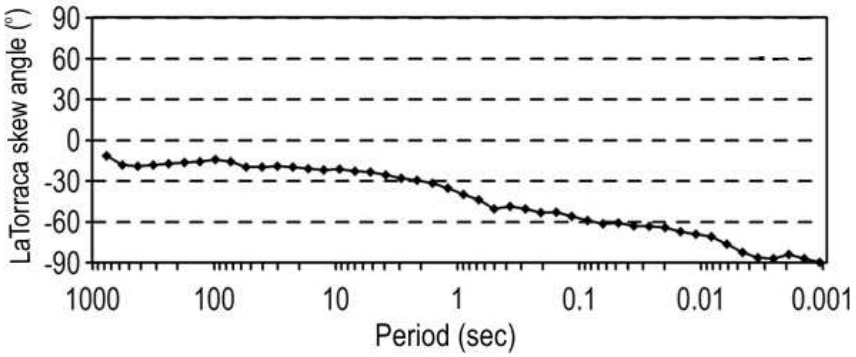

Figure 5.06: LaTorraca skew angle representing the deviation of **E** and **H** from orthogonality as a function of period.

5.3.5 PT approach

The GB approach assumes the regional structure to be 2-D in nature and attempts to recover regional impedance tensors by removing the effect of shear, twist and anisotropy from the observed impedance tensors. The presence of local near-surface heterogeneities can severely distort the observed electric field and can introduce static shift in the data. Further, the assumption of two-dimensionality may not hold for tectonically active regions such as collision belts. We, therefore also applied phase tensor (PT) technique to the data set to test whether the regional strike obtained by the GB approach is consistent with the results obtained by the GB and LT approaches. The results at four periods are shown in Figure 5.07 along with strike directions obtained by GB analysis and the values of angles are listed in Table 5.03. It is to be noted that GB strikes are for period bands whereas PT strikes are at a given period. The Φ_{max}values are normalized to keep the length of the major axis of ellipses the same across all plots. Φ_{min} are also normalized accordingly. The color of ellipses represent skew angle (β) (Selway *et al*. 2012).

We analyze the behavior of phase ellipses in all four sub-domains GFD, LHD, MCTZ, and HHC. Within GFB, the ellipticity increases with the increase in period. The circular nature of phase ellipses in the period band of 0.1-1s correlates with the presence of thick alluvial sediments in the region whereas large ellipticity at more than 10s period is possibly due to the crustal structural of the Indian plate. These ellipses are aligned in broadly N-S direction and consistent with the strike directions obtained by the GB approach. For some cases, for example in the 100-1000s band, the GB strike is orthogonal to the PT strike (Figure 5.07d). The strike values obtained by both approaches are listed in Table 5.3 and such values of the GB strike, marked in blue color, are rotated by 90^o.

Phase ellipses within LHD reveal fairly consistent pattern of broadly N-S strike the distortion of ellipses is very strong suggesting complex 3-D nature of the subsurface structure. This is also evident from the large values of β for sites SH15 to SH20 for periods larger than 10s (Table 5.03). The skew angle (β), a measure of the phase tensor's asymmetry, provides further information about the complexity of the subsurface structure. The ellipses within the LHD appear to be aligned (although large variations are present) along N-S direction indicating the preferred direction of the current flow (Heise *et al.* 2006).

An interesting aspect that the NNW strike within MCTZ is also obtained by phase tensor analysis evidenced by the transverse nature of the strike of ellipses at sites SH22 to SH26.

The strike direction is consistent for 10s and larger periods although the ellipticity changes. Such transverse MT strike is indicative of the presence of transverse tectonics in the region. The skew angle for sites SH26-SH23 is small except for sites SH26 and SH25 at 100s periods and site SH26 shows anomalous behavior with coordinate dependence of -45^o to 40^o. The sites within MCTZ show small values of β implying possibly 2-D nature of the subsurface structure, although β=0 is a necessary but not sufficient condition for a 2-D regional conductivity structure (Caldwell *et al.* 2004). The change in the strike directions between MCTZ and LHD together with the variations in the skew angle values implies a highly complex tectonic setup of the Sikkim Himalaya with LHD and MCTZ being significantly different in terms of geological strikes and complexities. The sites in HHC reveal approximately N-S direction at 10s period but do not yield a consistent direction at larger periods

5.4 Synthesis of results

5.4.1 Regional strike for the entire profile

The strike analyses by both the PT and the GB approaches indicate the dominance of an approximately N-S strike along the profile, except for MCTZ, is supported by both GB and PT analyses. Since estimation of MT strike suffers from the ambiguity of 90 degrees and prevailing geotectonic models argue for underthrusting of E-W striking Indian plate beneath the Himalaya, we assume N95˚E azimuth as the dominant regional strike direction. Finally, we perform the MSMF analysis by fixing the regional strike to N95˚E for the entire profile and obtained the distortion-corrected impedance tensors for all 31 sites. Now the regional impedances are decoupled into two modes. The Traverse Electric /E-polarization (TE) mode is along the strike direction whereas Transverse Magnetic /B/H-polarization (TM) mode is orthogonal to it.

5.4.2 Strike variations in different segments

A comparison of the results from period wise variations of strike directions by GB and PT approaches (Figure 5.07 and Table 5.03) reveals that the strike directions are broadly in good agreement except in the high frequency range (0.1-1s band). At some sites and frequency bands the GB strike matches well with the PT strike when rotated by 90^o (rotated values marked in blue in Table 5.03). The disagreement at high frequencies implies the dominant effect of the distortions due to near-surface localized heterogeneities, especially the effect of

topography in this rugged mountain terrain. GB local strike values at larger than 1s periods also support transverse trend for the sites within MCTZ. The local strike directions within MCTZ by LT approach are somewhat different than those obtained by PT and GB approaches but these also reveal the transverse trend of the subsurface structure. These results also bring out the difference in the geological strikes of the MCTZ and LHD and are in agreement with the conclusion drawn about the transverse tectonic trend of MCTZ obtained by PT and GB analyses.

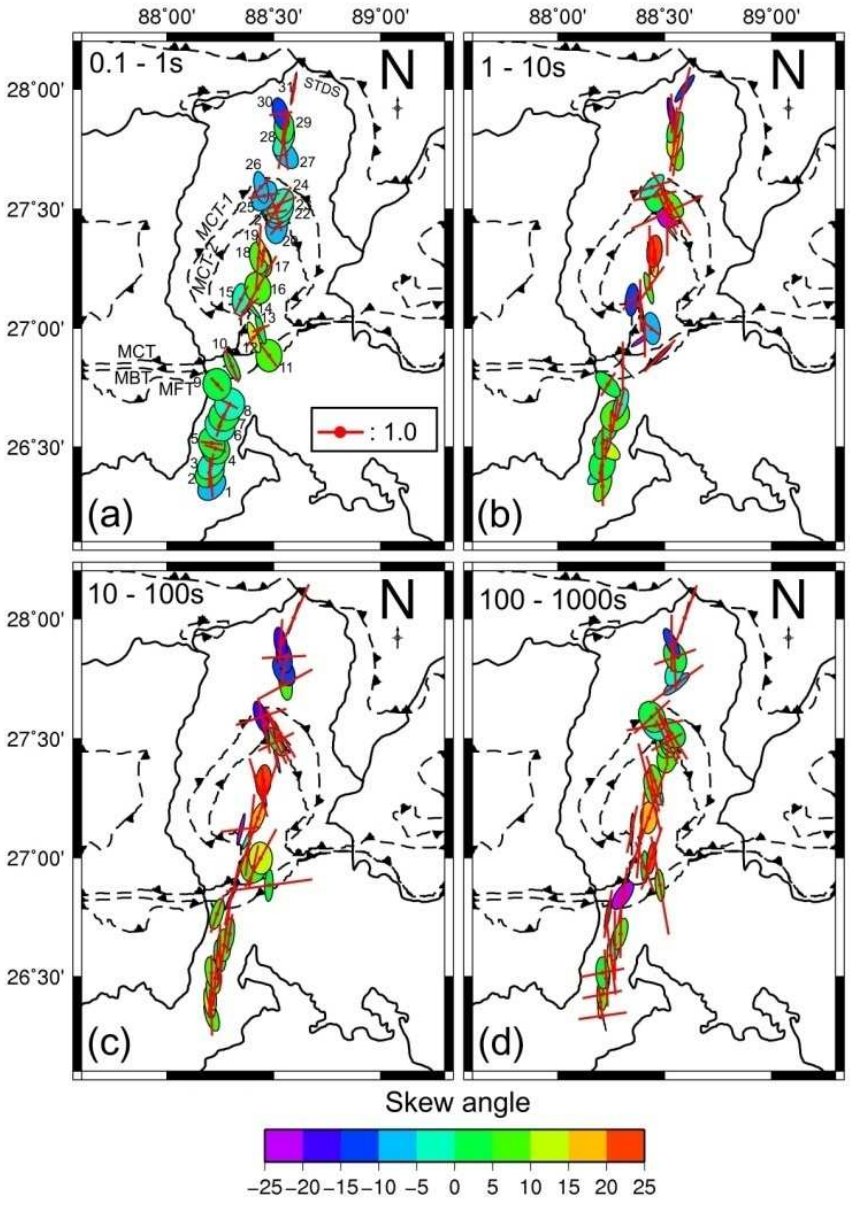

Figure 5.07: Strike directions at various sites for four different period bands obtained by GB (bars) and PT (ellipses) approaches. Bar lengths is scaled to (RMS Error)$^{-1/2}$. Large bars indicate good fit. PT ellipses are also normalized so that major axes at all sites are of the same length

Table 5.03: Strike values obtained from LT, PT and GB analyses

Site Nr. (S-N)	Code	GB (1-10s)	PT(10s)		GB (10-100s)	PT(100s)		GB (100-1000s)	PT(1000s)	
			α-β	β		α-β	β		α-β	β
1	SH01	179	21	8	179	163	8	**172**	167	30
2	SH02	3	48	-5	183	172	11	173	182	17
3	SH03	2	14	4	180	171	7	**169**	180	8
4	SH04	**95**	127	12	184	179	7	177	184	12
5	SH05	0	15	4	180	171	9	**160**	178	0
6	SH06	2	16	4	180	174	4	173	179	10
7	SH07	9	28	6	188	180	6	0	4	-3
8	SH08	13	18	-2	188	185	4	1	15	7
9	SH09	**121**	136	1	19	16	8	9	19	8
10	SH10	0	138	2	13	25	-24	9	34	-33
11	SH11	44	46	-26	**172**	182	4	170	175	5
12	SH12	0	55	-21	12	12	7	160	180	4
13	SH13	130	172	-7	208	176	14	18	8	26
14	SH14	179	169	39	6	27	-3	5	7	18
15	SH15	41	5	-11	**173**	193	-26	12	3	34
16	SH16	35	167	5	19	21	15	19	3	19
17	SH17	181	175	12	177	167	18	166	151	-1
18	SH18	180	175	24	163	163	26	166	171	8
19	SH19	171	185	22	172	185	21	162	171	7
20	SH20	180	142	13	180	157	-6	180	10	7
21	SH21	156	138	16	154	154	1	154	186	9
22	SH22	**155**	171	-21	**153**	151	4	**151**	165	2
23	SH23	156	144	16	155	155	-3	154	162	3
24	SH24	149	140	8	149	139	2	149	138	1
25	SH25	**168**	178	0	168	164	-11	**170**	146	-2
26	SH26	72	42	-3	**162**	162	-19	**137**	154	3
27	SH27	189	172	8	**151**	172	8	54	50	-8
28	SH28	9	11	11	192	154	-11	177	202	-5
29	SH29	5	20	0	**177**	169	-11	**160**	158	1
30	SH30	179	169	-19	184	170	-15	180	156	-14
31	SH31	14	35	-14	24	19	-44	20	14	25

The three different approaches reveal variations in the local strike directions within Sikkim Dome. First, we focus on PT approach assigning more weight to these results as phase tensors are unaffected by galvanic distortions in observed MT impedances (Caldwell *et al.* 2004). In general, the local strike by PT analysis at 10s and larger periods is NNW to NW for the sites SH26-SH23 but there are spatial variations among different frequency bands (Figure 5.07 and Table 5.03). For example, at 10 and 100 s the transverse trend is seen up to site SH20. The local strike is more variable at 0.1 s period. Further south (SH15-SH19), the local strike is approximately NNW to N. The local strike for site SH26 is also approximately

N-S in the period range of 10-100 s but it changes to NE-SW for 500s period. Based on these results, the region can be broadly sub-divided into two zones, one consisting of sites SH22-26 (geological domain MCTZ) and other sites SH15-SH19 (geological domain LHD) with site SH20 representing the transition zone.

A synthesis of results from MSMF and SSMF analysis in four period bands indicates that the deeper structure (10-1000s period), barring GFB, appears to be more homogeneous in terms of electrical conductivity distribution. The RMS errors for the sites situated in GFB obtained after MSMF are in general smaller than two for all three period bands. While the lower period data reveals the regional strike direction consistent with the E-W strike of the Indian plate, the data of 1-10s period yield regional strike direction of N51^{o}E, indicating the presence of NE-SW (or its conjugate) structure in the north Bengal Basin of GFB covered by these sites.

5.4.3 Correlation with seismicity

All three analyses reveal the presence of transverse MT strike directions in MCTZ which is contrary to the general northward convergence direction of the Indian plate at the Himalayan collision front. This is in agreement with the seismotectonic models of the Sikkim Himalaya based on focal mechanisms of moderate earthquakes and composite fault plane solutions of microearthquakes. Focal mechanisms of the most recent Sikkim earthquake (Mw 6.9, centroid depth 46 km) of 18 September, 2011 and its aftershocks (*http://www.globalcmt.org*) also revealed strike-slip motion on a nearly vertical NW-SE striking fault further strengthening the view that the seismotectonics of the Sikkim Himalaya is different from the Himalayan Seismic Belt model envisaged by Seeber *et al.* (1981). Although there are some differences in the epicentral location and focal depth of this earthquake estimated by various agencies ([27.7°N, 88.2°E, 10km] *http://www.imd.gov.in*; [27.73°N,88.15°E, 50km] *http://earthquake.usgs.gov*; [27.44°N,88.35°E,46km] http://www.globaSH27mt.org), the epicentral location (event 6, Figure 5.08) from USGS catalog (*http://earthquake.usgs.gov*) coincides with the transverse tectonic trend obtained by the present MT strike analysis for MCTZ.

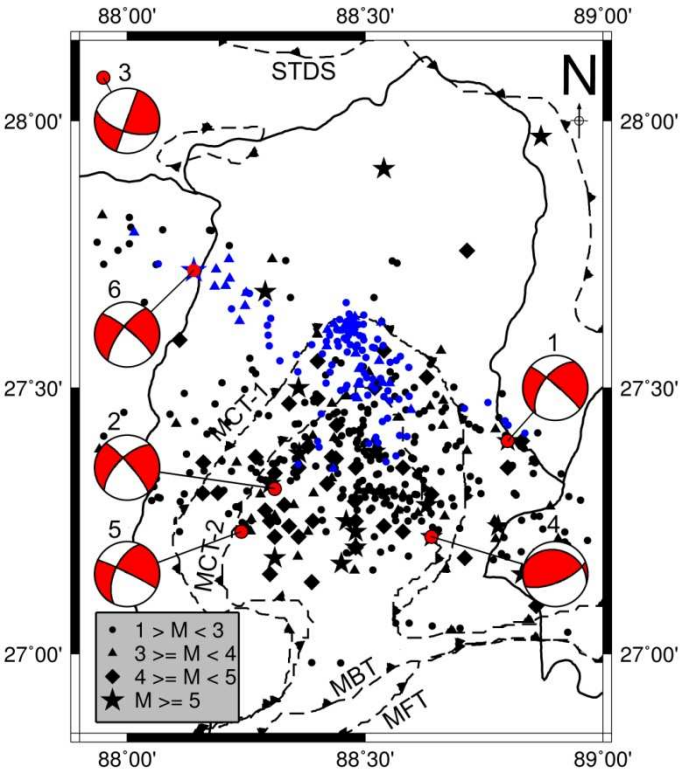

Figure 5.08: Seismicity of the Sikkim region (black symbols) recorded by local networks operated during 1999 to 2002 (Nath *et al.*2005) and 2006 to 2007 (Hazarika *et al.*2010). Blue symbols represent microearthquakes after 18 September 2011 earthquake (Kumar *et al.*2012). Sources for focal mechanisms: 1 (Dasgupta *et al.*1987), 2-5 (Hazarika *et al.* 2010), 6 (http://earthquake.usgs.gov). Events: 1-19801119, 2- 20010212, 3-20050326, 4-20060214 5-20070520, 6-20110918

An aftershock study in the region post September 18, 2011 earthquake by Kumar *et al.* (2012), using a dense coverage of broadband seismic stations and HypoDD earthquake location algorithm, brings out the NW trend of the seismic activity (Blue symbols in Figure 5.08). The epicenters are mostly confined within MCTZ close to our MT sites within Kangchendzonga reserve forest area. Focal depths of these earthquakes confine along a nearly vertical structure and reach down to about 50 km depth. A correlation between the NW trend of the epicentral distribution of aftershocks (Figure 5.08) and the NNW to NW strike of geoelectric structures in MCTZ obtained by different MT strike analysis approaches strengthens our results that the MT strike in this region is transverse to the anticipated E-W strike of the Indian plate.

5.5 Summary

Strike analysis of MT data estimated from the GB technique yields a dominant regional structural strike of N95^{o}E. The east-west strike is in consistent with the strike of undergoing Indian plate beneath the Himalaya. Phase tensor analysis of the entire data also supports the estimated E-W strike from GB analysis. The shear and twist values obtained by MSMF mode for most of the sites lie much below the limit for validation of 2-D approximation. The RMS errors estimated by SSMF and MSMF analyses are also below 2. We therefore decoupled the decomposed MT impedance tensors into respective TE and TM by constraining the strike angle to N95^{o}E. These decomposed data are then used for 2-D inversion.

Detailed strike analysis for different geological domains of the region in various frequency bands (0.1-1s, 1-10s, 10-100s, 100-1000s) in view of high shear and twist values at some sites by GB approach (in MSMF and SSMF modes) has revealed local variations in the strike directions within the MCTZ. The strike direction is NNW to NW in MCTZ. The orientation of major axis of the phase ellipse obtained from PT analysis in all the four period bands and LT analyses of the sites in Sikkim dome also suggest the transverse nature of the MT strike within the zone. The estimated transverse feature correlates well with the trend of recent seismicity in this region and provides further support to the transverse tectonic model of the Sikkim Himalaya.

The study suggests that the deeper structure (10-1000s period), barring GFB, appears to be more homogeneous in terms of electrical conductivity distribution. The lower period data reveal the regional strike direction consistent with the E-W strike of the Indian plate. The data of 1-10s period yield regional strike direction of N51^{o}E, indicating the presence of NE-SW (or its conjugate) structure in the north Bengal Basin of GFB covered by these sites.

Chapter 6

2-D inversion and results

In the previous chapter, it has been pointed out that the recorded MT data after correcting for near-surface heterogeneities (in terms of shear, twist and anisotropy) using GB decomposition scheme suggest a dominantly two dimensional structure with a regional strike of N95^{o}E (considering 90^{o} ambiguity in the estimated tensor principal direction) in the frequency range 0.01-1000s. The overall E-W strike direction of the region is consistent with the strike of underthrusting Indian plate beneath the Himalaya. The RMS misfits estimated through MSMF technique over the frequency range are less than 2 for the maximum number of sites. These suggest that a 2-D description of the regional resistivity structure is valid and appropriate. However transverse strike (N30^{o}W) appears to be prevailing in the MCTZ inferred from various strike analysis schemes (Groom-Bailey, LaTorraca and Phase Tensor) as well as the analysis of RMS misfits of each site after GB decomposition. A close look of MSMF decomposition results for the sites (SH1-SH9) located in the GFB also shows distinct strike direction (N51W or with 90^{o} ambiguity) at shallow levels (1-10s). However, to fully interpret the MT data in terms of regional 2-D scenario, it is necessary to consider a regional strike of the region and convert the frequency domain apparent resistivity and phase data into a model of electrical resistivity as a function of horizontal position and depth. In this chapter, I would like explain the 2-D inversion processes, analysis of the results and examine the consequence of these strike variations in the 2-D interpretation of the data.

6.1 2-D inversion of the data

An electric strike angle of N95^{o}E estimated from the directionality analysis of impedance tensors of all 31 sites have been used to obtain the transverse electric (E-polarization, TE) and transverse magnetic (B or H -polarization, TM) mode data. MSMF decomposition scheme (McNeice & Jones, 2001) is used to decompose the data into TE- and TM-mode by fixing the

regional strike to N95^{o}E. For the present case, the TE mode is along the direction of N95^{o}E and TM mode is perpendicular to it. The resultant TE- and TM- modes are now subjected to the joint inverse (both TE & TM) modeling to delineate the 2-Dcrustal geoelectric structure along the profile as a function of depth.

The 2-D algorithm used for inversion of the present MT data is by Rodi & Mackie (2001). The forward modeling part is described in Mackie *et al.* (1988) and the inversion is based on a nonlinear conjugate gradients (NLCG) scheme implemented to minimize a regularized objective function (Rodi & Mackie, 2001). The NLCG method solves minimization problems that are not quadratic by selectively penalizing data residuals and spatial derivatives of the resistivity distribution (Rodi & Mackie, 2001). The algorithm gives regularized solutions to the 2-D inverse problem for MT data by minimizing an objective function ψ that is the sum of the normalized data misfits and the smoothness of the model. A brief description of various MT inversion schemes including NLCG algorithm are described in *chapter -3*.

6.1.1 WinGLink

WinGLink is a geophysical data modeling and interpretation package (*Geosystem SRL, Italy*) that includes forward and inverse modeling modules of various geophysical data such as Magnetotellurics, Gravity and Magnetics, Time domain electromagnetic, DC and well-logging. For the present work, we have used the package version 2.07.05b.

The MT module of *WinGLink* incorporates the 2-D forward modeling and inversion algorithm of Mackie *et al*. (1988) and Rodi & Mackie (2001) that computes a regularized solution of the inverse problem. It is based on the finite difference approximation of the Maxwell's equations and uses rectangular meshes to discretize the model for solving the forward problem. The finite difference mesh consists of cells of isotropic resistivity and extends much beyond the extent of the profile in the lateral direction and the depth of interest in the vertical direction to minimize the numerical artifacts. These extents are automatically prescribed using the concept of skin depth but can also be controlled manually. Starting from an initial guess model, the algorithm seeks a minimum structure model that minimizes the least squares misfit between observed and modeled data for each iteration. Although any initial guess model can be created using graphical interface of *WinGLink*, the normal practice is to start from anisotropic half-space model of uniform resistivity. The code has been found very stable and capable of reducing the model misfit to accepted levels (Solon *et al*. 2005).

6.1.2 Setting up of model

Six decades of the data with a minimum period of 0.001s have been considered for the inversion. Since our goal is delineation of crustal geoelectric structure of the region, we used the data of period $\geq 0.01s$ and excluded the high frequency data. The exclusion of high frequency data will also account for minimizing the inductive effects due to shallow structural heterogeneities as the inductive effects are frequency dependent and decrease with decrement in frequency (Jiracek, 1990).Vertical magnetic transfer function data have not been included in the present inversion process. At some sites especially located at high altitudes of north Sikkim we were unable to bury the vertical magnetic field sensor well deep due to hard rocks and tough terrain. Therefore, more rigorous tests are needed to ensure the quality of the Hz data before using these for inversion.

We considered the starting model as a homogeneous half-space of 100Ωm resistivity. As the topography along the profile varies considerably, from 20m at the southern end to about 5km at the northern end, we included topography in the model. This resulted in the inclusion of dense grids within the air domain above the topography. At first, we generated the grid by auto-meshing, performed joint inversion up to 100 iterations starting with the homogeneous half-space model, and then added further refined grids in the regions showing sharp variations in the resistivity in the inverted model. The discrete model thus generated consists of 180 rows and 180 columns having irregular grid spacing.

6.1.3. Control parameters

The 2-D inversion module of *WinGLink* requires setting of various control parameters such as smoothing parameter (τ), minimum horizontal (H) and vertical (V) dimensions of the cell and their respective scale factors α and β, resistivity of the initial model, assignment of error floors and range of data to be inverted. The result of the inversion scheme depends on these parameters so these are to be carefully chosen. Some experimentation with these parameters is also needed to ensure that the inverted model is not too sensitive to the changes in these control parameters. Below, I describe these inversion parameters and assigned values to these for the present work. The values of control parameters used in the present study are listed in Table 6.01.

In the smoothest model inversion, we used standard Laplacian operator as regularization operator and successive minimization of integral of Laplacian for $regularization\ order$ to

calculate the final 2-D model. 'Standard' smoothing algorithm uses a definition of smoothness that is consistent with the model dimensions. The uniform grid Laplacian operator will likely give relatively smooth models and assumes that for the purposes of computing the regularization function that the dimensions of the model are equal. (*WinGLink* manual). So we selected standard grid. Weight factors α and β control the smoothness of the model operator. An increase in α increases the horizontal smoothness of the model and an increase in β increases the vertical smoothness of the model. We have used default values of these parameters i.e. $\alpha = 1$ & $\beta = 1.5$ with respective cell dimensions of $H = 500$ & $V = 500$.

Table 6.01: Control parameters used in 2-D inversion

Parameter	**Value/ option**
Regularization scheme	Solve for smoothest model Regularization $Laplacian$ = Standard grid $Laplacian$ operator Regularization order = minimize integral of $\|Lapalcian\|^2$
Error floor (both modes)	Apparent resistivity - 20% Phase - 10%
Regularization parameterτ	Experimented for a range of values; final value 10
Weighting function parameters	$\alpha = 1;\ \beta = 1.5;\ H = 500; V = 500$
Mesh dimension	180 x 180; non-uniform grids
Initial model	Half-space of 100 Ω.m resistivity

Although individual data have associated error values, normally an error floor is used as the average error level in the data to restrict the inversion algorithm from fitting very small values of errors in the data and thus yielding a rough model (Parker, 1983). Further, in the absence of an error floor inversion will preferentially fit the frequency band having smaller errors ignoring data in other bands (Li *et al.* 2003). Hence with an adequate error floor, a better overall fit to a large frequency band of the MT data can be achieved. Comparably large error floor for apparent resistivity data could reduce the influence of static shift. Therefore, we have assigned an error floor of 20% for TE-mode apparent resistivity, 10% for TM-mode apparent resistivity and 5% for TE- and TM-mode phase data.

Thiel *et al.* (2009) analyzed the effect of localized band of conductive sediments in a long narrow valley orthogonal to a regional 2-D structure by 3-D forward modeling approach and concluded that MT response along the strike of the 2-D structure (i.e. TE-mode for 2-D case) would be affected by charge accumulations on either side of the conductive sediments. We,

therefore, set a large error floor for the TE-mode apparent resistivity. The down-weighting of the apparent resistivity data will not only accommodate the static shift in the inversion but also readjust the unrealistically small errors in the final inverted model. Becken *et al*. (2008) also demonstrated through a synthetic model study that down-weighing of TE-mode apparent resistivity helps in minimizing 3-D effects when the data are interpreted for 2-D structures.

An important step is the determination of a suitable value for the regularization parameter τ for the final inversion run. The regularization parameter controls the trade-off between data misfit and the model smoothness. Large values of τ lead to smooth models that have relatively larger data misfits whereas small values result in better fit to the data at the expense of decreased smoothness (Mackie *et al*. 1997). In such cases even minor jitter in the observed responses can lead to unacceptable accumulation of high conductance in localized regions, which has adverse influence on further convergence of the model. Thus, an optimum value of this parameter is needed for optimum solution.

We executed a number of experimental runs, starting with the homogeneous half-space as the initial model, for different values of τ ranging between 2 and 100 and iterated the solution up to 30 iterations. A tradeoff curve between the RMS error of misfit and model roughness is shown in Figure 6.01. From this analysis, an optimum value of τ equals to 10 is selected for the main inversion run.

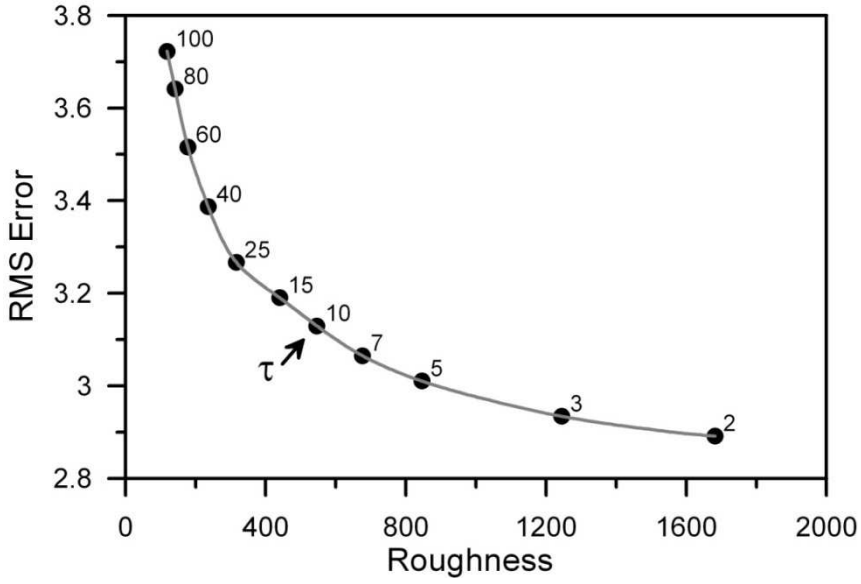

Figure 6.01: Curve showing tradeoff between normalized RMS error and model roughness for various values of the regularization parameter.

6.1.4 Joint Inversion of the MT data

We selected both TE- and TM-mode data to perform simultaneous (joint) inversion. The joint inversion (JI) scheme is generally used to estimate finest image of the electrical structure of the subsurface (Lemonier *et al*. 1999). The inversion process was initiated without considering static shifts. As such the data do not show any indication of static shift. However, we set large error floors for apparent resistivity in order to include the possibility of static shift because static shift affects apparent resistivity but not phase. For main inversion runs, we considered the starting model as a homogeneous half-space of 100Ωm resistivity and have used the grid including topography as described in section 6.1.2.

The RMS error of misfit is defined as (Xiao, 2004; Israil *et al*. 2008):

$$\text{RMS Error} = \sqrt{\frac{1}{2NM}\sum_{j=1}^{M}\sum_{i=1}^{N}\frac{\left(\rho_{ij}^{data}-\rho_{ij}^{data}\right)^2}{e_{ij}^{r2}}+\frac{1}{2NM}\sum_{j=1}^{M}\sum_{i=1}^{N}\frac{\left(\varphi_{ij}^{data}-\varphi_{ij}^{data}\right)^2}{e_{ij}^{p2}}}, \qquad (6.1)$$

where e^r and e^p are the standard errors associated with the resistivity and phase data, respectively; N and M are the number of sites and number of frequencies, respectively, is used to check the convergence of the inversion process.

6.2 Results

6.2.1 2-D geoelectric structure

Starting from the value of 10.23, the normalized RMS error decreased rapidly during the first six iterations beyond which the decrease was gradual. The solution became stable with insignificant decrease in the RMS error after 100 iterations. We therefore performed inversion up to 120 iterations. The final normalized RMS error is 3.0 at the end of iterations.

In order to get better appreciation of the relative contributions of different sites to the RMS error, we show site-specific RMS errors in Figure.6.02a. It is evident from the figure that the sites within GFB (sites SH1-SH9) provide excellent fit to the data. The largest errors are contributed by the sites within MCTZ (sites SH21-SH26) and those located at the northernmost end (sites SH30-SH31) of the profile. The change in the local strike direction for sites within MCTZ due to the transverse nature of the subsurface structure in this sub-domain (De & Kayal 2004; Hazarika *et al*. 2010) is likely to yield large errors for these sites.

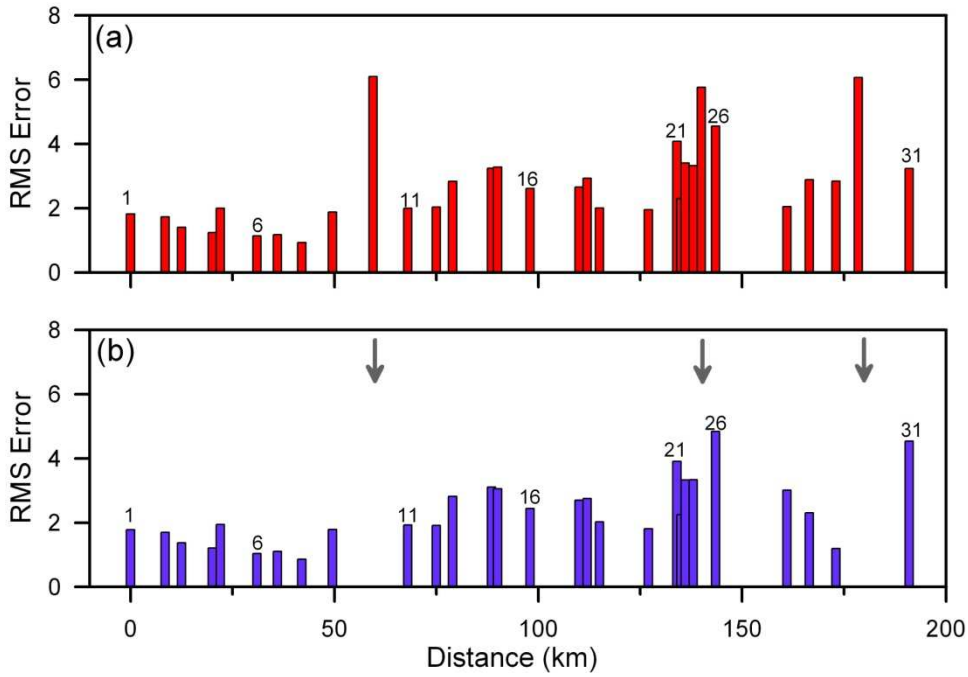

Figure 6.02: RMS misfit at every site along the profile for the inverted model for (a) 31 sites, and (b) 28 sites. Arrows in (b) represent the sites that have been dropped

The 2-D geoelectric model obtained after joint inversion is shown in Figure 6.03a. This model reveals salient features in the form of an assemblage of conductive and resistive zones. In the foreland basin region (sites SH1-SH9), the sediments/ sedimentary rocks of GFB occur as high conductivity (< 50 Ωm) layer of 4-6 km thickness underlain by a moderately conductive basement. Although top of a conductor and the total conductance are better resolved in MT method than the thickness of the conductor, the sharp contrast between the high and moderately conductive zones in this region possibly represents the basement (top of the Indian plate) and indicates that the Indian plate dips smoothly in this section of the profile. The SHD bounded between MFT and MBT is conductive in the uppermost 5 km showing continuation of the sedimentary rocks of GFB in this part. Further deep, the inversion results reveal the presence of a highly resistive steeply dipping block spanning 10 to 35km depth of the model. The geoelectric structure for the LHD shows the presence of an assemblage of many resistive and conductive blocks in the upper 15 km of the section and moderate resistivity for the deeper section beneath the entire LHD (Figure 6.3a).

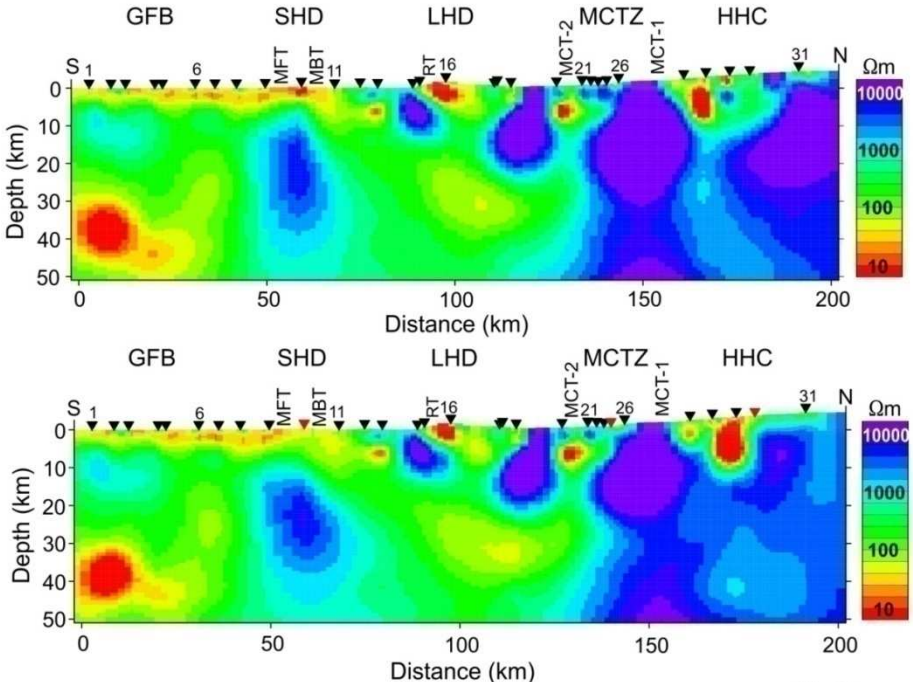

Figure 6.03: The geoelectric structure along the profile obtained after 2-D joint inversion of TE- and TM-mode data using (a) 31 sites, and (b) 28 sites. The red color symbols represent the omitted MT sites.

In the Sikkim Himalaya, MCT occurs as a several-km-wide zone bounded by MCT-1 and MCT-2. This is seen in the obtained geoelectric structure of the MCTZ. Here, we have delineated another nearly vertical highly resistive structure covering almost the entire depth range of the model. At shallow levels, the region close to MCT-2 is moderately resistive with the presence of a highly conductive structure just beneath MCT-2 at the depth of 5 to 10km but highly resistive block is located in the proximity of MCT-1. This type of structural configuration is in agreement with the geological understanding that MCTZ is a zone of intense deformation consisting of rocks representing both the Lesser and the Higher Himalaya (Dasgupta *et al.* 2004). Further north, the HHC region is also highly resistive at depths greater than 20km but in the shallow part < 20km, the presence of conductive and resistive zones is seen. The presence of a conductive block at 20-to-40km depth beneath GFB is also interesting.

As the site-specific RMS error values show large errors for some sites (Figure 6.02a), we have analyzed the influence of these sites on the inversion results by removing three sites (SH10, SH25, and SH30) having RMS errors of greater than 4.5. The data of the remaining 28 sites were inverted keeping all other control parameters the same as used for the model discussed above. The final normalized RMS error now reduces to 2.5 after 120 iterations. The

site-specific errors for this case are shown in Figure 6.02b. The removal of sites SH10 and SH25 does not have significant effect on the RMS errors of the neighboring sites but removal of site SH30 results in decrease in the RMS error of site SH29 and increase in RMS error of site SH31. The final 2-D model for this case is shown in Figure 6.03b. The broad subsurface structure is largely the same as obtained by using 31 sites. However, the conductive structure in HHC is now more pronounced.

6.2.2 Pseudo sections

Pseudo sections are interpolated and contoured images of apparent resistivity and phase values versus period, with period increasing downward as a proxy for depth. Although these images might be distorted due to the representation of distances as period instead of true depth, some major features can be recognized. TE-mode apparent resistivity pseudo-section (Figure 6.04) suggests a vertical resistor sandwiched between two conductors at the northern segment of the profile. Two highly conductive zones, one below LHD and another below HHC region are seen from TM-mode pseudo-sections. A high resistivity zone is commonly appeared in both modes apparent resistivity pseudo-sections at northernmost end of the profile. High phase values below MCTZ in TM mode and low phase values below GFB in TE-mode are the remarkable features seen in the pseudo-sections. A comparison of the responses for the final inverted model with the pseudo-sections of the observed data is shown in Figure. 6.04. These results highlight that a majority of synthetic responses corresponding to the final 2-D model correlate well with the observed data.

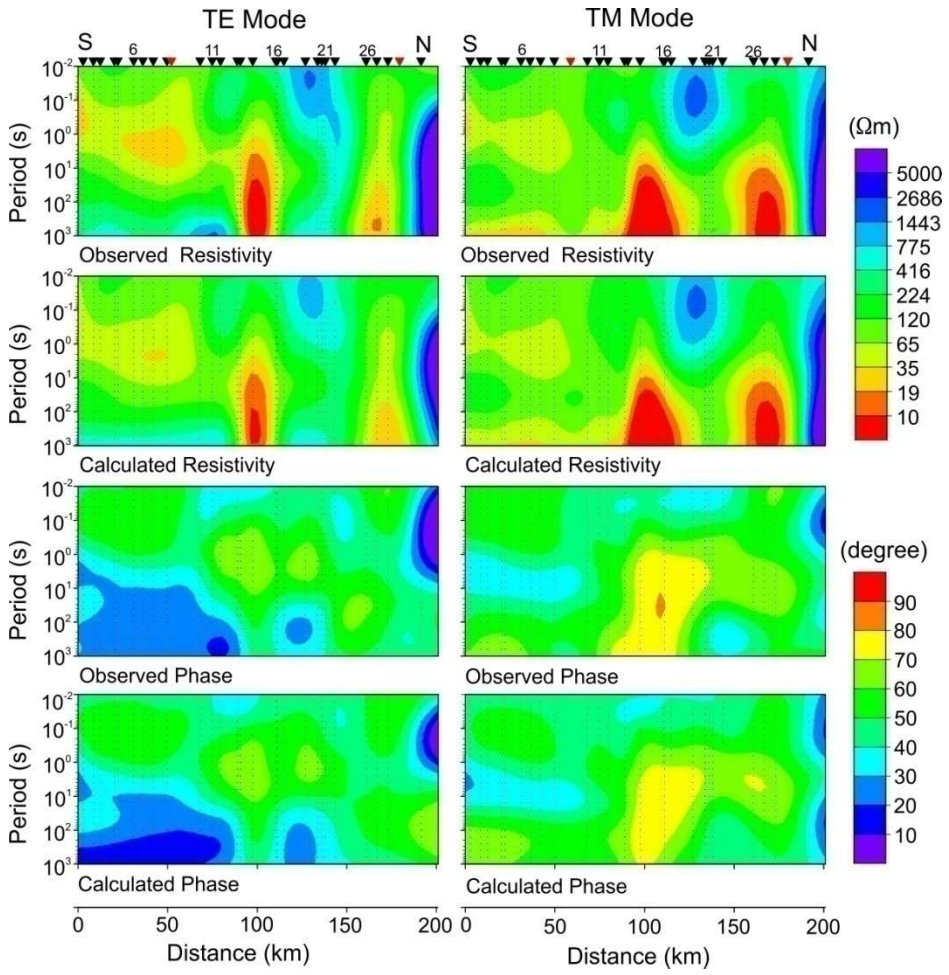

Figure 6.04: Pseudo-sections showing observed and computed responses for both TE- and TM-mode data for the geoelectric model shown in Fig.6.03b. Black dots in the images represent data points.

6.2.3 Individual TE- and TM-mode inversions

We further analyzed the relative contribution of TE- and TM-mode data to the final 2-D geoelectric structure shown in Figure 6.03b by inverting the data of these modes individually by keeping the control parameters same as used for JI. Theoretical studies demonstrate the varying sensitivity of MT data for different geoelectric structures. The TE-mode impedance is more sensitive to the buried deep lithospheric conductors whereas the TM-mode is poorly sensitive to the deep conductive structures. On the contrary, TM-mode is more sensitive to lithospheric resistance than the TE-mode one (Berdichevsky *et al*. 1998).

The RMS errors at the end of 120 iterations are 2.37 and 1.70, respectively, for the individual TE- and TM-mode data. The results (Figure 6.05) reveal that both modes contribute to the final JI model and the high resistivity block beneath MCTZ that now

extends beneath LHD is seen in TE-mode suggesting that TE-mode inversion is incapable of resolving deep resistive structures. TM-mode reveals a high conductivity block beneath LHD. The deep conductive anomaly in the depth range of 30-45km below GFB is observed in TE-mode inversion (Figure 6.05a) but not in TM-mode suggesting that the TE-mode impedance is more sensitive to the buried deep lithospheric conductors than TM-mode. In contrast, the resistive feature below SHD is well resolved in TM-mode result (Figure 6.05b) but is replaced by a conductor in TE-mode.

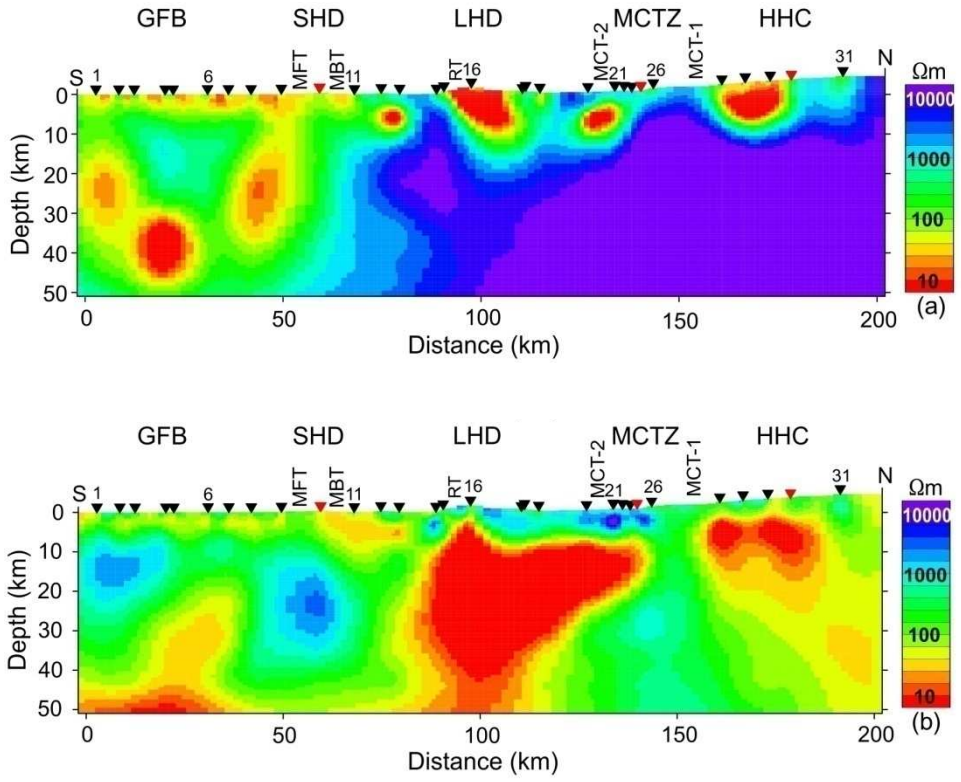

Figure 6.05: 2-Dgeoelectric section obtained by individual TE (a) &TM (b) mode inversion

6.3 Sensitivity analysis and constrained inversion

6.3.1 Sensitivity analysis

The sensitivity image for the 2-D geoelectric section using 28 sites is shown in Figure 6.07 to give an idea about the quality of the inverted model. The values are calculated by summing up column wise the absolute values of the error-weighted sensitivity matrix using the code of Mackie *et al.* (1997). These sums are normalized by cell area and assigned to the respective grid elements. The structures with sensitivity matrix values of above 0.0001are considered to be resolved features here following several other works like Brasse *et al*. (2002) and Ledo &

Jones (2005). A large value of the sensitivity parameter (red, yellow, and green colors) indicates a well-resolved region. A general decrease of sensitivity with depth becomes visible, which is more rapid beneath SHD. In general, conductive zones are better resolved than the resistive zones but we get large sensitivity values also for the resistive structure beneath MCTZ.

We also test the robustness of various features of final 2-D model marked as blocks A-E in Figure 6.07 by removing these blocks one at a time and then computing the resulting RMS error. Removal of conductive block A (Figure 6.07) leads to moderate increase in the RMS error at sites SH1-SH8 (Figure 6.08) whereas removal of resistive block B affects sites SH10 and SH12. The RMS errors in respective locations increase many-fold when any of the conductive blocks C, D, and E are removed (Figure 6.08) implying that these features are necessary to fit the observed impedances.

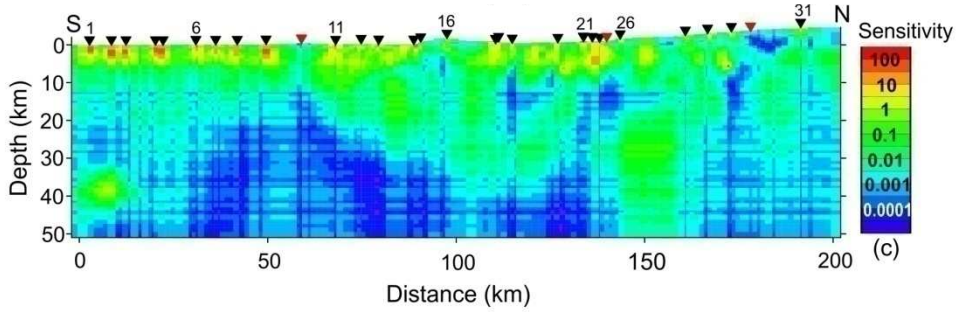

Figure 6.06: Sensitivity map corresponding to the figure 6.03b

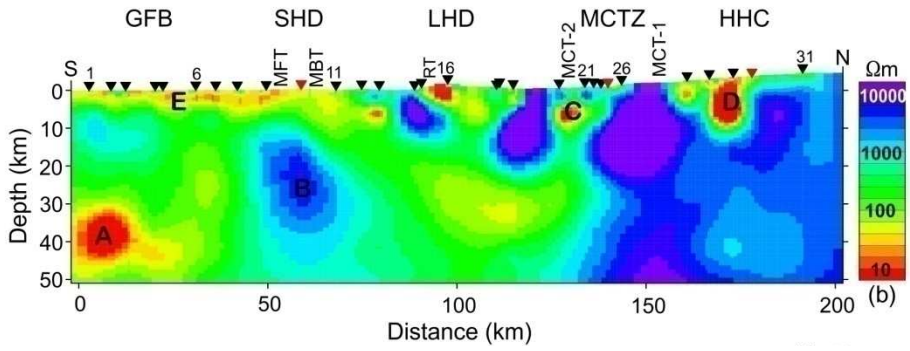

Figure 6.07: The 2-D model with major conducive and resistive blocks marked as A-E

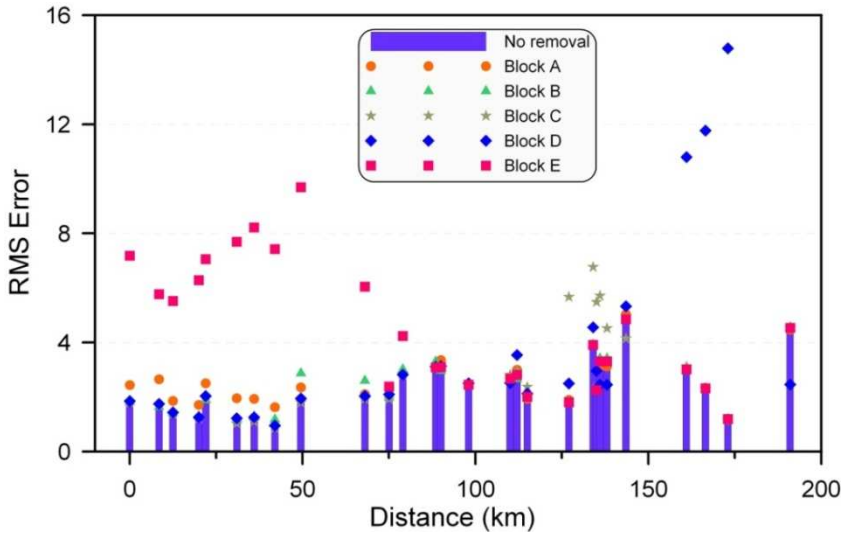

Figure 6.08: Effect of removing various blocks shown in Fig.6.07 on the RMS error

6.3.2 Constrained Inversion

Inversion of geophysical data suffers from the problem of non-uniqueness. It is therefore important to test the robustness of inverted model. Inversion of geophysical data suffers from the problem of non-uniqueness. It is therefore important to test the robustness of the inverted model. Generally, constrained inversion is performed to check the robustness of features in the inverted model (Li *et al.* 2003; Unsworth *et al.* 2004). Figure 6.03b shows an assemblage of several conductive and resistive blocks. We performed constrained inversion for seven conductive and resistive features (Figure 6.09a) to analyze the robustness of these features. For this purpose, we removed the feature to be analyzed by setting its resistivity to the background value and then performed inversion from this model as the a priori model. We inverted the data till the converge of the RMS error is achieved keeping the control parameters the same as used to obtain the final model (Figure 6.03b).The RMS errors for all cases are close to 2.50 and major features remain largely unchanged among all models. The inverted models corresponding to blocks B3, B5 and B6 are similar to Figure 6.09b and the RMS errors of corresponding neighboring sites are not very different from the RMS errors of these sites for the final model (Figure 6.03b). Therefore, the structures only for the remaining blocks are shown. Figure 6.09e shows the relative difference in percentage of the site specific RMS errors. A value of less than zero means that the RMS error of the model after constrained inversion is less than the RMS error of the final model. The inverted model for block B1 (MCTZ) now shows the presence of a conductive zone sandwiched between two resistive blocks (Figure 6.09a) at the depth of 20-30 km, coinciding with the inferred depth of

MHT in this region (Figure 6.15), although the RMS error remains largely unaffected. The resistive blocks seem to be robust features. Constraining the block B2 in HHC does not change the gross subsurface structure implying that this conductive feature is also robust (Figure 6.09b). However, the RMS errors of neighboring sites within MCTZ and HHC show significant improvement. The conductor B4 beneath GFB seems to be not well constrained as the constrained inversion results show absence of any such conductive blocks (Figure.6.9c). The RMS error is improved. Constrained inversion after the removal of conductive and resistive blocks marked as B7 has significant influence on the RMS error, which is significantly deteriorated, compared to the final model errors even though the conductive and resistive blocks are re-produced after constrained inversion (Figure 6.09d). These results indicate that all blocks except B4 are robust and are needed to explain the observed responses.

6.3.3 Down-weighting TE-mode data

Becken *et al*. (2008) have demonstrated through a synthetic model study that downweighing of TE-mode apparent resistivity helps in minimizing 3-D effects when the data are interpreted for 2-D structures. They analyzed that 100% down-weighing of TE-mode apparent resistivity data even take cares the strong 3D effects in the observed data while interpreting interms of 2-D. So, we further tested the effect of down-weighting TE-mode data in the derived 2-D resistivity model. We have used same inversion parameters (Table 6.01) as used for the final 2-D model. The final RMS error for this case is very much same to the previous model. The resultant model then obtained is shown in Figure 6.10 The 2-D geoelectric section for this case also shows the same conducive/resistive feature except below HHC. In the northern end of the profile, the shallow high conductive zone observed in the final model disappeared and the high resistivity at mid crustal levels in the final 2-D structure is replaced by moderate resistivity of 100-200 Ω.m in current model.

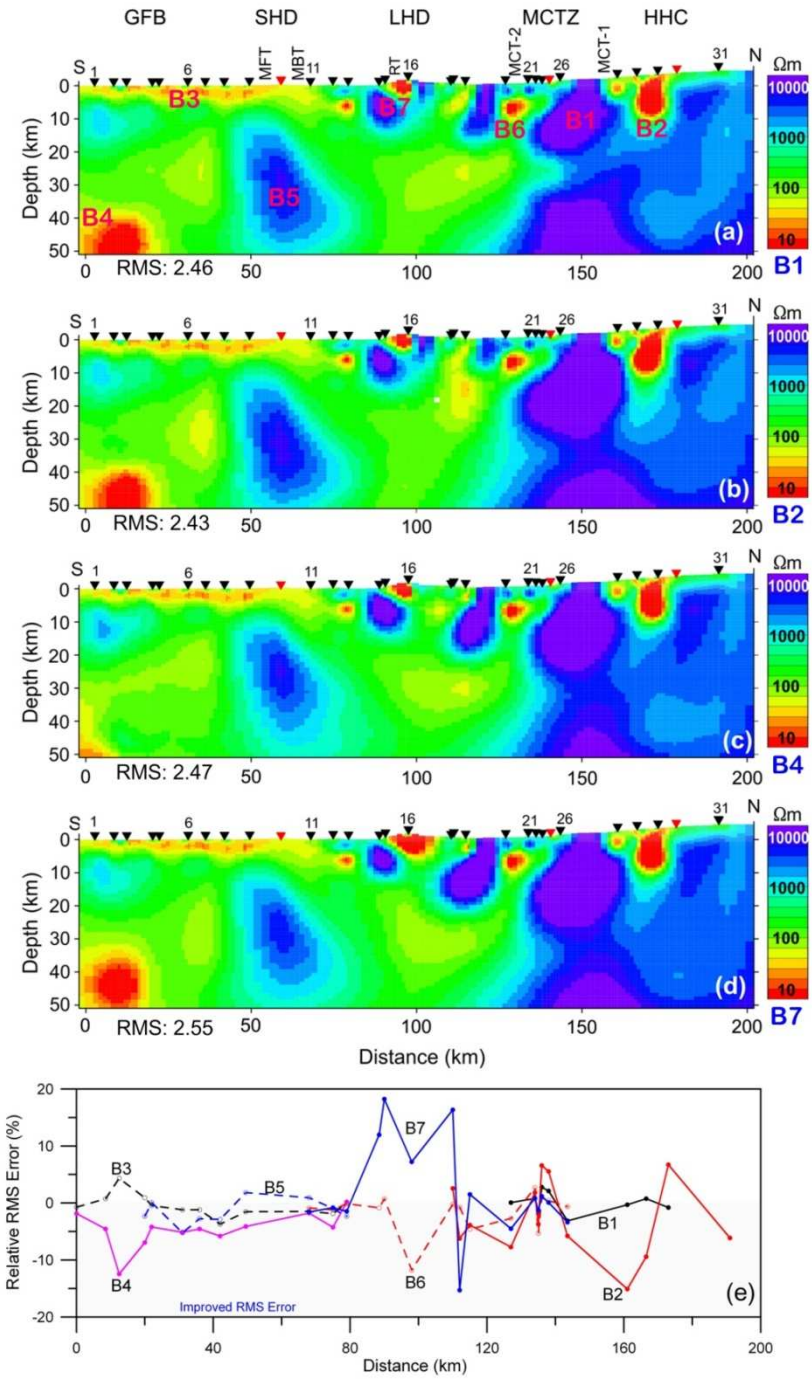

Figure 6.09: (a-g) Results of constrained inversion after fixing the resistivity of individual blocks (marked as B1 to B7) one at a time, and (h) geoelectric structure after joint inversion assigning equal error floors to TE- and TM-mode data

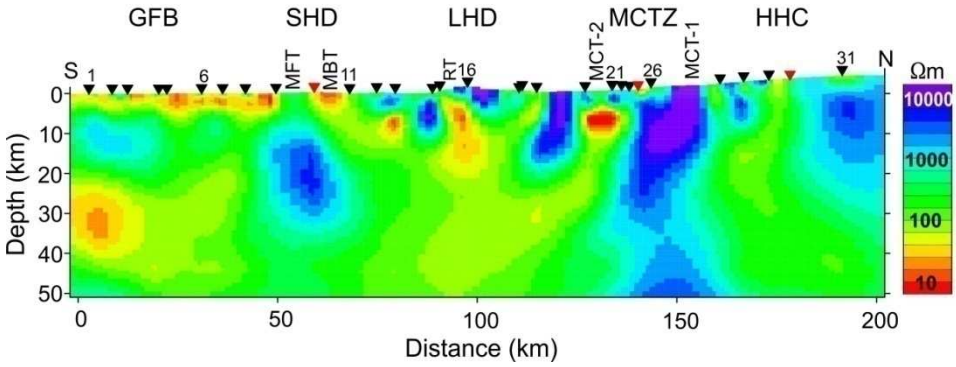

Figure 6.10: 2-D geoelectric section obtained after 100% down weighting TE mode apparent resistivity data

6.4 Comparison with earlier MT study

Patro and Harinarayana (2009) delineated the crustal geoelectric structure of the region along an approximately NNE-SSW profile (hereafter termed as PH2009) (Figure 6.11, top panel). The dominant regional strike obtained by the study was N80^{o}E. The results from the present work (Figure 6.11, bottom panel) bring out fine geoelectric structure and considerable variations are seen particularly in the MCTZ region. The present 200km long profile extends the both southern (GFB region) and northern limits (close to STDS) of the PH profile.

If we broadly compare the features in both the models, the feature B in the present study is similar to R1 (PH). The shallow resistive feature R2 in PH2009 model is observed in the present study that lies beneath sites SH13 to SH15 at <10km depth. Further, instead of the high resistive anomaly seen in PH2009 model (R3) moderate resistivity (<100 Ω.m) is observed below the LHD in greater depths. The other features obtained in the present work, particularly fine resistivity contrasts below LHD, highly resistive vertical zone below MCTZ and shallow conductive feature below HHC, are not present in the PH2009 model. It could be due to more MT sites in this region that have possibly helped in deciphering the fine-scale structure. Similarly the deeply located highly conductive feature in the PH2009 model labeled C4 is not observed in the 2-D structure obtained in the present study at that depth levels but confined to shallow levels labeled ‘C’.

6.5 Analysis of the results

6.5.1 Integration with Seismotectonics of the region

We analyze the obtained crustal geoelectric section (Figure 6.03b) in terms of seismicity and tectonics of the region. Nath *et al*. (2005) reported focal depths of 80 events of magnitude ($3 \leq M \leq 5.6$) recorded by Sikkim Strong Motion Array during 1998 - 2003. Hazarika *et al*. (2010) used data of 11 broadband stations operated in Sikkim by CSIR-NGRI during 2006 - 2007 and relocated 356 events by using hypoDD program. We have compiled the data from these two studies and have superimposed these on Figure 6.03b as black open circles. We have also included a few events from Dasgupta *et al*. (1987) falling within the present region. Spatial distribution of these events is shown in Figure 5.08 of chapter 5. Although projection of spatially scattered epicentral locations on the profile is a simplification, we superimpose these events on the subsurface structure along the profile to check whether there is any noticeable correlation between the hypocentral locations and the conductive/resistive blocks delineated by the present study. Figure 6.12 shows geoelectric section with superimposed depth distribution of seismicity. Even though the seismicity distribution is diffused, there seems to be concentration of events between 100 to 125km lateral distances. In an earlier study, De & Kayal (2003) analyzed the data of microearthquake surveys during 1993 and 1999 and proposed that MBT in Sikkim Himalaya is seismogenic and mantle-reaching fault. It does not converge with the plane of detachment unlike in the western Himalaya (Seeber *et al*. 1981). We have superimposed traces of MBT, MCT, detachment plane (MHT) and the Moho shown by De & Kayal (2003) on Figure 6.12 to see if these features reveal any correlation with the geoelectric section.

It is interesting to note that the seismicity is largely confined between MBT and MCT (white dashed curves in Figure 6.12) of De & Kayal (2003) but does not concentrate along the MBT or at its intersection with the Moho as proposed in their study. In fact, more concentration of seismicity is seen beneath sites SH17-SH20 at the depth of about 15 to 20km at the base of the resistive block. If we mark a fault trace (orange dashed curve) from site SH15 downward separating the conductive and resistive blocks and extend it up to this zone of concentration of seismicity then the seismicity correlates with the intersection of this fault with the MHT. We thus infer the presence of a seismogenic fault in the region situated between MBT and MCT-2, which could be responsible for the recurrent seismicity in this

region. An improvement in the location of hypocenters to constrain the diffuse nature of seismicity is never-the-less needed to further characterize this fault.

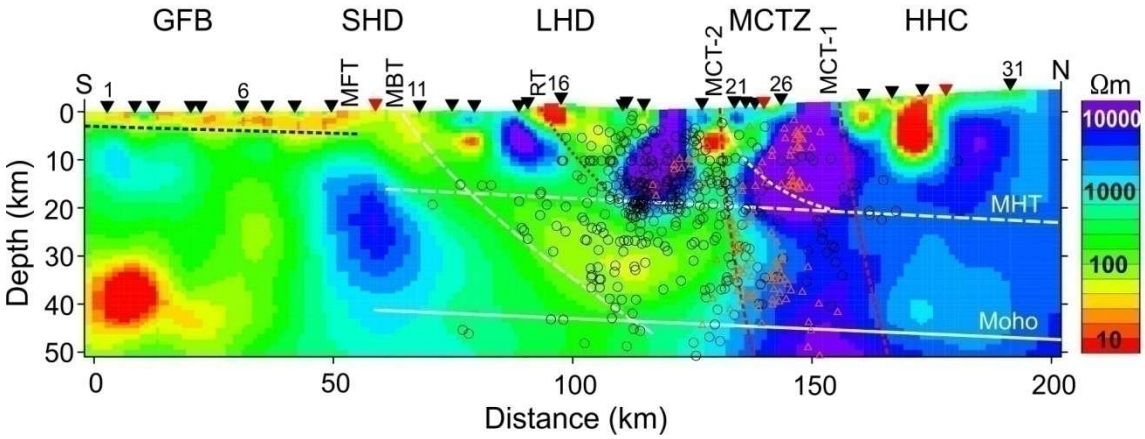

Figure 6.12 Geoelectric model shown in Figure 6.03b with micro-seismicity (black open circles) and other faults superimposed. Microearthquake data from Hazarika *et al.* (2010), Nath *et al.* (2005), and Dasgupta *et al.* (1987). Traces of MBT, MCT, MHT, and the Moho (white dashed curves/ lines) are from De & Kayal (2003). Hypocentral distribution of microearthquakes after the September 18, 2011 Sikkim earthquake is shown in red open triangles (Ravi Kumar *et al.* 2012). The basement (black dashed line) and traces of MCT-1, MCT-2 and an intermediate thrust fault (thick dashed curves in color) are inferred in the present study

Mukul (2010) argues from structural geology considerations that MBT is unlikely to be seismogenic because it has been folded in this region by South Kalijhora Thrust (SKT) and faults get folded by younger footwall faults in fold-thrust belts once they become inactive (Boyer & Elliott, 1982). He also proposed that earthquake hypocenters could be related to the MHT and/or out-of-sequence or reactivated thrusts in LHD (here LHD refers to Lesser Himalayan Duplex). The surface location of our inferred fault is near MT site SH15, which lies in the proximity of the RW exposing Gondwana rock. This location also approximately coincides with the RT (Mukul, 2010). Therefore, the fault inferred by the present MT study could be the Ramgarh thrust which is probably seismogenic leading to recurrent seismicity in this region. In such a scenario, high conductivity zone along the fault in the uppermost 5km between sites SH15 and SH16 could be related to the Gondwana rocks, which are being upthrusted and exposed due to erosion along the fault.

The MCTZ in the geoelectric section appears mainly as a high resistivity nearly vertical zone consisting of two extremely resistive blocks separated by a relatively low (but still very high) resistivity zone. The trace of MHT (De & Kayal, 2003) passes through the base of the

first high resistivity block. Since any conductive feature, if present within the middle relatively low resistivity zone is not resolvable, we infer that MCT-1 and MCT-2 are steeply dipping faults (dashed curves bounding MCTZ in Figure 6.12) that bound the resistive zone unlike a single MCT trace (white dashed curve in Figure 6.12) shown by De & Kayal (2003). The low resistivity zone in the upper 10km at MCT-2 supports the geological observations that rocks of LHD and HHC co-exist in MCTZ. If we assume the low resistivity region as representing LHD rocks, then these rocks taper at depth and more resistive HHC rocks dominate. We have also projected the hypocentral distribution of microearthquakes recorded after the September 18, 2011 earthquake (Mw 6.9) (Ravi Kumar *et al.* 2012) along the MT profile in Figure 6.12 (red open triangles) to see if these have any correlation with the resistivity structure obtained in the present study. Spatial distribution of these microearthquakes is also shown in Figure 5.08 of previous chapter. This earthquake occurred at the depth of 50km on a NW-SE trending nearly vertical fault (Ravi Kumar *et al.* 2012). These microearthquakes are confined to the resistive zone or at the contact between the resistive MCTZ and conductive LHD. Thus, nearly vertical resistive MCTZ seems to have an important control on the tectonics and seismicity of the region.

The region north of MCT-1, geologically demarcated as consisting of High Himalayan Crystallines, also shows the presence of high conductivity block beneath sites SH26 and SH 30. Patro & Harinarayana (2009) also reported such a high conductivity block north of MCT although none of their MT stations lies above this block. Their profile is east of our profile and the southern end 100 line of the INDEPTH profile (Unsworth *et al*. 2005) is further east (Figure 6.13). We compare in Figure 6.13 the structures of these three regions that fall in almost same latitude range but are longitudinally separated. The color scales in the three images are different but comparing the numerical values it may be inferred that a conductive zone (< 10Ωm) is present within the high resistivity rocks of HHC. Joining the high conductivity zones delineated by the present study and PH2009 (Figure 6.13) implies a NNW-SSE trend of the conductive zone but PT and GB results for the period band of 0.1-1s and 1-10s preclude any such trend. A detailed coverage of this conductive zone with more MT stations at close spacing would be needed to ascertain the extent of this anomaly.

The crustal structure of the Sikkim Himalaya north of MBT, as delineated by the present study, consists of at least three major conductors in the uppermost 20 km depth section. The first conductor between sites 15 and 16 correlates well with the Gondwana rocks exposed in the Rangit Window. Therefore, we attribute this conductor to the presence of thick

Gondwana sequence. The cause for the other two conductors, one between sites SH20 to SH24 and the other between sites SH27 to SH30, is less obvious. The most acceptable explanations for electrical conductors invoke the presence of aqueous fluids or partial melts (Hyndman & Shearer 1989; Li *et al*. 2003; Unsworth *et al.* 2005). Patro & Harinarayana (2009) linked the high conductivity to the presence of fluids released due to metamorphic dehydration. The heat flow values may distinguish between the above two competing causes. However, in absence of heat flow values the question of what causes these conductive anomalies in an actively deforming collision belt remains open. For the conductor within HHC an alternative explanation is also possible. The geological map (Figure 2.01) demarcates STDS, separating high-grade crystalline rocks of HHC from the Cambrian and Eocene sedimentary rocks of the Tethyan belt, further north of our MT sites. If STDS lies further south of its present shown position then the conductor could be linked to the sedimentary rocks. We infer such a model to explain the conductive zone within HHC although the role of fluids/partial melts is not ruled out. A photograph (Figure 6.14) from a location close to the site SH30 supports the presence of young poorly lithified sedimentary rocks in the region south of the presently demarcated position of STDS. If it represents partial melts then the conductor could be linked to the mid crustal partial melts beneath southern Tibet as delineated by INDEPTH study.

Figure 6.12 reveals a sharp contrast in the electrical resistivity of the crust across MCT-2, the southern segment being in general moderately conductive and northern segment highly resistive. The model is significantly different from those obtained for western Himalaya (Israil *et al.* 2008) or central Himalaya (Lemonnier *et al*. 1999) showing a crustal ramp structure associated with downthrough of MHT. Crustal seismic and MT results along the 100-line of INDEPTH profile characterize MHT as moderately conductive north dipping seismic reflector (Unsworth *et al.* 2005). The depth of MHT at the longitude of our site SH27 is about 25 km in INDEPTH section (Figure 6.13). The location of MHT beneath this site taken from De & Kayal (2003) (Figure 6.13) is also in agreement with INDEPTH results. However, it is difficult to place MHT beneath the MCTZ region in the present model because the structure appears to be nearly vertical and continuing over the entire depth range. A slight reduction in the resistivity of the structure in the depth range of 20-30km (more clearly seen in Figure 6.09a) could be attributed to the presence of a conductive MHT in this region but the ambiguity in its depth is large. We have attempted to resolve this ambiguity in the next subsection.

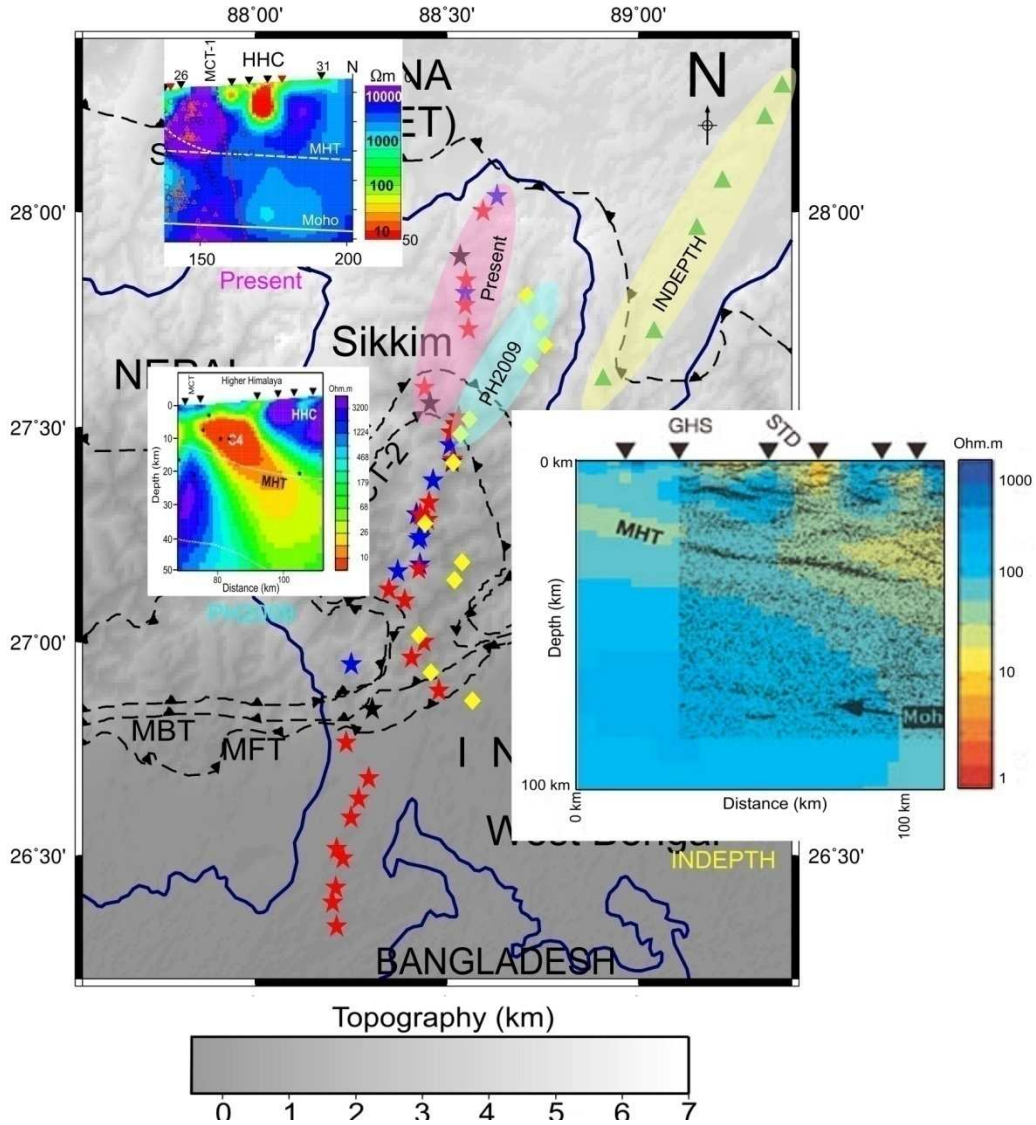

Figure 6.13: A comparison of the models of the crustal structure of north Sikkim obtained by the present study, Patro & Harinarayana (2009) (referred in the figure as PH2009), and Unsworth *et al*. (2005) along 100 line of the INDEPTH. Locations of MT sites from these studies are superimposed on the topography map (shaded background map) of the Sikkimregion. Red and black stars show our sites, yellow diamonds the sites from Patro & Harinarayana (2009), and green triangles the sites from the INDEPTH profile. Blue stars are sites that we have discarded due to bad data quality

Figure 6.14: A photograph showing young poorly lithified sedimentary rocks taken in a area close to site SH30

6.5.2 Effect of transverse tectonics

In the above study, we have considered a dominant regional strike direction of N95^{o}E for the entire profile and inverted the decomposed apparent resistivity and phase data under the assumption of two-dimensionality of subsurface structure. Seismological (De & Kayal 2004; Hazarika *et al*. 2010) as well as present magnetotelluric strike analyses studies however have revealed the presence of transverse tectonics especially in the region of MCTZ. The detailed strike analysis of the entire data set by both GB and PT approaches, discussed in section 5.4.2, has further supported the presence of transverse features. We analyze the effect of transverse features beneath MCTZ on the 2-D geoelectric section of the crust. The RMS errors of MSMF analysis (Figure 5.02) has revealed that the effect of transverse tectonics is prominent up to 10s period beyond which the errors of misfit for N95^{o}E and N30^{o}W regional strike are comparable. Therefore, we have inverted the data in the period bands of 0.01-10s. We replaced the TE- and TM-mode data of sites 21-26 with those obtained by decomposing impedance tensors by fixing the rotation direction to transverse strike direction keeping the data of other sites the same as used for previous joint inversion. Although such a stitching of data sets is inconsistent with the assumption of regional two-dimensionality, we have attempted this approach on experimental basis. The data sets in the period band of 0.01-10s

were inverted keeping all control parameters unchanged. The RMS error is 2.0 after 120 iterations. The results (Figure 6.15a) indicate the presence of a conductor beneath MCT-2 coinciding with the inferred MHT. Therefore, we infer that MHT is at the depth of 20-to-22 km beneath MCTZ and correlates well with the projection of MHT obtained by INDEPTH study to this region. The deeper structure is not resolved because we have used data up to 10s period. Sandwiched conductive zone obtained after constrained inversion shown in model Figure 6.09a for block B1 also supports the possible location of MHT at the depth range of 20-30 km.and correlates well with the projection of MHT obtained by INDEPTH study to this region.

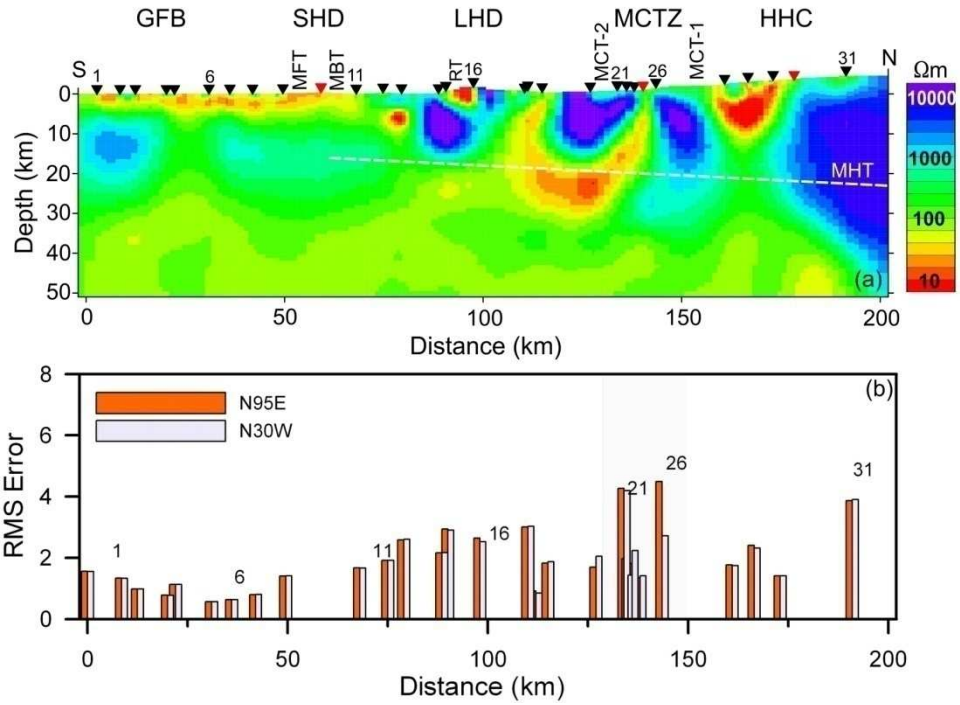

Figure 6.15: (a) The geoelectric structure obtained by joint inversion of TE- and TM-mode data of 0.01- 10s period band after incorporating the effect of transverse tectonics for sites SH21-SH26, and (b) RMS error of misfit at every site for the present model (grey color) and the model shown in Figure 6.3a (orange color).

6.5.3 Inversion in two different period bands

The SSMF and MSMF analyses of the MT data indicate that the error of misfit is in general large in the period band of 0.001 – 10s compared to the error at larger periods. The transverse strike of the subsurface structure within MCTZ seen up to 10s period is also not distinct at larger periods as the errors of misfit for N95^{o}E and N30^{o}W regional strike are comparable. Therefore, we have inverted the data in the period bands of 0.001-10s and 10-1000s respectively to isolate the effect of shallow (upper 10-15km) and deeper structures on the

observed responses. The inversion steps, control parameters and initial model were the same as used for joint inversion of TE- and TM-mode data of 28 sites.

The subsurface structure up to 10km depth obtained from the first period band (Figure 6.16a) is very similar to Figure 6.15. The only major difference is seen beneath MCT-2 (sites SH19-SH20) where the resistive block terminates at 6-7 km depth and is followed by the presence of a conductive zone. The subsurface structures below 10km depth are different. The subsurface structure delineated for the larger period band (Figure 6.16b) is comparable to Figure 6.15a. The major conductors at depths shallower than 10km including the sediments of GFB are also recovered in this model but the resistive block beneath sites SH14-SH16 is faint in this figure. Thus, the impedance tensors at period larger than 10s appear to be adequate to delineate the subsurface structure of the region.

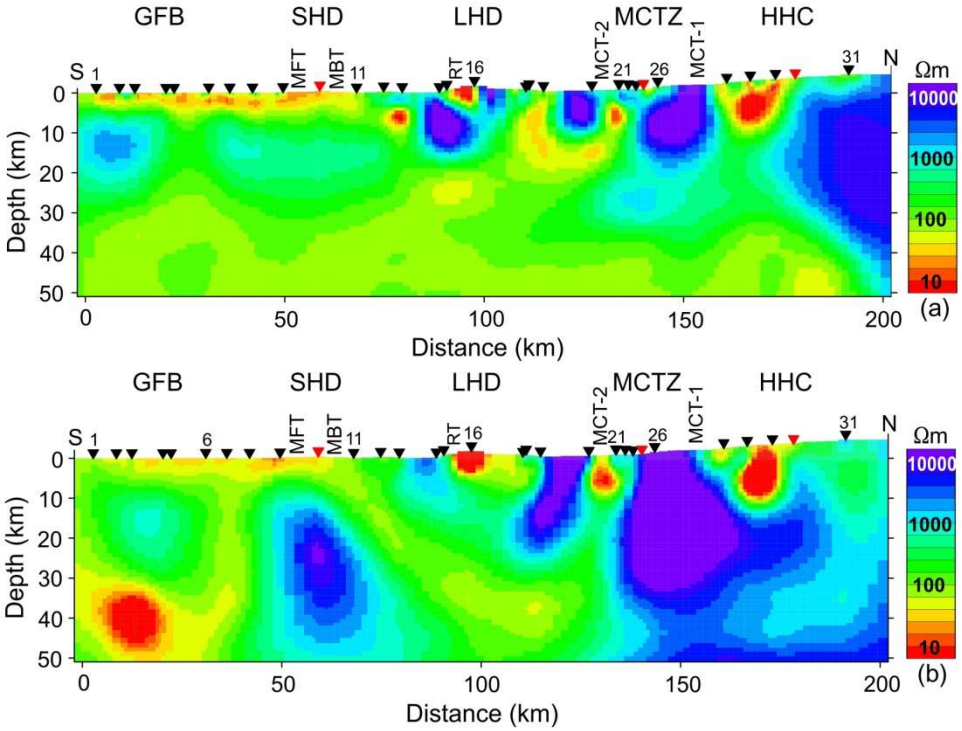

Figure 6.16: The geoelectric structure obtained by joint inversion of data of (a) 0.01-10s, and (b) 10-1000s period bands

6.6 Summary

The crustal geoelectric structure obtained by 2-D joint inversion of the TE- and TM-mode data in the frequency band of 0.01 – 1000s, acquired along the profile traversing across the Sikkim Himalaya and the adjoining northern Ganga Basin, shows several interesting features.Starting from the southern end, the top of the Indian plate (presumably MHT) dips gently and is overlain by alluvial sediments and probably Gondwana rocks, both together appearing as a high conductivity layer that thickens from about 4 km at the southern end to 6 km at MFT. Here, a ramp structure is formed and MHT is displaced downward by about 15 km. Further north, MHT again appears to be dipping at a smooth angle. The ramp structure can be correlated with one of the thrust sheets (MHT, MBT or intermediate SKT). In the Garhwal (Israil *et al.* 2008) and central Nepal (Lemonnier *et al.* 1999) Himalaya the mid-crustal ramp has been reported at MCT and has been correlated with intense seismicity associated with a deep conductive zone. In our model, seismicity is largely confined within LHD. The present results are a remarkable departure from those reported for the western and central Himalaya and support the view that the Sikkim Himalaya is tectonically complex. We further infer a major fault located between MBT and MCT-2, the surface trace of which at about 100 km profile distance correlates with the Ramgarh Thrust (RT), as a major seismogenic fault rather than steeply dipping MBT, as proposed earlier by De & Kayal (2003), causing recurrent seismicity in the region.The high conductivity zone along this fault may be representing the Gondwana rocks exposed along Ramgarh Thrust in the Rangit Window.

Patro & Harinarayana (2008)	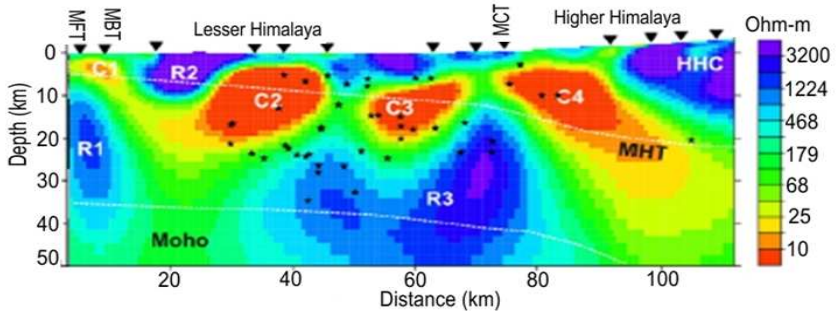 **Nr. of Sites : 13**	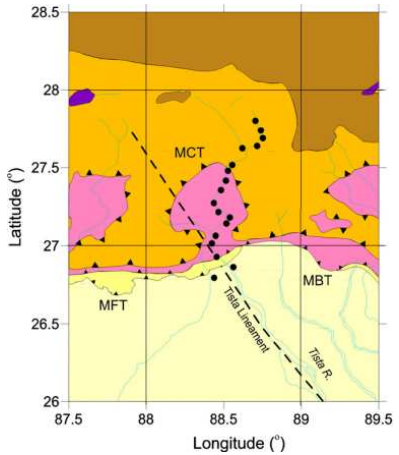 **Profile length: ~ 110km**
Present work	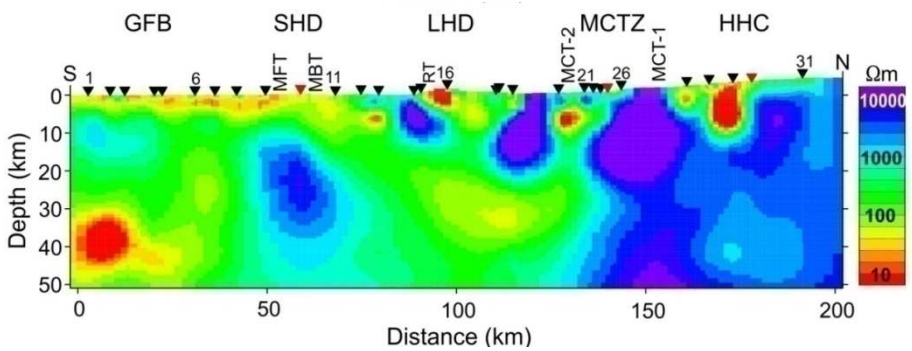 **Nr. of Sites: 28**	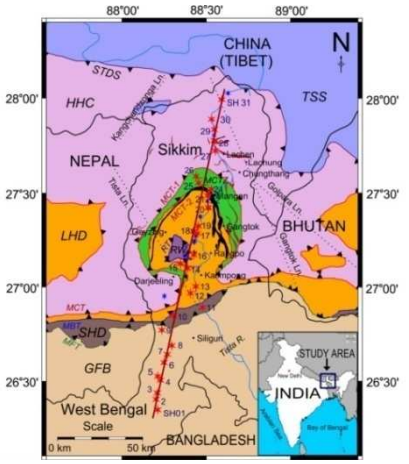 **Profile length : ~200km**

Figure 6.14: Comparison of the PH model and the geoelectric structure obtained in the present study

Chapter 7

Analysis of anomalous phase behavior

7.1 Introduction

Observed MT responses are many times distorted due to cultural and geological noise. Local shallow small-scale conductivity anomalies can lead to galvanic distortions and/or current channeling causing frequency independent scaling of the MT resistivity curves leaving phase unaltered. These effects are normally minimized through tensor decomposition analyses and regional strike determination (Groom & Bailey, 1989; McNeice & Jones, 2001). In chapter 5, we performed distortion and dimensionality analysis and estimated the regional geoelectric strike (described in chapter 5) for our dataset. Besides analyzing the dimensionality of the MT data, another objective is to find out whether the entire dataset can be explained with a 2-D regional model or has some regions along the profile where the regional electric field is strongly distorted and polarized in one direction due to high concentration of currents that are channelled by the local conductors. This analysis was stimulated by the observation that our measured MT data from some sitesshow impedance phases of the yx- component of the electric field exceeding 90◦, therefore manifesting strong distortion effect. Jones (1983, 1988) suggested thatin some special geological setups MT curves can be severely distorted by strong current channeling which manifests itself in the form of phase values exceeding 90° due to the current deflection/channeling/gathering. This leads to violation of observation that MT phase curves are bounded within a specific phase quadrant (Weidelt & Kaikkonen, 1994) for simple 1-D (2-D) model with isotropic layers (blocks). In such situations, most of the tensor decomposition schemes are unable to recover the regional 2-D strike due to the *a-prioiy* assumptions described in chapter 5.

The work in the chapter is published in J. of Asian Earth Sciences, 2013

7.2 Large phase anomalies observed in the present study

In present MT study, phase values exceeding 90^{o} are observed for some sites after processing the recorded MT data. The phase anomalies are observed atsites SH14, SH16, SH18, SH20, SH26 and SK27 situated in SHD, RW, LHD, MCTZ and at the northern boundary of HHC (close to STDS), respectively. The locations of these MT sites are shown in Figure. 7.01. Most of these large phase values are observed in the off-diagonal components and at lower frequency bands (except SK27, where high frequency bands also show higher order phases).

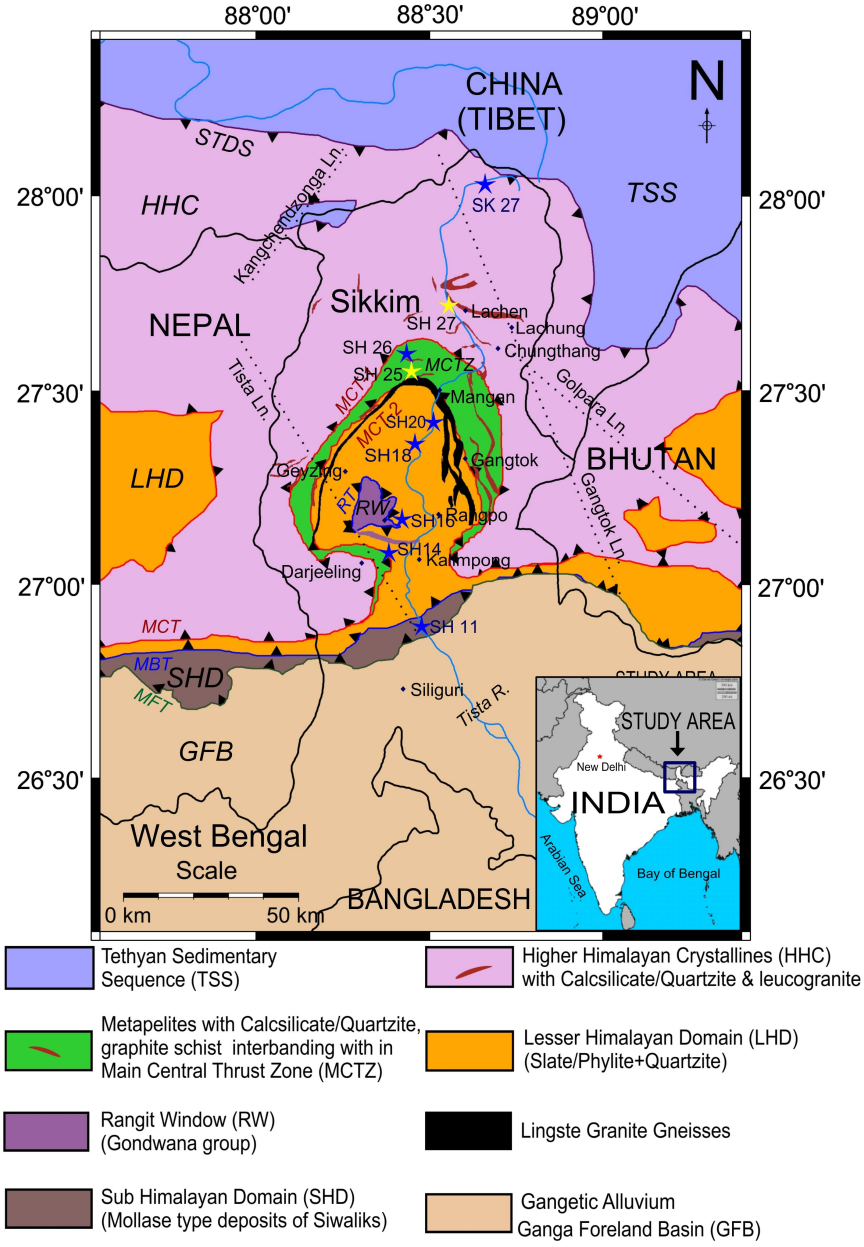

Figure 7.01: Map showing location of the MT sites that exhibit anomalous phases with blue color stars and sites considered for the analysis of anamolous phase at SH26 (yellow color stars, SH25 & SH27)

Figure 7.02 shows the apparent resistivity and phase curves for the site SH18 located in the LHD. The xy-component of the phase tensor shows a fairly uniform variation over a broad frequency range but its yx-component starts increasing sharply for lower frequencies and exceed 90^{o}. Other diagonal components of the impedance phase tensor (xx- and yy-) also show the similar type of behavior as shown by yx and xy, respectively. Initially, we suspected that the data are affected by strong current channelling, as these sites are in the vicinity of major faults having regional E-W strike.

Two classes of models have been proposed to explain these anomalous phases. In both explanations, it is suggested that anomalous current flow (popularly known as current channeling) could be the possible cause for anomalous phase behavior. In first model, special geometries of 3-D conductors in the host medium cause large electrical currents in the conductor leading to out-of-quadrant phase. In second model, particular combination of 2-D anisotropic blocks/layers leads to current deflection and channeling causing anomalous phase.

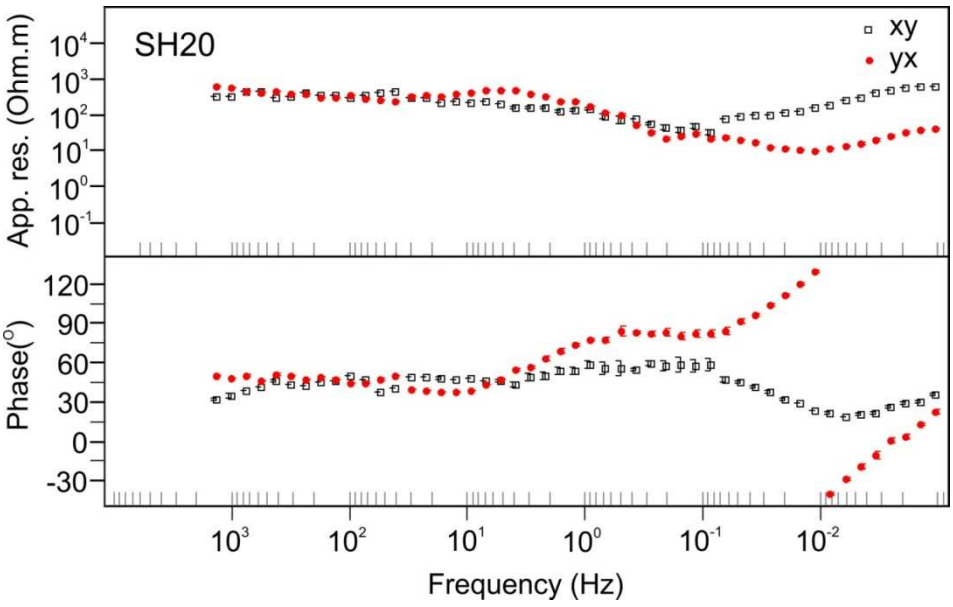

Figure 7.02: Apparent resistivity and phase responses at site SH20 showing phases out of quadrant for frequencies < 10Hz

7.3 Models of current channelling – anomalous phases

Weidelt (1977) introduced the notion of current channeling (conductive channeling) in magnetotellurics. Using thin sheet approximation, he examined plane wave model consisting of an upper inhomogeneous layer comprising highly conducive channel and a homogeneous

two-layered sub-stratum of moderate resistivity. It was observed that the density of the anomalous current is significantly enhanced within the conductive channel. This concentration effect is termed as current channeling and is defined as the concentration of induced currents in highly conductive elongated structures (Weidelt, 1977; Jones, 1983).

Initially, it was considered that galvanic distortions caused by strong channeling of currents lead to phases leaving the quadrant. Since traditional 1-D and 2-D models were unable to explain these effects, it was generally considered that current channeling effect is of three-dimensional nature and requires complex three dimensional treatments. Egbert (1990) proposed a theoretical model consisting of a thin conductive sheet broken by resistive lines and separated from a uniform half-space by a thin perfectly resistive layer to achieve the reversal of electric field direction leading to phase exceeding 90°. Livelybrooks *et al.* (1996) explained large phase anomaly, observed over Sudbury sulfide body, through current channeling by 3-D induction within the ore body bounded by faults. Pous *et al.* (2004) and Weckmann *et al.* (2003) have modeled the problem by considering the highly conductive ring structures. Pous *et al.* (2004) suggested that medium comprising interconnected graphite or highly graphite rich schists can give rise to phases exceeding 90^{o}. Weckmann *et al.* (2003) inferred that the detailed analysis of large phase anomalies in terms of tectonics can reveal the internal structure of a fault or lineament. Lezaeta & Haak (2003) observed anomalous phase at several sites in the Andean subduction zone and interpreted this in terms of magnetic distortion due to an electromagnetic coupling between the conductive ocean and the continental elongated conductors along the Atacama fault system close to the Pacific Ocean. In an approach by Ichihara & Mogi (2009), they considered a three dimensional L- shaped model of electric conductor consisting a regional elongated conductor and a small conductor attached to its one edge. The anomalous phase behaviour was obtained for this model due to the reverse flow of electrical currents by strong twist caused by small local conductor. In this model, they enforced certain conditions on the model parameters to observe the large phase anomalies. First, the resistivity contrast between the background and the regional conductor was very large, and second the local conductor was attached to one end of the regional conductor.

In addition to explanation for phase anomalies via current channeling by 3-D-models, there are also other explanations for anomalous current flow due to 2-D anisotropic models leading to phases exceeding 90 degrees. Pek & Verner (1997) explained the phenomenon by considering the medium as consisting of two anisotropic layers having azimuthal anisotropy

strikes perpendicular to each other. In this model, the perpendicular currents are reversed with respect to the telluric field due to different anisotropic axes. Consequently, the co-linearity property of strike, perpendicular currents and telluric fields are diminished. Because of the non-co-linearity, a large distortion in the phases occurs. Heise & Pous (2003) performed detailed model parameters analysis for a synthetic 2-D anisotropic model consisting of an anisotropic layer overlain by a shallow anisotropic block of limited lateral extent. They varied geometry of the block and thickness of the layer and their anisotropy ratios and strikes to interpret MT data from SW Iberia and concluded that the anomalous phase occurs when the anisotropy ratio and the angle between anisotropy strikes of the block and the layer are large.

Lilly & Weaver (2010) analyzed the anomalously large phases using the Mohr circle diagrams. The Mohr circle shows the phases greater than 90^o are possible by certain rotation of the axes and the condition for the phase out of the quadrant is that one or both of its real and quadrature parts should be negative. Berdichevsky & Dmitriev (2012) gave a simple 2-D model through which channeling of currents have been observed. The 2D model consists of the central resistive block bordered by the deep conducive faults, which connect the conductive upper layer (sediments) with deep (crustal) conductive layers localized within the side resistive blocks. Another simple 2-D explanation for negative phases in TE magnetotelluric data given by Selway *et al.* (2012).They have shown that a shallow, laterally extensive, bounded, low resistivity zone that overlies a higher resistivity region with sufficient resistivity contrast (1000 or greater) can also produce negative TE mode phases. With this background, we have analysed the phase anomaly observed at the site SH26 located at the northern boundary of MCTZ.

7.4 Analysis of anomalous phases at the MCTZ

We have observed the anomalous phase behavior at the site SH26 in the vicinity of the northern boundary of the MCTZ shown in Figure 7.01 along with its neighboring sites, SH25 and SH27 situated to its southern and northernside, respectively. These sites lie in the high mountainous area with dense forest cover of Kanchenjunga reserve forest. Sites SH27 and SH26 were difficult to access and it was not possible to reach SH27 directly from SH26. Therefore, we took a circuitous route by road, encompassing the high mountains, to reach SH27 near Lachen in north Sikkim. Due to the inaccessibility of the area, we could not occupy any more MT sites between the SH26 and SH27.

The observed apparent resistivity and phase curves along with error bars as a function of period for two sites are shown in Figure 7.03. The error bars are very small and are not visible for most data points. The xy- and yx-components of the apparent resistivity and phase curves of SH25 (Figure 7.04b) vary smoothly with period. The general trend of the apparent resistivity curves indicates a change from resistive to more conductive structures with increasing period (depth). The phase values are in the expected quadrant between 0 and 90°. However, phase exceeding 90° is obtained at SH26 (Figure 7.04a) located in the vicinity of the northern boundary of MCTZ. The xy-component of the phase shows a uniform variation over a broad frequency range but its yx-component starts increasing sharply for frequencies lower than 10Hz and exceeds 90^o at 1 Hz. The diagonal (xx- and yy-) components of the impedance phase tensor are also large and of similar magnitude. The apparent resistivity curves, however, show a uniform variation.

7.4.1 Localized enhancement of the magnetic fields – evidence of current channeling

As discussed in the previous session, the anomalous phase behaviors are difficult to be explained by simple 2-D models because these phase distortions might arise due to the current channeling in the presence of localized 3-D conductors or due to subsurface structure consisting of anisotropic blocks/layers having special configuration of anisotropy strike directions and anisotropy ratio. Although it is difficult to discriminate between these two models based only on the data showing anomalous phase behavior, the presence of current channeling can be identified through the estimation of relative strength of horizontal magnetic fields from synchronous time series data of neighboring sites. Horizontal magnetic fields are enhanced over the conducting channel and their phase relationship can give clues on the orientation of the channel as well as regional induced currents, which form the source of channeled currents. We have synchronous time series of four days duration in the frequency band of 0.01-1 Hz (LF3 band as defined in Mapros) for the sites SH25 and SH26 of which we have extracted good quality time series of 18hr duration and computed stacked spectra using window length of 4096 samples (Figure 7.04).

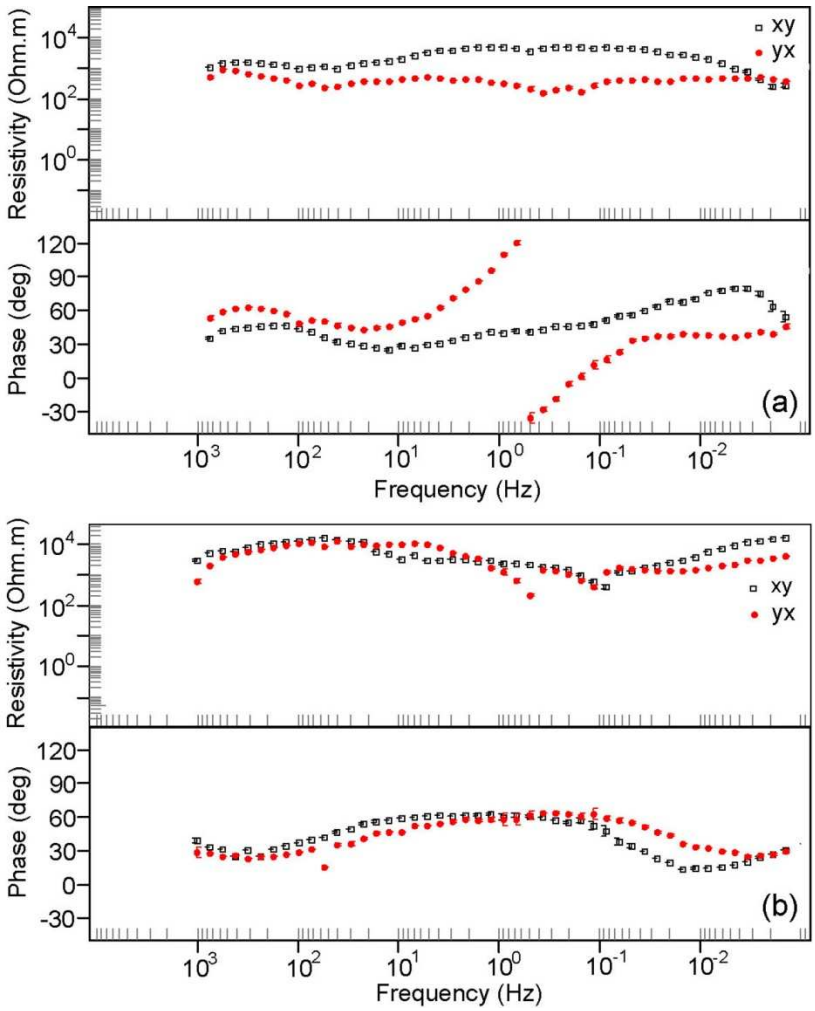

Figure 7.03: Observed apparent resistivity and phase responses at two sites within the MCTZ. (a) Site SH26 and (b) site SH25 marked in Figure. 7.01. The yx-component of phase at site SH26 exceeds 90°

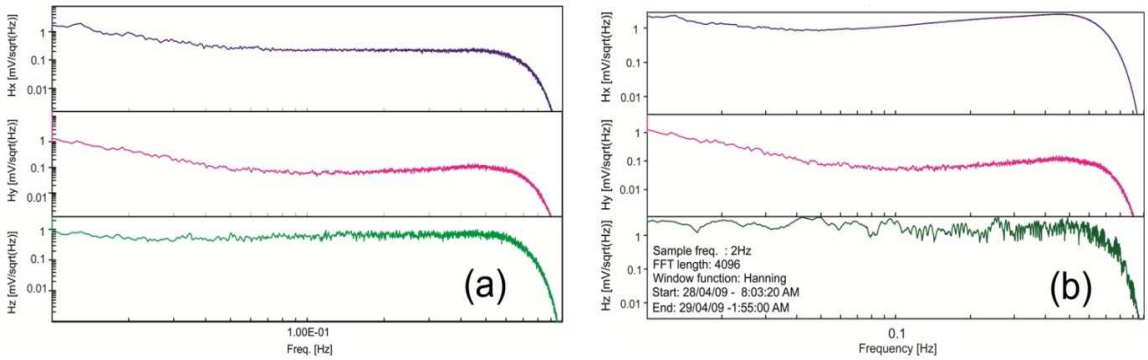

Figure 7.04: Stacked spectra of time synchronous magnetic field at (a) site -SH25 (b) site -SH26

The magnetic field strength at SH26 is then normalized with respect to the strength at SH25 and the results are shown in Figure 7.06. The strength of the horizontal magnetic field at SH26 is enhanced by an order of magnitude around 2s period (Figure 7.06a) indicating the presence of current channeling at SH26. It gradually decreases to almost normal values at 100s period. The dominant direction of the horizontal field at SH25 is N30^{o}E whereas it is aligned in the north direction at SH26. Figure 7.06b shows the current channeling direction at SH26 with respect to SH25. We have also computed the ratio of the vertical to the horizontal magnetic field at both sites (Figure 7.06c). The ratios of vertical field to horizontal magnetic fields at both sites are shown in Figure 7.06d. The vertical field at SH25 is negligible compared to the horizontal field indicating the 2-D nature of the subsurface. Site SH26 shows strong localized perturbations as revealed by the enhancement in the vertical field. These results support the presence of localized channeling effect at SH26.

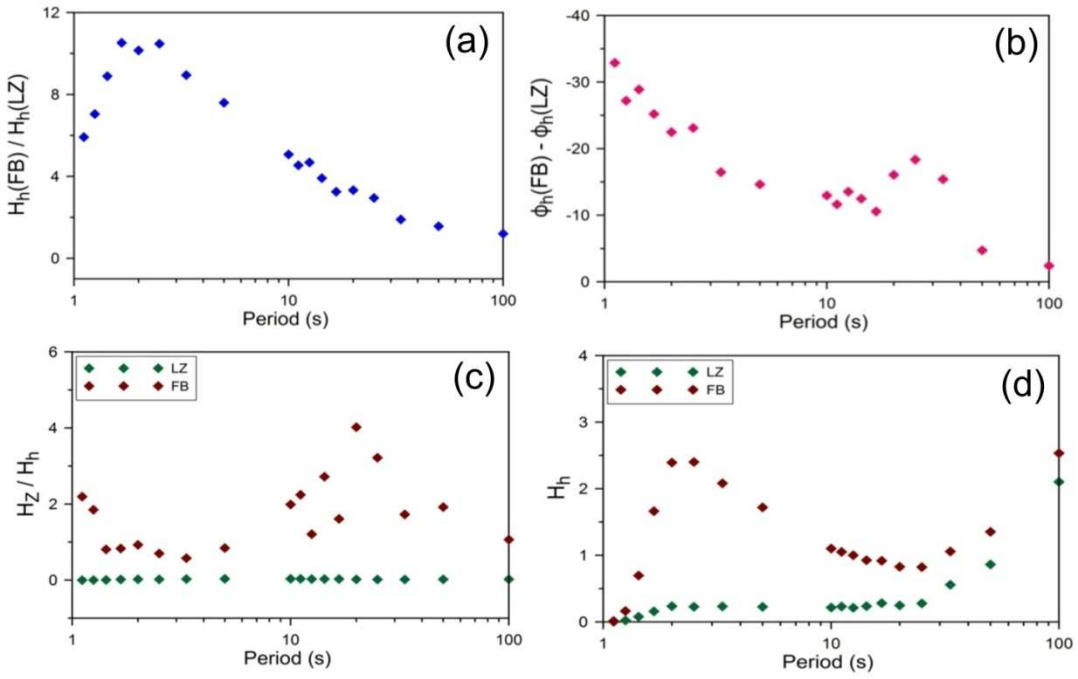

Figure 7.05: (a) Strength of the horizontal magnetic field (Hh) at the sites SH26 and SH25, (b) enhancement in the strength of the Hh at SH26 compared to the field at SH25, (c) change in the azimuth of Hh at SH26 with respect to that at SH25, and (d) ratio of vertical field to H_h at both sites

7.4.2 Forward modelling – 2-D anisotropic model

The MT site SH26, showing phase exceeding 90°, is located within the MCTZ consisting of high grade crystalline gneisses. The occurrence of thin bands of graphitic schists at the

northern boundary of MCTZ and in north Sikkim has been reported. These schists grade into graphitic quartzite with increasing quartz content. The presence of graphite bearing schists within crystalline gneisses could provide necessary anisotropy conditions leading to MT phase distortion. Further, strong resistivity contrast across the northern boundary of the MCTZ favors strong current channeling. The importance of electrical anisotropy associated with crustal-scale fault zones was also recognized in MT studies of the KTB area (Eisel & Haak, 1999), the Abitibi sub-province in Canada (Tournerie & Chouteau, 1998) and the Southern Alps in New Zealand (Davey *et al.* 1998). In view of the geological setup, we attribute the observed anomalous phase behavior to the presence of anisotropy in the medium and analyze the data.

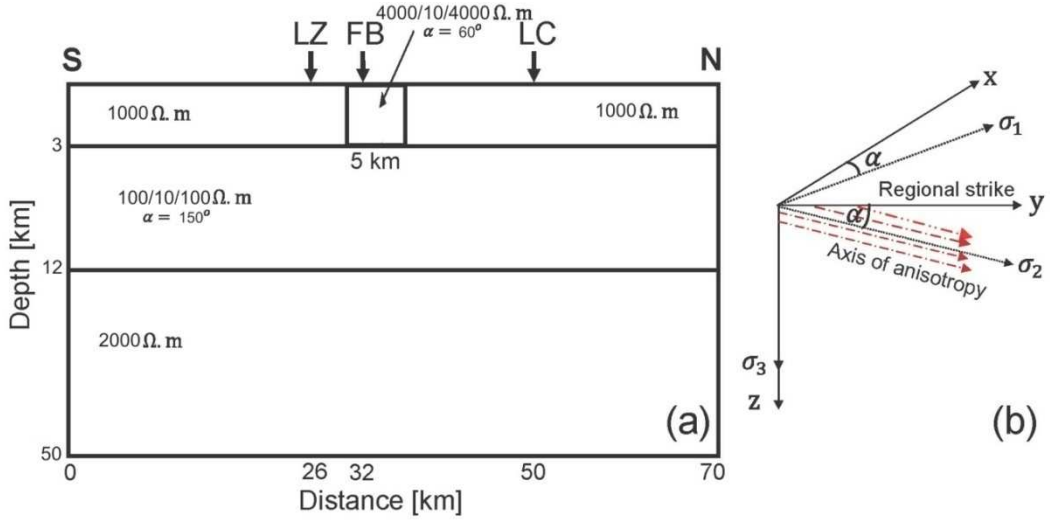

Figure 7.06: (a) A schematic diagram of the 2-D model consisting of an anisotropic layer overlain by an anisotropic block with different principal resistivities and anisotropy axes. (b) Nature of azimuthal anisotropy.

We consider a model (Figure 7.06a) similar to the one proposed by Heise & Pous (2003) and compute synthetic responses using 2D anisotropic forward modeling code (Pek & Verner, 1997). The model consists of a 3 km thick strongly anisotropic block of 5 km width embedded in an isotropic layer of the same thickness and 1000 Ω. m resistivity. Site SH26 lies within this block. The block is underlain by another anisotropic layer of 9 km thickness followed by a 38 km thick isotropic layer of 2000 Ω. m resistivity. The vertical resistivity values and thicknesses in this model have been assigned taking into consideration the available regional 2-D crustal structure obtained by Patro & Harinarayana (2009) after applying decomposition methods that minimize localized 3-D effects in data. For the anisotropic layer, we consider the vertical resistivity of 100 Ω. m which is in agreement with

the resistivity values in the depth range of 5-15 km in their model. Although our sites are several tens of km away from their profile, we use their model in absence of any other estimates of the resistivity structure from the study region. Inclusion of the anisotropic layer is somewhat arbitrary but is essential to obtain the desired anomalous phase behavior (Heise & Pous, 2003). In the present model, the profile direction can be considered approximately N-S. Thus, the layers have E-W strike, which is also consistent with the regional strike of N95^{o}E obtained by the present study. We, therefore, use the resistivity and phase tensors without any rotation of the data.

For a general anisotropic block, a conductivity tensor σ (consisting of values σ_{xx}, σ_{yy}, σ_{zz} and three rotation angles) is assigned instead of a scalar conductivity σ. This means any orientation of the principle axes of the conductivity tensor in space can be achieved. We assume azimuthal anisotropy with the principal axis σ_1 of the anisotropic system at an angle α from the profile direction (Figure 7.06b). The value of α is constrained by the results of current channeling direction (Figure 7.05). The conducting channel at SH26 makes an angle of -30^o with respect to the source field at SH25. Assuming the profile direction to be N-S, the anisotropy azimuth can be taken as -30^o or 60^o with 90^o ambiguity. We have considered α equal to 60^o for the anisotropic block and 150^o for the anisotropic layer. The angle for the anisotropic layer is orthogonal to that for the anisotropic block. The resistivity of the medium is very large along $\sigma_1$direction compared to the resistivity along the principal axis σ_2. With the inclusion of anisotropy, the diagonal components of the impedance tensor are no longer zero. Hence, we attempt to fit all four components of the observed impedance tensor (xx-, xy-, yx-, yy- components) through 2-D anisotropic modeling.

Forward responses have been computed for various combinations of anisotropy ratio of principal resistivities and geometry of the anisotropic block as well as the parameters of the underlying anisotropic layer. We obtain good fit between the observed and synthetic responses (Figure 7.08) for a model that has principal resistivities of 4000/10/4000 Ω.m for the block and 100/10/100 Ω.m for the underlying anisotropic layer (model M0, Table 7.01). The observed data are shown by filled squares in Figure 7.07 and the synthetic response corresponding to the model M0 are shown by thick curves.

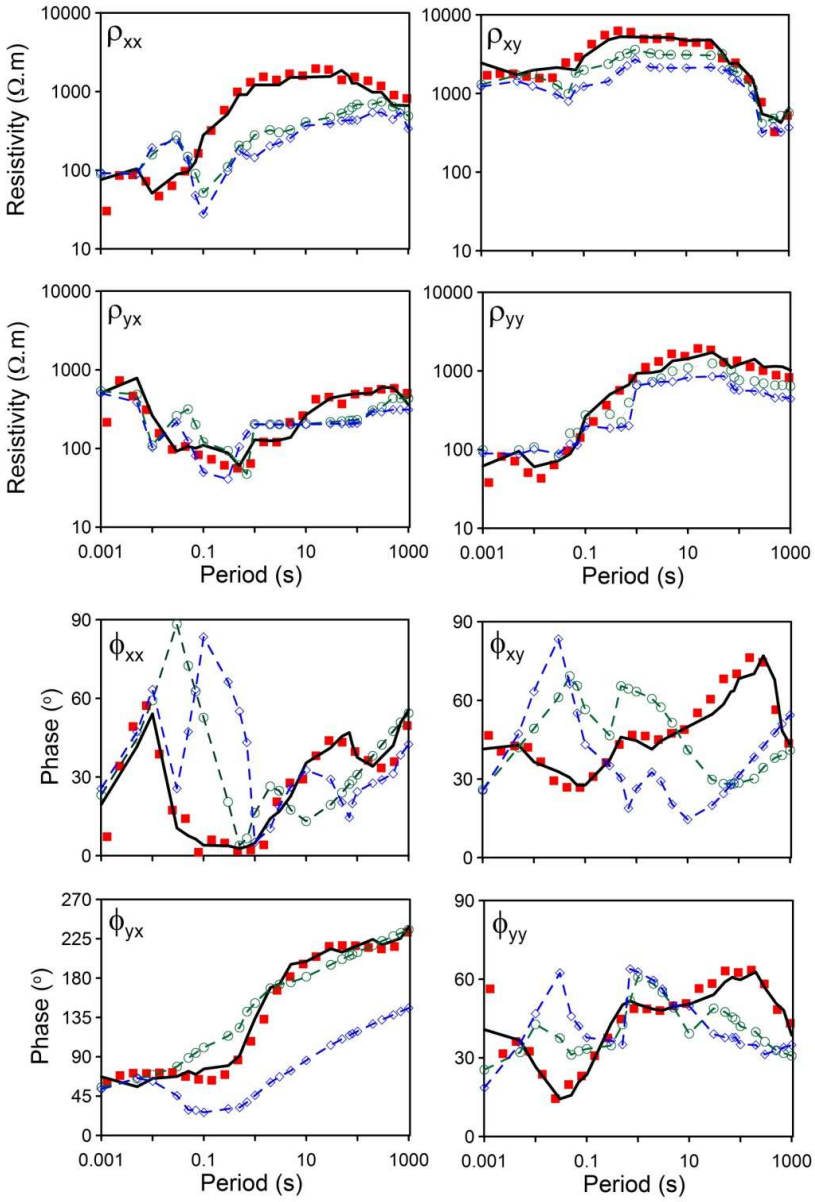

Figure 7.07: Response of best-fit model (thick curve, model M0) at site SH26 obtained through forward modeling. This model has azimuthal anisotropy $\alpha = 60°$ for the block. Observed apparent resistivity and phase tensor components are shown by filled squares. Two other response curves are also shown corresponding to $\alpha = 45°$ (open circles, model M1) and $\alpha = 30°$ (open diamonds, model M2) keeping other parameters the same as for the best-fit model. Please note that y-axis for ϕ_{yx} plot is different.

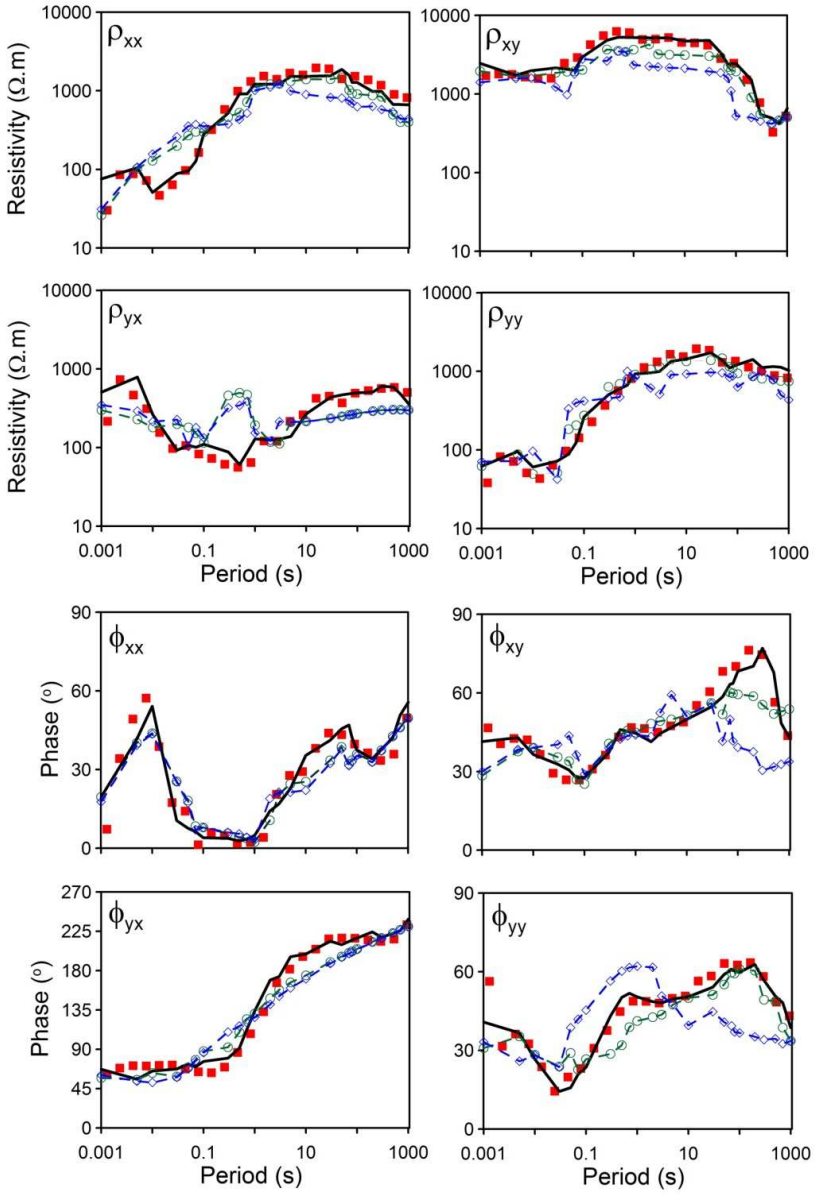

Figure 7.08 Responses showing sensitivity of forward responses to the parameters of the anisotropic block. An increase in the thickness of the block to 6 km (open circles, model M3) or an increase in the width of the block to 6 km (open diamonds, model M4) deteriorates the fit to the observed data (filled squares). Please note that y-axis for ϕ_{yx} plot is different.

In order to quantify the goodness of fit between the observed and computed responses, we define the normalized root mean square (NRMS) error between ij^{th} component of the observed and computed apparent resistivity (phase), $\varepsilon_{\rho}^{ij}(\varepsilon_{\phi}^{ij})$, as:

$$\varepsilon_{\rho}^{ij} = \sqrt{\frac{1}{N}\sum_{k=1}^{N}\left(\frac{\rho_{ij}^{o}-\rho_{ij}^{c}}{\rho_{ij}^{o}}\right)^{2}} \quad , \quad \varepsilon_{\phi}^{ij} = \sqrt{\frac{1}{N}\sum_{k=1}^{N}\left(\frac{\phi_{ij}^{o}-\phi_{ij}^{c}}{\phi_{ij}^{o}}\right)^{2}}, \tag{7.1}$$

where N is the total number of frequencies and i and j represent x- and y-components of the impedance tensor. $\rho^{o}(\phi^{o})$, $\rho^{c}(\phi^{c})$are observed and computed apparent resistivity (phase), respectively.

Similarly, we define the average NRMS error as

$$\varepsilon = \left[\frac{1}{N}\sum_{k=1}^{N}\left\{\frac{1}{8}\sum_{i=1}^{2}\sum_{j=1}^{2}\left(\left(\frac{\rho_{ij}^{o}-\rho_{ij}^{c}}{\rho_{ij}^{o}}\right)^{2}+\left(\frac{\phi_{ij}^{o}-\phi_{ij}^{c}}{\phi_{ij}^{o}}\right)^{2}\right)\right\}\right]^{\frac{1}{2}}. \tag{7.2}$$

The NRMS errors for various components of the impedance tensor for the model M0 are listed in Table 7.02. The average NRMS error for this model is 0.32.

Table 7.01: Model parameters used to compute the forward responses

Model	Anisotropic block				Anisotropic layer		
	Width (km)	Thickness (km)	Strike (deg)	Resistivity (Ω.m)	Thickness (km)	Strike (deg)	Resistivity (Ω.m)
M0	5	3	60	4000/10/4000	9	150	100/10/100
M1	5	3	45	4000/10/4000	9	150	100/10/100
M2	5	3	30	4000/10/4000	9	150	100/10/100
M3	5	6	60	4000/10/4000	9	150	100/10/100
M4	6	3	60	4000/10/4000	9	150	100/10/100

The responses are sensitive to the model parameters. Figure 7.07 also shows the effect of variation in the anisotropy strike of the block. A change in the strike to 45° keeping other model parameters unchanged (model M1, Table 7.1) shows significant deviations in the resistivity components $\rho_{xx}$and ρ_{xy}. The misfit is more pronounced for the phase values (curve with open circles in Figure 7.08). The average NRMS error increases to 1.02. A decrease in the anisotropy strike to 30° (model M2, Table 7.1) further deteriorates the fit

(curve with open diamonds in Figure 7.08) to the observed responses. Thus, the model response is sensitive to the strike of the anisotropic block.

Table 7.02: Normalized RMS error for various components of the impedance tensor and the average error for different model cases

Model	Resistivity				Phase				Average
	ε_{ρ}^{xx}	ε_{ρ}^{xy}	ε_{ρ}^{yx}	ε_{ρ}^{yy}	ε_{ϕ}^{xx}	ε_{ϕ}^{xy}	ε_{ϕ}^{yx}	ε_{ϕ}^{yy}	Error (ε)
M0	0.36	0.30	0.59	0.37	0.28	0.26	0.10	0.31	0.32
M1	1.27	0.79	0.82	0.63	1.45	1.85	0.28	1.04	1.02
M2	1.40	1.13	0.88	0.91	1.59	1.97	1.15	1.49	1.32
M3	0.58	0.68	1.08	0.38	0.39	0.51	0.21	0.61	0.56
M4	0.42	1.20	0.25	1.23	0.90	0.99	0.94	0.78	0.84

We also analyzed the effect of increase in the thickness of the block as well as in its lateral extent on the computed responses. These results are shown in Figure 7.08. For the first model (model M3, Table 7.01) we have doubled the thickness of the anisotropic block without changing any other parameters. The resulting response curves (curve with open circles) show some deviations from the observed data for all components of the resistivity and phase. Significant deviations are seen for ρ_{yx} and ϕ_{xy}. The results (curve with open diamonds) seem to be more sensitive to the increase in the width of the block compared to its thickness. An increase in the width by only 1 km (model M4, Table 7.01) leads to the deterioration in the fit of $\rho_{xy}, \rho_{yx}, \phi_{xy}$ and ϕ_{yy} components. The normalized average error for this case is 0.84.

7.4.3 Discussion

The above results, invoking a suitable combination of the parameters of the anisotropic block and the underlying anisotropic layer to explain the anomalous MT phase behavior observed at the site SH26 in the vicinity of the northern boundary of the MCTZ, support the presence of anisotropy in the medium. Geologically, the presence of graphite bearing schists within the High Himalayan Crystallines can induce macro-anisotropy in the medium with large contrast in the principal resistivities leading to large anisotropy ratio. Therefore, the proposed model fits the anomalous field data and has consistency with the geology of the region. The neighboring site SH25 does not show the anomalous phase behavior even though it is located only about 4.5 km southward of SH26 indicating that the inferred anisotropic block does not extend southward providing a tight constraint on the southern limit of the block. The absence

of anomalous phase for the site SH27 further 20 km north also limits the extent of the anisotropic block. However, the data gap between sites SH26 and SH27 due to the inaccessibility of the area limits further constraining of the northern extent of the block. We have computed some models (e.g. model M4 in Table 7.01) by varying the width of the block to constrain this limit and find that, for the parameters regime chosen, the synthetic response (curve with open diamonds in Figure 7.09) at SH26 starts deviating from the observed data for a moderate increase in the width of the anisotropic block. Thus, we infer that the anisotropic block is localized around the site SH26.

7.5 Summary

Among the two competing models, the anisotropic block/ anisotropic layer model with large differences in their anisotropy strikes and the local conductor models with special geometry and strong conductivity contrast, we have considered the anisotropy model to analyze the anomalous phase behavior at the site SH26 in view of the local geology. It might also be possible to generate 3-D models with combinations of local and regional conductors to achieve similar results because the site is in the vicinity of the northern boundary of the MCTZ. Therefore, a strong resistivity contrast across this boundary is not ruled out which in the presence of some localized electrical conductor can provide favorable conditions for the current channeling. The distinction between these two competing models, giving similar effects in MT responses, may be made when detailed crustal structure by other geophysical methods becomes available, especially from the inaccessible area lying between the sites SH26 and SH27 or using vertical magnetic field component in the modeling process.

Chapter 8

Conclusions and future scope

8.1 Conclusions

Broadband MT data have been acquired at 48 sites along a 200kmlong profile traversing across major geotectonic sub-domains the Sikkim Himalaya and the adjoining northern Ganga Basin. After pre-processing of this dataset, 31 sites have been selected for further modelling and analysis. The decomposition analyses, 2-D inversion, and 2-D anisotropic modeling have provided some interesting results for improved understanding of deep structure and seismotectonics of the region. The major results obtained in the present work are listed below.

- The 2-D joint inversion of decomposed TE- and TM-mode data in the period band of 0.01-1000s has revealed a crustal geoelectric structure in which
  - The Ganga Foreland Basin shows the presence of a 4-6 km thick sedimentary layer overlying the basement (top of the Indian plate).
  - The Lesser Himalayan Domain (LHD) consists of an assemblage of conductive and resistive blocks down to about 15km depth, below which the resistivity is moderate.
  - The conductive zone at the profile location of about 100km coincides with the Rangit Window exposing Gondwana rocks.
  - The MCTZ occurs as a resistive nearly vertical zone bounded by two thrust planes. A moderate decrease in the resistivity within this zone at the depth of 20-30km could be due to the Main Himalayan Thrust (MHT) but it is not resolved in the 2-D section.
  - A conductive zone is present within the High Himalayan Crystallines (HHC) north of MCTZ.
- The 2-D geoelectric model indicates that the crustal and tectonics structure of the Sikkim Himalaya is significantly different from that of the western Himalaya,

especially that we don't get the mid-crustal ramp beneath the Higher Himalaya as delineated in the western Himalaya. We rather get a highly resistive nearly vertical feature beneath MCTZ.

- The presence of a thick conductive zone within HHC is also interesting. In the western Himalaya, HHC has been interpreted as a highly resistive block. We infer that this conductive zone could be due to possible presence of partial melts linked to mid crustal fluids beneath southern Tibet or sedimentary rocks at depth of the Tethyan sequence exposed north of STDS.

- Integrating the geoelectric model with the depth distribution of seismicity for the region reveals that a fault within LHD, rather than Main Boundary Thrust (MBT) as suggested earlier, could be the main seismogenic fault causing recurrent seismicity in the region. The surface location of this inferred fault correlates with the Ramgarh Thrust along which Gondwana rocks are exposed in the Rangit Window.

- Strike analysis of broadband MT data of the sites in the Sikkim Himalaya by GB, LT, and PT approaches has revealed a predominantly NNW to NW strike in MCTZ. The transverse nature of the MT strike within MCTZ correlates well with the trend of recent seismicity in this region and provides independent evidence for transverse tectonics in the Sikkim Himalaya as reported by various seismological studies and earthquake focal mechanisms.

- The RMS errors for MSMF decomposition analysis of all sites in the period band of 1-10s are in general large compared to longer periods for sites (SH01-SH09) within GFB. MSMF analysis of only these nine sites reveals the regional strike direction consistent with the E-W strike of the Indian plate for longer period whereas the data of 1-10s period yield regional strike direction of N51^{o}E, indicating the presence of NE-SW (or its conjugate) structure in the north Bengal Basin of GFB covered by these sites.

- The presence of transverse features in the MCTZ region as well as anomalous phase at some sites along the profile indicates that the crustal structure of the Sikkim Himalaya is more complex.

- The anomalous phase obtained at the northern boundary of MCTZ is possibly due to the presence of complex subsurface structure, a highly conductive N-S trending localized

body intruding into the regional NNW striking geological structure. The localized enhancement of the vertical magnetic field at this site supports current channeling. Therefore, at least some parts of the profile especially MCTZ seem to have complex 3-D/ anisotropic structure.

- Among the two competing models, the anisotropic block/anisotropic layer model with large contrast in their anisotropy strikes and the local conductor models with special geometry and strong conductivity contrast, we have considered the anisotropy model to analyze the anomalous phase behaviour at the site SH26 in view of the local geology. Geologically, the presence of graphite bearing schists within the High Himalayan Crystalline can induce macro-anisotropy in the medium with large contrast in the principal resistivities leading to large anisotropy ratio.

- Analysis of the anomalous phase data by 2-D forward modelling including anisotropy in the media invoking strong anisotropic block overlying an anisotropic layer explains the anomalous MT phase. Therefore, the proposed model fits the anomalous field data and has consistency with the geology of the region.

- The neighbouring site SH25 does not show the anomalous phase behaviour even though it is located only about 4.5 km southward of SH26 indicating that the inferred anisotropic block does not extend southward providing a tight constraint on the southern limit of the block. The absence of anomalous phase for the site SH27 further 20km north also limits the extent of the anisotropic block. However, the data gap between sites SH27 and SH26 due to the inaccessibility of the area limits further constraining of the northern extent of the block. We infer that the anisotropic block is localized around the site SH26.

- It might also be possible to generate 3-D models with combinations of local and regional conductors to achieve similar results because the site is in the vicinity of the northern boundary of the MCTZ. Therefore, a strong resistivity contrast across this boundary is not ruled out which in the presence of some localized electrical conductor can provide favourable conditions for the current channelling.
- The distinction between these two competing models, giving similar effects in MT responses, may be made when detailed crustal structure by other geophysical methods

becomes available, especially from the inaccessible area lying between sites SH26 and SH27.

8.2 Future scope

In the present study, we have used impedance tensor data for delineation of 2-D subsurface resistivity structure. At most of the sites, we have also acquired vertical magnetic field data. However, at some sites, particularly those located at high altitudes, we were unable to layout the vertical magnetic coil due to logistic problems. Therefore, we have not used the vertical magnetic field data in the present joint-inversion study. The magnetic transfer functions may be included in the future in inversion to improve the present results, especially for better constraining of the localized conductors in the vicinity of major thrust faults in the region.

The GB decomposition a-priori assumes a regionally 2-D subsurface model the MT response of which is distorted by local 3D structures. The real earth structure is never the less 3-D in nature and its treatment as 2-D structure is a simplification. Therefore, robust analysis of data in terms of dimensionality and directionality should be free from the above assumption. The PT approach overcomes this limitation of the GB approach and is therefore useful for the dimensionality analysis and identification of the current flow direction. In the present work, we have used both GB and PT analyses mainly to explore the extent of distortion and for determination of the dominant regional strike direction and then decomposed the impedance data by GB approach for 2-D inversion. In the future, phase tensor inversion can be applied to this dataset. This could help in treating the unresolved structures in the region.

The decomposition and dimensionality analyses of the MT data reveal that the region is more complex at least in some parts of the profile, especially the segment covered by MCTZ suggesting transverse nature of the structures. The complex nature of MCTZ is also seen in the geoelectric section. We have delineated nearly vertical highly resistive structure covering almost the entire depth range of the model. In the future, MT data acquisition suitable for 3-D analysis, subject to accessibility to suitable sites in this tough terrain, could be attempted to resolve the 3-D nature of MCTZ.

The result of forward modeling study incorporating 2-D anisotropic medium to explain the anomalous phase suggests that electric anisotropy could be a viable explanation for the occurrence of anomalous phase at the northern boundary of MCTZ. In view of this inference,

the future work can be extended to anisotropic modeling and inversion studies. Pek & Sanots (2008) have developed an algorithm for inversion of MT data for anisotropic media. Application of the algorithm to the present dataset might provide better constraints on the anisotropy parameters.

The 2-D geoelectric section shows the presence of a high conductivity zone in the mid-to-lower crust within the Indian shield at the southern end of the profile. However, we do not include this feature in the final interpretation of the data as it might be an artifact due to the edge effect. Gravity and magnetic model of the region south of our profile (Tiwari *et al*. 2006) invoked an igneous intrusive body just beneath the basement to explain the observed Bouguer gravity and total magnetic intensity anomalies and correlated this with the Rajmahal volcanics. Although, we don't see any signature of such a body in the upper crust, it could be possible that the lower crustal conductive zone revealed by the present study represents volcanics presumably belonging to the Rajmahal plume activity. Never-the-less, some more MT sites further south of the profile is needed to ascertain that it is not an artifact due to the edge effect. Therefore, the present profile needs to be extended further south, up to the south Bengal Basin, to ensure that it is not an artifact and to map the extent of the conductive zone.

References

1) Acharya, S.K. and Sastry, M.V.A., 1979. *Stratigraphy of Eastern Himalaya*. Geological Survey of India Misc. Pub., 41: 49–67

2) Acharya, S.K., 1975. *Structure and stratigraphy of the Darjeeling frontal zone, Eastern Himalaya.* Geological Survey of India Misc. Pub., 24: 71-90

3) Acharyya, S.K., 1980. Structural framework and tectonic evolution of the Eastern Himalaya. *Himalayan Geology,* 10: 412 - 439

4) Acton, C.E., Priestley, E., Mitra, S. and Gaur, V.K., 2011. Crustal structure of the Darjeeling–Sikkim Himalaya and southern Tibet. *Geophys. J. Int.,* 184: 829–852

5) Archie G. E., 1942. The electrical resistivity log as an aid in determining some reservoir characteristics. *Trans. Am. Inst. Min. Metall. Pet. Eng.,* 146:54–62

6) Armbruster, J., Seeber, L. and Jacob, K.H., 1978. The northwestern termination of the Himalayan mountain front: Active tectonics from microearthquakes, *J. Geophys. Res.,* 83(B1): 269-282

7) Arora, B. R. and Singh, B. P., 1992. Geomagnetic and geo- electric investigations for seismicity and seismotectonics of the Himalayan region; *Geol. Soc. India Memoir*, 23: 223–263

8) Arora, B., Unsworth, M. J., Rawat, G., 2007. Deep resistivity structure of the Northwest Indian Himalaya and its tectonic implications. *Geophys. Res. Lett.* 34: L04307 doi: 10.1029/ 2006GL029165

9) Backus, G.E. and Gilbert, F., 1967. Numetical applications of formalism for geophysical inverse problems. *Geophys. J. Roy. Astr. Soc.* 13: 247-276

10) Bahr, K., 1988. Interpretation of the magnetotelluric impedance tensor, regional induction and local telluric distortion. *J. Geophysics*, 62: 119-127

11) Bailey, R.C., and Groom, R.W., 1987. Decomposition of the magnetotelluric impedance tensor which is useful in the presence of channeling. Contrib. Paper at 57th Society of Exploration Geophysicists, International Meeting and Exposition. Tulsa, OK, Expanded Abstracts 57: 154-156

12) Barazangi, M. and Ni, J., 1982. Velocities and propagation characteristics of Pn and Sn beneath the Himalayan Arc and Tibetan Plateau: possible evidence for underthrusting of Indian continental lithosphere beneath Tibet. *Geology* 10: 179–185

13) Becken, M. and Burkhardt, H., 2004. An ellipticity criterion in magnetotelluric tensor analysis. *Geophys. J. Int.,* 159: 69–82

14) Becken, M., Ritter, O., Park, S. K., Bedrosian, P. A., Weckmann, U. and Weber, M., 2008. A deep crustal fluid channel into the San Andreas Fault system near Parkfield, California, *Geophys. J. Int.,* 173: 718-732

15) Beloussov, V.V., Belyaevsky, N.A., Borisov, A.A., Volvovsky, B.S., Volkovksy, I.S., Resvoy, D.P., Tal-Virksy, B.B., Khamrabaev, I.Kh., Kaila, K.L., Narain, H., Marussi, A. and Finetti, J., 1980. Structure of the lithosphere along the deep seismic sounding profile: Tien Shan–Pamirs–Karakorum–Himalayas, *Tectonophysics*, 70: 193–221

16) Berdichevsky, M.N. and Dmitriev, V.I., 2008. *Models and Methods of Magnetotellurics*, Springer, ISBN:978-3-540-77811-0

17) Berdichevsky, M. N., Dmitriev, V.I. and Pozdnjakova, E. E. 1998. On two-dimensional interpretation of magnetotelluric soundings. *Geophys. J. Int.,* 133: 585–606

18) Berdichevsky, M.N., Vanyan, L.L. and Dmitriev, V.I., 1989. Methods used in the USSR to reduce near-surface inhomogeneity effects on deep magnetotelluric soundings, *Phys. Earth planet. Inter.,* 53: 194–206.

19) Bhattacharya, K. and Mitra, G., 2009. A new kinematic evolutionary model for thegrowth of a duplex: an example from the Rangit duplex, Sikkim Himalaya, India. *Gondwana Research,* 16: 697-715.

20) Bhattacharya, S.N. and Kayal, J.R., 2005. Seismicity of the Himachal Himalaya: Constraint from local seismic network. *Geol. Surv. India Sp. Pub.,* 85: 71-79.

21) Bilham, R. and Ambraseys, N., 2005. Apparent Himalayan slip deficit from the summation of seismic moments for Himalayan earthquakes, 1500–2000. *Curr. Sci*. 88(10): 1658–1667.

22) Bilham, R., 2001. Slow tilt reversal of the Lesser Himalaya between 1862 and 1992 at 78^{o} E and bounds to the southeast rupture of the 1905 Kangra earthquake. *Geophys. J. Int*., 144: 1-23

23) Bilham, R., Frederick, B., Rebecca, B. and Gaur, V.K., 1998. Geodetic constraints on the Translation and deformation of India: Implications for future great Himalayan earthquakes. *Curr. Sci*., 74 :213-229

24) Bilham, R., Gaur, V.K. and Molnar, P., 2001. Earthquakes: Himalayan seismic hazard. *Science*, 293: 1442-1444

25) Bilham, R., Larson, K. and Freymuller, J., 1997. GPS measurements of present-day convergence across the Nepal Himalaya. *Nature*, 386: 61-64

26) Bilham, R., Larson, K., Freymuller, J., Project IDYL-HIM members, 1997. Indo-Asian convergence rates in the Nepal Himalaya. *Nature*, 386 : 61–66

27) Bird, P., 1978. Initiation of intracontinental subduction in the Himalaya, *J. Geophys. Res.*, 83: 4975-4987

28) Blackman, R.B. and Tukey, J.W.,1959. *The Measurement of Power Spectra from the Point of View of Communications Engineer*ing , Dover, New York

29) Bostick, F. S., Jr., and Smith, H. V., 1962. Investigation of large-scale inhomogeneities in the earth by the magnetotelluric method, *l'roc. IRE*, 50: 2339-2346

30) Boyer, S.E. and Elliott, D., 1982. Thrust systems. *Am. Assoc. Petrol. Geol*., 66: 1196–1230

31) Brasse, H., Kapinos, G., Li, Y., Mutschard, I. and Eydam, D. 2009. Structure electrical anisotropy in the crust at south-central Chilean continental margin as inferred from geomagnetic transfer function. *Phys. Earth Planet. Int.*, doi: 10.1016/j pepi

32) Brasse, H., Lezaeta, P., Rath, V., Schwalenberg, K., Soyer, W., Haak, V., 2002. The Bolivian Altiplano conductivity anomaly. *J. Geophys. Res.*, 107 (B5), 2096

33) Brewitt-Taylor, C.R. and Weaver, J.T., 1976a. A computer program for the solution of electromagnetic induction problems, Geophysics Report, Dept. Phys., Univ. Victoria British Columbia

34) Brewitt-Taylor, C.R. and Weaver, J.T., 1976b. On finite difference solution of two-dimensional induction problems, *Geophys. J. R. astr. Soc.*, 47: 375-396

35) Brown, L.D., Zhao,W., Nelson, K.D., Hauck, M., Alsdorf, D., Ross, A., Cogan, M., Clark, M., Liu, X., Che, J., 1996. Bright spots, structure, and magmatism in Southern Tibet from INDEPTH seismic reflection profiling. *Science*, 274: 1688–1690

36) Cagniard, L., 1953. Basic theory of the magnetotelluric method of geophysical prospecting. *Geophysics*, 18: 605-635

37) Caldwell, T.G., Bibby, H.M. and Brown, C., 2004. The magnetotelluric phase tensor. *Geophys. J. Int.*, 158: 457-469

38) Caldwell, W.B., Klemperer, S.L., Lawrence, J.F., Rai, S.S and Ashish., 2013. Characterizing the Main Himalayan Thrust in the Garhwal Himalaya, India with receiver function CCP stacking. *Earth Planet. Sci. Lett.*, 367: 15–27

39) Caldwell, W.B., Klemperer, S.L., Rai, S.S., Lawrence, J.F., 2009. Partial melt in the upper-middle crust of the northwest Himalaya revealed by Rayleigh wave dispersion. *Tectonophysics*, 477: 58–65

40) Campbell, W. H., 2003. *Introduction to Geomagnetic Fields*, Second Edition, Cambridge University Press, Cambridge, 342 pp

41) Cantwell, T. 1960. *Detection and Analysis of Low-Frequency Magnetotelluric Signals*, PhD Thesis, Massachusetts Institute of Technology, Cambridge, Massachusetts

42) Cantwell, T., Nelson, P. and Webb, J., 1965. Deep resistivity measurements in the Pacific Northwest, *J. Geophys. Res.*, 70: 1931-1937

43) Catlos, E.J., Dubey, C.S., Harrison, T.M. and Edwards, M.A., 2004. Late Miocene movements within the Himalayan main central thrust zone, Sikkim, north-east India. *J. Metamorph. Geol*., 22: 207-226

44) Cattin, R., Martelet, G., Henry, P., Avouac, J.P., Diament, M., Shakya, T.R., 2001. Gravity anomalies, crustal structure and thermo-mechanical support of the Himalaya of

Central Nepal. *Geophys. J. Int.,* 147 (2), 381–392. doi:10.1046/ j.0956-540x.2001.01541.x

45) Chakridi, R., Chouteau, M. and Mareschal, M. 1992. A simple technique for analysing and partly removing galvanic distortion from the magnetotelluric impedance tensor: Application to Abitibi and Kapuskasing data (Canada). *Geophys. J. Internat*., 108, 917-929

46) Chandra, U., 1992. Seismotectonics of Himalaya. *Curr. Sci.*, 62, 40-71

47) Chatterjee, S.N. and Bhattacharya, S.N., 1992. Microearthquake surveys and seismicity in western Himalaya. *Geol. Soc. India Mem*., 23: 23-44

48) Chave, A. D., and J. T. Smith. 1994 , On electric and magnetic galvanic distortion tensor decompositions, *J. Geophys. Res.*, 99: 4669– 4682

49) Chave, A.D. and Thomson, D.J., 2004. Bounded influence magnetotelluric response function estimation, *Geophys. J. Int.,* 157 : 988–1006

50) Chen, L., Booker, J.R., Jones, A.G., Wu, N., Unsworth, M.J., Wei, W. and Tan, H., 1996. Electrically conductivity crust in Southern Tibet from INDEPTH magnetotelluric surveying. *Science,* 274: 1694–1696

51) Chen, W.P., and Molnar, P. 1977. Seismic moments of major earthquakes and the average rate of slip in central Asia. *J. Geophys. Res.,* 82: 2945-2969

52) Coggon, J.H., 1971. Electromangetic and electric modeling by the finite-element method. *Geophysics*, 36: 132-155

53) Constable, S. C., Parker, R. L., and Constable, C. G. 1987. Occam's inversion: A practical algorithm for generating smooth models from electromagnetic sounding data. *Geophysics*, 52(3) : 289-300

54) Counil, J. L., LeMouel, J. L., and Menvielle, M. 1986. Associate and conjugate directions concepts in magnetotellurics: *Ann. Geophys.,* B4: 115-130

55) Dasgupta, S., Ganguly, J. and Neogi, S., 2004. Inverted metamorphic sequence in the Sikkim Himalayas, crystallization history, P.T. gradient and implementations. *J. Metamorph. Geol*., 22: 395-412

56) Dasgupta, S., Mukhopadhyay, M., Nandy, D.R., 1987. Active transverse features in the central portion of the Himalaya. *Tectonophysics*,136: 225–264

57) Dasgupta, S., Sivaji, Ch., 2006. Vision paper on future directions of research in the Sikkim-Darjeeling Himalaya. Dept. of Science & Technology, Govt. of India, 20pp

58) Davey, F.J., Henyey, T., Holbrook, W.S., Okaya, D., Stern, T.A., Melhuish, A., Henrys, S., Anderson, H., Eberhart-Phillips, D., McEvilly, T., Uhrhammer, R., Wu, F., Jiracek, G.R., Wannamaker, P.E., Caldwell, G., Christensen, N., 1998. Preliminary results from a geophysical study across a modern, continent-continent collisional plate boundary – the Southern Alps, New Zealand. *Tectonophysics*, 288, 221–235

59) De, R. and Kayal, J.R., 2003. Seismotectonic model of the Sikkim Himalaya, constraint from microearthquake surveys. *Bull. Seismol. Soc. Am*., 99: 1395-1400

60) De, R. and Kayal, J.R., 2004. Seismic activity at the MCT in Sikkim Himalaya. *Tectonophysics*, 386: 243-248

61) De, R., 1996. A microearthquake survey in the Himalaya Foredeep region, north Bengal area. *J. Himalayan Geol.*, 17: 71-79

62) De, R., 2000. A microearthquake survey at the main boundary thrust in Sikkim Himalaya. *J. Geophys*., 21: 1-8

63) DeGroot-Hedlin, C. and Constable, S., 1990. Occam's inversion to generate smooth two-dimensional models from magnetotelluric data. *Geophysics*, 55: 1613–1624

64) Dewey, J.F. and Bird, J.M., 1970. Mountain belts and the new global tectonics. *J. Geophys. Res.*, 75: 2625-2647

65) Dewey, J.F. and Burke, K.C.A., 1973. Tibetan, variscan and Precambrian basement reactivation: product of continental collision; *J. Geol*., 81(6) : 683-692

66) Drukpa, D., Velasco, A.A., Doser, D.I., 2006. Seismicity in the Kingdom of Bhutan (1937–2003): Evidence for crustal transcurrent deformation. *J. Geophys. Res*. 111, B06301, doi:10.1029/2004JB003087

67) Egbert, G.D., 1990. Comments on 'Concerning dispersion relations for the magnetotelluric impedance tensor' by E. Yee and K.V. Paulson. *Geophys. J. Int*. 102, 1–8

68) Egbert, G.D., 1997. Robust multiple-station magnetotelluric data processing. *Geophys. J. Int.*, 130: 475–496

69) Egbert, G.D., Booker, J.R., 1986. Robust estimation of geomagnetic transfer functions. *Geophys. J. R. Astr. Soc.*, 87: 173–194

70) Eggers, D.E., 1982. An eigen state formulation of the magnetotelluric impedance tensor. *Geophysics* 47, 1204-1214

71) Eisel, M. and Haak, V., 1999. Macro-anisotropy of the electrical conductivity of the crust: a magnetotelluric study of the German Continental Deep Drilling Site (KTB). *Geophys. J. Int.*, 136, 109–122

72) Ellis, D. and Singer, J., 2008. *Well Logging for Earth Scientists*. Dordrecht: Springer Science & Business Media.

73) Ellis, R. G. and Oldenburg, D.W., 1994. The pole-pole 3-D DC-resistivity inverse problem: A conjugate gradient approach, *Geophys. J. lnt.*, 119: 187-194

74) Feldl, N. and Bilham, R., 2006. Great Himalayan earthquakes and the Tibetan plateau. *Nature*, 444, doi:10.1038/nature05199

75) Fletcher, R. and Reeves, C.M., 1964. Function minimization by conjugate gradients, *Comput. J.*, 7: 149- 154

76) Friedrichs, B., 2003. MAPROS: magnetotelluric data processing software. Metronix GmbH, Braunschweig, Germany

77) Gansser, A., 1964. *Geology of Himalayas*. Inter-Science Publisher, New York.

78) Gansser, A., 1977. The great suture zone between Himalaya and Tibet a preliminary account, Editions du C.N.R.S., 268: 181-191

79) Gansser, A., 1980. A significance of the Himalayan suture zone, *Tectonophysics*, 62: 37-52

80) Gokarn, S. G., Rao, C. K. and Gupta, G., 2002a. Crustal structure in the Siwalik Himalayas using magnetotelluric studies. *Earth Planets Space*, 54:19–30

81) Gokarn, S.G., Gupta, G., Rao, C.K. and Selvaraj, C., 2002b. Electrical structure across the Indus Tsangpo suture and Shyok suture zones in Northwest Himalaya using magnetotelluric studies. *Geophys Res. Lett*., 29 :1–4

82) Gokarn, S.G., Gupta, G., Walia, D. and Dutta, S., 2005. Magnetotelluric studies in Sikkim Himalaya. *DST news letter*. 25(1): 16-17

83) Gokarn, S.G., Gupta, G., Walia, D., Sanabam, S. S. and Hazarika, N., 2008. Deep geoelectric structure over the lower Brahmaputra Valley and Shillong Plateau, NE India using magnetotellurics. *Geophys. J. Int.*, 173: 92–104

84) Groom, R. W. and Bailey, R.C., 1991. Analytic investigations of the effects of near-surface three-dimensional galvanic scatters on MT tensor decompositions. *Geophysics,* 56: 496-518

85) Groom, R.W. and Bailey, R.C., 1989. Decomposition of Magnetotelluric impedance tensors in the presence of local three-dimensional galvanic distortion. *J. Geophys. Res*., 94: 1913–1925

86) Groom, R.W., Kurtz, R.D., Jones, A.G. and Boerner, D.E., 1993. A quantitative methodology for determining the dimensionality of conductivity structure and the extraction of regional impedance responses from magnetotelluric data. *Geophys. J. Int.,* 115: 1095-1118

87) GSI, 2000. *Seismotectonic atlas of India and its environs*. pp.87, Geological Survey of India, India.

88) Gupta, H.K. and Narain, H., 1967. Crustal structure in Himalayas and Tibet Plateau region from a surface wave dispersion. *Bull SeismoL Soc. Am.,* 57 (2): 235-248

89) Gupta, S., Das, A., Goswami, S., Modak, A., and Mondal, S., 2010, Evidence for Structural Discordance in the Inverted Metamorphic Sequence of Sikkim Himalaya: Towards Resolving the Main Central Thrust Controversy. *J. Geol. Soc. India*: 75: 3-13

90) Gutenberg, B. and Richter, C.F., 1954. *Seismicity of the Earth and Associated Phenomena.* Princeton University Press, New Jersey, 310 p

91) Haber, E., Ascher, U., Aruliah, D., and Oldenburg, D. W., 2000. On optimization techniques for solving non linear inverse problems, *Inverse Problems,* 16: 1263-1280

92) Haines, S., Klemperer, S.L., Brown, L., Guo, J., Mechie, J., Meissner, R., Nelson, K.D., Ross, A., Zhao, W., 2003. Crustal thickening processes in central Tibet: implications of INDEPTH III seismic data. *Tectonics*, 22: 1–18

93) Hazarika, P., Ravi Kumar, M., Srijayanthi, G., Solomon Raju, P., Purnachandra Rao, N. and Srinagesh, D., 2010. Transverse Tectonics in the Sikkim Himalaya: Evidence from Seismicity and Focal-Mechanism Data. *Bull. Seismol. Soc. Am.,* 100: 1816-1822, doi: 10.1785/0120090339

94) Heise, W. and Pous, J., 2003. Anomalous phases exceeding 90^o in magnetotellurics: anisotropic model studies and a field example. *Geophys. J. Int.*, 155: 308–318

95) Heise, W., Caldwell, T.G., Bibby, H.M., Brown, C., 2006. Anisotropy and phase splits in magnetotellurics. *Phys. Earth Planet. Inter.,* 158: 107–121

96) Hermance, J. F., 1973. Processing of magnetotelluric data. *Phys. Earth planet. Int.,* 7: 349-364

97) Hermance, J. F., 1979. The electrical conductivity of materials containing partial melt: A simple model from Archie's law. *Geophys. Res. Lett.,* 6: 613–616, doi: 10.1029/GL006i007p00613

98) Hestenes, M.R. and Stiefel, E.L., 1952. Methods of conjugate gradients for solving linear systems, *J. Research Nat. Bur. Standards,* 49: 409-436

99) Hete' nyi, G., Cattin, R., Vergne, J., Na' belek, J.L., 2006. The effective elastic thickness of the India Plate from receiver function imaging, gravity anomalies and thermomechanical modelling. *Geophys. J. Int.,* 167 (3): 1106–1118, URL http:// dx.doi.org/10.1111/j.1365-246X.2006.03198.x.

100) Hirn, A., Sapin, M., Le´pine, J.-C., Diaz, J., Jiang, M., 1997. Increase in melt fraction along a south–north traverse below the Tibetan plateau: evidence from seismology. *Tectonophysics*, 273: 17–30

101) Hirn, A., Diaz, J., Sapin, M. and Veinante, J. L., 1998. Variation of shear wave residuals and splitting parameters from array observations in southern Tibet. *Pure Appl. Geophys.,* 151: 407–431

102) Hirn, A., G. Jobert, G. Wittlinger, X. Zhong-Xin, and G. En-Yuan., 1984. Main features of the upper lithosphere in the unit between the High Himalayas and the Yarlung Angbo Jiang suture, *Ann. Geophys.,* 2: 113– 118

103) Hirn, A., Sapin, M., 1984. The Himalayan zone of crustal interaction—suggestions from explosion seismology. *Ann. Geophys.,* 2 (2), 123–130

104) Hohmann, G.W., 1971. Elecromagnetic scattering by conductors in the earth near a line source of current. *Geophysics*, 36: 101-131

105) Huang, S. Pollack, H.N and Shen, Po-Yu., 2000. Temperature trends over the past five centrures reconstructed from borehole temperature. *Nature,* 403: 756-758

106) Hyndman, R.D., Shearer, P.M., 1989. Water in the lower continental crust; modelling magnetotelluric and seismic reflection results. *Geophys. J. R. Astr. Soc.*, 98 (2): 343–365

107) Ichihara, H. and Mogi, T., 2009. A realistic 3-D resistivity model explaining anomalous large phase Magnetotelluric phases: the L-shaped conductor model. *Geophys. J. Int*., 179: 14-17

108) IS: 1893-2002. Indian Standard Criteria for Earthquake Resistant Design of Structures, Bureau of Indian Standards, New Delhi.

109) Israil, M., Tyagi, D.K., Gupta, P.K. and Sri Niwas., 2008. Magnetotelluric investigations for imaging electrical structure of Garhwal Himalayan corridor, Uttarakhand, India. *J. Earth Syst. Sci*., 117: 189–200

110) Jade, S., Mukul, M., Bhattacharyya, A.K., Vijayan, M.S.M., Jaganathan, S., Kumar, A., Tiwari, R.P., Kumar, A., Kalita, S., Sahu, S.C., Krishna, A.P., Gupta, S.S., Murthy, M.V.R.L., and Gaur, V.K., 2007, Estimates of interseismic deformation in Northeast India from GPS measurements. *Earth Planet. Sci. Lett.,* 263: 221-234

111) Jiménez-Munt, I., Fernandez, M., Verges, J and Platt, J.P., 2008. Lithosphere structure underneath the Tibetan Plateau inferred from elevation, gravity and geoid anomalies, *Earth Plant. Sci. Lett.,* 267:276-289

112) Jin, Y., McNutt, M.K., Zhu, Y.S., 1996. Mapping the descent of Indian and Eurasian plates beneath the Tibetan Plateau from gravity anomalies. *J. Geophys. Res.*, 101: 11, 275–11, 290

113) Jiracek, G.R., 1990. Near-surface and topographic distortions in electromagnetic induction, *Surv. geophys.*, 11, 163–203

114) Jones, A. G., 1988. Static shift of magnetotelluric data and its removal in a sedimentary basin environment: *Geophysics*, 53: 967–978

115) Jones, A.G and Price, A.T. 1970. The perturbations of alternating geomagnetic fields by conductivity anomalies. *Geophys. J.R. astr. Soc.*, 20 : 317-334

116) Jones, A.G., 1983. The problem of "current channelling": a critical review, *Geophys. Surv. (now Surv. Geophys.)*, 6: 79-122

117) Jones, A.G.,1983. On the equivalence of 'Niblett' and 'Bostick' transformations in the magnetotelluric method, *Geophys. Prosp.*, 27: 876-901

118) Jones, F. W., and Pascoe, L. J., 1972. The perturbation of alternating geomagnetic fields by three-dimensional conductivity inhomogeneities: *Geophys. J. Roy. Astr. Soc.*, 27: 479-485

119) Jones,A.G., and Dumas, I., 1993, Electromagnetic images of a volcanic zone. *Phys. Earth Plan. Int.*, 81: 289–314

120) Joshi, J.C, Sengupta, S. and Kandpal, G.C. 2010. Macroseismic Study of 20th May 2007 Sikkim Earthquake – Its Seismotectonic Implications for the Region, *J. Geol. Soc. India.*,75: 383-392

121) Kaila, K.L., Tripathi, K.M. and Dixit, M.M., 1984. Crustal structure along Wular lake-Gulmarg-Naoshera profile across Pir Panjal range of the Himalayas from deep seismic soundings. *J. Geol. Soc. India.*, 25(11): 706-718

122) Kaufman, A.A., and Keller, G.V., 1981. *Magnetotelluric prospecting*. Elsevier Sci. Pub. Co. 595pp; ISBN:0-444-418636

123) Kayal, J.R. and Bhattacharya, S.N., 2006. Seismicity of the Himachal Himalaya: Constraint from local Seismic Network. *Geol. Surv. India Sp. Pub.*, 85: 71-79

124) Kayal, J.R., 1996. Precursor seismicity, foreshocks and aftershocks of the Uttarkashi earthquake of October 20, 1991 at Garhwal Himalaya. *Tectonophysics*, 263: 339-345

125) Kayal, J.R., 2001. Microearthquake activity in some parts of the Himalaya and the tectonic model. *Tectonophysics*, 339, 331-351

126) Kayal, J.R., De, Reena and Chakraborty, P., 1993. Microearthquakes at the main boundary thrust in eastern Himalaya and the present-day tectonic model. *Tectonophysics*, 218, 375-381

127) Kayal, J.R., Ghosh, B., Chakraborty, P. and De, R., 1995. Aftershock sequence of the Uttarkashi earthquake of October 20, 1991 by a temporary microeqrthquake network. *Geol. Soc. India. Mem.,* 30: 25-41

128) Kayal, J.R., Santanu, B., Saurabh, B., Aurabh, B., Gautam, J.L., Arefiev, S.S. and Tatevossian, R., 2011. The September 2011 Sikkim deeper Centroid Mw 6.9 Earthquake: Role of Transverse Faults in Eastern Himalaya. *DST new letter*. Deep Continental Studies in India, v.21(2), pp.13-16

129) Kayal, J.R., Sing, O.P., Charaborthy, P.K and Karunakar, G., 2001. Aftershock sequence of the Chamoli earthquake of March 1999 in the Garhwal Himalaya, *Bull. Seismol. Soc. Am.* 93: 109–117,

130) Khattri, K., Chander, R., Gaur, V., Sarkar, I. and Kumar, S., 1989. New seismological results on the tectonics of the Garhwal Himalaya, *Earth planet. Sci. Lett.,* 98: 91–109

131) Khattri, K., Wyss, M., Gaur, V.K., Saha, S.N. and Bansal, B.K., 1983. Local seismic activity in the region of the Assam gap, northeast India. *Bull. Seism. Soc. Am*., 73, 459-469

132) Khattri, K.N. and Tyagi, A.K., 1983. Seismic patterns in the Himalayan plate boundary and identification of areas of high seiemic potential. *Tectonophysics*, 96: 281-297

133) Khattri, K.N., 1992. Local seismic investigations in the Garwal-Kumaon Himalaya. *Geol. Soc. India Mem.*, 23, 45-66

134) Kious, W.J. and Tilling, R.I., 1994, *This Dynamic Earth: The Story of Plate Tectonics.* U.S. Geological Survey, Washington, D.C., 77 p.

135) Kisak, E and Silveser, P. 1975. A finite element package for magnetotelluric modeling. *Comp. Phys. Comm.*, 10: 421-433

136) Kumar, P., Yuan, X., Kind, R. and Kosarev, G., 2005. The lithosphere-asthenosphere boundary in the Tien Shan-Karakoram region from S receiver functions: Evidence for continental subduction. *Geophys. Res. Lett*., 32, L07305, doi: 10.1029/2004GL022291.

137) Kumar, P., Yuan, X., Kind, R., Ni, J., 2006. Imaging the colliding Indian and Asian lithospheric plates beneath Tibet, 23. *J. Geophys. Res.*, 111, B06308. doi:10.1029/ 2005JB003930.

138) Kumar, P., Yuan, X., Ravi Kumar, M., Kind, R., Li, X. and Chadha. R.K., 2007. The rapid drift of the Indian tectonic plate. *Nature*. 449, doi:10.1038/nature06214

139) Kumar, P., Yuan, X.H. and Kind, R., 2006. Imaging the colliding Indian and Asian lithospheric plates beneath Tibet: *J. Geophys. Res.*, 111, B06308

140) Lanczos, C. 1961. *Linear Differential Operators*. Van Nostrand, London.

141) Larsen, J. C., 1977. Removal of local surface conductivity effects from low frequency mantle response curves. *Acta Geodaet., Geophys. et Montanis L Acad. Sci. Hung.* 12: 183-186

142) Larson, K., Burgmann, R., Bilham, R. and Freymueller, J.T., 1999. Kinematics of the India-Eurasia collision zone from GPS measurements. *J. Geophys. Res.*, 104: 1077-1093

143) LaTorraca, G.A, Madden, T.R., Korrinaga, J., 1986. An analysis of the magnetotelluric impedance for three dimensional conductivity structures. *Geophysics*, 51: 1819-1829

144) Lave, J. and Avouac, J.P., 2001. Fluvial incision and tectonic uplift across the Himalayas of central Nepal. *J. Geophys. Res.*, 106, 26561–26591

145) Le Fort, P., 1988. Granites in the tectonic evolution of the Himalaya – a model for its genesis and emplacement. *Amer. J. Geophys. Res.*, 86: 10545-10568

146) Le Fort, P., 1997, *Evolution of the Himalaya*, *in* Yin, A., and Harrison, M., eds., *The tectonic evolution of Asia*: Cambridge, Cambridge University Press, p. 95–109

147) Le Fort, P., Cuney, M., Deniel, C., France-lanord, C., Sheppard, S.M.F., Upreti, B.N. & Vidal, P., 1987. Crustal generation of the Himalayan leucogranites, *Tectonophysics*, 134: 39–57

148) Ledo, J. and Jones, A., 2005. Temperature of the upper mantel beneath the Intermontane Belt, northern Canadian Cordillera, determined from combining mineral composition, electrical conductivity laboratory studies and magnetotelluric field observations. *Earth Planet. Sci. Lett.* 236: 258-268

149) LeFort, P., 1975. Himalaya: the collided range. Present knowledge of the continental arc. *Am. J. Sci*., 275: 7-44.

150) Lemonnier , C., Marquis, G., Perrier, F., Avouac, J. P., Chitrakar, G., Kafle ,B.,

Sapkota, S., Gautam, U., Tiwari, D. and Bano, M., 1999. Electrical structure of the Himalaya of central Nepal: high conductivity around the mid crustal ramp along the MHT. *Geophys. Res. Lett*., 26: 3261–3264

151) Lepine, J.C., Hirn., A., Pandey, M.R. and Tater, J.M., 1984. Features of the P-waves propagated in the crust of the Himalayas. *Ann. Geophysicae*, 2: 119-121

152) Lewis, C.L.E., 2009. Doctoring geology: In medical origins of the Geological Society. In: Lewis C.L.E & KNELL. S.J. (eds) The Making of the Geological Society of London. Geological Society, London, Special publications, 317: 49-92

153) Lezaeta, P. and Haak, V., 2003. Beyond magnetotelluric decomposition: Induction, current channeling, and magnetotelluric phases over 90 degree. *J. Geophys. Res.,* 108, 2305, doi:10.1029/2001JB000990.

154) Li, S., Unsworth, M. J, Booker J. R, Wei, W., Tan, H. and Jones, A.G., 2003. Partial melt or aqueous fluid in the midcrust of Southern Tibet? Constraints from INDEPTH magnetotelluric data. *Geophys. J. Int.,* 153: 289–304

155) Li, Y.G., 2002. A finite-element algorithm for electromagnetic induction in two-dimensional anisotropic conductivity structures, *Geophys. J. Int.,* 148: 389–401

156) Lilley, F. E. M., 1998. Magnetotelluric tensor decomposition: 2. Examples of a basic procedure: *Geophysics,* 63: 1898–1907

157) Lilley, F.E.M. 1993. Magnetotelluric analysis using Mohr circles. *Geophysics,* 58: 1498-1506

158) Lilley, F.E.M. and Weaver, J.T., 2010. Phases greater than 90 degrees in MT data: analysis using dimensionality tools, *J. appl. Geophys.,* 70: 9–16

159) Livelybrooks, D., Mareschal, M., Blais, E. and Smith, J.T., 1996. Magnetotelluric delineation of the Trillabelle massive sulfide body in Sudbury, Ontario, *Geophysics,* 61: 971–986

160) Loewenthal, D. and Landisman, M., 1973. Theory for magnetotelluric observations on the surface of a layered anisotropic half space, *Geophys. J. R. astr. Soc.,* 35: 195–214

161) Lyon Caen, H. and Molnar, P., 1983. Constraints on the structure of the Himalaya from an analysis of the gravity anomalies and a flexural model of the lithosphere, *J.*

Geophys. Res., 88: 8171–8191

162) Lyon-Caen, H. and Molnar, P. 1985. Gravity anomalies, flexure of the Indian plate, and the structure, support and evolution of the Himalaya and Ganga Basin, *Tectonics*, 4: 513-538.

163) Mackie, R. L, 2002, User manual and software documentation for two-dimensional inversion of magnetotelluric data, GSY-USA, Inc., 2261 Market Street, PMB 643, San Francisco, California 94114, anisotropy version 6.7.

164) Mackie, R. L. and Madden, T. R. 1993. Three-dimensional magnetotelluric inversion using conjugate gradients. *Geophys. J. Int.*, 115: 215-229

165) Mackie, R. L., Livelybrooks, D. W., Madden, T. R., and Larsen, J. C., 1997, A magnetotelluric investigation of the San Andreas fault at Carrizo Plain, California: *Geophys. Res. Lett.*, 24, 1847–1850

166) Mackie, R.L., Bennet, B.R. and Madden, T.R., 1988. Long-period magnetotelluric measurements near the central California coast. *Geophys. J. Int.*, 95: 181–194

167) Madden, T and Nelson, P., 1964. A defense of Cagnaird's magnetotelluric method: MIT project NR : 371-401

168) Madden, T. and Swift, C.M., 1969. Magnetotellurics investigations of electrical conductivity of the crust and upper mantle, in Hart, J., Ed., The Earth's curst and Upper mantle. *Am. Geophys. union, Geophys*, Monogr. 13

169) Madden, T. R., 1972. Transmission system and network analogies to geophysical forward and inverse problems, *Rep.* 72-3, *Dep. of Earth and Planet. Sci., Mass. Inst. of Technol., Cambridge.*

170) Maggi, A., Jackson, J.A., Priestley, K. & Baker, C., 2000b. A re-assessment of focal depth distributions in southern Iran, the Tien Shan and northern India: do earthquakes really occur in the continental mantle?, *Geophys. J. Int.*, 143: 629–661

171) Mahesh, P., Gupta, S., Rai, S., Sarma, P.R., 2012. Fluid driven earthquakes in the Chamoli Region, Garhwal Himalaya: evidence from local earthquake tomography. *Geophys. J. Int.* 191(3): 1295–1304

172) Marquis, G., Jones, A.G. and Hyndman, R.D., 1995. Coincident conductive and

reflective lower crust across a thermal boundary in southern British Columbia, Canada. *Geophys. J. Internat.*, 20: 111-131

173) Maxwell, J.C., 1881. *A Treatise on Electricity and Magnetism*, 2nd edn, Clarendon, Oxford.

174) McKenzie, D.P and Parker, R.L. 1967 The North Pacific: an Example of Tectonics on a Sphere. *Nature*, 216(5122): 1276-1280

175) McNeice, G.W. and Jones, A.G., 2001. Multisite, multifrequency tenser decomposition of magnetotelluric data. *Geophysics*, 66: 158–173

176) Mehanee, S. and Zhdanov, M.S., 2002. Two dimensional magnetotellruicinversion of blocky geoelectric structures. *J. Geophys. Res.*, 107(B4), EPM:1-12

177) Menke, W., 1984. *Geophysical Data Analysis: Discrete Inverse Theory*. Vol. 45. International Geophysics Series.

178) Minister, J.B., Jordan, T.H., Molnar, P. and Haines, E., 1974. Numerical modeling of instantaneous plate tectonics. *Geophys. J. R. Astr. Soc.*, 36: 541-576

179) Mishra, D.C. and Rajasekhar, R.P., 2006, Crustal structure at the epicentral zone of the 2005 Kashmir (Muzaffarabad) earthquake and seismotectonic significance of lithospheric flexure: *Curr. Sci.*, 90: 1406-1412

180) Mitra, G., Bhattacharyya, K. and Mukul, M., 2010. The Lesser Himalayan Duplex in Sikkim: Implications for Variations in Himalayan Shortening. *J. Geol. Soc. Ind*., 75: 289-301

181) Mitra, S., Prestley, K., Bhattacharyya, A.K. and Gaur, V.K., 2005. Crustal structure and earthquake focal depths beneath northeastern India and south Tibet, *Geophys. J. Int.*, doi: 10.1111 j.1365-246X2004.02470.x

182) Mitra, S., Priestley, K., Gaur, V.K., Rai, S.S. and Haines, J., 2006. Variation of Rayleigh wave group velocity dispersion and seismic heterogeneity of the Indian crust and uppermost mantle, *Geophys. J. Int.*, 164: 88–98

183) Mohan, A., Windley, B.F., Searle, M.P., 1989. Geothermobarometry and development of inverted metamorphism in the Darjeeling–Sikkim region of the eastern Himalaya. *J. Metamorph. Geol.*, 7: 95–110

184) Molnar P. and Tapponnier P., 1975. Tectonics of Asia: Consequences and implications of a continental collision. *Science*, 189: 419-426

185) Molnar P., and Tapponnier P., 1978. Active tectonics of Tibet. *J. geophys. Res.* 83: 5361-5375

186) Molnar, P. and Gray, D., 1979. Subduction of continental crust: some constraints and uncertainties. *Geology*, 7: 58-62

187) Molnar, P. and Lyon-Caen, H., 1989. Fault plane solutions of earthquakes and active tectonics of the Tibetan Plateau and its margins. *Gephys. J. R. Astro. Soc*., 99: 123-153

188) Molnar, P., 1984. Structure and tectonics of the Himalaya: Constraints and implication of geophysical data. *Ann. Rev. Earth Planet. Sci.*, 12: 489-518

189) Molnar, P., 1988. A review of geophysical constraints on the deep structure of the Tibetan Plateau, the Himalaya and the Karakoram, and their tectonic implications. *Phil. Trans. R. Soc. Lond. A*, 326: 33-88

190) Molnar, P., Chen, W. P., Fitch, T. J., Tapponnier, P.,Warsi,W. E. K. and Wu, F., 1977. Structure and tectonics of the Himalaya: a brief summary of relevant geophysical observations, in *Himalaya: Sciences de la Terre*, Colloque Internationaux du CNRS no 268, pp. 269–294, Editions du Centre Nationale de la Recherche Scientifique, Paris.

191) Molnar, P., Fitch, T.J. and Wu, F.T., 1973. Fault plane solutions of shallow earthquakes and contemporary tectonics in Asia. *Earth Planet. Sc. Lett.*, 19: 101-112

192) Monsalve, G. et al. 2003. Earthquake locations, depths and source parameters from the Himalaya Nepal Tibet seismic experiment: Implications for continental lithospheric depth. Eos 84(46): S22A–-0414

193) Monsalve, G., Sheehan, A., Rowe, C., Rajaure, S., 2008. Seismic structure of the crust andthe upper mantle beneath the Himalayas: evidence for eclogitization of lower crustal rocks in the Indian plate. *J. Geophys. Res.*, 113: B08315. doi:10.1029/ 2007JB005424

194) Monsalve, G., Sheehan, A., Schulte-Pelkum, V., Rajaure, S., Pandey, M and Wu. F. 2006. Seismicity and one-dimensional structure of the Himalayan collision zone: earthquakes in the crust and upper mantle. *J. Geophys. Res.*, 111.

Doi:1029/2005JB004062.

195) Morgan, W. J., 1968. Rises, Trenches, Great Faults, and Crustal Blocks. *J. Geophys. Res.*, 1959-1982

196) Mukul, M., 2000. The geometry and kinematics of the Main Boundary Thurst and related neotectonics in the Darjeling Himalayan fold-and-thrust belt. West Bengal, India. *J. Struct. Geol.,* 22: 1261-1283

197) Mukul, M., 2010. First-order kinematics of wedge-scale active Himalayan deformation: Insights from Darjiling–Sikkim–Tibet (DaSiT) wedge. *J. Asian Earth Sci*., 39: 645–657

198) Mukul, M., Jaiswal, M. and Singhvi, A.K., 2007. Timing of recent out-of-sequence active deformation in the frontal Himalayan wedge: Insights from the Darjiling sub-Himalaya, India. *Geology*, 35(11): 999-1002

199) Nakata, T., 1972. Geomorphic history and crustal movements of foothills of the Himalaya. Sendai Institute of Geography, Tohuku University, 77 p.

200) Nakata, T., K. Otsuki, and S. H. Khan (1990). Active faults, stress field, and plate motion along Indo-Eurasian plate boundary, *Tectonophysics* 181, 83–95

201) Narula, P.L., Acharyya, S.K., Banerjee, J., 2000. *Seismotectonic Altas of India and its environs.* Geological Survey of India, Calcutta, India, 87 pp.

202) Nath, S.K., Vyas, M., Pal, I. and Sengupta, P., 2005. A seismic hazard scenario in the Sikkim Himalaya from seismotectonics, spectral amplifications, source parameterization, and spectral attenuation laws using strong motion seismometry. *J. Geophys. Res*., 110, B01301, doi: 10.1029/2004JB003199.

203) Nelson, K. D., Zhao, W., Brown, L.D., Kuo, J., Che, J., Liu, X., Klemperer, S.L., Makovsky, Y., Meissner, R., Mechie, J., Kind, R., Wenzel, F., Ni, J., Nabelek, J., Chen, L., Tan, H., Wei, W., Jones, A.G., Booker, J., Unsworth, M.J., Kidd, W.S.F., Hauck, M., Alsdorf, D., Ross, A., Cogan, M., Wu, C., Sandvol, E. and Edwards, M., 1996. Partially molten middle crust beneath southern Tibet: synthesis of project INDEPTH results. *Science,* 274: 1684–1687

204) Neogi, S., Dasgupta, S and Fukuota, M., 1998. High P-T-plymetamorphism,

dehydration melting and generation of migmatites and granites in the Higher Himalayan crystalline complex, Sikkim, India. *J. of Petrology*, 39: 61-99

205) Newman, G. A. and Alumbaugh, D. L. 2000. Three-dimensional magnetotelluric inversion using non-linear conjugate gradients. *Geophys. J. Int.*, 140(2): 410-424

206) Ni, J. and Barazangi, M., 1983. High-frequency seismic wave propagation beneath the Indian Shield, Himalayan Arc, Tibetan Plateau and surrounding regions: high uppermost mantle velocities and efficient Sn propagation beneath Tibet. *Geophys. J. R. Astr. Soc.*, 72: 665–689

207) Ni, J. and Barazangi, M., 1984. Seismotectonics of the Himalayan collision Zone: geometry of the underthrusting Indian plate beneath the Himalaya. *J. Geophys. Res.*, 89: 1147-1163

208) Ni, J.F., 1989. Active tectonics of the Himalaya. *Proc. Indian Acad. Sci. (Earth Planet Sci)*, 98: 71-89

209) Oldenburg, D.W., 1990. Inversion of electromagnetic data: an overview of new techniques. *Geophys. Surv.*, 11: 231-270

210) Oldham, T., 1883. *Catalogue of Indian earthquakes*. Geol. Surv. India Mem., 19, 163-215

211) Palacky, G.J., 1987. Resistivity characteristics of geological targets, In Nabighian, M.N., ed., Electromagnetic methods in Applied Geophysics Theory: Tulsa. Okla., Society of Exploration Geophysicists. Vol. 1, P 53-129

212) Pandey, M.R., Tandukar, R.P., Avouac, J.P., Lave, J. and Massot, J.P., 1995. Interseismic strain accumulation on the Himalayan crustal ramp (Nepal). *Geophys. Res. Lett*., 22: 751-754

213) Pandey, M.R., Tandukar, R.P., Avouac, J.P., Vergne, J. & Heritier, T., 1999. Seismotectonics of the Nepal Himalaya from a local seismic network, *J. Asian Earth Sci.*, 17, 703–712

214) Parasnis, D.S., 1986. Principles of Applied Geophysics. 4TH edition. Chapman & Hall Publisher

215) Parker, R.L., 1983. The magnetotelluric inverse problem. *Geophys. Surv*., 6: 5-25

216) Parker, R.L., 1980. The inverse problem of electromagnetic induction: existence and construction of solution based upon incomplete data, *J. Geophys. Res.,* 85: 4421–4428

217) Parkinson, W.D. 1962. The influence of continents and oceans on geomagnetic variations, *Geophys. J. R. Astr. Soc.,* 6: 441-449

218) Pascoe, L. J. and Jones, F. W., 1972. Boundary conditions and calculation of surface values for the general two-dimensional electromagnetic induction problem, *Geophys. J. R. Astr. Soc.*, 27: 179-193

219) Patro, P.K. and Harinarayana, T., 2009. Deep geoelectric structure of the Sikkim Himalayas (NE India) using magnetotelluric studies. *Phys. Earth Planet. Int*., 173: 171-176

220) Patton, H., 1980. Crust and upper mantle structure of the Eurasian continent from the phase velocity measurements and Q of surface waves. *Rev. Geophys.,* 18: 605-625

221) Pearson, O. N., and DeCelles, P. G., 2005, Structural geology and regional tectonic significance of the Ramgarh thrust, Himalayan fold-thrust belt of Nepal. *Tectonics*, 24(4): TC400810.1029/2003TC001617.

222) Pedersen, B., 1979. Constrained inversion of potential field data. *Geophys. Prospec.,* 27: 726-748

223) Pedersen, B., 1982. The magnetotelluric impedance tensor - its random and bias errors. *Geophys. Prosp.,* 30: 188-210

224) Pedersen, L.B., 1988. Some aspects of magnetotelluric field procedures. *Surveys in Geophysics*, 9: 245-257

225) Pek, J. and Verner, T., 1997. Finite-difference modeling of Magnetotelluric fields in two dimensional anisotropic media. *Geophys. J. Int*., 128: 505-521

226) Peltzer, G., and Saucier, F., 1996. Present-day kinematics of Asia derived from geological fault rates, *J. Geophys. Res.,* 101: 27943 – 27956

227) Pous, J., Munoz, G., Heise, W., Melgarej, J.C., Quesada, C., 2004. Electromagnetic imagining of Variscan crustal structures in SW Iberia: the role of interconnected graphite. *Earth Planet. Sci. Lett.,* 217: 435–450

228) Powell, C.M. and Conaghan, P.J., 1973. Plate tectonics and the Himalayas. *Earth*

Planet. Sci. Lett., 20: 1–12

229) Powell, C.M., 1979. A speculative tectonic history of Pakistan and surroundings – Some constraints from Indian Ocean. *In:* Geodynamics of Pakistan, A. Farah and A.K. Dee Jong (eds.). Geological Survey of Pakistan, Quetta, pp 5-24

230) Powers, P.M., Lillie, R.J. and Yeats, R.S., 1998. Structure and shortening of the Kangra and Dehradun reentrants. *Geol. Soc. Am. Bull*., 110: 1010-1027

231) Priestley, K., Debayle, E., McKenzie, D. and Pilidou, S., 2006. Upper mantle structure eastern Asia from multimode surface waveform tomography. *J. Geophys Res*., 111:B10304. doi:10.1029/2005JB004082

232) Priestley, K., Jackson, J. and McKenzie, D., 2008. Lithospheric structure and deep earthquakes beneath India, the Himalaya and southern Tibet. *Geophys. J. Int.*, 172: 345–362. doi:10.1111/j.1365-246X.2007.03636.x

233) Qureshy, M. N. and Midha, R. K., 1986. Deep crustal signature in India and contiguous regions from satellite and ground geophysical data. *In:* Reflection seismology, the continental crust, M. Barazangi and L. Brown (eds.). *Geodynamic series 14*, AGU Pub., pp. 77-94

234) Qureshy, M.N. and Warsi, W.E.K., 1980. A Bouguer anomaly map of India and its relation to broad tectonic elements of the sub-continent. *Geophys. J.R. Astron. Soc*., 61: 235-242

235) Qureshy,M.N. and Kumar, S., 1992. Isostasy and neotectonic of north west Himalaya and foredeep. *Mem. Geol. Soc. India*, 23:201-222

236) Rai, S.S., Priestley, K., Gaur, V.K., Mitra, S., Singh, M.P. and Searle, M., 2006. Configuration of Indian Moho beneath the NW Himalaya and Ladakh. *Geophys. Res. Lett.*, 33: L15308. doi:10.1029/2006GL026076

237) Rai, S.S., Priestley, K., Suryaprakasham, K., Srinagesh, D., Gaur, V.K. and Du, Z., 2003. Crustal shear velocity structure of the south Indian shield. *J. Geophys. Res*., 108(B2): 2088, doi: 10.1029/2002JB001776.

238) Rajendra Prasad, B., Klemperer, S.L., Rao, V.V., Tewari, H., Khare, P., 2011. Crustal structure beneath the Sub-Himalayan fold-thrust belt, Kangra recess, northwest India,

from seismic reflection profiling: implications for Late Paleoproterozoic orogenesis and modern earthquake hazard. *Earth Planet. Sci. Lett.*, 308 (1–2), 218–228

239) Ramesh, D.S., Kumar, M.R., Devi, E.U., Raju, P.S. and Yuan, X., 2005. Moho geometry and upper mantle images of northeast India. *Geophys. Res. Lett.*, 32: 14301-14304, doi: 10.1029/2005GL022789.

240) Rao, N.P., Ravi Kumar, M and Tsukuda, T., 2003. Current deformation of the Himalaya-Tibet-Buram Seismic belt: inferences from seismic activity and strain rate analysis, *J. Geodynamics*, 36: 485-496

241) Rastogi, B.K., 1974. Earthquake mechanisms and plate tectonics in the Himalayan region. *Tectonophysics*, 7: 137-157

242) Ravi Kumar, M., Hazarika, P., Srihari Prasad, G., Singh, A. and Saha, S., 2012. Tectonic implications of the September 2011 Sikkim earthquake and its aftershocks. *Curr. Sci.*, 102: 788-792

243) Ray, S.K., 2000. Culmination zones in Eastern Himalaya. Geological Survey of India Spec. Pub. 55: 85–94

244) Reddy, I. K. and Rankin, D., 1971. Magnetotelluric effect of dipping anisotropies, *Geophys. Prosp.*, 19: 84–97

245) Rodi, W.L. and Mackie, R.L., 2001. Nonlinear conjugate gradients algorithm for 2-D magnetotelluric inversion. *Geophysics*, 66: 174–187.

246) Rodi, W.L., 1976. A technique for improving the accuracy of finite element solutions for magnetotelluric data, *Geophys. J. R. astr. Soc.*, 44: 483-506

247) Sasaki, Y.: 2001. 'Full 3-D Inversion of Electromagnetic Data on PC', *J. Appl. Geophys.*, 46: 45–54

248) Schelling, D, and Arita, K., 1991. Thrust tectonics crustal shortening and the structure of the Far Eastern Nepal Himalaya, *Tectonics*,10: 851-862

249) Schmucker, 1963. Anomolies of geomagnetic variations in the southwestern United states, *J. Geomagn. Geoelectr.*, 15: 193-221

250) Schmucker, U. 1971. Interpretation of induction anomalies above non-uniform surface layers. *Geophysics*, 36: 156-165

251) Schmucker, U., 1970. Anomalies of geomagnetic variations in the southwestern United states. Bull. Scripps Inst. Oceanog. 13, Univ. Calif. Press.

252) Schulte-Pelkum, V., Monsalve, G., Sheehan, A., Pandey, M.R., Sapkota, S., Bilham, R.,Wu, F., 2005. Imaging the Indian subcontinent beneath the Himalaya. *Nature* 435 (7046): 1222–1225. doi:10.1038/nature03678.

253) Schuster, A. 1889. The Diurnal variation of terrestrial magnetism. *Phil. Trans. Roy. Soc. Lon.,* A180: 467-518

254) Seeber, L. and Armbruster, J.G., 1981. Great detachment earthquakes along the Himalayan arc and long-term forecasting. *In:* Earthquake Prediction – An International Review. *Manrice Ewing Ser., Am. Geophys. Union,* 4: 259-277

255) Seeber. L., Armbruster, J. and Quittmeyer, R.C., 1981. Seismicity and continental subduction in the Himalayan arc, *in Zagros–Hindukush–Himalaya Geodynamic Evolution*, pp.215–242, ed. Gupta, H., Delany, F., American Geophysical Union, Geodynamics Series 3.

256) Selway, K., Hand, M., Payne, J.L., Heinson, G.S. and Reid, A., 2011. Magnetotelluric constraints on the tectonic setting of Grenville-aged orogenesis in central Australia. *J. Geol. Soc. Lond.,* 168: 251– 264

257) Silvester, P. and Haslam, C.R.S., 1972. Magnetotelluric modelling by the finite element method. *Geophysical Prospecting*, 20: 872-891

258) Simpson, F. and Bahr, K., 2005. Practical magnetotellurics. University press, Cambridge, UK.

259) Sims, W. E., Bostick, F. X. and Smith, H. W., 1971. The estimation of magnetotelluric impedance tensor elements from the measured data, *Geophysics*, 36*:* 938-942

260) Sims, W.E. and Bostick, F.X., 1967. Methods of magnetotelluric analysis, Tech. rep. 58, Electr. Geophys. Res. Lab., Univ. of Texas.

261) Singh, A., Kumar, M. R. and Raju, P. S., 2010. Seismic structure of the underthrusting Indian crust in Sikkim Himalaya. *Tectonics*, 29, doi:10.1029/2010TC002722

262) Singh, A., Kumar, M.R. and Raju, P.S., 2007. Mantle deformation in Sikkim and adjoining Himalaya: Evidence for a complex lowpattern, *Phys. Earth planet. Inter.,* 164: 232–241

263) Singh, A., Kumar, M.R., Raju, P.S. and Ramesh, D.S., 2006. Shear wave anisotropy of the northeastern Indian lithosphere, *Geophys. Res. Lett.*, 33, L16302, doi:10.1029/2006GL026106.

264) Sinha-Roy, S., 1982. Himalayan Main Central Thrust and its implications for Himalayan inverted metamorphism. *Tectonophysics*, 84: 197–224

265) Sinha-Roy, S., 1973. Tectonic evolution of the Darjeeling Himalayas. *Quarterly J. Geol.,* Mining and Metallurgical Society of India 48: 167- 178

266) Siripunvaraporn, W., Egbert, G., and Lenbury, Y. 2002. Numerical accuracy of magnetotelluric modeling: A comparison of finite difference approximations. *Earth Planets Space*, 54: 721-725

267) Siripunvaraporn, W., Egbert, G., Lenbury, Y., and Uyeshima, M. 2005. Three dimensional magnetotelluric inversion: data-space method. *Phys. Earth Planet. Inte.*, 150: 3-14.

268) Smith, J. T. and Booker, J.R., 1991. Rapid inversion of two-dimensional magnetotelluric data. *J. Geophys Res.,* 96: 3905-3922

269) Smith, J.T., 1997. Estimating galvanic-distortion magnetic fields in magnetotellurics. *Geophys. J. Int.,* 130: 65–72

270) Snieder, R., 1998. The role of nonlinearity in inverse Problems, *Inverse Problems,* 14: 387-404

271) Solon, K.D., Jones, A.G., Nelson, K.D., Unsworth, M.J., Kidd, W.S.F., Wei, W., Tan, H., Jin, S., Deng, M., Booker, J.R., Li, S., Bedrosian, P., 2005. Structure of the crust in the vicinity of the Banggong-Nujiang suture in central Tibet from INDEPTH magnetotelluric data. *J. Geophys. Res.,* 110 (B10), 20

272) Spitz, S., 1985. The magnetotelluric impedance tensor properties with respect to rotations. *Geophysics*, 50: 1610-1617

273) Sripanya, W., 2013. Regularized inverse problem of magnetometric resistivity response over a layered earth. *Adv. Studies Theor. Phys.,* 7(4): 183 - 190

274) Swift, C.M., 1967. A magnetotelluric investigations of an electrical conductivity anomaly in the southwestern United States, Ph. D. dissertation, MIT

275) Tandon, A.N. and Srivastava, H.N., 1975. Focal mechanisms of some recent Himalayan earthquakes and regional plate tectonics. *Bull. Seism. Soc. Am.*, **65:** 963-969

276) Tapponnier, P. and Molnar, P., 1976. Slip-line field theory and large scale tectonics. *Nature*, London, 264: 319-324

277) Tapponnier, P. and Molnar, P., 1977. Active faulting and tectonics of China, *J. Geophys. Res.*, 82: 2905-2930

278) Tarantola, A. 1987. *Inverse problem theory*, Elsevier

279) Tarantola, A., 2004. *Inverse Problem Theory and Methods for Model Parameter Estimation*. Society for Industrial and Applied Mathematics, Philadelphia, pp342

280) Telford, W.M., Geldart, L.P and Sheriff, R.E., 1990. *Applied Geophysics*, Second Edition, Cambridge University Press, Cambrige, New Yark.

281) Thakur, V,C ., 2008. Active tectonics of the Himalaya. *Golden Jublee Mem. Geol. Soc. India*. 66: 227-258

282) Thiel, S., Heinson, G., Gray, D. R. and Gregory, R.T., 2009. Ophiolite emplacement in NE Oman: constraints from magnetotelluric sounding, *Geophys. J. Int.*, 176: 753–766

283) Tick, J. L., 1963. In: M. Rosenblatt (Editor), *Time Series Analysis*. Wiley, NewYork. 197 pp.

284) Tikhonov, A. and Arsenine, V. 1977. *Solutions of ill-posed problems*, Wiley, New York.

285) Tikhonov, A.N., 1950. On the determination of electric characteristics of deep layers of the earth's crust. *Dokl. Akad. Nauk*. S.S.S.R. 73: 295-297

286) Tiwari, V. M., Rajashekhar, R.P. and Mishra, D.C., 2008, Gravity Anomaly, Lithospheric Structure and Seismicity of Western Himalayan Syntaxis. *J. Seismology*. doi:10.1007/s10950-008-9102-6.

287) Tiwari, V.M., Vyghreswara Rao, M.B.S., Mishra, D.C. and Singh, B., 2006. Crustal structure across Sikkim Himalaya from new gravity and magnetic data. *Earth Planet. Sci. Lett*., 247: 61-69

288) Tournerie, B. and Chouteau, M., 1998. Deep conductivity structure in Abitibi, Canada, using long dipole magnetotelluric measurements. *Geophys. Res. Lett.* 25: 2317– 2320

289) Umadevi , E, Kumar, P. and Ravi Kumar, M. 2011. Imaging the Indian lithosphere beneath the eastern Himalayan region. *Geophys. J. Int.,* 187: 631-641

290) Unsworth, M. J., Wei, W., Jones, A.G., Li, S., Bedrosian, P.A., Booker, J.R., Jin, S. and Deng M., 2004. Crustal and upper mantle structure of Northern Tibet imaged with magnetotelluric data. *J Geophys. Res.*, 109:B02403. doi: 10.1029/2002JB002305

291) Unsworth, M.J., Jones, A.G., Wei, W., Marquis, G., Gokarn, S. and Spratt, J., 2005. Crustal rheology of the Himalaya and Southern Tibet inferred from magnetotelluric data. *Nature*, 438: 78–81. doi:10.1038/nature04154

292) Valdia, K.S. 1981. Tectonics of the central sector of the Himalaya, In Zagros, HinduKush, Himalaya, Geodynanic Evolution. *Gedyn. Ser., Am. Geophys. Union*. 3: 87-110

293) Valdiaya, K.S., 2010. The making of India-Geodynamic Evolution. Macmillan Publishers India Ltd., 816p

294) Valdiya, K.S., 1976. Himalayan transverse faults and their parallelism with subsurface. Tectonophysics, 32: 353- 355

295) Valdiya, K.S., 1980. The two intracrustal boundary thrusts of the Himalaya. *Tectonophysics*, 66: 323-348

296) Valdiya, K.S., 1984. *Aspects of tectonics: Focus on south central Asia*, Tata McGraw-

297) Verma, R.K. and Prasad, K.A.V.L., 1987. Analysis of gravity fields in the northeastern Himalayas and Kohistan region using deep seismic sounding data. *Geophys. J.R. Astro. Soc*., 91, 869-889

298) Vozoff, K. 1972. The magnetotelluric method in the exploration of sedimentary basins, *Geophysics*, 37: 98-141

299) Vozoff, K., 1991. The Magnetotelluric Method. In: NABIGHIAN, M.N. (ed), Electromagnetic Methods in Applied Geophysics. Society of Exploration Geophysicists Publications, Tulsa, 2, Chapter 8, 641-711

300) Wadia, D.N., 1961. *The Geology of India*, 3rd ed. Macmillan, London.

301) Wannamaker, P. E., 2005, Anisotropy versus heterogeneity in continental solid earth electromagnetic studies, *Geophys. Surveys*, 26: 733-765

302) Wannamaker, P.E. and Stodt, J.A., 1987. A stable finite element solution for two-dimensional magnetotelluric modelling. *Geophys. J. R. astr. Soc.,* 88: 277–296

303) Wannamaker, P.E., 1991. Advances in three-dimensional magnetotelluric modeling using integral equations. *Geophysics,* 56: 1716-1728

304) Weaver, J.T. and Brewitt-Taylor, C.R., 1978. Improved boundary conditions for the numerical solutions of E-polarization problems in geomagnetic induction problem. *Geophys. J.R.astr. Soc*., 54: 309-317.

305) Weaver, J.T., 1994. *Mathematical Methods for Geo-electromagnetic Induction*. John Wiley and Sons. Inc., New York-Toronto-Singapore.

306) Weckmann, U., Ritter, O. and Haak, V., 2003. A magnetotelluric study of the Damara Belt in Namibia: 2. MT phases over 90_ reveal the internal structure of the Waterberg Fault/Omaruru Lineament. *Phys. Earth Planet. Int.*, 138: 91–112.

307) Wegener, A., 1912. *Die Entstehung der Kontinente. Geologische Rundschau*, 3: 267–292

308) Wei, W. *et al.,* 2001. Detection of widespread fluids in the Tibetan Crust by magnetotelluric studies, *Science,* 292: 716–718

309) Weidelt, P., 1971. The electromagnetic inverse problem in two thin half-sheets. *J. Geophys.,* 37: 649-665

310) Weidelt, P., 1972. The inverse problem of geomagnetic induction. *J. Geophys*., 38: 257-289

311) Weidelt, P., 1975. Electromagnetic induction in three-dimensional structures. *J. Geophys.,* 41: 85-109

312) Weidelt, P. and Kaikkonen, P., 1994. Local 1-D interpretation of magnetotelluric B polarization impedances. *Geophys. J. Int.,* 117: 733–748

313) Wiese, H., 1962. Geomagnetische Tiefentellurik, Teil 2, Die Streichrichtung der Untergrundstrukturen des elekrischen Winderstandes, ersclossen aus geomagnetischen Variationen, *Geofis Pura. Appl.,* 52: 83-103

314) Wilson, J.T., 1965. A new class of faults and their bearing on continental drift. *Nature*, 207, 343-347

315) WinGLink, 2005. WinGLink user's guide, Geosystems SRL, 17 Viale Abruzzi, 20131, Milan, Italy, 2.07.04 ed., www.geosystems.net.

316) Wobus, C.W., Hodges, K.V., Whipple, K.X., 2003. Has focused denudation sustained active thrusting at the Himalayan topographic front? Geology 31 (10): 861–864

317) Wobus, C.W., Whipple, K.X., Hodges, K.V., 2006. Neotectonics of the central Nepalese Himalaya: constraints from geomorphology, detrital 40ar/39ar thermochronology, and thermal modeling. *Tectonics,* 25 (4), TC4011.

318) Xiao, W., 2004. Magnetotelluric exploration in the rocky mountain foothills, Alberta; Master of Science dissertation, Department of Physics, University of Alberta, Edmonton, Alberta.

319) Yee, E. and Paulson, K.V., 1987. The canonical decomposition and its relationship to other forms of magnetotelluric impedance tensor analysis. *J. Geophys.,* 61:173-189

320) Yin, A., 2006, Cenozoic tectonic evolution of the Himalayan orogen as constrained by along-strike variation of structural geometry, exhumation history, and foreland sedimentation, *Earth Sci. Rev.,* 76: 1– 131

321) Yuan, X., Ni, J., Kind, R., Mechie, J. and Sandvol, E., 1997. Lithospheric and upper mantle structure of southern Tibet from a seismological passive source experiment, *J. Geophys. Res.,* 102(B12): 27.491–27.500

322) Zhang, P., Perersen, L.B., Mareschal, M. and Chouteau, M., 1993. Channeling contribution to tipper vectors: a magnetic equivalent to electrical distortion. *Geophys. J. Inter.,* 113, 693-700

323) Zhang, P., Roberts, R.G. and Pedersen, L.B., 1987. Magnetotelluric strike rules. *Geophysics,* 52: 267-278

324) Zhang, P., Shen, Z., Wang, M., Gan, W., Burgmann, R. and Molnar, P., 2004. Continuous deformation of the Tibetan Plateau from global positioning system data. *Geology,* 32: 809–812

325) Zhdanov, M.S. and Keller, G., 1994, *The Geoelectrical Methods in Geophysical Exploration*, Elsevier, Amsterdam - London - New York - Tokyo, 873 pp

x-x-x